Simulations hémodynamiques pour l'IRM : contrôle qualité, optimisation et intégration à la pratique clinique

Présentée par MORGANE GARREAU
Le 21/11/2023

**Sous la direction de FRANCK NICOUD
et SIMON MENDEZ**

Devant le jury composé de

FRANCK NICOUD	Professeur, IMAG, Univ. Montpellier	Directeur
SIMON MENDEZ	Chargé de recherche, CNRS, Univ. Montpellier	Co-directeur
SEBASTIAN KOZERKE	Professeur, ETH Zürich	Rapporteur
MATTHIAS STUBER	Professeur, CIBM MRI CHUV-UNIL	Rapporteur
ALAIN LALANDE	MCU-PH, Physicien, CHU Dijon Bourgogne	Examinateur
OLIVIER MEYRIGNAC	PU-PH, Radiologue, Assistance Publique - Hôpitaux de Paris	Président du jury
MONICA SIGOVAN	Chargée de recherche, CNRS, CREATIS Lyon	Examinatrice
DANIEL GIESE	Magnetic Resonance, Siemens Healthcare GmbH, Erlangen	Invité
THOMAS PUISEUX	Spin Up, ALARA Group, Strasbourg	Invité
RAMIRO MORENO	Physicien médical, ALARA Expertise, ALARA Group, Strasbourg	Encadrant

UNIVERSITÉ DE MONTPELLIER

Résumé

Les maladies cardiovasculaires sont les maladies non transmissibles causant la plus forte mortalité dans le monde [1]. L'étude de l'hémodynamique, c'est-à-dire de la dynamique du sang, est considérée par la communauté médicale comme un biomarqueur essentiel pour caractériser l'apparition et le développement de ces pathologies. Ainsi, des examples d'études de l'hémodynamique en lien avec les anévrismes, l'athérosclérose, les sténoses ou encore les thromboses ont été rapportés [2, 3, 4].

Au cours des dernières décennies, des techniques d'imagerie médicale ont permis d'obtenir des informations sur la perfusion sanguine, et même de quantifier l'écoulement sanguin. Parmi celles-ci se trouve l'imagerie par résonance magnétique (IRM), technique non-invasive et non-ionisante, et en particulier l'IRM cinétique à contraste de phase tridimensionnelle, aussi appelée IRM de flux 4D [5]. En plus de produire une image 3D de la morphologie d'une région d'intérêt, cette dernière donne accès à l'évolution temporelle du champ de vitesse du sang (ou de tout autre liquide biologique en mouvement tel que le liquide cérébrospinal) dans les trois directions de l'espace. Bien que prometteuse, cette technique reste peu utilisée dans la pratique clinique étant donné sa faible résolution spatio-temporelle et sa longue durée d'acquisition. De plus, elle souffre d'artéfacts inhérents à la physique de l'IRM et au processus d'acquisition.

Une stratégie alternative pour mesurer l'hémodynamique consiste à utiliser la mécanique des fluides numérique (MFN, aussi connue sous son acronyme anglais CFD pour Computational Fluid Dynamics). Avec sa résolution spatio-temporelle plus fine, la MFN a le potentiel de donner accès à des biomarqueurs inatteignables en imagerie pure. Plusieurs études combinant données IRM et simulations de MFN ont été présentées dans la littérature, aussi bien pour valider les simulations numériques contre des données expérimentales [6, 7, 8] que pour vérifier in vitro la qualité d'images IRM par rapport à la MFN [9, 10]. Cependant, les simulations d'écoulements sanguins souffrent de certaines limitations notamment dues aux choix d'hypothèses de modélisation et aux approximations numériques [11, 12, 13].

D'autre part, des simulations numériques du processus d'acquisition IRM ont aussi été proposées dans la littérature. Ces simulations sont utiles pour le développement et l'optimisation de séquences IRM, car elles sont exemptes d'artéfacts expérimentaux et d'imperfections matérielles du scanner. Elles peuvent aussi être utilisées pour analyser des méthodes de reconstruction des images IRM ou à des fins éducatives [14, 15, 16]. Parmi ces simulateurs IRM, certains ont

été développées en particulier pour les séquences d'IRM à contraste de phase [17, 18, 19].

Ce manuscrit s'inscrit dans la continuité des travaux de thèse de Thomas Puiseux dans le contexte du contrôle qualité des séquences d'IRM de flux 4D, en particulier des séquences dites accélérées, et vers l'optimisation de paramètres grâce à la simulation numérique [20]. C'est le fruit de la collaboration entre le laboratoire académique IMAG (Institut Montpelliérain Alexandre Grothendieck) et la société Spin Up (Alara Group, Strasbourg, France) spécialisée dans la gestion des risques IRM (assurance qualité, sécurité, formations).

Le chapitre 1 est un chapitre introductif, donnant un aperçu de l'état de l'art à propos de la mesure hémodynamique et de sa modélisation. La modélisation du processus IRM est également évoquée, en particulier dans le cas de l'IRM à contraste de phase.

Le chapitre 2 est dédié à l'introduction de concepts fondamentaux de l'IRM. L'accent est mis sur l'IRM à contraste de phase, en particulier sur l'IRM de flux 4D. Les principaux artéfacts et limitations de l'IRM à contraste de phase sont détaillés. Enfin, des méthodes d'accélération du temps d'acquisition sont présentées.

Le chapitre 3 est consacré à la modélisation de l'IRM. Un "modèle-jouet" simplifié est tout d'abord présenté. Puis, le code de calcul YALES2BIO développé en interne est introduit. Finalement, des détails sont apportés sur le solveur implémenté dans YALES2BIO et dédié à la simulation d'acquisitions IRM à partir de séquences constructeur.

Dans le chapitre 4, l'influence de l'utilisation de séquences accélérées sur la qualité des champs de vitesse reconstruits est étudiée. En effet, l'un des enjeux de l'IRM de flux 4D est son long temps d'acquisition qui ralentit son adoption dans la pratique clinique. Deux types d'accélération sont étudiées ; d'une part le GRAPPA une technique d'imagerie parallèle, c'est-à-dire exploitant la dépendance spatiale des multiples éléments de l'antenne réceptrice du signal IRM, et d'autre part la méthode de l'acquisition comprimée (compressed sensing), qui consiste en une acquisition très sous-échantillonnée reconstruite via un processus itératif d'optimisation. Ainsi, en plus d'une acquisition non-accélérée, quatre acquisitions accélérées ont été réalisées sur un fantôme imageur de flux conçu en interne par Puiseux et al. [10] : trois acquisitions de type GRAPPA avec des facteurs d'accélération R = 2, 3, 4 et une acquisition de type compressed sensing avec R = 7.6. Des simulations MFN à partir des champs de vitesse mesurés expérimentalement sont également conduites. Les champs de vitesse obtenus sont comparés sur des quantités non-dérivées : profils de vitesse, débits et vitesses maximales. Qualitativement, toutes les modalités aussi bien expérimentales que simulées présentent des motifs hémodynamiques similaires (bien que très bruité

pour GRAPPA R = 4). Une visualisation tridimensionnelle des champs de vitesse
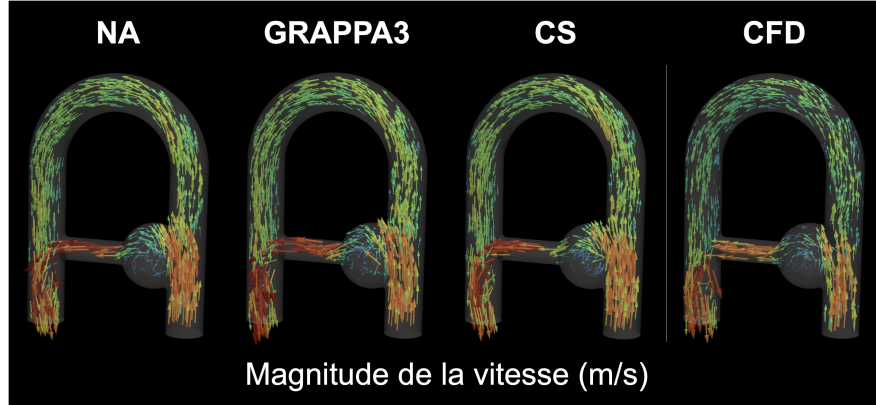est présentée sur la Fig. 1.

Figure 1: Visualisation tridimensionnelle des champs de vitesse. NA : non-accéléré,
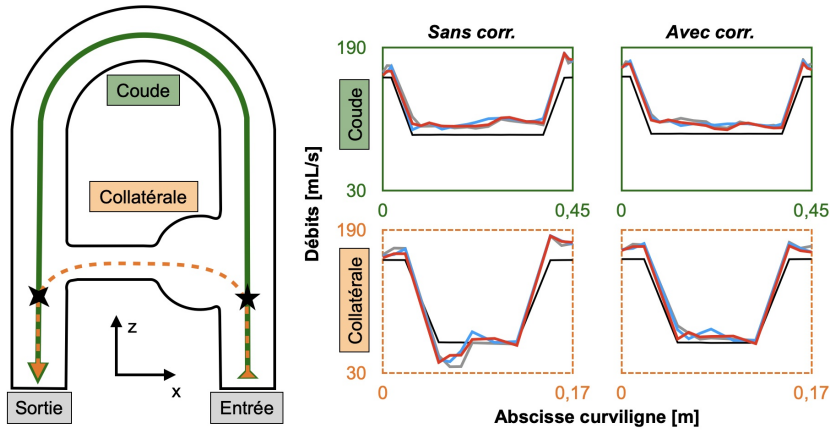CS : compressed sensing.

Figure 2: Illustration du fantôme de flux et débits pour les champs de vitesse
sans et avec correction des courants de Foucault. Les débits sont présentés au
pic systolique le long de deux chemins : coude en vert et collatérale en orange.
■ non-accéléré, ■ GRAPPA 3, ■ compressed sensing et ■ MFN.

Cependant, toutes les acquisitions IRM semblent surestimer les profils de vitesse
ainsi que les vitesses maximales par rapport aux acquisitions MFN dans des régions
associées avec une vitesse et/ou une accélération élevée. Des comparaisons voxel-à-
voxel entre les images IRM mettent en évidence que les erreurs les plus importantes
se trouvent dans les voxels proches de la paroi du fantôme. Enfin, la correction
des courants de Foucault dans les images IRM apparaît comme essentielle afin de
rapporter des mesures de débits respectant le principe de conservation de la masse
(cf Fig. 2). Une fois cette correction effectuée, de bons accords sont trouvés entre

les débits expérimentaux in vitro et ceux issus de la simulation numérique. Ces travaux ont fait l'objet d'un article scientifique publié sous Garreau et al. (2022) dans le journal Magnetic Resonance in Medicine [21].
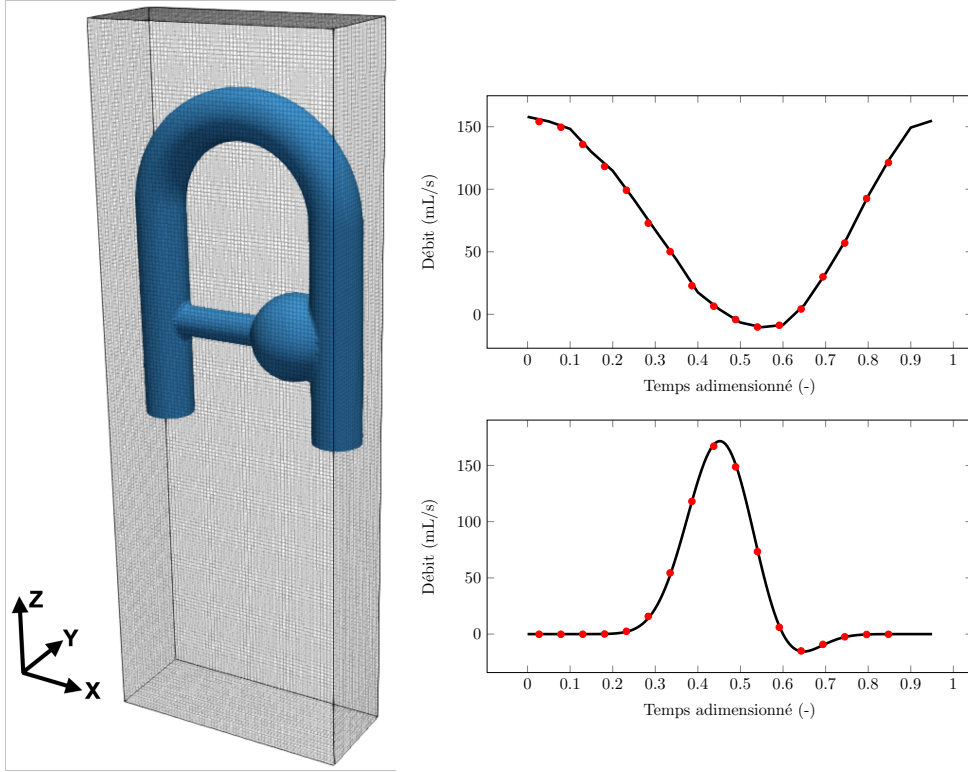

Figure 3: Champ de vision de l'acquisition IRM, fantôme numérique et débits. A droite, les deux débits étudiés sont présentés: en haut le débit quasi sinusoïdal issu de l'expérimental et en bas le débit suivant une fonction analytique modélisant un débit aortique. Les points rouges correspondent aux temps moyens de chaque phase cardiaque.

Le chapitre 5 est dédié à l'étude de l'écho partiel, un paramètre souvent utilisé en IRM à contraste de phase mais dont l'utilisation ne fait pas consensus au sein de la communauté de l'IRM de flux 4D [22]. En effet, cette technique permet de réduire le temps d'écho et donc d'atténuer des artéfacts dits de déplacement, voire elle permet dans certains cas d'avoir une résolution temporelle plus fine. Cependant, elle consiste par ailleurs à une réduction du volume de données acquises, et donc à une potentielle détérioration de la qualité des images reconstruites. Des simulations ont été réalisées avec le solveur dédié à la simulation d'IRM de flux 4D sur la configuration du fantôme de flux déjà utilisée dans le chapitre 4. Deux séquences ont été testées : une sans écho-partiel (écho complet) et l'autre avec un écho partiel tel que seulement 75% de l'écho complet est acquis. Deux régimes d'écoulement en entrée sont étudiés : l'un avec un débit expérimental

s'approchant d'une sinusoïdale et l'autre avec un débit suivant une fonction analytique modélisant un débit dans l'aorte ascendante (cf. Fig. 3). Pour chacun des deux débits, des motifs hémodynamiques similaires sont visuellement observés pour les simulations sans et avec écho partiel, ainsi que pour les simulations de MFN correspondantes. Des niveaux d'erreurs plus élevées sont rapportés pour l'écho complet que pour l'écho partiel par rapport aux simulations de MFN sur l'entièreté du cycle cardiaque. L'utilisation de l'écho partiel réduit les erreurs faites sur la composante de la vitesse encodée selon la direction de lecture (c'est-à-dire la direction de l'écho), comme présenté sur la Fig. 4. Cependant, les deux séquences engendrent des erreurs quand elles sont comparées aux simulations de MFN. L'énergie cinétique de turbulence et l'accélération apparaissent comme de bons indicateurs complémentaires des régions associées avec les niveaux d'erreurs les plus élevés. Etant donnée la nature pulsatile des écoulements étudiés, des images "fantômes" (artéfact de "ghosting") apparaissent pour certaines phases cardiaques. Cet artéfact pourrait être responsable des erreurs qui ne sont corrélées ni avec l'énergie cinétique de turbulence, ni avec l'accélération. En un mot, ce chapitre illustre le potentiel du cadre de simulation IRM en matière de prise de décision pour l'optimisation de paramètres, tout en permettant de reproduire des artéfacts intrinsèques au processus de l'acquisition IRM.
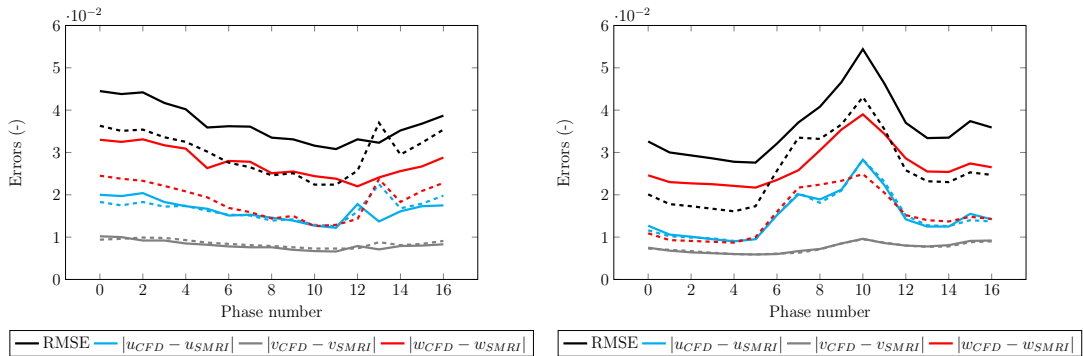

Figure 4: Evolution des erreurs au cours du cycle cardiaque, à gauche pour le débit "sinusoïdal" et à droite pour le débit "aortique". Les lignes pleines représentent les acquisitions sans écho partiel et les pointillées celles avec écho partiel. Les erreurs sont normalisées par la vitesse maximale attendue $V_{ENC} = 0.7$ m/s.

Enfin, les principaux résultats de cette thèse sont rappelés au chapitre 6 qui conclut ce manuscrit. Des perspectives pour des applications cliniques et de futures recherches sont données. Ainsi, bien que le simulateur IRM-MFN présenté dans cette thèse permet de simuler des séquences constructeurs réalistes, il ne modélise pas tous les phénomènes physiques présents dans l'acquisition IRM tels que les gradients concomitants (ou termes de Maxwell), les courants de Foucault ou les non-linéarités des gradients. Ajouter ces sources de distorsion du champ

magnétique permettrait d'étudier comment ceux-ci affectent les images reconstruites (morphologiques et de champs de vitesse). Cela permettrait aussi de tester des algorithmes de reconstruction. Les profils de sensibilité des bobines pourraient aussi être modélisés dans les simulations pour investiguer des méthodes de reconstruction d'imagerie parallèle. Avec l'émergence de l'apprentissage machine (machine learning) et des réseaux neuronaux dits "informés par la physique" (physics-informed neural networks, PINN), l'environnement de simulation IRM apparaît comme un outil précieux pour générer des ensembles de données synthétiques ou pour construire des dictionnaires de signaux utiles dans la technique dite d' "identification par les empreintes digitales" en résonance magnétique (magnetic resonance fingerprinting, MRF) [16, 23, 24].

A mon Papy,
merci pour les mathématiques de cuisine.

A ma Granine,
merci d'avoir fait plus que le diplôme de maîtresse de maison.

Remerciements

Quelle pression d'écrire cette partie, sûrement la plus lue de cette thèse, même si promis, il y a plein de belles images et de couleurs dans les pages qui suivent (*CFD, Colorful Fluid Dynamics* - O. Kaplan). Je tâcherai de remercier tous ceux qui ont participé de près ou de loin à l'accomplissement de ce travail. Je m'excuse par avance si j'en oublie certains, on m'a dit qu'on avait jusqu'à 3 mois après la soutenance pour corriger les erreurs du manuscrit.

First of all, I would like to express my sincere gratitude to Sebastian Kozerke and Matthias Stuber for taking the time to thoroughly review this thesis. I would also like to warmly thank all the committee members: Alain Lalande, Olivier Meyrignac and Monica Sigovan.

Mes remerciements vont ensuite à mes directeurs de thèse, Franck Nicoud et Simon Mendez. Merci d'avoir ouvert les portes de l'équipe Yales2Bio à une étrangère ne sortant pas du cursus "Mécanique et Interactions" de Polytech' Montpellier, et merci d'avoir toujours cru en moi, malgré les hauts et les bas. Je mesure la chance que j'ai eu de pouvoir travailler, apprendre et progresser à vos côtés. Malgré vos emplois du temps plus que chargés, vous avez toujours pris le temps d'organiser des réunions et de passer voir dans le bureau comment ça avançait. Je vous en suis grandement reconnaissante. Merci également pour toutes vos remarques et interrogations toujours pertinentes, et j'espère que j'ai pu vous éclairer un peu plus sur l'IRM.

Je souhaite aussi remercier chaleureusement Spin Up qui a permis la réalisation de cette thèse CIFRE. Merci à Ramiro Moreno pour m'avoir encadré lors de ce travail, et d'avoir apporté le point de vue de l'expérimentateur et du physicien médical au-delà de celui du mécanicien des fluides. Je remercie également Thomas Puiseux, qui a initié le travail développé dans cette thèse. Merci pour toutes ces réunions qui m'ont permis de me poser de nouvelles questions et merci de m'avoir accompagnée dans toutes les conférences à la rencontre des spécialistes de l'IRM. J'espère ne pas avoir trop abîmé ton solveur d'IRM in silico. Je passe désormais le flambeau à Alexis Caltran qui se chargera de s'amuser avec sur ses réseaux de neurones. Je remercie de façon plus globale Alara Group, en particulier Fanny Carbillet pour sa confiance.

pour les fêtes et les sorties plage/escalade/randonnée/ornithologie... : Omar, Soumaya, Cécile, Emma. Pour continuer sur les amitiés nouées à Montpellier, je remercie également Hosein de m'avoir appris quelques mots de farsi. Merci beaucoup à Yann, du labo d'à côté, dont nous avons eu la charge avec Damien au départ d'Alan. Merci Yann pour Black Sabbath et Iron Maiden, et pour m'avoir emmené à des concerts peut-être un peu chelous. Merci aussi pour avoir essayé de me trouver un post-doc, mais je crois que tu n'as toujours pas compris ce que je faisais. Un grand merci à Damien aussi justement, toujours discret mais indispensable à bien des égards.

Je voudrais remercier aussi des amitiés de plus longue date. Merci à Justin pour les robots, son savoir-faire pour être synthétique, et d'avoir failli me perdre dans les Cévennes. Merci à Joséphine, merci à Alix. Merci à Jeanne, Eléonore, Clémence, Coralie et Marie d'être toujours là. Tusind tak til mine danske veninder Cecilie, Bernarda og Huda. Jeg håber at finde lidt mere tid nu til at besøge København igen (eller Odense!)

Je remercie également Pascale, Denis et Ambre, ainsi que tout le mas Germain de m'avoir toujours chaleureusement accueillie et de m'avoir permis de terminer ma thèse dans le calme des rizières arlésiennes.

Merci enfin à mes parents, et à mes deux nouilles de sœurs préférées. Je remercie aussi ma famille au grand complet, Mamie, oncles et tantes, cousins-cousines qui ont grandement contribué à mon équilibre.

Le dernier remerciement revient à Barthélémy. Merci d'être mon meilleur co-bureau, mon meilleur coloc, et mon meilleur compagnon d'aventures. Merci de me supporter, dans tous les sens du terme.

Contents

Introduction

Chapter contents

1.1 Motivation

Cardiovascular diseases (CVDs) account for the largest number of deaths from non-communicable diseases. In 2017, 31.8% of the deaths worldwide could be imputed to CVDs, a number constantly rising since 1990 [1]. To alleviate this burden, research has been aiming towards providing metrics to diagnose CVDs, to monitor the disease progression, and to plan and adapt medical treatments [25]. Over the past decades, it has appeared that hemodynamic parameters are relevant biomarkers of the onset and development of cardiovascular pathologies. To name

a few, hemodynamics has been studied in relation with aneurysms, atherosclerosis, stenoses and thromboses [2, 3, 4]. Thus, useful insights on cardiovascular health can be gained by measuring the hemodynamics.

In recent decades, noninvasive imaging techniques to assess blood perfusion and even to quantify flow have known great and fast progress [26]. The present work focuses on the three-dimensional cine phase-contrast MRI, also known as 4D Flow MRI. This imaging modality allows retrospective flow quantification at any location within the acquired volume, hence giving access to hemodynamic biomarkers. Even though this technique could become the new gold standard to assess blood flow, its translation in the clinical practice remains hindered by its low spatio-temporal resolution and long scan times, as well as artifacts inherent to the physics and process of acquiring MR images. Over the years, various strategies have been proposed to accelerate the scan time, relying on coil design and geometry, and signal undersampling. The present work is part of the current research about quality control of accelerated MR scans, and towards parameters optimization through numerical simulations.

1.2 The cardiovascular system

The cardiovascular system is a closed circuit including the heart, blood vessels (arteries, veins, and capillaries) and blood. It is composed of two loops: the pulmonary circulation and the systemic circulation. In the first loop, the deoxygenated blood rich in carbon dioxide flows from the right side of the heart to the lungs. Gas exchange occurs in the pulmonary capillaries and the re-oxygenated blood low in carbon dioxide flows to the left heart. The systemic circulation describes the circulation of the oxygenated blood from the left heart to the extremities of the body and to other organs, and back to the right heart. The blood circulation permits delivering nutrients, dioxygen and hormones to cells throughout the body. It also participates in removing waste products. The cardiac cycle is continuously repeated with the heart acting as a muscular pump. The cardiovascular system is illustrated in Fig. 1.1.
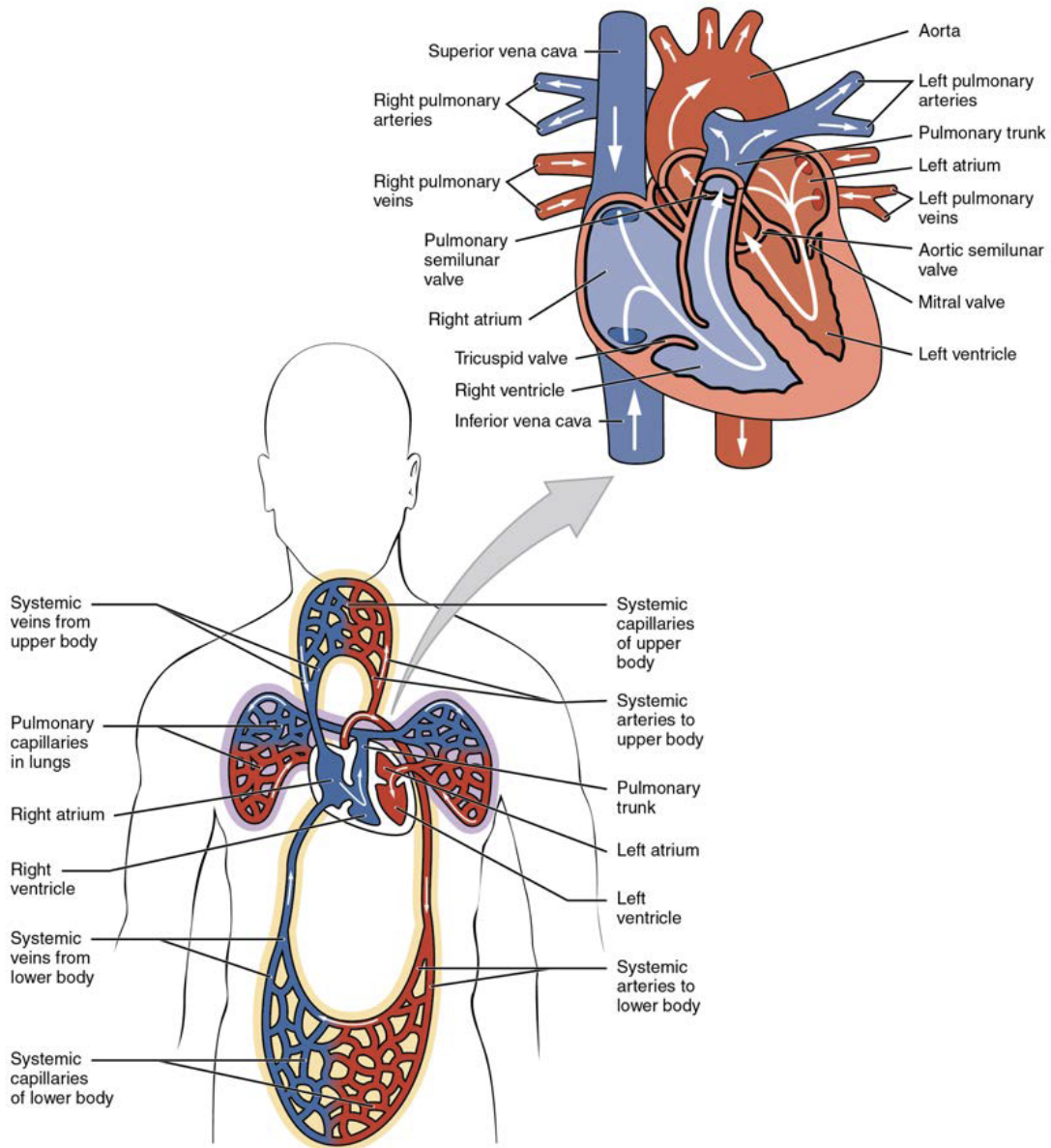
Figure 1.1: Sketch of the cardiovascular system and heart. The oxygenated blood is depicted in red, whereas the deoxygenated blood rich in CO_2 is in blue. Image extracted from [27].

1.2.1 Heart and cardiac cycle

The heart is composed of four chambers: on each side of the heart (right and left), the upper chamber is called the atrium and the lower chamber the ventricle. Four valves ensure unidirectional blood flow through the heart. The atria act as receiving chambers, collecting blood from the vena cava for the right atrium and from the pulmonary veins for the left one. The blood is pushed into the ventricles as the atria contract. The atrium and ventricle are separated by the tricuspid valve on the right side and by the bicuspid mitral valve on the left side. As the ventricles contract, they pump the blood respectively to the lungs through the pulmonary valve on the right side and to the rest of the body through the aorta via the aortic valve on the left side. Thereby, the heart can be seen as a double pump.
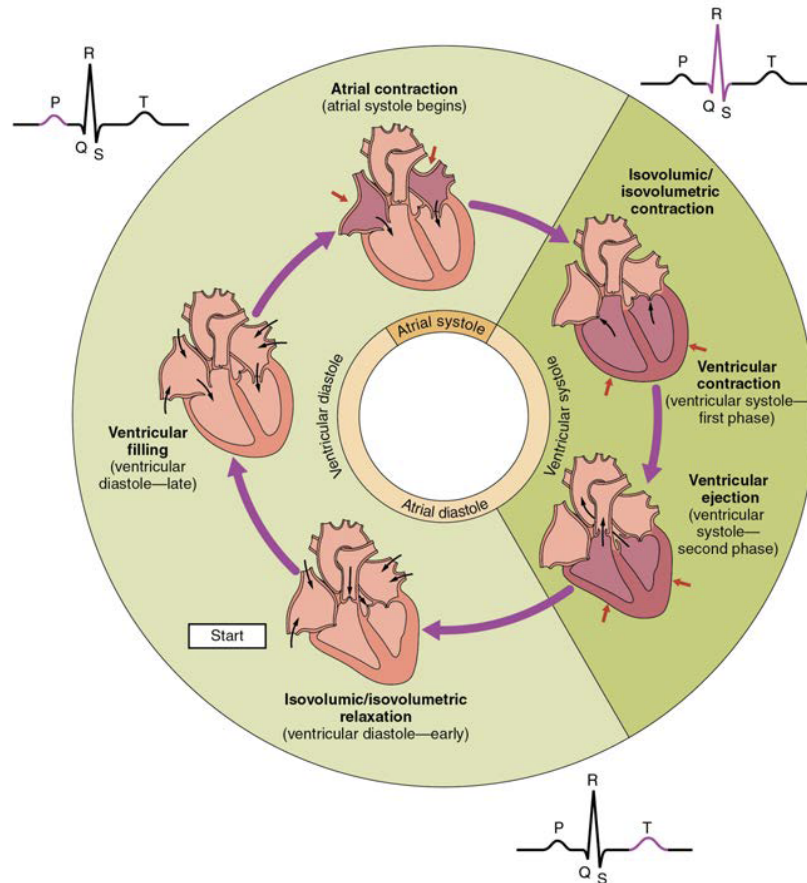
Figure 1.2: Sketch of the cardiac cycle. Image extracted from [27].

The cardiac muscle has a unique property: it possesses specialized cells that can initiate an electrical impulse at a fixed rate that propagates throughout the heart. It is this impulse that triggers the cardiac contractions and propel the blood. The electrical signal of the heart can be recorded with surface electrodes placed on the body. The recording is called electrocardiogram (ECG) and is a

useful clinical tool to investigate the heart function. The cardiac cycle along with the corresponding normal ECG are presented in Fig. 1.2. Note the large QRS complex, where the peak of the R-wave corresponds to the beginning of the ventricular contraction. The contraction of the heart is referred to as the systole, whereas the period of relaxation when the chambers are filled with blood is known as the diastole. As the R-wave is the most prominent peak on the ECG, the cardiac cycle duration can be calculated from the RR-interval.

1.2.2 Blood vessels

Blood vessels distribute the blood through the body. Three main types of blood vessels can be established: the arteries that carry blood away from the heart, veins that transport blood back to the heart and tiny capillaries at the merging of the two first types, where the nutrients and waste exchange occurs. The arteries form a relatively high-pressure system due to their proximity with the heart, whereas the venous system presents lower pressure. Thereby, the arteries have thicker walls and smaller lumens than the veins, and appear round in cross-section, in contrast to the flattened appearance of the veins. All vessels but the capillaries are composed of three layers called tunics. The most interior one is the tunica intima made up of epithelial and connective tissue layers. The middle layer is the tunica media and consists in smooth muscle and in connective tissue containing mostly elastic fibers. It is usually the thickest layer in arteries (except for the largest ones). Thus, especially in the arterial system, the vasoconstriction and vasodilation enabled by the smooth muscle can respectively decrease and increase the blood flow. Finally, the outer layer is called the tunica externa or adventia and is made up of connective tissue composed primarily of collagenous fibers. It is usually the thickest layer in veins and helps to keep the vessel in its relative position.

The largest arteries (typically larger than 10 mm in diameter) are the ones closest to the heart with the thickest walls. They have the particularity to contain a high percentage of elastic fibers in all three of their layers. Examples of the so-called elastic arteries are the aorta, pulmonary arteries and the aortic arch branches. The aorta, illustrated in Fig. 1.3, is the largest artery in the body. It consists in three main segments: the ascending aorta starting from the aortic valve, the aortic arch and the descending aorta, which then divides into the two common iliac arteries at the level of the fourth lumbar vertebra. Traveling along the arterial tree, the arteries diameter decreases, as well as their amount of elastic fibers. In addition to blood supply, the design of the arterial tree allows to cushion the heart pulsations, so that the blood flow is almost continuous in the capillaries. According to the consensus propagation model, the distribution of the elastic properties in the arteries allows the generation of a pressure wave along the tree and reflected retrograde waves. Whereas in young subjects the retrograde waves help in enhancing the coronary flow, elastic arteries dilate and stiffen with aging, leading to a higher aortic pulse wave velocity and thereby an increase in the peak
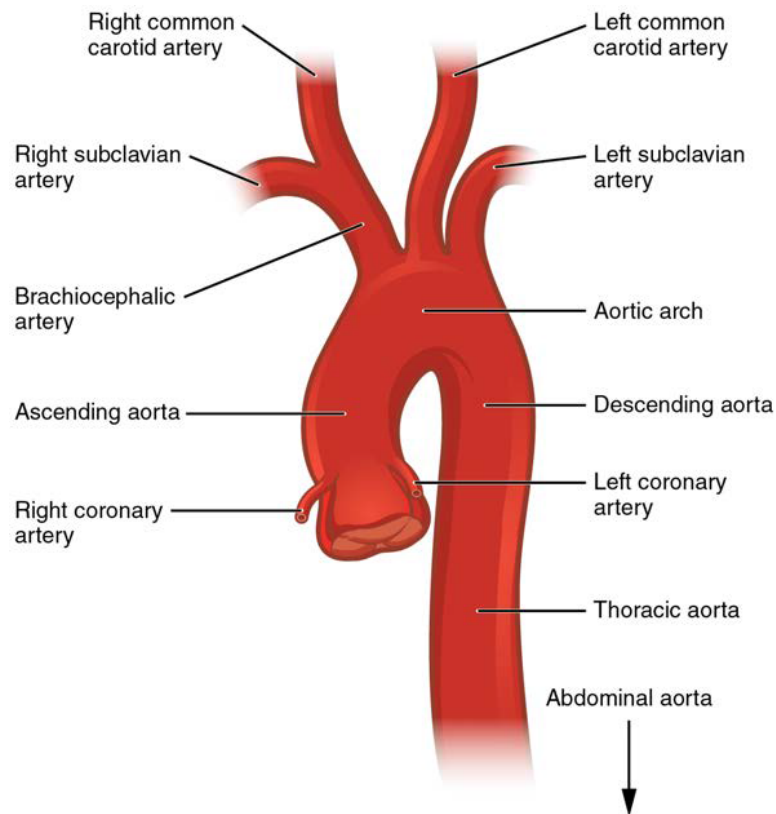
Figure 1.3: The aorta and its three main segments: the ascending aorta, the aortic arch and the descending aorta, which can be subdivided into the thoracic aorta above the diaphragm and the abdominal aorta below. The three major aortic arch branches are the brachiocephalic artery, the left common carotid artery, and the left subclavian artery ; all of which have elastic artery characteristics. Image extracted from [27].

systolic and end diastolic pressures [28, 29, 30].

1.2.3 Blood and hemodynamics

The last main component of the cardiovascular system is blood. While its primary function is to deliver oxygen and remove metabolic waste products from body cells, blood is also implicated in the immune system and maintenance of the chemical balance of the body (e.g. temperature, pH, water content of body cells). It is made up of cellular elements (red blood cells, white blood cells and platelets) in suspension in a fluid extracellular matrix, the plasma. This combination of fluid and solid components gives blood its complex rheology and its non-Newtonian behavior. Understanding the blood flow dynamics at the microscopic scale is an ongoing field of research. Hemodynamics also closely interacts with cell activity and arterial wall mechanics in the process of vascular growth and remodeling. Furthermore, the mechanical properties of blood and

blood vessels evolve through one's life due to aging, external factors such as smoking and air pollution, or diseases such as diabetes, obesity or cholesterol. Hemodynamics is also an important factor to take into account in the design and optimization of medical devices in contact with blood, which are prone to device-related thrombosis [31].

1.3 Measuring hemodynamics

1.3.1 Invasive measurements

Various invasive measurement techniques have been used to directly or indirectly measure hemodynamics. Catheters are widely used for such measurements, as they can be equipped with various type of sensors for pressure, temperature (thermodilution) [32] or blood flow velocity [33]. Catheterization is even considered as a gold standard in certain cases, e.g. for intraarterial pressure measurement [34], or risk stratification of arterial stenosis [35]. Another less invasive technique is transesophageal echocardiogram, where a transducer is introduced into the esophagus of anesthetized patients. This echocardiography can image the heart in one, two or three dimensions, and Doppler technique can be used to assess blood flow. As invasive technologies are associated with complications, research has been focusing on the past years in developing non-invasive techniques providing the same accuracy and precision. Yet, invasive procedures remain recommended for critically ill patients, and does not add additional risk in operations including catheters anyway [32, 34].

1.3.2 Echocardiography

As opposed to transesophageal echocardiography mentioned earlier, transthoracic echocardiography is a non-invasive imaging technique. It conventionally relies on the Doppler effect to measure blood flow in a method called color Doppler imaging, where a color map is used to display the magnitude and direction of blood flow. However, this technique only allows to catch the velocity component along the direction of the transmitted ultrasound beam. Hence, the measurement is restrained to a unidirectional velocity and depends on the beam-to-flow angle. Another method, called ultrasound vector flow imaging (VFI), has been developed over the past years, where both angle and magnitude of blood flow velocities are estimated. Several approaches have been investigated in order to achieve 2D or 3D [36] and even time-resolved imaging thanks to ECG-gating [37, 38]. An example of 4D ultrasound VFI is illustrated in Fig. 1.4.
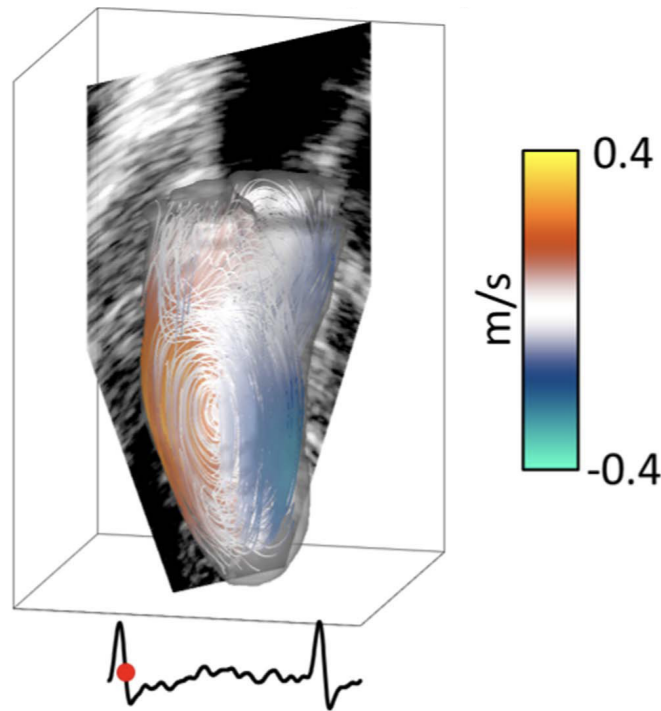
Figure 1.4: In vivo 3D intraventricular vector flow mapping, extracted from [38].

1.3.3 Phase-Contrast Magnetic Resonance Imaging (PC-MRI)

Magnetic Resonance Imaging (MRI) is a non-invasive technique used to image soft tissue anatomy, as well as physiological processes of the body. It relies on the phenomenon of nuclear magnetic resonance occurring when specific nuclei (e.g. hydrogen) are subjected to strong magnetic fields and high-frequency magnetic variations. Among MRI sequences, phase-contrast MRI allows to reconstruct the blood velocity, based on controlled dephasing of the measured MR signal. While the opportunity to encode velocity is known since the early developments of MRI [39], progress in hardware and computational power made it possible to expand this technique to three-dimensional time-resolved PC-MRI, often referred to as 4D Flow MRI [5, 40] and illustrated in Fig. 1.5. More details about fundamentals of MRI with a specific focus on PC-MRI can be found in Chapter 2. In a nutshell 4D Flow MRI gives access to 3D velocity fields in a volume of interest resolved in time. In contrast to PC-MRI where the slices of interest have to be positioned by the user beforehand, the slices can be freely chosen in a retrospective manner as the whole volume is being imaged in 4D flow MRI. Thereby, this technology appears a relevant tool to assess hemodynamics and has the potential to become a gold standard. Various hemodynamic biomarkers derived from 4D Flow velocity fields and pertinent to CVDs have already been reported in the literature, such as pressure field, wall shear stress and turbulent kinetic energy [41, 42, 43, 44]. However, the accuracy and reliability of 4D flow measurements can be put in

question due to limited spatio-temporal resolution. Furthermore, 4D flow does not give access to instantaneous velocity fields, but only to a time-averaged field due to its acquisition process. 4D flow MRI is also subjected to artifacts, such as partial volume effects at the vessel walls or misregistration due to time offsets between the different encodings that occur during the acquisition. Another limitation of conventional 4D flow MRI is its long acquisition time. Ongoing research effort has been put towards developing techniques to accelerate data acquisition, in particular parallel imaging and sparse undersampling techniques (e.g. compressed sensing) [45].
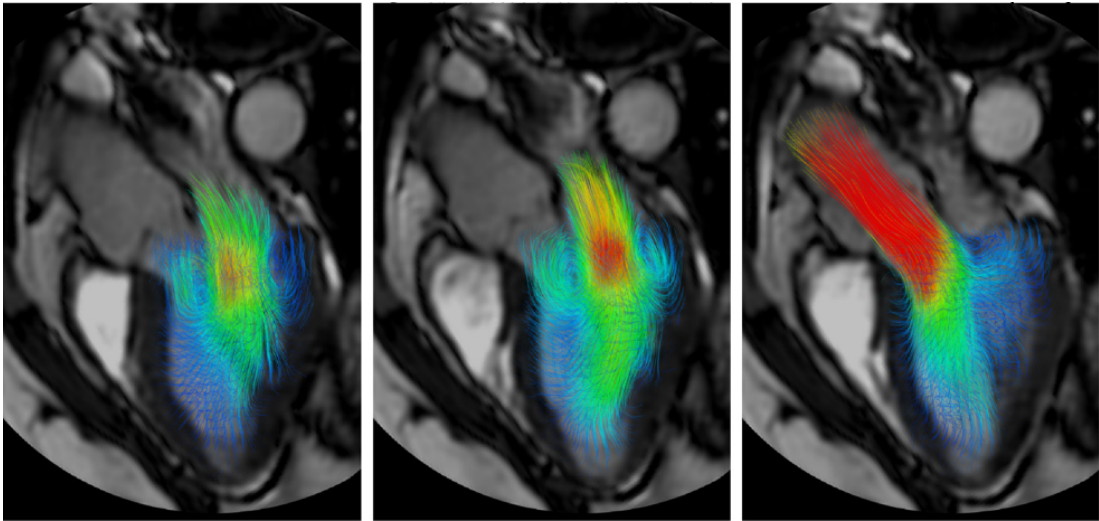
Figure 1.5: In vivo intracardiac 4D Flow MRI, extracted from [22].

1.4 Modelling hemodynamics

1.4.1 Computational Fluid Dynamics

Computational Fluid Dynamics (CFD) have known an increased interest to study physiologic flows and as a tool in cardiovascular medicine thanks to the progress in hardware and software, and the increase in computational power [46]. With its higher spatio-temporal resolution, it has the potential to grant assess to hemodynamics biomarkers not accessible with imaging techniques only, such as arterial wall shear stress. Thereby, CFD has already been investigated to study CVDs such as aortic [47, 48, 49] and cerebral aneurysms [50, 51], aortic dissection [52, 53] and coronary artery disease [54, 55]. CFD has also been used to design devices and to control their deployment and outcomes, in particular for stents [56] and ventricular assist device [57, 58].

Studies incorporating both MRI data and CFD simulations have been proposed in the literature. Both validation of the numerical simulation against 4D flow MRI measurements [6, 7, 8] and in vitro verification of MRI acquisitions with respect to CFD simulations have been presented [9, 10]. Both MRI and CFD

have also been included in cross-validation studies against other modalities, such as particle image velocimetry (PIV) [59, 60] and laser Doppler velocimetry [61]. CFD has been employed to create synthetic MRI-like data as well, e.g. to feed deep learning algorithms [62] or to compute velocity and turbulence maps [63], while having the matching highly resolved CFD as ground truth for comparison. Finally, CFD has been exploited to enhance 4D flow MRI [64, 65], and some research has been conducted towards data fusion of both modalities in order to address their inherent limitations [66, 67].

1.4.2 Limitations of CFD in the context of hemodynamics

Blood flow simulations also present some limitations, especially due to modelling assumptions and numerical approximations.

A first complexity comes from the modeling of blood. As blood is a dense suspension of cells, its behavior is far from being Newtonian. At the macroscopic level, blood is however often modelled as homogeneous and as a Newtonian or a shear-thinning fluid. Fung states that it is reasonable to consider the fluid as homogeneous in large blood vessels, as their diameter is much larger than the characteristic size of red blood cells (the largest cell type in blood) [68]. Furthermore, he reports experimental results showing that at high shear rate the blood behaves as a Newtonian fluid. Yet, this assumption does not hold in regions associated with low shear rate. For in vitro studies, a common choice is to use blood mimicking fluid whose rheology is perfectly characterized in order to avoid the modelling uncertainties associated with blood.

A second limitation occurs from turbulence handling. Indeed, turbulence may develop in the cardiovascular system, especially in the aorta and in regions such as stenoses, valves and bifurcations, as well as when flow decelerates [12]. Yet, this natural phenomenon is often neglected and the flow is assumed to be laminar [7, 65, 69]. Whereas direct numerical simulations are extremely demanding in computational power, two main approaches have emerged to simulate turbulence: Reynolds-Averaged Navier-Stokes (RANS) and Large-Eddy Simulation (LES). The first strategy consists in modelling all the scales of turbulent spectrum, while in the latter one only the smallest scales are modelled and the largest scales are explicitly resolved. Thereby LES is more computationally demanding. However, while RANS models perform well in the context of fully developed turbulence at very high Reynolds numbers, they are not predictive enough in capturing the laminar-turbulent transition [70]. LES models have proven to be more accurate when dealing with transitional flows and do no require adapting model parameters [12, 58].

Another important feature of CFD simulations is the choice of numerical scheme. Valen-Sendstad and Steinman warn about low-order stabilization terms often used by default in commercial CFD software for robustness and which generate artificial dissipation to the solution [11]. Concerning LES, dissipation-free schemes must

be preferred. For example, better results have been reported with second-order centered scheme than with higher-order upwind biased (dissipative) scheme [12].

A last limitation concerns the choice of boundary conditions in various aspects. Idealized velocity profiles such as blunt [71], flat [72] or fully developed profiles [63, 73] have been proposed as inlet boundary condition. Such idealized profiles can greatly impact the solution and can lead to erroneous results [13]. Morbiducci reports that prescribing experimental PC-MRI velocity profiles at the inlet may be accurate enough to capture disturbed shear, hence avoiding the need to prescribe realistic 3D profiles [74]. In the context of transitional flows, injection of small perturbations at the inlet has been shown to greatly improve the accuracy and robustness of the results with respect to turbulence prediction [58]. Additionally, the choice of the outflow boundary condition also has a significant impact on the resulting velocity and pressure fields. Many in vivo situations include multiple outlets, from the aorta bifurcation into the aortic arch branches (Fig. 1.3) to the complex networks such as the circle of Willis. Simplistic zero or constant pressure, as well as zero-traction condition, fail to reproduce the flow distribution in multi-outlet models [75, 76]. Good agreement with in vivo data have been reported when prescribing the more physiological dynamic three-element Windkessel model at each outlet. For in vitro models, outlets can be merged into a unique outlet to circumvent this issue (cf in-house phantom in Section 4.2.1). Finally, the rigid wall approximation is widely used, whereas blood vessels and in particular the aorta have moving compliant walls. Fluid-structure interactions models have been developed, but there is no consensus on how best to define the structural constitutive properties of vessel walls, as well as how these properties distribute within the vessel [52]. Image-based simulations are an alternative, where the motion of the walls is imposed thanks to medical imaging [77].

As presented in this section, numerical simulations rely on many assumptions and care should be taken in the choice of the CFD strategy for a given problem.

1.4.3 Modelling hemodynamics... and the process of MRI acquisition

Various numerical simulations of MRI experiments have been proposed in the literature [14, 15, 78, 79]. These simulations can serve a variety of purposes. They can be a useful tool in the field of pulse sequence development and optimization, since simulations are free of experimental artifacts and hardware imperfections. They can also serve to analyze reconstruction methods or for educational purposes [16]. Additionally, these simulations permit generating synthetic data, which can be used to train machine learning models, or to construct signal dictionaries in magnetic resonance fingerprinting [80, 81].

Among the MRI simulators, some have been developed specifically for phase-contrast MRI. Petersson et al. have simulated a 3D PC-MRI with three-directional flow-encoding on a turbulent non-pulsatile flow in a straight rigid pipe with a stenosis. Using an Eulerian-Lagrangian approach, the flow is first resolved with

LES for 125 timeframes. The Bloch equations are then solved for each spin using particle trajectories randomly chosen from the computed timeframes. The outcomes against experimental PC-MRI and intravoxel velocity standard deviation are successfully validated [17]. Xanthis et al. have simulated 2D PC-MRI on an analytic laminar flow within a straight tube thanks to the high performance multi-GPU MRISIMUL simulator, now commercialized for educational purposes by Corsmed (Stockholm, Sweden) [79, 82]. Klepaczko et al. have numerically investigated conventional 2D and 3D PC-MRI sequences against an EPI-accelerated 2D PC-MRI sequences in the context of kidney vasculature thanks to their computational framework [18]. Fortin et al. have implemented an extension to include 3D fluid flows in JEMRIS, one of the most used general MRI simulator. They have investigated in particular a 2D and a 3D PC-MRI sequence on a cerebral venous network [19]. It is worth mentioning that another trend consists in synthesizing PC-MRI or 4D flow MRI data from CFD simulations without solving the Bloch equations. Instead, these methods use a model equation for the MR signal based on the CFD velocity fields and turbulence data, and are less computationally expensive [63, 73, 83, 84].

Besides Bloch simulations, where the Bloch equations are solved in the spatial domain, extended phase graphs (EPG) have been proposed. In this approach, the Bloch equation are indirectly solved in the Fourier domain. In his review, Weigel discusses how motion can be accounted for using this formalism [85]. However, up to the author's knowledge, no simulations of PC-MRI has been proposed yet using EPG. Furthermore, Guenthner et al. have recently presented a hybrid approach that combined Bloch equations and EPG [81].

In the present work, the MR simulator initiated by Puiseux during his PhD thesis has been further developed [86]. This simulator has been initially sought to investigate time-resolved 3D PC-MRI sequences, i.e. 4D flow MRI, in the context of pulsatile transitional flows in complex geometries. It uses an Eulerian-Lagrangian formalism, where the Bloch equations are advanced on Lagrangian tracers simultaneously with the Navier-Stokes equations for the flow.

1.5 Thesis objectives and overview

1.5.1 Objectives

The present work follows on from Thomas Puiseux's PhD thesis [20]. It is a collaboration between the academic laboratory IMAG (Institut Montpelliérain Alexandre Grothendieck) and Spin Up (Alara Group, Strasbourg, France), a company working with management of risks in MRI (quality assurance, safety, trainings).

The first objective of this work takes place in the context of quality control and integration to the clinical practice. As mentioned earlier, the long scan times inherent to 4D flow MRI still hamper its clinical use. In the present work, two types of acceleration of MRI sequences are investigated: GRAPPA, a parallel

imaging technique which is nowadays conventionally used to acquire PC-MRI data [87], and the more recent compressed sensing method [88]. The quality of the reconstructed velocity images have been assessed against a fully-sampled MRI acquisition and CFD thanks to the framework proposed by Puiseux to compare experimental MRI data with corresponding CFD simulation. This framework includes the use of a well-controlled flow phantom presenting complex geometry yielding flow patterns similar to the structures observed in the cardiovascular system [10].

The second objective is related to optimization of existing PC-MRI sequences in order to investigate the influence of parameters on the reconstructed velocity field. As highlighted before, MRI simulation is the ideal tool, as it allows changing only a parameter at once without having to deal with experimental artifacts. The 4D Flow MRI simulation platform initiated by Puiseux is expanded in the present work, especially towards versatility to simulate constructor sequences.

1.5.2 Thesis overview

The second chapter of this thesis provides an introduction to fundamental concepts of MRI. It also includes a specific focus on PC-MRI, and in particular on 4D flow MRI. The main artifacts and limitations found in PC-MRI are detailed. Finally, typical methods to accelerate the scan time are presented.

The third chapter is devoted to MRI modelling. A toy model is first presented. Then the in-house YALES2BIO solver dedicated to the numerical simulation of blood flows is introduced. Finally, the in-house simulator of MRI acquisitions from constructor chronograms is detailed.

In the fourth chapter, accelerated sequences of 4D flow MRI using GRAPPA and compressed sensing are compared to conventional non-accelerated MRI and CFD. The acquisitions and simulations are performed on the pulsatile phantom developed by Puiseux et al. under complex flow conditions [10]. Hemodynamics biomarkers are investigated: velocity profiles, flow rates, and peak velocities. The content of this chapter has been published as Garreau et al. (2022) in the journal Magnetic Resonance in Medicine [21].

The fifth chapter is devoted to the study of partial echo, a technique often used in PC-MRI acquisition to reduce the echo time and potentially increase the temporal resolution. It appears that there is no consensus about partial echo in 4D flow MRI [22]. While using this technique reduces the volume of data acquired, which could deteriorate the reconstructed images, it also allows to reduce the misregistration artifact [89]. Simulations are performed using the 4D flow MRI simulation framework to better understand the impact of partial echo on the outcomes.

Finally, a summary of the main results is given in the last chapter. Perspectives for clinical applications and future researches are provided.

Fundamentals of Magnetic Resonance Imaging

Chapter contents

2.1   The Nuclear Magnetic Resonance phenomenon

The Nuclear Magnetic Resonance (NMR) is a phenomenon first described by Rabi in the 1930s [90]. It is a property of atomic nucleus possessing a non-zero nuclear spin when they interact with an external magnetic field. The NMR phenomenon is the basis for NMR spectroscopy, used to access the structure of organic compounds, as well as for Magnetic Resonance Imaging (MRI), a medical application where the hydrogen atoms are usually targeted to produce images.

Like its mass or charge, the nuclear spin I is a quantum property of each nuclear species. It can be either an integer or a half-integer. In the presence of a magnetic field $\boldsymbol{B}_0$, the nuclear spin gives rise to a spin magnetic moment $\boldsymbol{\mu}$ with an amplitude proportional to the nuclear spin. The spin magnetic moment precesses around the axis of the magnetic field $\boldsymbol{B}_0$, like a spinning top around its vertical axis. The precession frequency is called the Larmor frequency ω_0 and is proportional to the magnitude B_0 of the magnetic field such that

$$\omega_0 = \gamma B_0 \tag{2.1}$$

with γ the gyromagnetic ratio (in rad.T^{-1}.s^{-1}) and B_0 the magnitude of the magnetic field (in T). The γ constant is characteristic of each isotope. Note that isotope whose nuclear spin equals zero can not interact with the external magnetic field and thus can not be observed in NMR or MRI (e.g. ^{12}C and ^{16}O have a zero nuclear spin).

The equation of motion arising from the interaction between the spin and the external magnetic field can be derived as [91]:

$$\frac{d\boldsymbol{\mu}}{dt} = \gamma \boldsymbol{\mu} \times \boldsymbol{B}_0 \tag{2.2}$$

An illustration of the spin precession is given in Fig. 2.1. This figure corresponds to the $\gamma > 0$ case and results in a clockwise precession around $\boldsymbol{B}_0$, which is usually positively oriented along the z axis. Using the convention that the Larmor frequency ω_0 is positive, the associated angular velocity vector $\boldsymbol{\Omega}_0$ has to oppose to $\boldsymbol{B}_0$ such that $\boldsymbol{\Omega}_0 = -\omega_0 \hat{e}_z$.
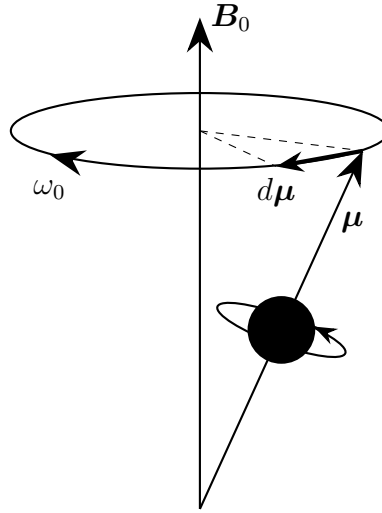
Figure 2.1: Precession of the magnetic moment vector $\boldsymbol{\mu}$ around the axis of the applied magnetic field $\boldsymbol{B}_0$.

Let us now consider a specific nuclear species, namely the hydrogen atoms. The hydrogen nuclei are composed of one proton H^+ with a spin $1/2$ and a gyromagnetic ratio $\gamma = 267.513 \times 10^6$ rad.T^{-1}.s^{-1}. Protons are mostly targeted in MRI, since they are highly present within biological tissues due to their high content in water. With their one-half spin, a proton can be seen as a small magnetic dipole, like a compass needle. Without any exterior magnetic field, it is oriented randomly. As soon as it is in the presence of an external magnetic field $\boldsymbol{B}_0$, the spin will align either parallel ("spin-up") or anti-parallel ("spin-down") to the field. According to quantum mechanics and the Zeeman effect, this leads to two discrete energy values:

$$E = -\boldsymbol{\mu} \cdot \boldsymbol{B}_0 \implies \begin{cases} E_{+1/2} = -\frac{1}{2}\gamma\hbar B_0 & \text{("spin-up")} \\[2mm] E_{-1/2} = +\frac{1}{2}\gamma\hbar B_0 & \text{("spin-down")} \end{cases} \tag{2.3}$$

where $\hbar = \frac{h}{2\pi}$ is the reduced Planck constant ($h = 6.626 \times 10^{-34}$ J.s). Based on energetic considerations, there will statistically be more spins "up" (lowest energy state) than "down". This excess in spins oriented parallel to $\boldsymbol{B}_0$ gives rise to a macroscopic magnetization $\boldsymbol{M}$ such that in a volume V containing N protons, we can add the contribution of each spin magnetic moment:

$$\boldsymbol{M} = \frac{1}{V} \sum_{i=1}^{N} \boldsymbol{\mu}_i \tag{2.4}$$

At thermal equilibrium, the resulting magnetic vector $\boldsymbol{M_0}$ can be defined as

$$\boldsymbol{M_0} \approx \frac{\rho_0 \gamma^2 \hbar^2}{4kT} \boldsymbol{B}_0 \tag{2.5}$$

where ρ_0 is the proton density per unit of volume, k the Boltzmann constant ($k = 1.380649 \times 10^{-23}$ J.K^{-1}) and T the temperature (in K).

2.2 NMR signal and Bloch equations

The principle of NMR relies on disrupting the precession movement of $\boldsymbol{M}$ around $\boldsymbol{B}_0$ thanks to an additional temporary $\boldsymbol{B}_1(t)$ magnetic field in the orthogonal plane. This first step of the NMR experience is called *excitation*. Once the $\boldsymbol{B}_1(t)$ field is removed, $\boldsymbol{M}$ will recover its initial movement around $\boldsymbol{B}_0$ only. This second step is called *relaxation*. When the $\boldsymbol{M}$ returns to equilibrium, it produces an electromagnetic field, which can be measured: the NMR signal.

2.2.1 Excitation and rotating frame of reference

By convention, $\boldsymbol{B}_0$ is oriented along the z-axis, so that $\boldsymbol{B}_0 = B_0 \hat{e}_z$, and $\boldsymbol{M_0} = M_0 \hat{e}_z$ at equilibrium. The $\boldsymbol{B}_1(t)$ magnetic field occurs in the (xy)-plane to rotate $\boldsymbol{M}$ away from the z-axis. Contrary to $\boldsymbol{B}_0$, which is a static magnetic field, $\boldsymbol{B}_1(t)$ is an oscillating magnetic field.

From then on, it appears natural not to work in the fixed laboratory frame of reference $(\hat{e}_x, \hat{e}_y, \hat{e}_z)$ any longer, but in the rotating frame of reference $(\hat{e}'_x, \hat{e}'_y, \hat{e}_z)$ illustrated in Fig. 2.2. Let us define $\boldsymbol{\Omega} = -\omega \hat{e}_z$ the rotational angular velocity vector associated with the latter frame of reference (clockwise-rotating frame of reference). For any magnetic field $\boldsymbol{B}$, combining Equations (2.2) and (2.4) leads to

$$
\begin{aligned}
\frac{d\boldsymbol{M}}{dt} &= \left(\frac{d\boldsymbol{M}}{dt}\right)' + \boldsymbol{\Omega} \times \boldsymbol{M} \\
\implies \left(\frac{d\boldsymbol{M}}{dt}\right)' &= \frac{d\boldsymbol{M}}{dt} + \boldsymbol{M} \times \boldsymbol{\Omega} \\
&= \gamma \boldsymbol{M} \times \boldsymbol{B} + \boldsymbol{M} \times \boldsymbol{\Omega} \\
&= \gamma \boldsymbol{M} \times \boldsymbol{B}_{\text{eff}} \qquad \text{with } \boldsymbol{B}_{\text{eff}} = \boldsymbol{B} + \frac{\boldsymbol{\Omega}}{\gamma}
\end{aligned} \tag{2.6}
$$

In the rotating frame of reference associated with the frequency ω_0, the static field contribution $B_0 \hat{e}_z = \frac{\omega_0}{\gamma} \hat{e}_z$ vanishes, and $\boldsymbol{B}_{\text{eff}} = \boldsymbol{B}_1(t)$.

The oscillating magnetic field $\boldsymbol{B}_1$ applied during the excitation step is called the Radio-Frequency (RF) pulse. In the laboratory frame, this field can be expressed as $\boldsymbol{B}_1(t) = B_1(t)\cos(\omega_1 t)\hat{e}_x - B_1(t)\sin(\omega_1 t)\hat{e}_y$. It can be rewritten in the rotating frame as

$$
\begin{aligned}
\begin{bmatrix} B_{1,x'}(t) \\ B_{1,y'}(t) \\ B_{1,z'}(t) \end{bmatrix} &= \begin{bmatrix} \cos(\omega t) & -\sin(\omega t) & 0 \\ \sin(\omega t) & \cos(\omega t) & 0 \\ 0 & 0 & 1 \end{bmatrix} \begin{bmatrix} B_1(t)\cos(\omega_1 t) \\ -B_1(t)\sin(\omega_1 t) \\ 0 \end{bmatrix} \\
&= \begin{bmatrix} B_1(t)\cos\left((\omega - \omega_1)t\right) \\ B_1(t)\sin\left((\omega - \omega_1)t\right) \\ 0 \end{bmatrix}
\end{aligned} \tag{2.7}
$$

To be able to tip the magnetization vector $\boldsymbol{M}$ out of its alignment with $\boldsymbol{B}_0$, the RF pulse has to be applied close to the Larmor frequency ω_0. If the on-resonance
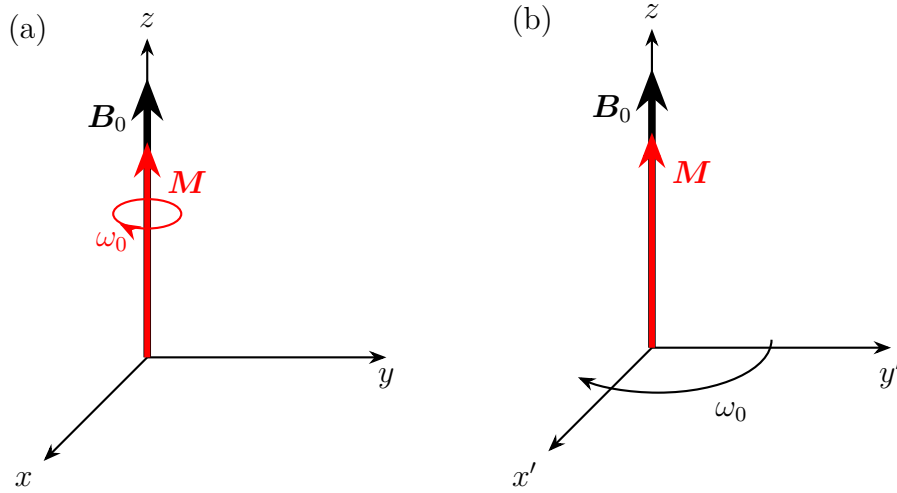
Figure 2.2: Magnetic vector $\boldsymbol{M}$ precession from (a) the laboratory frame of reference and (b) a rotating frame of reference. If the angular frequency of the rotating reference frame is equal to ω_0, the rotational motion of $\boldsymbol{M}$ is frozen.

condition is met, that is $\omega = \omega_0 = \omega_1$, Equation (2.7) reduces to $\boldsymbol{B}_1(t) = B_1(t)\hat{e}'_x$. Thereby, $\boldsymbol{M}$ rotates around the (x')-axis and is located in the $(y'z)$-plane. The angle by which $\boldsymbol{M}$ is tipped away from the axis (z) is called the flip angle α (presented in Fig. 2.3) and is defined as

$$\alpha = \gamma \int_0^{t_{rf}} B_1(t)dt \tag{2.8}$$

with t_{rf} the duration of the RF pulse (~ 1 ms) and $B_1(t)$ the envelope of the RF pulse.
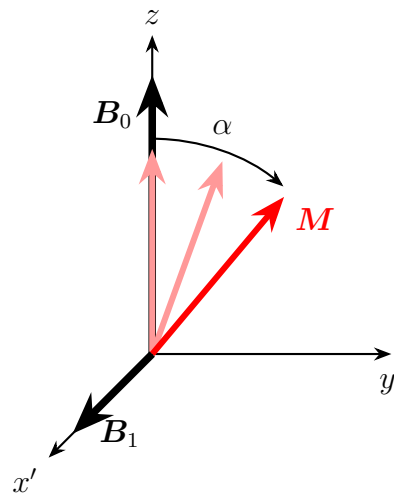
Figure 2.3: Flip angle α viewed from the rotating frame of reference.

19

2.2.2 Relaxation

After the RF pulse has been applied, the magnetization vector $\boldsymbol{M}$ relaxes towards its equilibrium state aligned with the $\boldsymbol{B}_0$-axis. That means that the longitudinal component M_z grows again to its initial value M_0, whereas the transverse components M_x and M_y disappear.

Felix Bloch proposed a model in 1946 to describe the NMR phenomenon [92]. He introduced two relaxation time constants, T_1 and T_2, which respectively reflects the regrowth of the longitudinal magnetization and the decay of the transverse components. These time constants depend on tissues and were defined phenomenologically. The T_1-relaxation comes from energy exchanges between the spins and their surroundings. The T_2-relaxation occurs because of several reasons: T_1-relaxation, spins dephasing due to local magnetic fields, spin-spin "flip-flop" interactions where a pair of spins exchange their longitudinal angular momentum leading to a loss of T_2 coherence.

In the laboratory frame of reference, the Bloch equations are given by

$$\frac{d\boldsymbol{M}(t)}{dt} = \underbrace{\gamma\boldsymbol{M}(t) \times \boldsymbol{B}(t)}_{\text{Precession}} + \underbrace{\frac{1}{T_1}(M_0 - M_z(t))\hat{e}_z - \frac{1}{T_2}(M_x(t)\hat{e}_x + M_y(t)\hat{e}_y)}_{\text{Relaxation}} \quad (2.9)$$

where M_0 is the longitudinal component of $\boldsymbol{M}$ at equilibrium: $\boldsymbol{M}(t \to \infty) = M_0\hat{e}_z$.

In the rotating frame, according to Eq. (2.6), they are rewritten as

$$\frac{d\boldsymbol{M}(t)}{dt} = \gamma\boldsymbol{M}(t) \times \boldsymbol{B}_{\text{eff}}(t) + \frac{1}{T_1}(M_0 - M_z(t))\hat{e}_z - \frac{1}{T_2}(M'_x(t)\hat{e}'_x + M'_y(t)\hat{e}'_y) \quad (2.10)$$

where $\boldsymbol{M}$ and $\boldsymbol{B}_{\text{eff}}$ have to be expressed in the rotating frame as well.

$$\boldsymbol{M}(t) = M'_x(t)\hat{e}'_x + M'_y(t)\hat{e}'_y + M_z(t)\hat{e}_z \quad (2.11)$$

and, according to Eq. (2.7),

$$\boldsymbol{B}_{\text{eff}}(t) = \boldsymbol{B}_0 + \boldsymbol{B}_1(t) + \frac{\boldsymbol{\Omega}}{\gamma} \quad (2.12)$$

$$= B_1(t)\cos\left((\omega - \omega_1)\,t\right)\hat{e}'_x + B_1(t)\sin\left((\omega - \omega_1)\,t\right)\hat{e}'_y + (B_0 - \frac{\omega}{\gamma})\hat{e}_z$$

The Bloch equations in the rotating frame (Eq. (2.10)) can be expressed in matrix form as

$$\frac{d}{dt}\begin{bmatrix} M'_x(t) \\ M'_y(t) \\ M_z(t) \end{bmatrix} = \gamma \begin{bmatrix} M'_x(t) \\ M'_y(t) \\ M_z(t) \end{bmatrix} \times \begin{bmatrix} B_1(t)\cos((\omega_1 - \omega)t) \\ -B_1(t)\sin((\omega_1 - \omega)t) \\ \frac{\omega_0 - \omega}{\gamma} \end{bmatrix} + \begin{bmatrix} -\frac{M'_x(t)}{T_2} \\ -\frac{M'_y(t)}{T_2} \\ \frac{M_0 - M_z(t)}{T_1} \end{bmatrix}$$

$$= \begin{bmatrix} -\frac{1}{T_2} & \Delta\omega_0 & \gamma B_1(t)\sin(\Delta\omega_1 t) \\ -\Delta\omega_0 & -\frac{1}{T_2} & \gamma B_1(t)\cos(\Delta\omega_1 t) \\ -\gamma B_1(t)\sin(\Delta\omega_1 t) & -\gamma B_1(t)\cos(\Delta\omega_1 t) & -\frac{1}{T_1} \end{bmatrix}\begin{bmatrix} M'_x(t) \\ M'_y(t) \\ M_z(t) \end{bmatrix}$$

$$+ \begin{bmatrix} 0 \\ 0 \\ \frac{M_0}{T_1} \end{bmatrix} \quad (2.13)$$

where $\Delta\omega_0 = \omega_0 - \omega$ and $\Delta\omega_1 = \omega_1 - \omega$.

If the on-resonance condition is met, i.e. $\omega = \omega_0 = \omega_1$, Eq. (2.13) reduces to

$$\frac{d}{dt}\begin{bmatrix} M'_x(t) \\ M'_y(t) \\ M_z(t) \end{bmatrix} = \begin{bmatrix} -\frac{1}{T_2} & 0 & 0 \\ 0 & -\frac{1}{T_2} & \gamma B_1(t) \\ 0 & -\gamma B_1(t) & -\frac{1}{T_1} \end{bmatrix}\begin{bmatrix} M'_x(t) \\ M'_y(t) \\ M_z(t) \end{bmatrix} + \begin{bmatrix} 0 \\ 0 \\ \frac{M_0}{T_1} \end{bmatrix} \tag{2.14}$$

A generalization of the Bloch equations to account for the transfer of magnetization by diffusion has been proposed in 1953 by H.C. Torrey [93]. The diffusion term $\nabla \cdot (\boldsymbol{D}\nabla\boldsymbol{M})$, where $\boldsymbol{D}$ is the diffusion tensor, is added in the Bloch-Torrey equations. This equation is however out of the scope of the present thesis.

2.2.3   Analytical solutions

Excitation

Because the RF is of short duration, it is considered that $\omega_1 \gg \dfrac{1}{T_1}, \dfrac{1}{T_2}$ and thereby the relaxation effects are often disregarded. In the on-resonance rotating frame of reference, Eq. (2.14) becomes

$$\frac{d}{dt}\begin{bmatrix} M'_x(t) \\ M'_y(t) \\ M_z(t) \end{bmatrix} = \begin{bmatrix} 0 & 0 & 0 \\ 0 & 0 & \gamma B_1(t) \\ 0 & -\gamma B_1(t) & 0 \end{bmatrix}\begin{bmatrix} M'_x(t) \\ M'_y(t) \\ M_z(t) \end{bmatrix} \tag{2.15}$$

To solve the system of differential equations, let $M'_{yz}(t) = (M'_y + iM_z)(t)$.

$$\frac{d}{dt}(M'_y + iM_z)(t) = -i\gamma B_1(t)(M'_y + iM_z)(t) \tag{2.16}$$

$$\implies \int_0^{t_{rf}} \frac{d((M'_y + iM_z)(t))}{(M'_y + iM_z)(t)} = -i\alpha$$

$$\implies (M'_y + iM_z)(t) = (M'_y + iM_z)(0)e^{-i\alpha}$$

where α is the flip angle introduced in Eq. (2.8). With the usual initial conditions $\boldsymbol{M_0} = (0, 0, M_0)$, Eq. (2.16) reduces to:

$$\begin{cases} M'_x(t) = 0 \\ M'_y(t) = M_0 \sin(\alpha) \\ M_z(t) = M_0 \cos(\alpha) \end{cases} \tag{2.17}$$

Thereby, when the on-resonance condition is met, the magnetization vector $\boldsymbol{M}$ is well tipped in the $(y'z)$-plane by the flip angle α. One can notice that if there are off-resonance terms ($\Delta\omega_0$ in Eq. (2.13)), the magnetization vector experiences an additional azimuthal angle.

Relaxation

As stated in the last paragraph, due to the short duration of the RF, it is considered that relaxation begins when $\boldsymbol{B}_1$ goes back to zero. Thereby, the Bloch equations on-resonance become

$$\frac{d}{dt}\begin{bmatrix} M_x'(t) \\ M_y'(t) \\ M_z(t) \end{bmatrix} = \begin{bmatrix} -\frac{1}{T_2} & 0 & 0 \\ 0 & -\frac{1}{T_2} & 0 \\ 0 & 0 & -\frac{1}{T_1} \end{bmatrix} \begin{bmatrix} M_x'(t) \\ M_y'(t) \\ M_z(t) \end{bmatrix} + \begin{bmatrix} 0 \\ 0 \\ \frac{M_0}{T_1} \end{bmatrix} \tag{2.18}$$

The transverse magnetization components M_x' and M_y' are decoupled from the longitudinal magnetization component M_z. Thus, the complex representation of the transverse magnetization is used: $M_{xy}'(t) = M_x'(t) + iM_y'(t) = |M_{xy}'(t)|e^{i\phi(t)}$, where $|M_{xy}'(t)|$ is the modulus of the transverse magnetization and $\phi(t)$ its phase. Note that an ensemble of spins with the same phase, meaning that they all precess at the same Larmor frequency, is call a spin *isochromat*. The physical concept of isochromat allows to study its behavior from a classical physics point of view, and not to deal with the particularities of quantum mechanics [94]. Yet, in the literature, the term "spins" is often used as a synonym for "(spin) isochromats".

The analytic solutions are given as

$$\begin{cases} M_{xy}'(t) = M_{xy}'(t_0)e^{-\frac{t-t_0}{T_2}} \\ M_z(t) = (M_z(t_0) - M_0)e^{-\frac{t-t_0}{T_1}} + M_0 \end{cases} \tag{2.19}$$

where $t_0 \geq t_{rf}$ denotes the end of the RF pulse., i.e. the beginning of relaxation. It is easy to express $\boldsymbol{M}$ back in the laboratory frame of reference, as rotating a complex number z through an angle θ results in multiplying z by $e^{i\theta}$. Hence, in the laboratory frame, Eq. (2.19) become

$$\begin{cases} M_{xy}(t) = M_{xy}(t_0)e^{-i\omega_0 t}e^{-\frac{t-t_0}{T_2}} = |M_{xy}(t_0)|e^{-i(\omega_0 t - \phi(t_0))}e^{-\frac{t-t_0}{T_2}} \\ M_z(t) = (M_z(t_0) - M_0)e^{-\frac{t-t_0}{T_1}} + M_0 \end{cases} \tag{2.20}$$

2.3 Radiofrequency coils

To produce the time-varying magnetic field $\boldsymbol{B}_1(t)$, radiofrequency coils are needed. This type of coils is also used to record the NMR signal. Transmit and receive RF coils are usually separate coils, but combined transmit/receive coil do exist and are used for specific applications (e.g. head and knee imaging, ultrahigh-field MRI).

2.3.1 Producing the $\boldsymbol{B}_1(t)$ field

To stimulate the spins, the $\boldsymbol{B}_1(t)$ field must have two characteristics. First, its components need to rotate near the resonant frequency ω_0, and secondly, it has to be applied perpendicular to the static magnetic field $\boldsymbol{B}_0$.

The $\boldsymbol{B}_1$ field is produced by RF-transmit coils, fed by powerful electrical currents. The transmit coils can be located in the inner walls of the MR scanner (body coils), or placed near the patient via cables (patient coils). Their design have two main goals: to provide a homogeneous $\boldsymbol{B}_1$ field in the sample to be investigated and to minimize the time needed to flip the magnetization.

Before arriving into the coils, the electrical currents have to go through a electronic chain. First, a frequency synthesizer produces a continuous sinusoidal carrier wave at or near the Larmor frequency. This signal will be used as a reference for demodulating the MR signal in the RF-receiver chain (see Section 2.3.2). In the RF-transmit chain, the carrier wave is then modulated by the desired low frequency RF-pulse envelope in the RF pulse generator and amplified. To achieve a field in the rotating frame such that $\boldsymbol{B}_1(t) = B_1(t)\cos(\omega_1 t)\hat{e}_x - B_1(t)\sin(\omega_1 t)\hat{e}_y = B_1(t)\hat{e}'_x$ (cf Eq. (2.7)), a circularly polarized transmission, also known as quadrature, is usually chosen. While a linearly polarized coil can only provide a one dimensional sinusoidal field, e.g. $\boldsymbol{B}_1(t) = B_1(t)\cos(\omega_1 t)\hat{e}_x$ in the laboratory frame, combining two linearly polarized RF fields allows to produce the desired $\boldsymbol{B}_1(t)$ field. The left-circularly polarized RF field is obtain by adding two linearly RF fields with the same frequency and peak amplitude. In addition to being perpendicular to the static field $\boldsymbol{B}_0$, they have to be localized perpendicularly to one another. With respect to time dependence, they need to be 90° out of phase. One can demonstrate that the quadrature coil arrangement provides a better RF spatial homogeneity and less power to produce the same flip angle compared to a single linearly polarized coil [91].

2.3.2   Signal detection

As the net magnetization relaxes, its precession around $\boldsymbol{B}_0$ results in a time-varying magnetic flux in the receive RF coil, which creates a voltage in the receive RF coil called the electromotive force (emf). It is a consequence of Faraday's law of induction. Let us consider a receive coil of area S and $\boldsymbol{B}(t)$ a time-dependent magnetic field. The magnetic flux Φ through the coil is defined as

$$\Phi = \iint_S \boldsymbol{B}(t) \cdot \boldsymbol{n} dS \tag{2.21}$$

where $\boldsymbol{n}$ is the unit vector normal to the surface S. According to Faraday's law of induction, the electromotive force is given as

$$emf = -\frac{d\Phi}{dt} = -\frac{d}{dt}\iint_S \boldsymbol{B}(t) \cdot \boldsymbol{n} dS \tag{2.22}$$

Based on the principle of reciprocity, Haacke et al. details in [91] how to express Eq. (2.22) not as a surface integration over the receive coil area any longer, but as a volume integration over a region of non-zero magnetization. Elements of explanation can be found in 7.1. Such a formulation appears more useful in MRI in order to understand the factors which act on the signal amplitude. In this

case, only the flux Φ_M through a coil due to a magnetization source is taken into account. Thereby, Eq. (2.22) can be reformulated as

$$emf = -\frac{d\Phi_M}{dt} = -\frac{d}{dt} \iiint_V \boldsymbol{M}(\boldsymbol{r}, t) \cdot \boldsymbol{\mathcal{B}}^r(\boldsymbol{r}) d^3r \tag{2.23}$$

where $\boldsymbol{\mathcal{B}}^r(\boldsymbol{r}) = \frac{\boldsymbol{B}(\boldsymbol{r})}{I}$ is the magnetic field per unit current that would be produced by the receive coil at the location $\boldsymbol{r}$. This quantity is also called the coil profile or sensitivity. Note that a spatial dependence is added to the magnetization vector $\boldsymbol{M}(\boldsymbol{r}, t)$, and that the emf has an implicit dependence on the excitation field $\boldsymbol{B}_1$ through $\boldsymbol{M}$ (cf Eq. (2.16)). The RMN signal is proportional to the emf.

2.3.3 Classic coil designs

For RF transmission, the most popular coil arrangement is the birdcage coil (see Fig. 2.4). This design equips almost all body coils, and it is common to image the head and knee [95, 96, 97, 98]. It presents a quadrature arrangement, with excellent radial field uniformity. However, its field homogeneity decays in the axial direction [91].
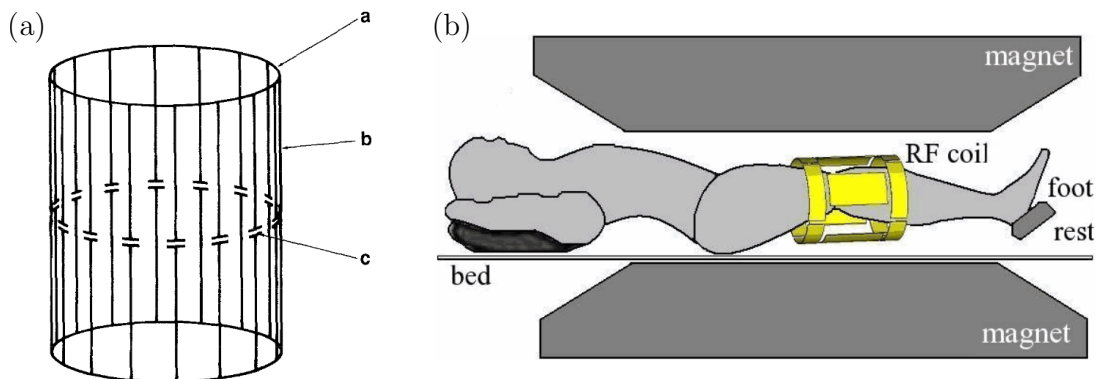
Figure 2.4: Birdcage designs. (a) Low-pass version of the birdcage as initially introduced by Hayes [95] (a - Circular end ring, b - leg, c - capacitor), (b) Illustration of the experimental setup to image a knee with a birdcage, extracted from [98].

For RF reception, the coils are designed to present two main properties: to maximize the Signal-to-Noise Ratio (SNR) achieved by the coil, and to insure homogeneity of the RF receive response over the sample to be imaged [91]. Concerning in particular receive coils, their SNR depends on their sensitivity and their associated noise. The noise originates from contributions of the coil itself, of the surrounding electronics and mainly of the sample being imaged. Thus, positioning the coil the closest to the region-of-interest increases the SNR. So does decreasing the volume to which the coil is sensitive to (i.e., the volume from which the coil receives a signal) [99].

Except for knee and head imaging for which birdcages are also particularly useful for signal reception, the most common type of receive RF-coils are surface coils. As this type of coils are placed directly on the patient's body, they are well adapted to image features that are close to the body surface [100]. The most basic surface coil consists in a single coil placed on the body, which does not allow the detection of quadrature magnetic fields. However, various surface coil designs exist of which circularly-polarized ones as well, as illustrated in Fig. 2.5.
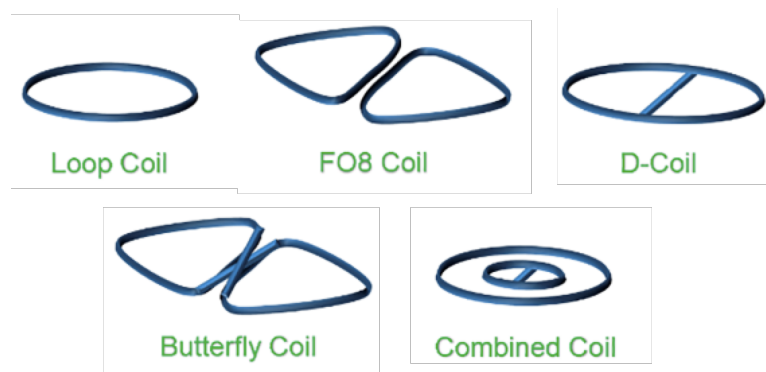
Figure 2.5: Various surface coil designs, adapted from [100]. Linearly-polarized coil configurations are presented in the first row, while circularly-polarized ones are displayed in the second row.

One or more surface coils can be used to image part of the body. They can be assembled in a set, called a phased array coil. Examples of phased arrays are shown in Fig. 2.6. By combining the signals received in each coil, a larger region can be covered uniformly than if an individual coil had been used. Furthermore, utilizing a set of small individual coils offers higher SNR compared to a single large coil [100, 101]. However, care should be taken with respect to the noise, that has to be uncorrelated from coil to coil. Each coil should have its own electronic receive circuit and the neighbor coils are usually overlapping in order to achieve a zero mutual inductance between them by using the principle of reciprocity and Faraday's law of induction [91].

A particular type of phased arrays are parallel arrays. These arrays are used in parallel imaging, an MRI acceleration technique that exploit the spatial dependence and sensitivity of the individual elements of the array [101]. More details will be given about parallel imaging in Section 2.9.2. To be able to take advantage of these additional information, each individual coil element has to be free of magnetic interactions. Usually it is done by using a coil decoupling circuitry and by placing the coil elements apart from one another at a distance large enough to minimize their interaction [100].
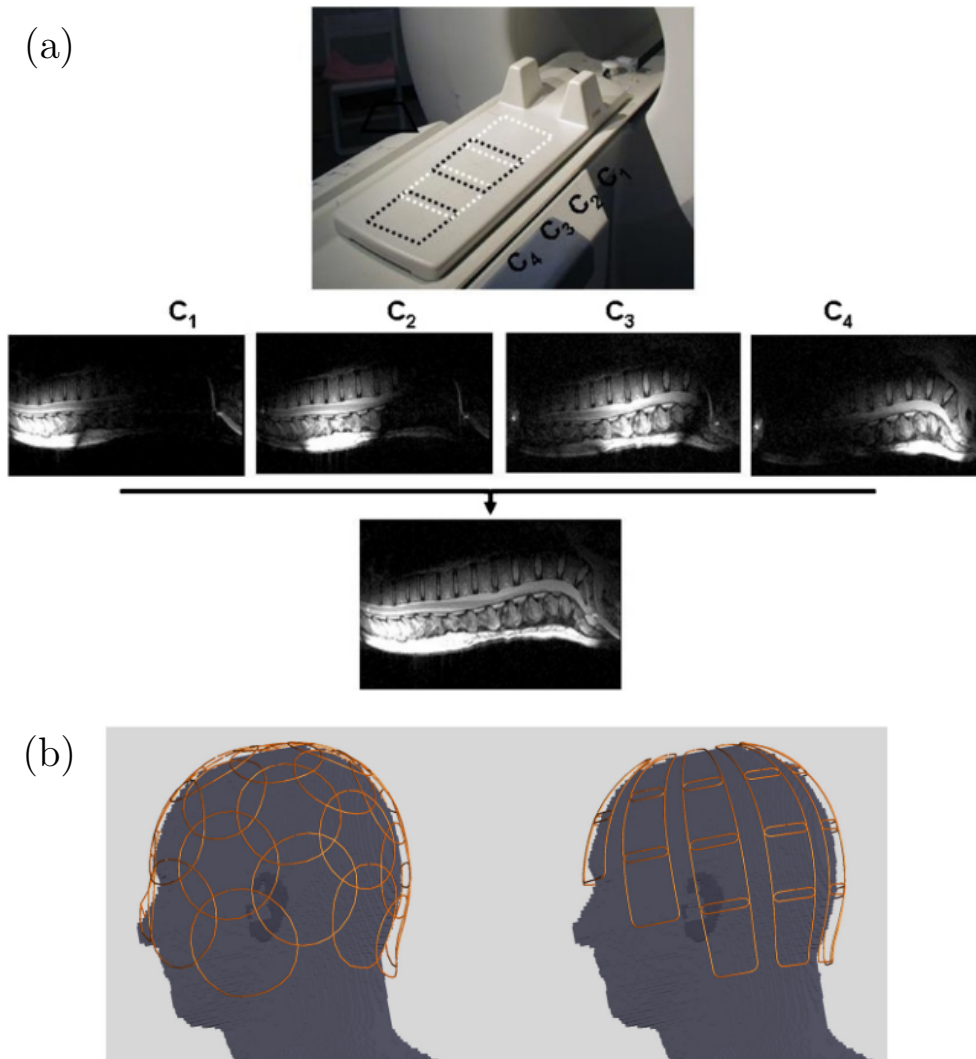
Figure 2.6: Phased array coils. (a) Phased array of four coils to image the spine, extracted from [101]. Each coil element $C_{i=\{1,2,3,4\}}$ produces an image weighted by its sensitivity. These four images can be combined into the bottom image. (b) Two designs of 32-channel phased arrays for brain imaging, extracted from [102].

2.4 Basic types of NMR signals

As seen previously, RF pulses produced by specific coils are used to excite the spins and detect the signal that they produce as they relax to the equilibrium net magnetization. Additional coils called the *gradient coils* can be used to interact with the magnetization. This section focuses on basic NMR signals obtained using one RF pulse only, multiple RF pulses, or an RF pulse combined with a gradient.

2.4.1 Free Induction Decay

The simplest MRI experiment is the Free Induction Decay (FID). It consists in a single RF excitation pulse applied uniformly to the sample, which produces a global signal of all excited spins. According to Eq. (2.23), the RMN signal $s(t)$ is proportional the emf such that

$$s(t) \propto -\frac{d}{dt} \iiint_V \left(M_x(\boldsymbol{r}, t)\mathcal{B}_x^r(\boldsymbol{r}) + M_y(\boldsymbol{r}, t)\mathcal{B}_y^r(\boldsymbol{r}) + M_z(\boldsymbol{r}, t)\mathcal{B}_z^r(\boldsymbol{r}) \right) d^3r \quad (2.24)$$

Recalling the expression of $\boldsymbol{M}$ in Eq. (2.20) in the laboratory frame, the time-derivative are such that

$$\frac{dM_{xy}}{dt} = -\left(i\omega_0 + \frac{1}{T_2} \right) |M_{xy}(\boldsymbol{r}, t_0)| e^{-i(\omega_0 t - \phi(\boldsymbol{r}, t_0))} e^{-\frac{t-t_0}{T_2}}$$
$$\frac{dM_z}{dt} = -\frac{1}{T_1}(M_z(\boldsymbol{r}, t_0) - M_0)e^{-\frac{t-t_0}{T_1}} \quad (2.25)$$

As ω_0 is at least 4 orders of magnitude larger than $\frac{1}{T_1}$ and $\frac{1}{T_2}$, the longitudinal magnetization is neglected, and the transverse magnetization is approximated as:

$$\frac{dM_{xy}}{dt} \approx -i\omega_0 |M_{xy}(\boldsymbol{r}, t_0)| \left(\cos(\omega_0 t - \phi(\boldsymbol{r}, t_0)) - i\sin(\omega_0 t - \phi(\boldsymbol{r}, t_0)) \right) e^{-\frac{t-t_0}{T_2}}$$

$$\implies \begin{cases} \frac{dM_x}{dt} \approx -\omega_0 |M_{xy}(\boldsymbol{r}, t_0)| \sin(\omega_0 t - \phi(\boldsymbol{r}, t_0))e^{-\frac{t-t_0}{T_2}} \\ \frac{dM_y}{dt} \approx -\omega_0 |M_{xy}(\boldsymbol{r}, t_0)| \cos(\omega_0 t - \phi(\boldsymbol{r}, t_0)) e^{-\frac{t-t_0}{T_2}} \end{cases} \quad (2.26)$$

Thereby, the signal presented in Eq. (2.24) reduces to

$$s(t) \propto \omega_0 \iiint_V e^{-\frac{t-t_0}{T_2}} |M_{xy}(\boldsymbol{r}, t_0)| \left(\sin(\omega_0 t - \phi(\boldsymbol{r}, t_0))\mathcal{B}_x^r(\boldsymbol{r}) \right.$$
$$\left. + \cos(\omega_0 t - \phi(\boldsymbol{r}, t_0))\mathcal{B}_y^r(\boldsymbol{r}) \right) d^3r \quad (2.27)$$

Eq (2.27) can be further simplified, when expressing the transverse sensitivity of the receive coil as a complex number: $\mathcal{B}_{xy}^r(\boldsymbol{r}) = |\mathcal{B}_{xy}^r(\boldsymbol{r})|e^{i\theta_{\mathcal{B}^r}(\boldsymbol{r})}$. The signal is then given as

$$s(t) \propto \omega_0 \iiint_V e^{-\frac{t-t_0}{T_2}} |M_{xy}(\boldsymbol{r}, t_0)||\mathcal{B}_{xy}^r(\boldsymbol{r})| \sin(\omega_0 t + \theta_{\mathcal{B}^r}(\boldsymbol{r}) - \phi(\boldsymbol{r}, t_0))d^3r \quad (2.28)$$

The signal is dominated by the rapid oscillations at the Larmor frequency ω_0 in the sinusoidal term. These oscillations are removed by an electronic step called the *demodulation*, based on the reference sinusoidal carrier wave used to generate the $\boldsymbol{B}_1(t)$ field (cf Section 2.3.1). The on-resonance hypothesis $\omega = \omega_0 = \omega_1$ is assumed. The demodulation results in viewing the signal from the rotating frame of reference.

The demodulation is performed by multiplying the signal by $\sin(\omega_0 t)$ on the one hand and by $-\cos(\omega_0 t)$ on the other hand, resulting in two *channels* to store the signal. The first channel is called the *real* channel and the second the *imaginary* channel. Let us focus on the first sinusoidal term with $\beta = \theta_{\mathcal{B}^r}(\boldsymbol{r}) - \phi(\boldsymbol{r}, t_0)$:

$$\sin(\omega_0 t)\sin(\omega_0 t + \beta) = \frac{1}{2}\left(\cos(-\beta) + \sin(2\omega_0 t + \beta)\right) \qquad (2.29)$$

The high-frequency 2$^{\text{nd}}$ term is eliminated by low pass filtering. Thereby, the demodulated and low pass filtered real channel is

$$s_{re}(t) \propto \omega_0 \iiint_V e^{-\frac{t-t_0}{T_2}} |M_{xy}(\boldsymbol{r}, t_0)||\mathcal{B}_{xy}^r(\boldsymbol{r})| \cos\left(\phi(\boldsymbol{r}, t_0) - \theta_{\mathcal{B}^r}(\boldsymbol{r})\right) d^3 r \qquad (2.30)$$

$$\propto \omega_0 \iiint_V e^{-\frac{t-t_0}{T_2}} |M_{xy}(\boldsymbol{r}, t_0)||\mathcal{B}_{xy}^r(\boldsymbol{r})| \Re\left(e^{i(\phi(r, t_0) - \theta_{\mathcal{B}^r}(r))}\right) d^3 r$$

Similarly, the demodulated and low pass filtered imaginary channel is

$$s_{im}(t) \propto \omega_0 \iiint_V e^{-\frac{t-t_0}{T_2}} |M_{xy}(\boldsymbol{r}, t_0)||\mathcal{B}_{xy}^r(\boldsymbol{r})| \sin\left(\phi(\boldsymbol{r}, t_0) - \theta_{\mathcal{B}^r}(\boldsymbol{r})\right) d^3 r \qquad (2.31)$$

$$\propto \omega_0 \iiint_V e^{-\frac{t-t_0}{T_2}} |M_{xy}(\boldsymbol{r}, t_0)||\mathcal{B}_{xy}^r(\boldsymbol{r})| \Im\left(e^{i(\phi(r, t_0) - \theta_{\mathcal{B}^r}(r))}\right) d^3 r$$

Finally, the signal collected by the receive coil is a complex signal $S(t) = s_{re}(t) + i s_{im}(t)$ given by

$$S(t) \propto \omega_0 \iiint_V e^{-\frac{t-t_0}{T_2}} |M_{xy}(\boldsymbol{r}, t_0)||\mathcal{B}_{xy}^r(\boldsymbol{r})| e^{i(\phi(r, t_0) - \theta_{\mathcal{B}^r}(r))} d^3 r \qquad (2.32)$$

$$\propto \omega_0 \iiint_V M_{xy}(\boldsymbol{r}, t)\mathcal{B}_{xy}^*(\boldsymbol{r}) d^3 r$$

where $\mathcal{B}_{xy}^*(\boldsymbol{r}) = |\mathcal{B}_{xy}^r(\boldsymbol{r})| e^{-i\theta_{\mathcal{B}^r}(\boldsymbol{r})}$ is the complex conjugate of $\mathcal{B}_{xy}^r(\boldsymbol{r})$ and $M_{xy}(\boldsymbol{r}, t) = e^{-\frac{t-t_0}{T_2}} |M_{xy}(\boldsymbol{r}, t_0)| e^{i\phi(r, t_0)}$ the transverse magnetization as viewed from the rotating frame of reference due to the demodulation. That is why the term $\omega_0 t$ is missing in the complex exponential in comparison to Eq. (2.20).

The FID experiment chronogram and its corresponding signal are represented in Fig. 2.7. The continuous emf signal is sampled by the analog-to-digital converter (ADC).
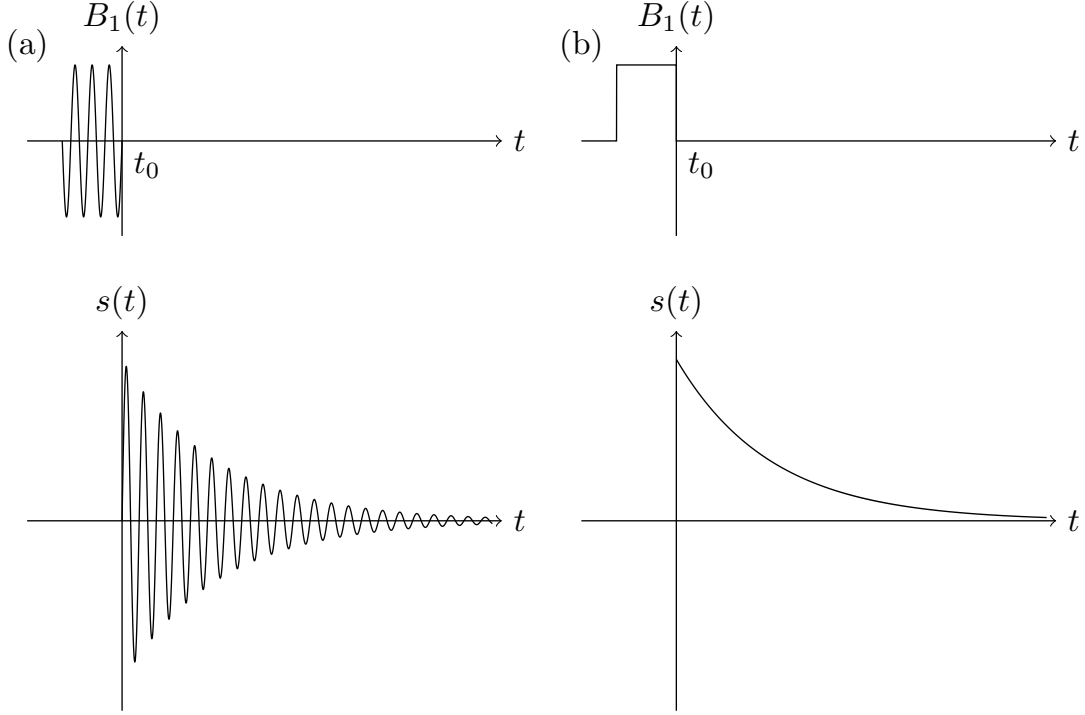
Figure 2.7: FID experiment before demodulation viewed from (a) the laboratory frame of reference (Eq. (2.27)) and (b) the rotating frame of reference. The signal $s(t)$ in (b) can also be interpreted as one of the channels of the demodulated signal.

In practice, the precession frequency of an isochromat at position $\boldsymbol{r}$ can have a spatio-temporal dependency because of variations in the z-component of the local magnetic field. Instead of precessing at the Larmor frequency ω_0, it precesses at

$$\omega(\boldsymbol{r}, t) = \omega_0 + \gamma B_z(\boldsymbol{r}, t) = \omega_0 + \Delta\omega(\boldsymbol{r}, t) \tag{2.33}$$

where $\Delta\omega(\boldsymbol{r}, t)$ represents the frequency shift. The phase of the transverse magnetization in the laboratory frame is then expressed as:

$$\phi(\boldsymbol{r}, t) = \phi(\boldsymbol{r}, t_0) - \int_{t_0}^{t} \omega(\boldsymbol{r}, t')dt' = \phi(\boldsymbol{r}, t_0) - \omega_0(t - t_0) - \int_{t_0}^{t} \Delta\omega(\boldsymbol{r}, t')dt' \tag{2.34}$$

Recall from Fig. 2.1 that the precession is left-handed with respect to the magnetic field, hence the minus sign in front of the integral. In the rotating frame, the $\omega_0(t - t_0)$ term vanishes and Eq. (2.34) reduces to:

$$\phi(\boldsymbol{r}, t) = \phi(\boldsymbol{r}, t_0) - \int_{t_0}^{t} \Delta\omega(\boldsymbol{r}, t')dt' \tag{2.35}$$

When taking into account the spatio-temporal dependence, the complex signal in Eq. (2.32) becomes

$$S(t) \propto \iiint_V \omega(\boldsymbol{r}, t) e^{-\frac{t-t_0}{T_2}} |M_{xy}(\boldsymbol{r}, t_0)| |\mathcal{B}_{xy}^r(\boldsymbol{r})| e^{i(\phi(\boldsymbol{r}, t_0) - \int_{t_0}^{t} \Delta\omega(\boldsymbol{r}, t')dt' - \theta_{\mathcal{B}^r}(\boldsymbol{r}))} d^3r \tag{2.36}$$

As $\omega(\boldsymbol{r}, t)$ is largely dominated by ω_0, it can be taken out of the integrand, but it cannot be ignored in the phase. Introducing a constant Λ including the gain factors due to the electronic detection system, the complex signal is then expressed as:

$$S(t) = \omega_0 \Lambda \iiint_V e^{-\frac{t-t_0}{T_2}} |M_{xy}(\boldsymbol{r}, t_0)| |\mathcal{B}_{xy}^r(\boldsymbol{r})| e^{i(\phi(\boldsymbol{r}, t_0) - \int_{t_0}^t \Delta\omega(\boldsymbol{r}, t')dt' - \theta_{\mathcal{B}^r}(\boldsymbol{r}))} d^3r \quad (2.37)$$

Instead of expressing the complex signal as a function of the magnetization $\boldsymbol{M}$, it can be rewritten in terms of the proton spin density (per unit volume). Indeed, at t_0, combining Eq. (2.5) and (2.17), the transverse magnetization equals to

$$|M_{xy}(\boldsymbol{r}, t_0)| = M_0(\boldsymbol{r}) \sin(\alpha) = \rho_0(\boldsymbol{r}) \frac{\gamma^2 \hbar^2}{4kT} \sin(\alpha) B_0 \quad (2.38)$$

The signal can be finally written under the condensed form

$$S(t) = \iiint_V e^{-\frac{t-t_0}{T_2}} \rho(\boldsymbol{r}) e^{i\phi(\boldsymbol{r}, t)} d^3r = \iiint_V \rho(\boldsymbol{r}, T_2) e^{i\phi(\boldsymbol{r}, t)} d^3r \quad (2.39)$$

where $\rho(\boldsymbol{r}, T_2) = e^{-\frac{t-t_0}{T_2}} \rho(\boldsymbol{r}) = e^{-\frac{t-t_0}{T_2}} \omega_0 \Lambda \frac{\gamma^2 \hbar^2}{4kT} \sin(\alpha) B_0 \mathcal{B}_{xy}^*(\boldsymbol{r}) \rho_0(\boldsymbol{r})$ represents the effective spin density.

2.4.2 Spin Echo (SE)

Until now, the decay of the transversal magnetization has been considered to be described by the relaxation time T_2. A more accurate definition is to take into account an additional phase dispersion (*dephasing*) of the magnetization due to external field inhomogeneities. The observed relaxation time T_2^* is thus defined as

$$\frac{1}{T_2^*} = \frac{1}{T_2} + \frac{1}{T_2'} \quad (2.40)$$

where T_2 arises from thermodynamic effects, while T_2' accounts for machine and sample dependent variations in the external magnetic field. The T_2' signal loss can be recovered in the spin echo RF pulse sequence. This sequence is characterized by the use of two successive RF pulses: a first pulse applied along the x'-axis of flip angle $\alpha = 90°$ (the $\frac{\pi}{2}$-pulse), followed by a π-pulse along the y'-axis of flip angle. This second *refocusing* RF-pulse allows to compensate the dephasing at a specific time T_E, called the echo time.

Let us investigate the accumulated phase of a spin at the position $\boldsymbol{r}$ through the steps of the spin echo. The $\frac{\pi}{2}$-pulse is applied at $t = t_0$ and the π-pulse at $t = \tau$, where both are assumed to be instantaneous. Besides the main static homogeneous field $\boldsymbol{B}_0 = B_0 \hat{e}_z$, a small time-independent constant spatial variation $\boldsymbol{B}_0(\boldsymbol{r}) = b_{0z}(\boldsymbol{r}) \hat{e}_z$ is present, such that the magnetic field along the z-direction and its associated precession frequency are expressed as :

$$B_z(\boldsymbol{r}) = B_0 + b_{0z}(\boldsymbol{r}) \quad ; \quad \omega(\boldsymbol{r}, t) = \omega_0 + \gamma b_{0z}(\boldsymbol{r}) \quad (2.41)$$

Similarly to Eq. (2.35), the phase of the MR signal from an excited isochromat at position $\boldsymbol{r}$ is given by:

$$\phi(\boldsymbol{r}, t) = \phi(\boldsymbol{r}, t_0) - \gamma \int_{t_0}^{t} b_{0z}(\boldsymbol{r}) dt' = \phi(\boldsymbol{r}, t_0) - \gamma b_{0z}(\boldsymbol{r})(t - t_0) \qquad (2.42)$$

With the initial phase $\phi(\boldsymbol{r}, t_0) = 0$ and $t_0 = 0$, the phase evolves through the pulse sequence such that

$$\begin{aligned} \text{for } 0 < t < \tau^-: &\qquad \phi(\boldsymbol{r}, t) = -\gamma b_{0z}(\boldsymbol{r})t \qquad\qquad\qquad (2.43)\\ \text{at } t = \tau^+: &\qquad \phi(\boldsymbol{r}, \tau^+) = -\phi(\boldsymbol{r}, \tau^-) = \gamma b_{0z}(\boldsymbol{r})\tau\\ \text{for } t > \tau^+: &\qquad \phi(\boldsymbol{r}, t) = \phi(\boldsymbol{r}, \tau^+) - \gamma b_{0z}(\boldsymbol{r})(t - \tau) = -\gamma b_{0z}(\boldsymbol{r})(t - 2\tau) \end{aligned}$$
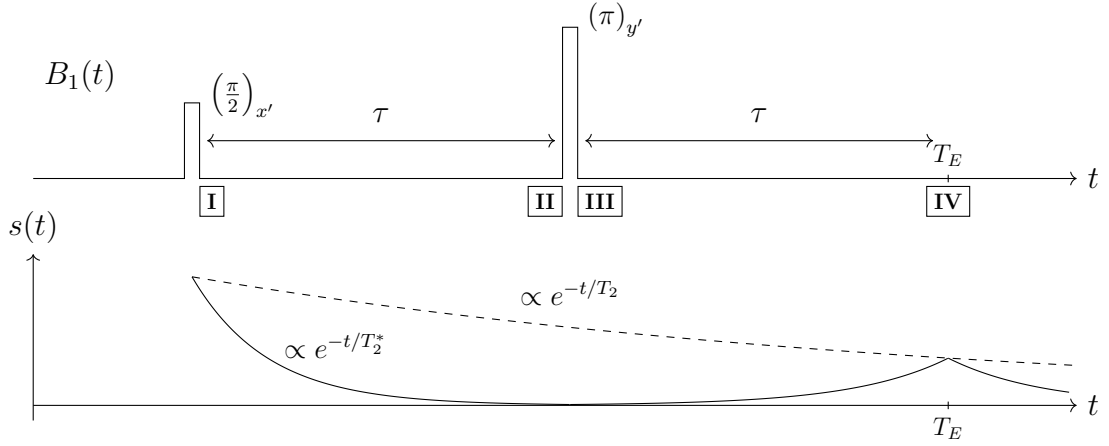
(a) Pulse sequence and signal viewed from the rotating frame of reference. The numbers **I-IV** refer to Fig. 2.8b.
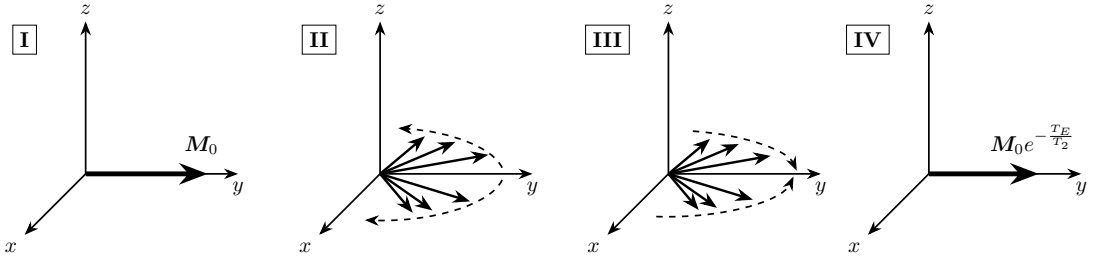
(b) Evolution of groups of spins during SE - **I.** Tipping in the transverse plane, **II.** Spins groups precess at different angular speeds due to local microscopic fields, **III.** Spins groups are flipped, and start to rephase as they continue to precess, **IV.** Complete rephasing at $T_E = 2\tau$.

Figure 2.8: Spin Echo experiment.

The echo time is defined as $T_E \equiv 2\tau$ and corresponds to the time instant where the phase of all spins in the sample returns to zero, no matter their position $\boldsymbol{r}$ or the value of b_{0z}. The realignment of the spins at T_E is called the spin echo. The

chronogram of the sequence is presented in Fig. 2.8 together with a sketch of the behavior of spin isochromats during the experiment. As highlighted in Fig. 2.8b, the first RF pulse tip all spins in the transverse plane. As a flip angle of $\frac{\pi}{2}$ is used, the transverse magnetization just after the pulse is equal to the initial longitudinal magnetization M_0. Because of local microscopic fields, the isochromats perceive magnetic fields which differ from $\boldsymbol{B}_0$ only depending on their position $\boldsymbol{r}$. Thereby, the isochromats do not dephase in the same manner; some are precessing more rapidly and others slowlier (Fig. 2.8b - II). Due to this additional dephasing (T_2'), the signal does not follow a T_2 decay but a T_2^* decay (Fig. 2.8a). The second RF pulse allows to reverse the phase. The dephasing continue, but in the opposite direction as if the isochromats were retracing their steps. It is the rephasing, which is illustrated in Fig. 2.8b - III. Finally, as shown in Eq. (2.43), the isochromats are totally rephased at $t = 2\tau$, and the T_2' signal loss is recovered.

Repeating the experiment for various values of τ or collecting the data for several echoes by applying multiple π-pulses after a single $\frac{\pi}{2}$-pulse gives access to the relaxation time T_2 thanks to an exponential fit.

2.4.3 Gradient Echo (GRE)

Another way to create an echo is to use a spatially linearly varying field, called a *gradient*, after the application of a unique RF pulse. Unlike Spin Echo, GRE sequences typically have an RF flip angle less than 90°, which allows them to be faster since the T_1 recovery occurs over a shorter period of time [89]. The gradient $\boldsymbol{G}(t)$ is defined as

$$
\begin{aligned}
\boldsymbol{G}(t) &= G_x(t)\hat{e}_x + G_y(t)\hat{e}_y + G_z(t)\hat{e}_z \\
&= \frac{\partial B_z}{\partial x}(t)\hat{e}_x + \frac{\partial B_z}{\partial y}(t)\hat{e}_y + \frac{\partial B_z}{\partial z}(t)\hat{e}_z
\end{aligned}
\tag{2.44}
$$

The magnetic field gradients are applied through additional coils. After the RF pulse, the effective magnetic field and the precession frequency of an isochromat at position $\boldsymbol{r}$ become:

$$
\begin{aligned}
\boldsymbol{B}_{\text{eff}}(t) &= \boldsymbol{B}_0 + \boldsymbol{G}(t) \cdot \boldsymbol{r}\hat{e}_z \\
&= \left(\frac{\omega_0}{\gamma} + G_x(t)x + G_y(t)y + G_z(t)z \right) \hat{e}_z
\end{aligned}
\tag{2.45}
$$

$$
\omega(\boldsymbol{r}, t) = \omega_0 + \gamma \boldsymbol{G}(t) \cdot \boldsymbol{r}
\tag{2.46}
$$

In the rotating frame of reference, the associated phase is given by:

$$
\phi(\boldsymbol{r}, t) = \phi(\boldsymbol{r}, t_0) - \gamma \int_{t_0}^{t} \boldsymbol{G}(t') \cdot \boldsymbol{r} dt'
\tag{2.47}
$$
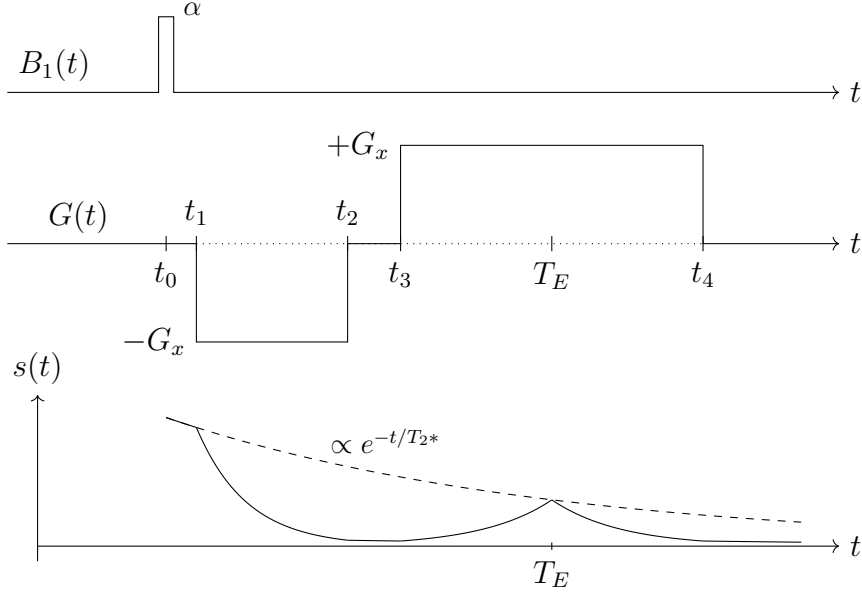
Figure 2.9: Gradient echo (GRE) pulse sequence and signal viewed from the rotating frame of reference.

Let us focus on a gradient that acts only on the x-direction, so that $\boldsymbol{G}(t) = G(t)\hat{e}_x$. The gradient echo is formed after the application of two lobes of the gradient of opposite polarity. As presented in Fig. 2.9, after an RF-pulse of flip angle $\alpha \leq 90°$ is applied at $t_0 = 0$, the gradient is equal to $-G_x$ between t_1 and t_2, G_x between t_3 and t_4 and 0 elsewhere. The phase of a spin due to the gradient at the position $\boldsymbol{r}$ in the rotating frame is such that

$$
\begin{aligned}
&\text{for } 0 < t < t_1: &&\phi_G(\boldsymbol{r}, t) = 0 \\
&\text{for } t_1 < t < t_2: &&\phi_G(\boldsymbol{r}, t) = \gamma G_x(t - t_1)x \\
&\text{for } t_2 < t < t_3: &&\phi_G(\boldsymbol{r}, t) = \gamma G_x(t_2 - t_1)x \\
&\text{for } t_3 < t < t_4: &&\phi_G(\boldsymbol{r}, t) = \gamma G_x(t_2 - t_1)x - \gamma G_x(t - t_3)x
\end{aligned}
\tag{2.48}
$$

The echo time $T_E \equiv t_3 + t_2 - t_1$, when the phase returns to 0 for all values of x. The first lobe is usually referred to as the 'dephasing lobe', while the second one is called the 'rephasing lobe'. The phase during the rephasing lobe can be rewritten in function of T_E:

$$
\phi_G(\boldsymbol{r}, t) = -\gamma G_x(t - T_E)x
\tag{2.49}
$$

Note that the echo occurs during the rephasing lobe at a time delay equal to the duration of the dephasing lobe ($T_E - t_3 = t_2 - t_1$).

In contrary to the spin echo experiment, the gradient echo does not allow to recover the dephasing due to static-field inhomogeneities. Indeed, when considering an additional spatial variation in the magnetic field such as in Eq. (2.42), there is no process in the GRE sequence to rephase the isochromats in contrast to the

second RF pulse used in the SE sequence as illustrated in Fig. 2.8 - III. The T_2^*-decay can cause a significant reduction in signal intensity before the gradient echo occurs.

2.5 Localization of the signal

In the previous sections, basic pulse sequences to acquire the global NMR signal of a whole sample have been presented. The aim of MR imaging is to be able to spatially localize the magnetic contribution of each isochromat in order to reconstruct an image. To do so, additional gradient magnetic fields presented in Section 2.4.3 are used. They provide a spatial magnetic field variation, which adds to the homogeneous static field $\boldsymbol{B}_0$. The frequency content of the MR signal received allows to determine the local spatial distribution of the spins. In the following sections, the conventional 3D gradient echo sequence is presented step-by-step.

2.5.1 One-dimensional localization: frequency-encoding

The simplest gradient echo sequence presented in Section 2.4.3 composed of a unique RF pulse followed by two lobes of opposite gradient strength G_x allows to localize the signal in one direction. With the relaxation effects neglected, the signal given in Eq. (2.39) can be written as

$$S(t) = \int \rho(x)e^{i\phi(x,t)}dx \tag{2.50}$$

where $\rho(x) = \iint \rho(\boldsymbol{r})dydz$ represents the effective 1D spin density.

The signal is collected during the rephasing lobe, also called the readout gradient, of duration τ_r equal to two times the duration of the dephasing lobe, also known as the prephasing gradient. Let us first consider a continuous infinite reception of the signal during this gradient:

$$S(t) = \int_{-\infty}^{+\infty} \rho(x)e^{i\int_0^t(-\gamma G_x(t')x)dt'}dx \tag{2.51}$$

$$= \int_{-\infty}^{+\infty} \rho(x)e^{-i\gamma x\int_0^t G_x(t')dt'}dx$$

The MR image that one would like to reconstruct is the distribution of the spin density ρ along the x-direction. The form of Eq.2.51 reminds of the Fourier transform. As a remainder, for a function f, its Fourier transform $\hat{f}$ is given as

$$\hat{f}(k) = \int_{-\infty}^{+\infty} f(x)e^{-i2\pi kx}dx \tag{2.52}$$

By analogy, the time-dependent spatial frequency $k_x = k_x(t)$ associated with the x-direction is defined as

$$k_x(t) = \frac{\gamma}{2\pi}\int_0^t G_x(t')dt' \tag{2.53}$$

Concerning the spin density, it can be found by taking the inverse Fourier transform of the signal. The signal $S(k_x)$ and the image $\rho(x)$ form a *Fourier transform pair* given as (note that the convention used to define the Fourier integrals with the factor 2π in the complex exponentials suppresses the need for normalization factors $\frac{1}{2\pi}$ or $\frac{1}{\sqrt{2\pi}}$):

$$S(k_x) = \hat{\rho}(k) = \int_{-\infty}^{+\infty} \rho(x)e^{-i2\pi k_x x}dx \tag{2.54}$$

$$\rho(x) = \int_{-\infty}^{+\infty} S(k_x)e^{+i2\pi k_x x}dk \tag{2.55}$$

However, the signal is sampled over a gradient of finite duration, i.e. a finite number of spatial frequencies. Sampling the signal is mathematically modeled as multiplying it with a sum of evenly spaced Dirac delta functions, while truncating the signal results in multiplying it by a rectangular window function. N points are sampled, so that the width of the window function is $W = N\Delta k_x$ where Δk_x represents the spacing between the Dirac functions. The measured signal distribution s_m (m stands for *measured*) is then given by

$$s_m(k_x) = \Delta k_x \sum_{p=0}^{N-1} S(p\Delta k_x)\delta(k - p\Delta k_x) \tag{2.56}$$

Hence, the reconstructed image for finite sampling rho_r (r stands for *reconstructed*) is found to be

$$\rho_r(x) = \int_{-\infty}^{+\infty} s_m(k_x)e^{i2\pi k_x x}dk \tag{2.57}$$

$$= \Delta k_x \sum_{p=0}^{N-1} S(p\Delta k_x)e^{i2\pi p\Delta k_x x} \tag{2.58}$$

Note the periodicity property of the Fourier transform: $\rho_r(x) = \rho_r(x + \frac{1}{\Delta k_x})$. The interval $L_x = \frac{1}{\Delta k_x}$ corresponds to the spatial distance over which the reconstructed image replicates itself and is often referred to as the field-of-view (FOV). According to the Nyquist sampling criterion, the object to be imaged in MRI has to be smaller than L_x. If the object is bigger, the image will fold over itself, an artifact called *aliasing*.

Just like the measured signal, the reconstructed image is discretized and truncated as well. As both measured signal and reconstructed image form a Fourier-pair, it is obvious that N spatial points will be reconstructed over a spatial interval of length $L_x = N\Delta x$, where Δx represents the *resolution* of the reconstructed image. Similarly to Eq. (2.56), the reconstructed image is given by

$$\rho_r(x) = \Delta x \sum_{q=0}^{N-1} \rho(q\Delta x)\delta(x - q\Delta x) \tag{2.59}$$

$$\implies s_m(k_x) = \Delta x \sum_{q=0}^{N-1} \rho(q\Delta x)e^{-i2\pi k_x q\Delta x}$$

Moreover, the steps Δx and Δk_x are related:

$$\Delta k_x \Delta x = \frac{1}{L_x} \frac{L_x}{N} = \frac{1}{N} \tag{2.60}$$

Finally, the Fourier pair composed of the finite-discrete measured signal and reconstructed image, presented in Eq. (2.57) and (2.59), can be expressed as

$$s_m(p\Delta k_x) = \Delta x \sum_{q=0}^{N-1} \rho_r(q\Delta x) e^{-i2\pi \frac{pq}{N}} \tag{2.61}$$

$$\rho_r(q\Delta x) = \Delta k_x \sum_{p=0}^{N-1} s_m(p\Delta k_x) e^{+i2\pi \frac{pq}{N}} \tag{2.62}$$

Since the signal is collected by sweeping over all spatial frequencies $k_x(t)$, this type of encoding is called the frequency encoding. Recalling that the relaxation effects have been neglected so far, each collected signal is in fact weighted by the multiplying term $e^{-\frac{t-t_0}{T_2}}$ in the sum of the reconstructed image, where t matches the time instant of sampling and t_0 the center of the RF pulse.

As the signal is measured on both sides of the echo time T_E during the readout gradient and $k(T_E) = 0$ in this most simple GRE sequence, the convention in MRI is to consider the signal sampled at T_E to match the 0th spatial frequency (DC point). The spatial frequencies occurring before T_E are called negative k_x values, while the ones happening after are the positive k_x values. The coverage of the k values, from the most negative to the most positive, is referred to as the *k-space*. Thereby, the summation in Eq. (2.62) is rather done from $-n$ to n for an odd number of frequencies $N = 2n + 1$, and from $-n$ to $n - 1$ for an even number $N = 2n$ in order not to straddle the DC point. This slightly asymmetric pattern is the most common sampling strategy, as the Fast Fourier Transform (FFT) is an efficient algorithm to calculate the discrete Fourier transform for a number of points equals to a power of two.

Example with 3 spin isochromats

To illustrate the process of acquiring and reconstructing an image, an example is given below in considering $N = 3$ isochromats. Let us define three positions $x_A = -\Delta x$, $x_B = 0$ and $x_C = +\Delta x$ and their associated spin densities ρ_A, ρ_B and ρ_C, respectively. The pulse sequence described in Section 2.4.3 is played, and the signal is sampled at the time instants $t_3 = T_E - \Delta t$, T_E and $t_4 = T_E + \Delta t$. According to Eq. (2.49), the phase is given as

$$\phi(x, T_E - \Delta t) = \gamma G_x \Delta t \; x = 2\pi \Delta k_x x \tag{2.63}$$
$$\phi(x, T_E) = 0$$
$$\phi(x, T_E + \Delta t) = -\gamma G_x \Delta t \; x = -2\pi \Delta k_x x$$

Δt is in fact a machine-parameter related to the bandwidth BW of the receive coil. The bandwidth, in Hz per pixel, is the inverse of the total sampling time. That

is the sometimes called dwell time $\Delta t = \frac{1}{N \times BW}$ with N the number of collected points, or pixels reconstructed in the MR image. Hence, it appears that the gradient strength G_x is completely determined by the pulse sequence and machine parameters.

Let us write the signal collected over the frequencies $-\Delta k_x$, 0 and Δk_x:

$$s_m(-\Delta k_x) = \Delta x \sum_{q=-1}^{1} \rho_r(q\Delta x) e^{-i2\pi \frac{(-1) \times q}{3}} = \Delta x \left(\rho_A e^{-i\frac{2\pi}{3}} + \rho_B + \rho_C e^{+i\frac{2\pi}{3}} \right)$$

$$s_m(0) = \Delta x \sum_{q=-1}^{1} \rho_r(q\Delta x) e^{-i2\pi \frac{(0) \times q}{3}} = \Delta x \left(\rho_A + \rho_B + \rho_C \right)$$

$$s_m(+\Delta k_x) = \Delta x \sum_{q=-1}^{1} \rho_r(q\Delta x) e^{-i2\pi \frac{(1) \times q}{3}} = \Delta x \left(\rho_A e^{+i\frac{2\pi}{3}} + \rho_B + \rho_C e^{-i\frac{2\pi}{3}} \right) \quad (2.64)$$

The spin density reconstructed in the first pixel is given by:

$$\rho_r(-\Delta x) = \Delta k_x \sum_{p=-1}^{1} s_m(p\Delta k_x) e^{+i2\pi \frac{p \times (-1)}{3}}$$

$$= \Delta k_x \Delta x \left(\left(\rho_A e^{-i\frac{2\pi}{3}} + \rho_B + \rho_C e^{+i\frac{2\pi}{3}} \right) e^{+i\frac{2\pi}{3}} + \left(\rho_A + \rho_B + \rho_C \right) e^0 \right.$$
$$\left. + \left(\rho_A e^{+i\frac{2\pi}{3}} + \rho_B + \rho_C e^{-i\frac{2\pi}{3}} \right) e^{-i\frac{2\pi}{3}} \right)$$

$$= \frac{1}{3} \left(3\rho_A + \rho_B(e^{\frac{2\pi}{3}} + 1 + e^{-i\frac{2\pi}{3}}) + \rho_C(e^{\frac{4\pi}{3}} + 1 + e^{-i\frac{4\pi}{3}}) \right)$$

$$= \frac{1}{3} \left(3\rho_A + \rho_B \underbrace{(e^{\frac{2\pi}{3}} + 1 + e^{i\frac{4\pi}{3}})}_{=0} + \rho_C \underbrace{(e^{\frac{4\pi}{3}} + 1 + e^{i\frac{2\pi}{3}})}_{=0} \right)$$

$$= \rho_A$$

$$(2.65)$$

To derive the solution, properties of roots of unity are used, especially the fact that the sum of nth roots of unity is zero, i.e. $\sum_{h}^{n-1} e^{\frac{2\pi i h}{n}} = 0$ for $h > 2$. Similarly, the spin density are well reconstructed as $\rho_r(0) = \rho_B$ and $\rho_r(+\Delta x) = \rho_C$.

2.5.2 Two-dimensional localization: phase-encoding

Similarly to the frequency-encoding, a gradient G_y is added to the sequence to encode the y-direction. The measured signal definition can be extended to a double summation:

$$s_m(p_x\Delta k_x, p_y\Delta k_y) = \Delta x \Delta y \sum_{q_x=0}^{N_x-1} \sum_{q_y=0}^{N_y-1} \rho_r(q_x\Delta x, q_y\Delta y) e^{-i2\pi(\frac{p_x q_x}{N_x} + \frac{p_y q_y}{N_y})} \quad (2.66)$$

In analogy with $k_x(t)$, the spatial frequencies associated with the y-axis are introduced as $k_y(t) = \frac{\gamma}{2\pi} \int_0^t G_y(t')dt'$. The definition of the k-space is extended to a 2D space of size $N_x \times N_y$. The most frequent strategy to fill the k-space is the

Cartesian trajectory, presented in Fig. 2.10. The idea is to first select a line along the k_y axis, before collecting the signal from $k_{x,min}$ to $k_{x,max}$ in the same way as presented for frequency encoding.
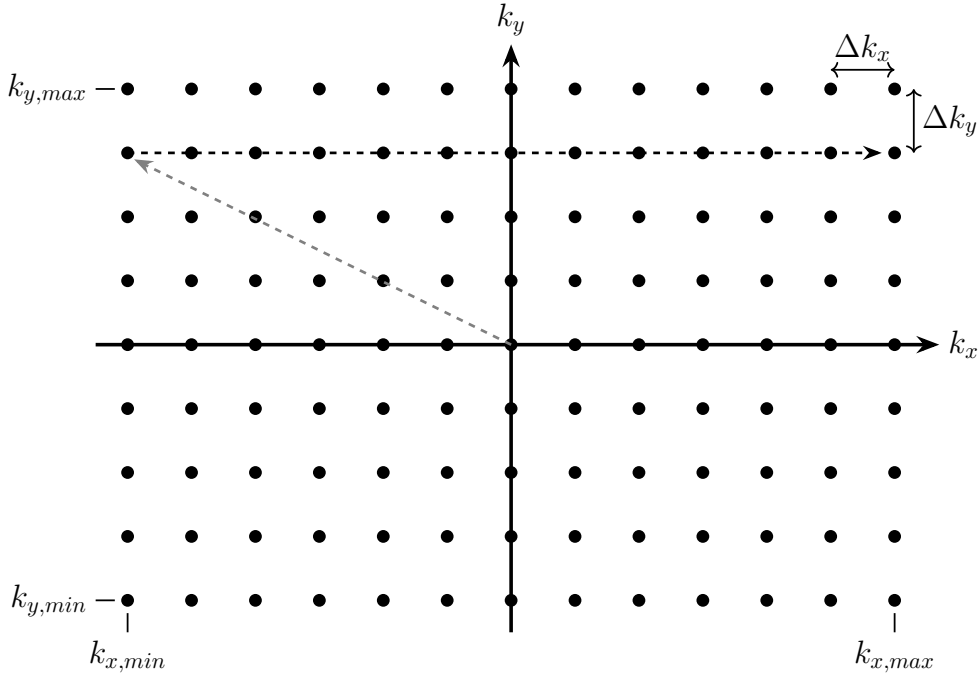
Figure 2.10: Example of a Cartesian k-space of size $N_x = 13 \times N_y = 9$. The dashed line represents the acquisition of one line. The k-space is usually swept from left to right and from top to bottom.

Two conclusions are drawn from this pattern. First the encoding along k_y has to be performed before the frequency-encoding occurs. Then the sequence has to be looped over as many times as lines to be encoded. Each repetition is done with the same two-lobe gradient G_x but a different gradient G_y in order to sweep over all k_y frequencies. In practice, a gradient of constant duration τ_y is chosen and its strength G_y will vary in a step-like manner for each repetition of duration T_R. This pattern can be referred to as a gradient table and is added into the sequence illustrated in Fig. 2.11. Thus, for the ith repetition time,

$$k_y(T_E) = \frac{\gamma}{2\pi} \int_{t_y}^{t_y + \tau_y} G_y(T_{R,i}) dt = \frac{\gamma}{2\pi} G_y(T_{R,i}) \tau_y \qquad (2.67)$$
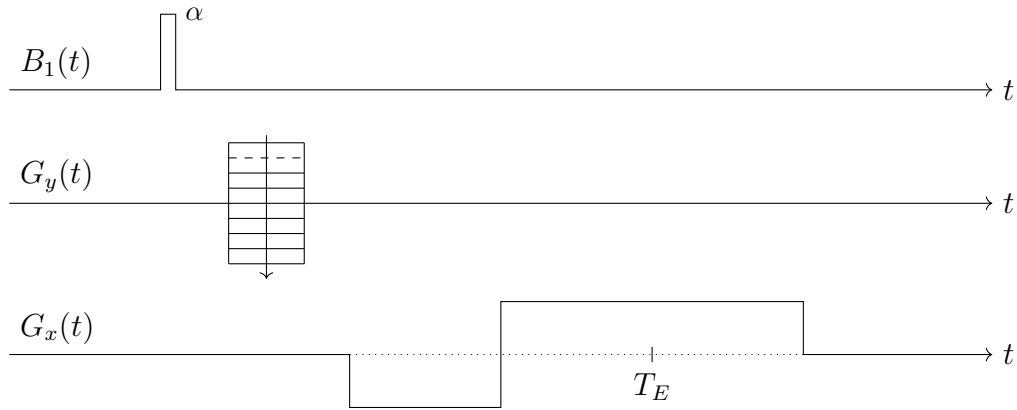
Figure 2.11: Two-dimensional GRE pulse sequence. The dashed line corresponds to the one highlighted in Fig. 2.10.

By definition $k_{y,max} = \frac{\gamma}{2\pi} G_{y,max} \tau_y$. As there are maximal specifications for the values of the gradient, the minimal τ_y achievable only depends on the sequence and maximal gradient strength (related to machine parameters or MR safety requirements). During the application of the gradient G_y, the isochromats experience a local change in frequency depending on their position along the y-axis. Once the gradient returns to zero, their precession frequency returns to the Larmor frequency ω_0 (if no other gradient is played simultaneously). However, they are dephased with respect to each other, as after application of the gradient $G_y(T_{R,i})$ the phase is modified by $\phi_{G_y}(\boldsymbol{r}, t) = \gamma G_y(T_{R,i}) \tau_y y$. Hence, this type of encoding is called phase-encoding.

2.5.3 Slice-selection

In the previous sections, how to excite the spins of a specific slice has been omitted. The usual convention in MRI is to define the z-axis as the slice selection axis, which is by definition the direction orthogonal to the plane of the desired slice. Another coordinate system than the gradient coordinate system is usually used in medical imaging based on the patient anatomy. The patient is usually positioned within the MRI magnet head first and lying on the back. If the slice-selection is along the axis from head to toes, the slice-orientation is said to be transverse. If it is oriented along the left-right axis, it is said to be sagittal and finally the posterior-anterior axis defines a coronal slice-orientation. These three anatomical planes are summarized in Fig. 2.12.
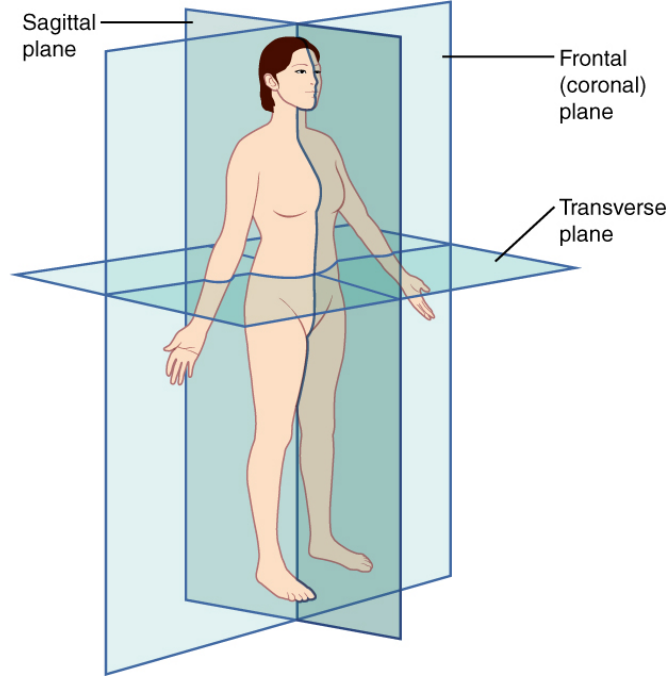
Figure 2.12: The three anatomical planes used in medical imaging.

The slice-selection is made by combining a spatially selective RF pulse with a gradient field in the z-direction. Adding a slice-selection gradient field G_{SS} along the z-direction induces a change in the precession frequency such that $\omega(\boldsymbol{r}, t) = \gamma G_{SS} z$ in the rotating frame. The goal of the slice selection is to excite uniformly the isochromats in a specific slice centered at the position z_0 and of thickness Δz, that means that within the slice the isochromats must have the same phase and flip angle after slice selection. Thereby, only the isochromats in the spatial interval $[z_0 - \frac{\Delta z}{2}, z_0 + \frac{\Delta z}{2}]$ have to be excited, which corresponds to the precession frequencies between $\Delta\omega = [\gamma G_{SS}(z_0 - \frac{\Delta z}{2}), \gamma G_{SS}(z_0 + \frac{\Delta z}{2})]$. Thereby, the desired RF pulse should have a frequency profile equals to unity over $\Delta\omega$ and zero outside. The ideal RF pulse should therefore be proportional to a rectangular function of bandwidth BW_{RF}

$$BW_{RF} = \frac{\Delta\omega}{2\pi} = \frac{1}{2\pi}\left(\gamma G_{SS}\left(z_0 + \frac{\Delta z}{2}\right) - \gamma G_{SS}\left(z_0 - \frac{\Delta z}{2}\right)\right) = \frac{\gamma}{2\pi}G_{SS}\Delta z \tag{2.68}$$

Back to the time domain, as the inverse Fourier transform of a rectangular function is a sinc function, the temporal envelope of the RF pulse is such that

$$B_1(t) \propto \text{sinc}(\pi BW_{RF}(t - t_0)) \tag{2.69}$$

$$\propto \text{sinc}\left(\frac{\pi(t - t_0)}{\Delta t_{RF}}\right) \tag{2.70}$$

where t_0 denotes the time instant when the peak RF amplitude occurs (middle of the pulse) and Δt_{RF} is one-half the width of the central lobe (interval from t_0

to the first zero-crossing). To produce a perfect rectangular slice-selection, the sinc function has to be infinite. In practice, the sinc function is truncated in time, which is equivalent to a multiplication of the RF pulse by a rectangular function of duration τ_{RF}. In the frequency domain, this operation results in a convolution of the rectangular slice-selective function with a sinc function, which will cause ripples along the rectangular function. This artifact, known as Gibbs ringing, can be mitigated thanks to a process called apodization, which consists of multiplying the truncated sinc function by a window function.

$$B_1(t) = \begin{cases} AW(t)\operatorname{sinc}\left(\dfrac{\pi(t - t_0)}{\Delta t_{RF}}\right) & \text{for } -\frac{\tau_{RF}}{2} < t < \frac{\tau_{RF}}{2} \\ 0 & \text{otherwise} \end{cases} \tag{2.71}$$

Common apodization functions used in MRI are the Hanning and the Hamming windows functions:

$$W(t) = (1 - \alpha) + \alpha \cos\left(\frac{\pi(t - t_0)}{N_c \Delta t_{RF}}\right) \tag{2.72}$$

with N_c the number of zero-crossings and $\alpha = 0.5$ for the Hanning window and $\alpha = 0.46$ for the Hamming one.

The isochromats of interest are well selected. However, due to the slice-selecting gradient, they are dephased with respect to one another. Similarly to the pair of dephasing-rephasing lobes to produce the gradient echo, an additional rephasing gradient is needed. In the approximation that the spins are flipped instantaneously in the transverse plane at the time instant t_0, the dephasing occurs only in the second half of the RF-pulse. Under this hypothesis, the rephasing gradient is of inverse polarity $-G_{SS}$ and lasts half the duration of the slice-encoding gradient, that is $\frac{\tau_{RF}}{2}$. This approximation is only valid for small flip angles.

Contrary to the analytical solutions for excitation presented in Section 2.2.3, there is a concurrent gradient so that Eq. (2.15) becomes

$$\frac{d}{dt}\begin{bmatrix} M_x'(t) \\ M_y'(t) \\ M_z(t) \end{bmatrix} = \begin{bmatrix} 0 & \gamma G_z z & 0 \\ -\gamma G_z z & 0 & \gamma B_1(t) \\ 0 & -\gamma B_1(t) & 0 \end{bmatrix} \begin{bmatrix} M_x'(t) \\ M_y'(t) \\ M_z(t) \end{bmatrix} \tag{2.73}$$

For small tip angles ($\alpha < 30°$), $\cos(\alpha(t)) \approx 1$ with $\alpha(t)$ the instantaneous flip angle at any point during the RF pulse [89]. Hence, it can be hypothesized that $M_z(t) \approx M_0$ during the RF pulse, and thus $\frac{dM_z(t)}{dt} \approx 0$. Eq. (2.73) then reads simply:

$$\frac{d}{dt}\begin{bmatrix} M_x'(t) \\ M_y'(t) \\ M_z(t) \end{bmatrix} = \begin{bmatrix} 0 & \gamma G_z(t)z & 0 \\ -\gamma G_z(t)z & 0 & \gamma B_1(t) \\ 0 & 0 & 0 \end{bmatrix} \begin{bmatrix} M_x'(t) \\ M_y'(t) \\ M_0 \end{bmatrix} \tag{2.74}$$

This leads to the following complex differential equation for the transverse magnetization M_{xy}':

$$\frac{dM_{xy}'}{dt}(t) = -i\gamma G_z(t)z M_y'(t) + i\gamma B_1(t)M_0 \tag{2.75}$$

The equation can be solved using the integrating factor technique that states that for a first order ordinary different equation of the form $\frac{dy(x)}{dx} + f(x)y(x) = g(x)$, the equation can be solved as $e^{F(x)}y(x) = \int g(x)e^{F(x)}dx$ where $F(x) = \int f(x)dx$. With the initial magnetization state $\boldsymbol{M}(t_0 - \frac{\tau_{RF}}{2}) = [0, 0, M_0]$, the solution at the end of the RF pulse, i.e. $t = t_0 + \frac{\tau_{RF}}{2}$, is given as:

$$e^{i\gamma z \int_{t_0 - \frac{\tau_{RF}}{2}}^{t_0 + \frac{\tau_{RF}}{2}} G_z(s)ds} M'_{xy}(t) = i\gamma M_0 \int_{t_0 - \frac{\tau_{RF}}{2}}^{t_0 + \frac{\tau_{RF}}{2}} B_1(t)e^{i\gamma z \int_{t_0 - \frac{\tau_{RF}}{2}}^{t} G_z(s)ds} dt \qquad (2.76)$$

$$M'_{xy}(t) = i\gamma M_0 \int_{t_0 - \frac{\tau_{RF}}{2}}^{t_0 + \frac{\tau_{RF}}{2}} B_1(t)e^{i\gamma z \left(\int_{t_0 - \frac{\tau_{RF}}{2}}^{t} G_z(s)ds - \int_{t_0 - \frac{\tau_{RF}}{2}}^{t_0 + \frac{\tau_{RF}}{2}} G_z(s)ds \right)} dt$$

$$M'_{xy}(t) = i\gamma M_0 \int_{t_0 - \frac{\tau_{RF}}{2}}^{t_0 + \frac{\tau_{RF}}{2}} B_1(t)e^{-i\gamma z \int_{t}^{t_0 + \frac{\tau_{RF}}{2}} G_z(s)ds} dt$$

For a constant gradient $G_z(t) = G_{SS}$ during the RF pulse, $\int_{t}^{t_0 + \frac{\tau_{RF}}{2}} G_z(s)ds = G_{SS}(\frac{\tau_{RF}}{2} - t)$ and the equation becomes

$$M'_{xy}(t) = i\gamma M_0 e^{-i\gamma z G_{SS} \frac{\tau_{RF}}{2}} \int_{t_0 - \frac{\tau_{RF}}{2}}^{t_0 + \frac{\tau_{RF}}{2}} B_1(t)e^{+i\gamma z G_{SS}(t-t_0)} dt \qquad (2.77)$$

$$= i\gamma M_0 e^{-i\gamma z G_{SS} \frac{\tau_{RF}}{2}} \mathcal{F}^{-1}(B_1(t)) \qquad (2.78)$$

where $\mathcal{F}^{-1}$ denotes the inverse Fourier transform. As stated in [91], if $B_1(t)$ is a real and symmetric function, so is its inverse Fourier transform. The dephasing across the slice is thereby only contained in the exponential term $e^{-i\gamma z G_{SS} \frac{\tau_{RF}}{2}}$. To refocus the isochromats, the rephasing gradient G_{RP} of duration τ_{RP} should verify $G_{RP}\tau_{RP} = -G_{SS}\frac{\tau_{RF}}{2}$. At the end, the choice of a rephasing gradient of value $-G_{SS}$ and duration $\frac{\tau_{RF}}{2}$ is well adapted to compensate the dephasing induced during slice selection.

2.5.4 3D volume imaging

To image a volume, one strategy is the multi-slice 2D imaging, which is based on the slice selection presented in Section 2.5.3. To recreate the volume, various RF pulses are used, each of them centered at a different frequency and hence exciting a different slice. The RF profiles are imperfect by nature, as they are not infinite in time. Thereby, isochromats close to the excited slice might be excited as well. To avoid the artifact called *slice crosstalk* and ensure that the spins are back to the equilibrium before their slice is excited, it is common to leave a gap between the slices, or to encode the slices such that two consecutive slices are not adjacent.

A more conventional 3D imaging strategy consists in exciting a thicker slice corresponding to the volume of interest, called a slab. The slices within the slab, called partitions, are phase-encoded by adding a second gradient table along the slice selection direction. The phase-encoding works the same way as presented in Section 2.5.2 for 2D imaging sequence. The dephasing due to the

two phase-encoding steps before the readout gradient starts is such: $\phi_G(\boldsymbol{r}, t) = \gamma(G_y \tau_y y + G_z \tau_z z)$, such that every line in every slice has a different phase encoding before being frequency encoded. To keep the same notations as the other directions, Δz denotes the partition thickness and the slab thickness is $TH = N_z \Delta z$, where N_z corresponds to the number of slices encoded. The k-space where the data are collected is generalized to 3D and the measured signal definition is extended:

$$s_m(p_x \Delta k_x, p_y \Delta k_y, p_z \Delta k_z)$$
$$= \Delta x \Delta y \Delta z \sum_{q_x=0}^{N_x-1} \sum_{q_y=0}^{N_y-1} \sum_{q_z=0}^{N_z-1} \rho_r(q_x \Delta x, q_y \Delta y, q_z \Delta z) e^{-i2\pi \left(\frac{p_x q_x}{N_x} + \frac{p_y q_y}{N_y} + \frac{p_z q_z}{N_z} \right)} \quad (2.79)$$
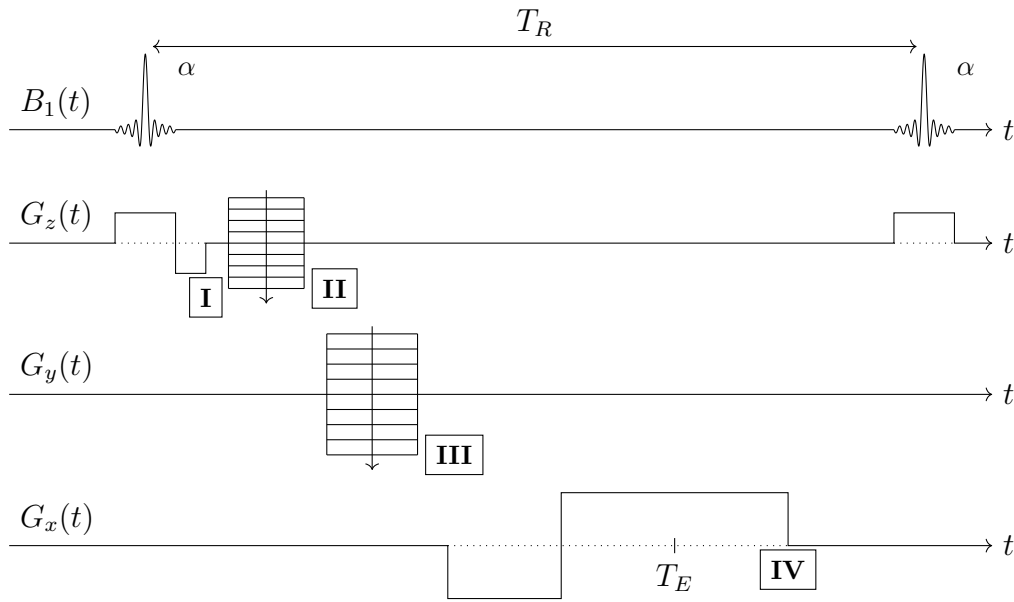
(a) Pulse sequence. The numbers **I-IV** refer to Fig. 2.13b
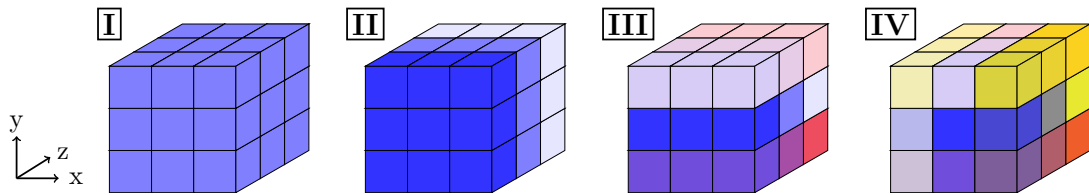
(b) Illustration of the encoding process on a FOV of $3 \times 3 \times 3$ voxels, where voxels of the same color represent the same dephasing. **I.** FOV excitation, **II.** Slice selection, **III.** Phase-encoding, **IV.** Frequency-encoding.

Figure 2.13: Three-dimensional GRE pulse sequence.

The 3D gradient echo imaging experiment is presented in Fig. 2.13, where the lines and slices directions, orthogonal to the read direction, are both phase encoded. Note that two combinations of gradients are needed along the z-axis: the first dephasing-rephasing couple corresponds to the slab selection (Fig. 2.13a

- I), while the second gradient represented by a phase-encoding gradient table corresponds to the slice-selection within the excited slab (Fig. 2.13a - II). Should this figure represent the multi-slice 2D imaging strategy, this second gradient would not be needed, but the dephasing-rephasing slice-selecting gradients would change for each repetition in order to excite different slices. In 3D volume imaging, the same slab is excited throughout the sequence, which means that the same dephasing-rephasing gradients are used for every repetition.

To encode one line, the time needed is the repetition time T_R. Hence, to encode all lines in the images, the experiment has to be repeated the number of phase encoding steps. The total acquisition time for the 3D GRE is given by

$$T_{acq} = N_y N_z T_R \tag{2.80}$$

Note that in the sequence shown in Fig. 2.13, the gradients are played one after the other. They can also be played concurrently, except for the readout gradient in order to collect parallel lines of data in the 3D k-space in the Cartesian strategy. Other sampling patterns do exist such as radial [103, 104] or spiral [105, 106] paths. These strategies are out of scope of the present thesis, and difficult to reconstruct as they lead to non-rectilinear k-spaces, and hence the Fourier transform can not be directly performed.

2.6 Fast gradient echo imaging

In addition to the echo time T_E, the already mentioned repetition time T_R is an important parameter of the MR pulse sequence. For a GRE sequence, it corresponds to the time between two consecutive RF excitation pulses. Recall that the relaxation is governed by two time constants, namely T_1 for the recover of the longitudinal magnetization and T_2 for the decay of the transverse magnetization, where $T_1 > T_2$ (except in specific cases, which are not observed in the clinical practice [107]). If $T_R \gg T_1$, the magnetization vector goes back to its equilibrium state $\boldsymbol{M_0}$ between each repetition. In basic GRE imaging, $T_R \gg T_2$, so that the transverse component of the magnetization has completely decayed before the new repetition. However, the longitudinal component can not recover completely. After a few RF excitations, it will converge towards a reduced value, called the steady-state magnetization. Finally, in the case where $T_R < T_2$, a situation referred to as fast GRE imaging, the transverse magnetization does not completely disappear before the next RF excitation pulse. Strategies to destroy the transverse magnetization prior to the next RF pulse can be adopted, such as RF-spoiled GRE.

2.6.1 Steady-state

Let us first focus on the case $T_R \gg T_2$, but $T_R < T_1$. According to the analytical solutions derived in Section 2.2.3, after the application of a first RF pulse of flip

angle α centered on $t_0 = 0$, the longitudinal magnetization is such that

$$M_z(0^+) = M_0 \cos(\alpha)$$

$$M_z(T_R^-) = (M_z(0^+) - M_0)e^{-\frac{T_R}{T_1}} + M_0$$

$$= M_z(0^-) \cos(\alpha)e^{-\frac{T_R}{T_1}} + M_0(1 - e^{-\frac{T_R}{T_1}}) \tag{2.81}$$

where the notations $^+$ and $^-$ refer to time instants respectively after and before an RF pulse and $M_z(0^-) = M_0$. After n repetitions, it can be derived from Eq. (2.81) that the longitudinal magnetization is equal to:

$$M_z(nT_R^-) = M_z((n-1)T_R^-) \cos(\alpha)e^{-\frac{T_R}{T_1}} + M_0(1 - e^{-\frac{T_R}{T_1}}) \tag{2.82}$$

For a sufficient number n of RF pulses, the longitudinal magnetization reaches a new equilibrium M_z^{SS} called the steady-state such as:

$$M_z(nT_R^-) = M_z^{SS} \tag{2.83}$$

This phenomenon is called partial saturation. Once the steady-state is met, two consecutive RF pulses repetitions $m - 1$ and m verify $M_z(mT_R^-) = M_z((m-1)T_R^-) = M_z^{SS}$. Hence, based on Eq. (2.82), an expression of M_z^{SS} can be found:

$$M_z^{SS} = M_z^{SS} \cos(\alpha)e^{-\frac{T_R}{T_1}} + M_0(1 - e^{-\frac{T_R}{T_1}})$$

$$M_z^{SS} = \frac{M_0(1 - e^{-\frac{T_R}{T_1}})}{1 - \cos(\alpha)e^{-\frac{T_R}{T_1}}} \tag{2.84}$$

Repetitions of RF pulses are usually performed at the beginning of GRE sequences in order to achieve this longitudinal magnetization before starting to collect data.

An optimal flip angle α to maximize the signal can be derived. This corresponds to finding the α value, which maximizes the transverse magnetization. According to Section 2.2.3 and Eq. (2.84), the steady-state transverse magnetization M_{xy}^{SS} is given by:

$$M_{xy}^{SS} = M_z^{SS} \sin(\alpha) = M_0 \frac{\sin(\alpha)(1 - e^{-\frac{T_R}{T_1}})}{1 - \cos(\alpha)e^{-\frac{T_R}{T_1}}} \tag{2.85}$$

The transverse magnetization is maximized when its derivative with respect to α cancels out:

$$\frac{dM_{xy}^{SS}}{d\alpha} = M_0 \frac{\left(1 - e^{-\frac{T_R}{T_1}}\right)\left(\cos(\alpha) - e^{-\frac{T_R}{T_1}}\right)}{\left(1 - \cos(\alpha)e^{-\frac{T_R}{T_1}}\right)^2} = 0$$

$$\iff \cos(\alpha) = e^{-\frac{T_R}{T_1}}$$

$$\iff \alpha = \arccos\left(e^{-\frac{T_R}{T_1}}\right) \tag{2.86}$$

This optimal flip angle is called the Ernst angle, often denoted θ_E. More than optimizing the intensity for a specific T_1, meaning a specific type of tissue (e.g. the blood with or without injection of contrast agent), the goal in MR imaging is often to optimize the contrast between different tissues. Hence, the Ernst angle might not always be appropriate.

2.6.2 Spoiling

Fast GRE, also known as steady-state free precession (SSFP) sequences, correspond to the case where $T_R \ll T_1$ and $< T_2$. This leads to the build-up of a steady-state of the transverse magnetization as well, as it does not fully decay before each new RF pulse. Thereby in addition to α, T_R and T_1, signal intensities also depend on T_2, which might make the contrast in the image difficult to interpret and cause image artifacts. With this in mind, the transverse magnetization needs to be eliminated prior the next RF pulse, a process call *spoiling*.

A first method consists in adding gradients at the end of the repetition, that is between the readout and the next RF pulse. These gradients are called spoiler gradients and are meant to dephase the isochromats within each voxel. Consider isochromats in one arbitrary voxel. If the phase dispersion is sufficient within this voxel, the sum of the contributions of each isochromat within the voxel averages to zero. Hence, the contribution of the voxel to the total transverse magnetization is zero. It is often enough to implement a spoiler along a single axis, usually along the slice-select direction, and whose strength varies from one repetition time to the next. As gradients produce spatially-varying magnetic fields, this type of spoiling suffers from spatial non-uniformities.

Note that spoilers gradients might also refer to the simple lengthening of the readout gradient, that is without varying its strength between each repetition time. This causes some dephasing, but residual transverse magnetization subsists, making the reconstructed images prone to motion- and flow-induced artifacts [108].

A more efficient and frequent strategy is the RF-spoiling, often combined with the latest definition of spoiler gradient. This method consists of quadratically incrementing the phase of the RF pulse from repetition to repetition. RF pulses provide the same flip angle, but the orientation of the magnetization in the transverse plane (xy) varies. Zur et al. showed that for a phase increment of 117° or 123°, the transverse magnetization is efficiently spoiled. [109]. To avoid spatial-dependency of the RF spoiling, additional phase-encoding rewinder gradients are needed. These gradients are meant to "rewind" the effect of the phase-encoding gradients used at the beginning of the repetition, and consists in applying the same gradients but with inverse polarity.

2.7   Phase-contrast imaging

Magnetic resonance angiography (MRA) gathers the pulse sequences, which aim to image blood vessels. Among them, phase-contrast MRI (PC-MRI) is a technique used to quantify blood velocity. Until now, only static isochromats, localized by their time-independent position, have been considered. However, the presence of moving spins (e.g. blood, cerebrospinal fluid...) causes additional phase shift, proportional to their velocity. Hence, the phase of the collected signal can provide quantitative spatially-encoded information on the velocity.

Recall the expression of the phase for an isochromat at position $\boldsymbol{r}(t)$ given in Eq. (2.47) at the echo time T_E (where $t_0 = 0$ is defined as the center of the RF pulse):

$$\phi(\boldsymbol{r}, T_E) = \phi_0 - \gamma \int_0^{T_E} \boldsymbol{G}(t) \cdot \boldsymbol{r}(t) dt \qquad (2.87)$$

where $\phi_0 = \phi(\boldsymbol{r}, 0) + \gamma \int_0^{T_E} b_{0z}(\boldsymbol{r}(t)) dt$ is an additional background phase depending on the initial phase and potential field inhomogeneities. The position $\boldsymbol{r}(t)$ of the isochromats can be expanded in Taylor series at an arbitrary time instant t_{exp} such that

$$\boldsymbol{r}(t) = \sum_{n=0}^{\infty} \frac{r^{(n)}(t_{exp})}{n!}(t - t_{exp})$$

$$= \boldsymbol{r}(t_{exp}) + (t - t_{exp})\frac{d\boldsymbol{r}}{dt}\bigg|_{t_{exp}} + \frac{(t - t_{exp})^2}{2}\frac{d^2\boldsymbol{r}}{dt^2}\bigg|_{t_{exp}} + ... \qquad (2.88)$$

The development of $\boldsymbol{r}(t)$ is introduced in Eq. (2.87), leading to a new expression of the phase:

$$\phi(\boldsymbol{r}, T_E) = \phi_0 - \gamma \boldsymbol{r}(t_{exp}) \cdot \underbrace{\int_0^{T_E} \boldsymbol{G}(t) dt}_{\mathcal{M}_0} - \gamma \boldsymbol{u}(t_{exp}) \cdot \underbrace{\int_0^{T_E} \boldsymbol{G}(t)(t - t_{exp}) dt}_{\mathcal{M}_1}$$

$$- \gamma \frac{\boldsymbol{a}(t_{exp})}{2} \cdot \underbrace{\int_0^{T_E} \boldsymbol{G}(t)(t - t_{exp})^2 dt}_{\mathcal{M}_2} + ... \qquad (2.89)$$

where the following notations are introduced for the sake of clarity: $\boldsymbol{u}(t_{exp}) = [u(t_{exp}), v(t_{exp}), w(t_{exp})] = \frac{d\boldsymbol{r}}{dt}\big|_{t_{exp}}$ and $\boldsymbol{a}(t_{exp}) = \frac{d^2\boldsymbol{r}}{dt^2}\big|_{t_{exp}}$. Furthermore, $\mathcal{M}_n = \int_0^{T_E} \boldsymbol{G}(t)(t - t_{exp})^n dt$ denotes the nth gradient moment with respect to t_{exp}.

In phase-contrast MRI, the assumption is made that the velocity is constant over a repetition time, hence the acceleration and terms of superior order are neglected. Thereby, the velocity is independent of time over a repetition time: $\boldsymbol{u} = [u, v, w]$ and $\boldsymbol{a} = [0, 0, 0]$. Velocity encoding is usually performed using bipolar gradients, which are gradients composed of two lobes of inverse polarity but same duration. This kind of gradients cancels out the zeroth-order moment at T_E, but

not the first-order term $\mathcal{M}_1$, as shown below. Let us investigate adding a bipolar gradient G_u of duration τ_u along the x-direction, as illustrated in Fig. 2.14.
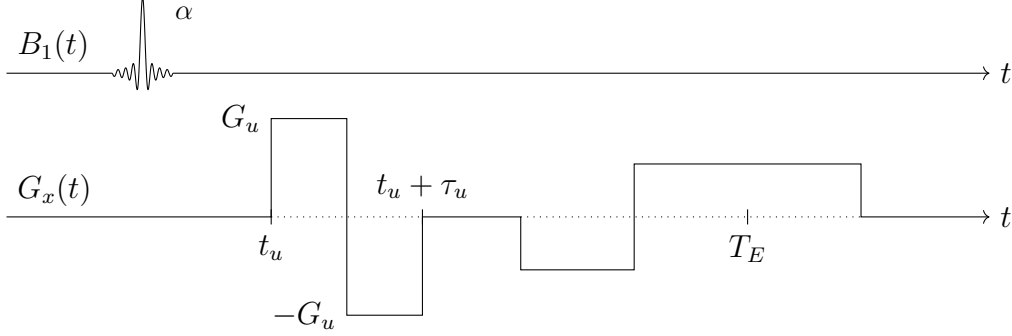
Figure 2.14: One-dimensional GRE pulse sequence with bipolar gradient.

For $t_0 = 0$, the dephasing $\phi_u(\boldsymbol{r}, t)$ due to this bipolar gradient is such that:

$$
\begin{aligned}
\phi_u(\boldsymbol{r}, t_u + \tau_u) &= \phi_0 - \gamma \boldsymbol{r}(t_{exp}) \cdot \int_0^{t_u + \tau_u} \boldsymbol{G}(t) dt - \gamma \boldsymbol{u} \cdot \int_0^{t_u + \tau_u} \boldsymbol{G}(t)(t - t_{exp}) dt \\
&= \phi_0 - \gamma x(t_{exp}) G_u \underbrace{\left([t - t_{exp}]_{t_u}^{t_u + \frac{\tau_u}{2}} - [t - t_{exp}]_{t_u + \frac{\tau_u}{2}}^{t_u + \tau_u} \right)}_{=0} \\
&\quad - \gamma u G_u \left(\left[\frac{(t - t_{exp})^2}{2} \right]_{t_u}^{t_u + \frac{\tau_u}{2}} - \left[\frac{(t - t_{exp})^2}{2} \right]_{t_u + \frac{\tau_u}{2}}^{t_u + \tau_u} \right) \\
&= \phi_0 + \gamma u G_u \left(\frac{\tau_u}{2} \right)^2 \\
&= \phi_0 - \gamma u \mathcal{M}_1
\end{aligned}
$$

(2.90)

The phase still includes the background phase ϕ_0. To remove its effect and thus isolate the velocity-encoded phase shift, two measurements are needed with different moments $\mathcal{M}_1$. A bipolar gradient of inverse polarities can be played in order to create a first moment of opposite sign than the first measurement. Another possibility is to perform a second measurement, where both $\mathcal{M}_0$ and $\mathcal{M}_1$ are cancelled at T_E. Such a measurement is said to be flow-compensated. In the readout direction, the flow-compensation is performed by adding two extra lobes to the couple of dephasing-rephasing lobes. One lobe of same duration and opposite gradient strength is added before the rephasing lobe, and a second lobe of same duration and value is superposed to the rephasing lobe. The design is presented on Fig. 2.15.
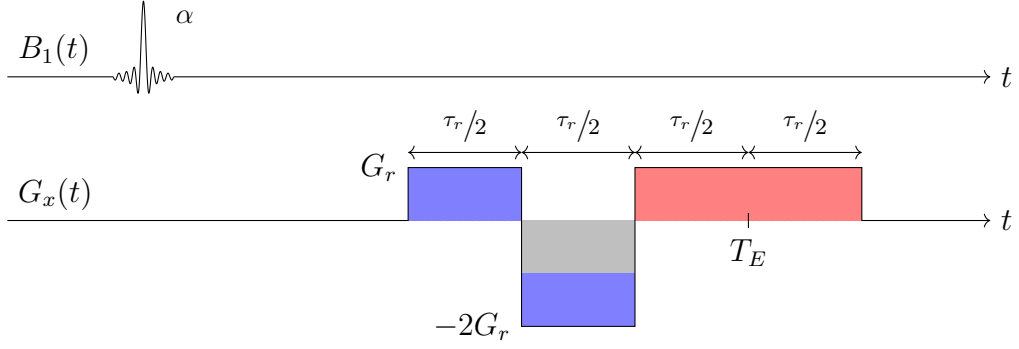
Figure 2.15: One-dimensional GRE pulse sequence (prephasing and readout gradient in ▆ and ▆, respectively) with flow compensation (in ▆).

The flow-compensated phase $\phi_{fc}(\boldsymbol{r}, t)$ throughout the sequence reads:

$$
\begin{aligned}
\phi_{fc}&(\boldsymbol{r}, T_E) \\
&= \phi_0 - \gamma x(t_{exp})G_r \left([t - t_{exp}]_{t_{fc}}^{t_{fc}+\frac{\tau_r}{2}} - 2 [t - t_{exp}]_{t_{fc}+\frac{\tau_r}{2}}^{t_{fc}+\tau_r} + [t - t_{exp}]_{t_{fc}+\tau_r}^{t_{fc}+\frac{3\tau_r}{2}} \right) \\
&\quad - \gamma u \frac{G_r}{2} \left(\left[(t - t_{exp})^2\right]_{t_{fc}}^{t_{fc}+\frac{\tau_r}{2}} - 2 \left[(t - t_{exp})^2\right]_{t_{fc}+\frac{\tau_r}{2}}^{t_{fc}+\tau_r} + \left[(t - t_{exp})^2\right]_{t_{fc}+\tau_r}^{t_{fc}+\frac{3\tau_r}{2}} \right) \\
&= \phi_0 - \gamma x(t_{exp})G_r \underbrace{\left(\frac{\tau_r}{2} - 2\frac{\tau_r}{2} + \frac{\tau_r}{2} \right)}_{=0} \\
&\quad - \gamma u \frac{G_r}{2} \left(\left(t_{fc} + \frac{3\tau_r}{2} - t_{exp}\right)^2 - (t_{fc} - t_{exp})^2 + 3 \left(t_{fc} + \frac{\tau_r}{2} - t_{exp}\right)^2 \right. \\
&\qquad\qquad\qquad\qquad\qquad\qquad\qquad\qquad\qquad\qquad \left. - 3 \left(t_{fc} + \tau_r - t_{exp}\right)^2 \right) \\
&= \phi_0 - \gamma u \frac{G_r}{2} \underbrace{\left(\frac{3\tau_r}{2} \left(2(t_{fc} - t_{exp}) + \frac{3\tau_r}{2}\right) + 3 \left(\frac{-\tau_r}{2}\right) \left(2(t_{fc} - t_{exp}) + \frac{3\tau_r}{2}\right) \right)}_{=0}
\end{aligned}
$$
(2.91)

Note that if the velocity of interest is along the readout direction, both sequences have to be flow-compensated, and one of them has to include the velocity-encoding bipolar gradient on top of that. Indeed, if there is only a bipolar gradient followed by the dephasing-rephasing readout gradient, the phase will include extra dephasing due to these two lobes. The design of a flow-compensated phase-encoding waveform is presented by Nishimura et al. The details about this flow-compensation can be found in [110]. However, they state that these type of gradients are at least 2.41 times longer than non-compensated phase-encoding tables.

The two sequences are acquired as two distinct k-spaces, which can both be reconstructed by inverse Fourier transform (cf Section 2.5). Here, the two sequences can refer either to two sequences with opposite polarity of their bipolar gradient, or to one sequence with flow-compensation and the other with flow-compensation and

a bipolar gradient. Note that the reconstructed images are complex-valued due to the extra dephasing that they include (background phase, velocity-encoding). They can be reconstructed as magnitude images on the one hand and phase images on the other hand. The velocity is reconstructed by subtracting the phase images. The subtraction order depends on the sequences considered. For example, let us consider $\phi^{(0)}$ the phase for the flow-compensated subsequence and $\phi^{(x)}$ the phase associated with the flow-compensated velocity-encoded along the x-axis subsequence. The phase difference is given by

$$\Delta\phi(\boldsymbol{r}, T_E) = \phi^{(x)}(\boldsymbol{r}, T_E) - \phi^{(0)}(\boldsymbol{r}, T_E) = \gamma u \Delta\mathcal{M}_1^{(x)} \tag{2.92}$$

where $\Delta\mathcal{M}_1^{(x)} = \mathcal{M}_1^{(x)} - \mathcal{M}_1^{(0)} = -G_u \left(\frac{\tau_u}{2}\right)^2$ denotes the moment difference. The expression of the velocity is obtained as

$$u = \frac{\Delta\phi(\boldsymbol{r}, T_E)}{\gamma\Delta\mathcal{M}_1^{(x)}} \tag{2.93}$$

The phase $\phi(\boldsymbol{r}, t)$ is the argument of the complex transverse magnetization $M_{xy}(\boldsymbol{r}, t)$, and thereby it is defined on the interval $]-\pi, +\pi]$, and so is the phase difference $\Delta\phi(\boldsymbol{r}, t)$. The gradients design, and consequently the moment difference, have to be chosen so that the maximal velocity present within the field-of-view results in a phase difference of π. This user-defined parameter, which needs an a priori knowledge of the expected flow, is called the velocity sensitivity or velocity encoding and is defined in the x direction as:

$$u_{enc} = \frac{\pi}{\gamma\Delta\mathcal{M}_1^{(x)}} \tag{2.94}$$

If $|u| > u_{enc}$, a phenomenon called phase aliasing (or phase wrapping) occurs, in which the velocity is incorrectly encoded. On the other hand, MR images suffer from noise, and in particular for PC-MRI, the noise is proportional to u_{enc} [111]. The choice of the velocity sensitivity has to be a compromise between these two aspects.

The method to encode the velocity along the readout direction can be expanded to the other spatial directions. This is done by playing additional identical sequences, yet with a bipolar velocity-encoding gradient along the phase-encoding direction or the slice-select direction. It can be noticed that the flow-compensated sequence can be used as a common reference to encode the three spatial directions, hence only four measurements are required instead of six if one were to use bipolar gradients only. Defining the maximal velocity vector as $V_{ENC} = [u_{enc}, v_{enc}, w_{enc}]$, the velocity is reconstructed as:

$$
\begin{aligned}
u &= \frac{u_{enc}}{\pi}\Delta\phi_x(\boldsymbol{r}, T_E) \\
v &= \frac{v_{enc}}{\pi}\Delta\phi_y(\boldsymbol{r}, T_E) \\
w &= \frac{w_{enc}}{\pi}\Delta\phi_z(\boldsymbol{r}, T_E)
\end{aligned}
\tag{2.95}
$$

To encode in velocity the three spatial directions, other schemes can be followed. Instead of using only one bipolar gradient per sequence, bipolar gradients along various directions can be combined. The velocity vector $[u, v, w]$ is then reconstructed by linear combinations of the phase obtained for each sequence [112].

2.7.1   4D flow MRI: three-dimensional cine PC-MRI

In order to take into account the pulsatile nature of blood flow in the human vascular system, namely in the heart and great vessels, there is a need to resolve the velocity field not only in space, but also in time with respect to the cardiac cycle. Three-dimensional cine PC-MRI sequences, often referred to as 4D flow MRI (3D in space and 1D in time), have emerged since the late 1990s [40, 113, 114].

4D flow MRI is based on an RF-spoiled 3D GRE sequence, already presented in Section 2.6. Bipolar gradients and flow-compensation are added to this sequence to be able to reconstruct the velocity field, as mentioned in the previous section. In order to add a fourth dimension in time, the cardiac cycle is recorded simultaneously with the MRI signal, via an electrocardiogram (ECG) or a peripheral pulse transducer. The cardiac cycle of averaged duration T_c is divided into time frames, or cardiac phases, of duration Δt_p. At each cardiac cycle, only a few lines per k-space can be filled for each cardiac phases. Indeed, a cardiac cycle is well shorter than the acquisition time, and the reference and velocity-encoded k-spaces are filled progressively over numerous cardiac cycles. The k-space is said to be segmented, where the number of segments N_{seg} refers to the number of lines that can be acquired within a cardiac phase [114]:

$$\Delta t_p = 4 T_R N_{seg} \tag{2.96}$$

Note the multiplying factor of 4, as in the most usual scheme, one reference and 3 velocity-encoded k-spaces are acquired. The total acquisition time is thus given by:

$$T_{acq} = \frac{N_y N_z}{N_{seg}} T_c \tag{2.97}$$

The synchronization of the MR signal with the ECG is a process called triggering or gating, which can be prospective or retrospective. In prospective gating, the MR data acquisition begins after the detection of a desired physiologic event, such as the R-peak of the ECG. The signal is then acquired for a user-defined number of phases N_p, where $\Delta t_p N_p \leq T_c$. Once the N_p cardiac phases have been filled, no data is acquired up to the next R-peak, as it is represented in Fig. 2.16. Thereby, some part of the cardiac cycle is never acquired.
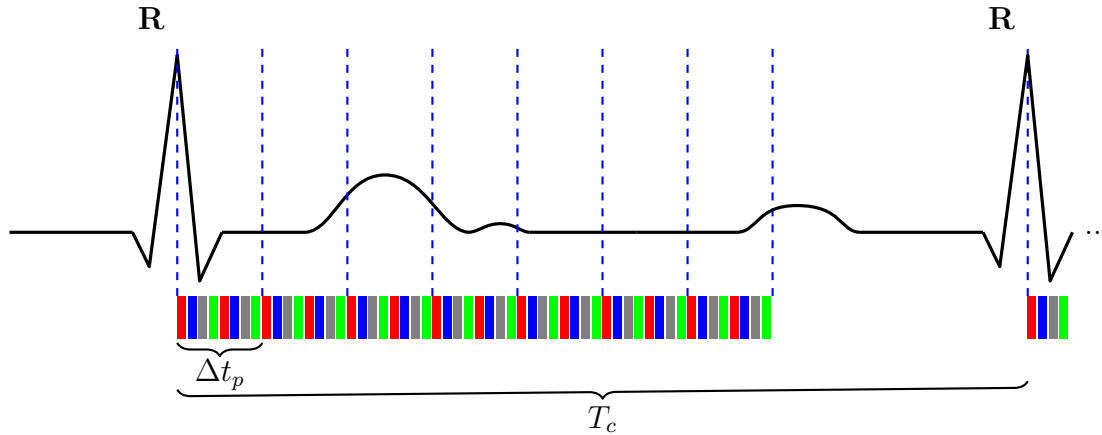
Figure 2.16: Scheme of a prospective ECG-gated 4D flow, where 2 segments are encoded by cardiac phase. T_c refers to the average duration of a cardiac cycle and Δt_p is the duration of a cardiac phases. The rectangles represent the k-space being filled: ▮ reference, ▮ u, ▮ v ▮ w.
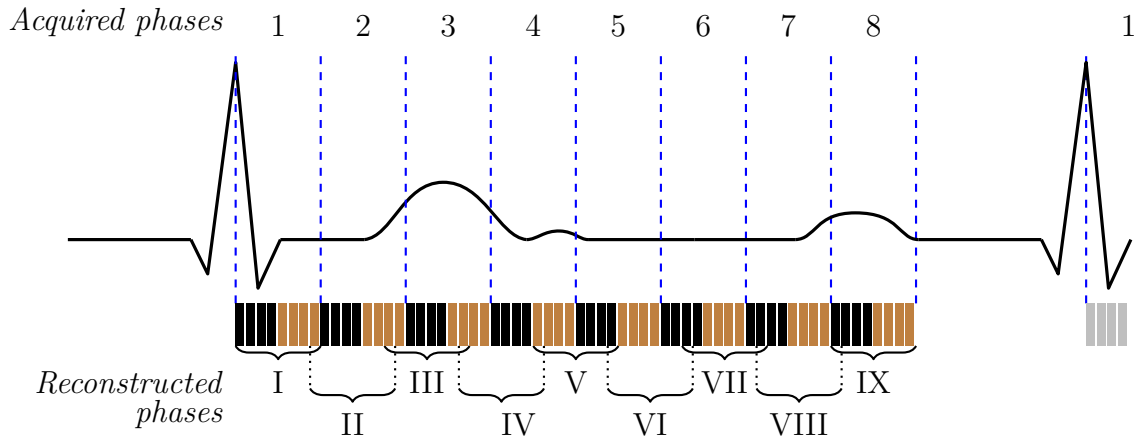
Figure 2.17: View-sharing principle, based on the scheme presented in Fig. 2.16. Here the rectangles ▮ and ▮ represent two different line number encoded in the k-spaces. The 8 acquired phases are indicated above in Arabic numerals, while an example to reconstruct 9 phases by view-sharing from these data is presented below in Roman numerals. Phase I corresponds to phase 1; phase II to the artificial phase 1.875 ($= 1 \times \frac{1}{8} + 2 \times \frac{7}{8}$); phase III to the artificial phase 2.75 ($= 2 \times \frac{2}{8} + 3 \times \frac{6}{8}$) etc.

In retrospective gating, the MR signal is continuously recorded without any physiological trigger, so that the whole cardiac cycle is covered. A physiological signal, such as an ECG, a pulse or a respiratory level, is stored simultaneously. This physiological data allows to retrospectively reorder the MR signal and group it into cardiac phases after the acquisition. This is the typical gating used in 4D flow MRI. This type of gating is often combined with a technique called

view-sharing [115]. The main idea of this process is to reuse k-space data from adjacent acquired cardiac phases in order to create a combined k-space, matching an artificial straddling time frame. The procedure is illustrated in Fig. 2.17, where an example to reconstruct 9 cardiac phases from 8 acquired phases is presented.

2.8 MRI artifacts

Artifacts related to MR imaging have been mentioned at different places throughout this chapter. Indeed, artifacts are almost always present in MRI. They come from different sources: motion, hardware, physics etc. A brief non-exhaustive overview of MR artifacts, particularly relevant to PC-MRI, is given in this section.

2.8.1 Motion-related artifacts

As it has been seen along the last sections, the whole k-space data collected over the MR acquisition time is required to reconstruct an MR image. The quality of the reconstructed MR image is thus particularly sensitive to motion, as it will lead to errors in the magnetization magnitude and phase.

Patient motion

Patient motions are inevitable during MR acquisition. They can be distinguished in two categories: aperiodic and period motion. Aperiodic motions, such as bulk patient motion, eye movement, swallowing or peristalsis, induce blurring in the images and are rather difficult to correct due to their random character. Periodic motions, like cardiac motion, arterial pulsation and respiration, are responsible for well-known ghosting artifacts. Ghosts are repeated copies of image features overlapping the true morphological image. Various methods to mitigate periodic motion artifacts exist. Patient can be asked to hold their breath for certain rapid imaging sequences ($< 20 - 30$ s). During longer free-breathing measurements, as for 4D flow MRI, it is common to monitor respiratory displacement via a diaphragmatic navigator. In the usual respiratory gating, the data collected is accepted only if the diaphragm position lies into a predefined acceptable range (usually during end expiration when the diaphragmatic motion is minimal). Other methods exist where the data is continuously acquired. The data is then either retrospectively triggered, corrected or the respiratory motion can be resolved as well [116].

Misregistration and velocity displacement artifact

Misregistration artifacts, also known as (spatial) displacement artifacts, happen whenever the moving spins change position between phase- and frequency-encoding. As illustrated in Fig. 2.18, this artifact occurs especially in oblique flows with respect to the gradient axes. The higher the velocity and/or the longer the time

between phase-encoding and readout, the greater the displacement. In sequences not meant to measure spin velocities, this artifact can be eliminated with flow-compensation [117]. In PC-imaging, it leads to mapping the velocities to incorrect spatial locations [118].
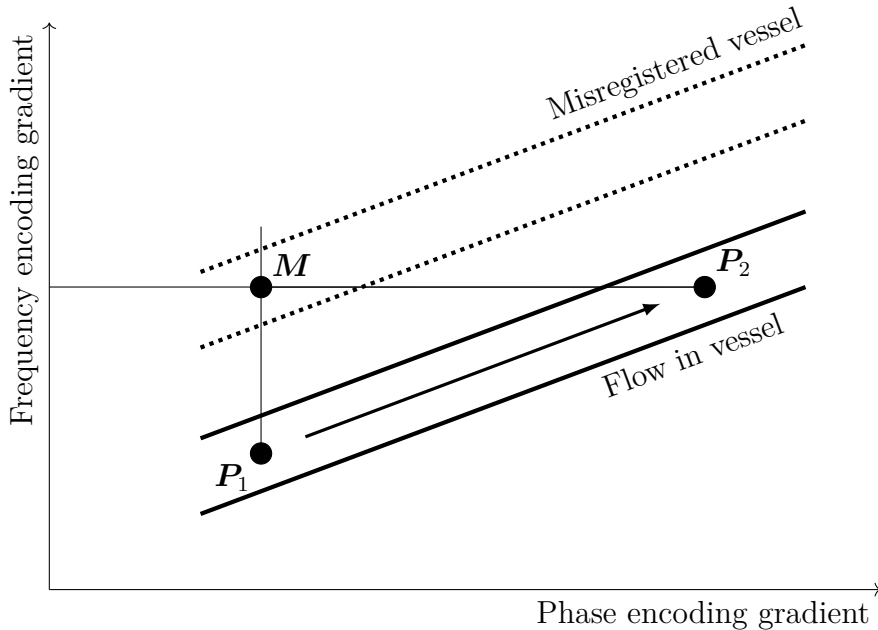
Figure 2.18: Misregistration artifact. Within the vessel, a moving spin is encoded in phase at position P_1, yet in frequency at position P_2 due to flow, inducing a misregistration at position M.

Velocity displacement artifact, also called acceleration artifact, is a second kind of misregistration. It is due to the acceleration of spins during spatial and velocity encodings, which leads to incorrect velocities assigned to the spatial locations. Indeed, 4D flow MRI relies on the assumption of negligible acceleration during a repetition time, which is not always accurate. However, Kouwenhoven et al. warn not to misinterpret the Taylor expansion of the phase given in Eq. (2.89). The common choice is to define t_{exp} as the center of the RF excitation pulse t_0. This choice for t_{exp} can result in an apparent sensitivity to acceleration, since t_0 does not match the time when velocity is actually encoded. They introduce the concept of gradient gravity time center to determine the exact time point at which velocity is encoded, which correspond to nullify $\mathcal{M}_2$ in Eq. (2.89). This time point turns out to be a more logical expansion time for the Taylor series [119]. Note that this expansion time differs according to the direction investigated.

Based on these conclusions, the misregistration artifacts can be mitigated by synchronizing the spatial and velocity encoding to occur simultaneously. It is possible in conventional Cartesian 4D flow MRI, except for the spatial frequency-encoding which necessarily occurs during the readout [117]. An interesting pa-

rameter to investigate the displacement artifact is the so-called displacement time T_D, which is the time difference between the velocity encoding and T_E.

Inflow

Inflow effect, also known as flow enhancement, is a consequence of partial saturation presented in Section 2.6.1. After the application of successive RFs with short T_R, the spins within the FOV reach a steady-state longitudinal magnetization M_z^{SS}. However, moving spins ("fresh" blood) entering the imaged volume have not experienced the train of RF pulses. These unsaturated spins produce a signal that is significantly higher than the signal produced by the partially-saturated spins. The artifact is astutely used in time-of-flight (TOF) MRA to image the vascular system without contrast agent.

2.8.2 Tissue-related artifacts

Chemical shift

Chemical shift artifact occurs due to small changes in a given proton's resonance frequency due to magnetic field variations induced by its molecular surroundings. Indeed, atomic nuclei are encompassed in electron clouds, which act as a shield against the main magnetic field and thereby modify the magnetic field experienced by protons. A well known example of chemical shift appears at fat/water interfaces. The protons of fat find themselves primarily in long chains of triglycerides. They are more shielded from $\boldsymbol{B}_0$ effects than water protons. Thereby, a fat proton resonates at a slightly lower frequency than a water proton. This results in an incorrect mapping of fat and water pixels in the MR image. Techniques have been developed to separate water and fat in MR images, or to eliminate the signal coming from either water or fat.

Magnetic susceptibility

Magnetic susceptibility, or magnetizability, is a property characterizing the ability of a material to become magnetized in an applied magnetic field. Materials that disperse the main field are called diamagnetic, while materials that concentrate the field are said to be paramagnetic. Almost all biological tissues are weakly diamagnetic, but accumulation of metals in some tissues can make them become paramagnetic. Furthermore, many metallic foreign bodies are ferromagnetic, meaning that they possess permanent magnetization. These additional contributions to the magnetic field lead to a spatially nonlinear field, and thus a nonlinear variation in protons precession frequencies. This results in image distortion, especially near metals (e.g. implants, dental restorations, jewelry...) and air cavity, as air is slightly paramagnetic. Shorter T_E and increased gradient strength can mitigate this artifact.

2.8.3   Technique-related artifacts

Partial volume effect

Partial volume effects appear when voxels are larger than the object features to be imaged, for example when there is more than one type of tissues within a voxel. This results in the reconstructed voxel as an average of these features. This occurs in particular at tissue boundaries. One way to alleviate this artifact is to reduce the voxel size.

Aliasing

Aliasing, also known as wrap-around or folding, occurs when the Nyquist sampling theorem, which states that the digital sampling rate must be at least twice the highest frequency contained within the signal, is violated. Although rare, it can occur along the frequency-encoding direction. However, it is more frequent along the phase-encoding directions. It happens when spins are excited beyond the prescribed range of the FOV (i.e. the imaged object is larger than the FOV). The phase of the excited spins outside the FOV is misidentified, and their associated object regions beyond the FOV appear as folding over the true anatomical image as illustrated in Fig. 2.19. This artifact can be solved with phase oversampling, which consists in an increased FOV, but where only the original smaller FOV is reconstructed.
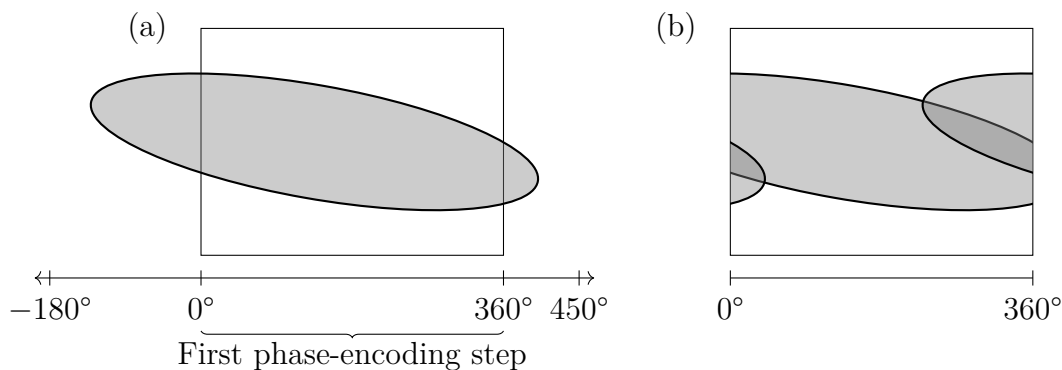
Figure 2.19: Aliasing artifact. In the first phase-encoding step, the gradient is set to produce a 360° phase shift across the FOV (rectangle). As the object to be imaged (gray ellipse) encompasses the FOV dimensions in (a), regions outside the FOV are incorrectly phase-encoded, resulting in the aliased image in (b).

In PC-MRI, velocity-aliasing can occur due to similar causes. In analogy to the choice of a FOV, which is too small in comparison with the object to be imaged, the choice of a V_{enc} that is too low in comparison to the maximal velocity to be imaged causes velocity aliasing, also known as phase wrap-around. The velocity that are above V_{enc} (or below $-V_{enc}$) are incorrectly mapped to the 2π range of phase variation between $[-V_{enc}, V_{enc}]$. It appears in velocity-images as voxels that

flow in the opposite direction in comparison to their neighbors. Algorithms have been developed to correct this artifact in post-processing [120, 121, 122].

Gibbs ringing

Gibbs' ringing, or truncation artifact, is caused by the lack of high-frequency components to describe sharp boundaries within the MR image. They are found in the directions associated with a few number of voxels, usually the phase-encoding directions. They are noticeable on the images as ripples parallel to sharper edges. Gibbs ringing may be avoided by increasing the matrix size (i.e. the number of voxels) for a given FOV. The ringing can also be softened by filtering the k-space data prior to the Fourier transformation.
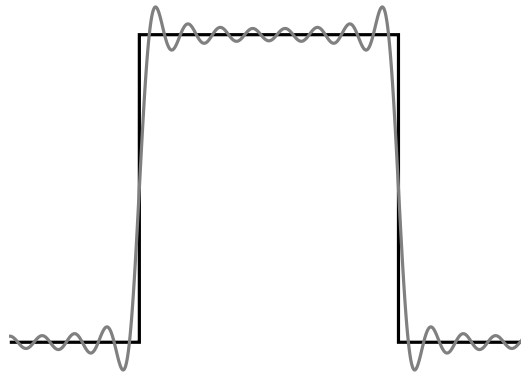
Figure 2.20: Gibbs' ringing artifact. A rectangular function and its description as a Fourier series using only the first 8 harmonics.

2.8.4 Gradient field distortions

Concomitant gradients

Whenever a linear magnetic field gradient is activated, it generates additional nonlinear spatially dependent magnetic fields as a consequence of Maxwell's equations. Bernstein et al. show that the magnitude of the magnetic field vector presented in equation (2.45) becomes $B_0 + \boldsymbol{G} \cdot \boldsymbol{r} + B_C$, where at the lowest order:

$$B_C(x,y,z,t) = \frac{1}{2B_0}\left(G_x^2 z^2 + G_y^2 z^2 + G_z^2 \frac{x^2+y^2}{4} - G_x G_z xy - G_y G_z yz\right) \quad (2.98)$$

This contribution is referred to as concomitant field-terms or Maxwell terms [123]. As it can be seen from Eq. (2.98), the Maxwell terms are more important at low fields (i.e. small B_0) and/or with stronger gradients. If not corrected, they are associated with a variety of artifacts: geometric distortion, image shift, ghosting etc. [89]. Phase correction during image reconstruction based on the knowledge of the gradient waveforms in the pulse sequence have been developed to correct these terms [123, 124, 125].

Eddy currents

Eddy currents, also known as Foucault's currents, are a consequence of the Faraday's law of induction. They appear particularly due to the rapidly changing magnetic field gradients, which induce electrical currents resulting in unwanted time-varying gradients and contamination of the main field $\boldsymbol{B}_0$. The higher the gradient amplitude or the faster the slew rates, the most significant the eddy currents. They can be mitigated with actively shielded gradient coils. Furthermore, gradients waveforms can be pre-emphasized. That means that the current waveform input into the gradient coil is distorted beforehand, so that this distortion cancels the subsequent eddy-current distortion [89]. Usually the pre-emphasis compensates up to the first-order of the spherical harmonic expansion of the eddy-current magnetic field. An illustration of the waveform pre-emphasis is given in Fig. 2.21.
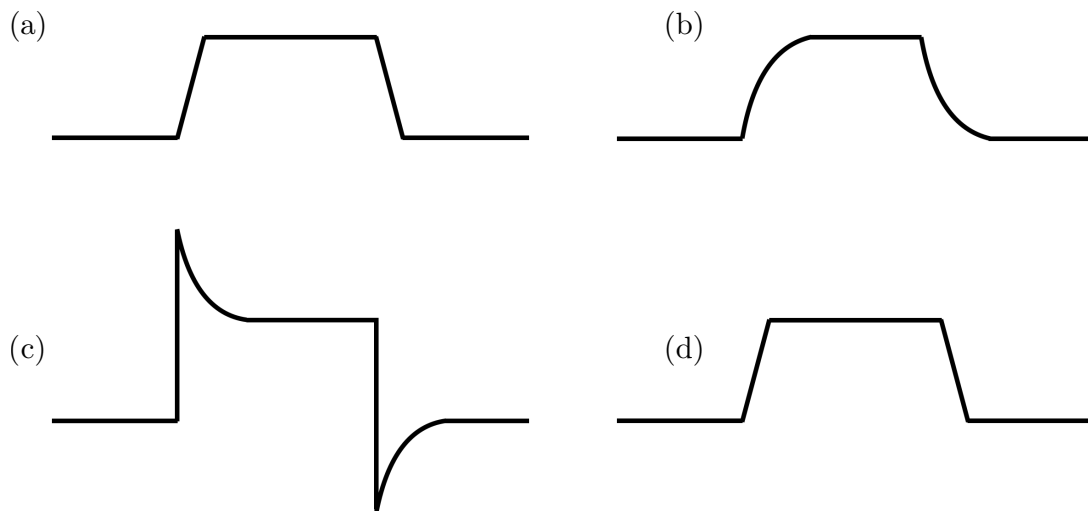
Figure 2.21: (a) Original gradient waveform and (b) the resulting distorted gradient due to eddy currents. (c) Pre-emphasized gradient waveform and (d) the resulting corrected gradient. Figure adapted from [126].

Gradient nonlinearities

Although linear near the magnet isocenter, gradient coils linearity drops off significantly towards the periphery of the magnet. This creates spatial distortions and blurring at the margins of MR images. These artifacts can be reduced by positioning the region to be imaged close to the scanner isocenter and by shimming, a correction process to remove field inhomogeneities in the magnet. Post-processing techniques are also available to correct the geometric distortions, such as precomputed displacement tables and phase mapping. For PC-MRI, Markl et al. report that gradient nonuniformity affects both the magnitude of encoded velocity and the direction of velocity-encoding. They propose a method to correct for the gradient nonlinearities in the reconstruction of the velocity fields in [127].

2.9   Reducing the scanning time in MRI

As highlighted by Eq. (2.97), the long time acquisition of 4D flow MRI scans is an obstacle to its adoption in clinical practice. A broad range of techniques have been developed over the years to shorten the scanning time. Some of them are presented in this subsection and will be investigated in the coming chapters.

2.9.1   Partial Fourier

Partial Fourier is a technique where the data is not collected symmetrically: one half of the k-space is completely filled, while only a small amount of the other half is. It relies on the fact that if a real object is imaged, its Fourier transform is Hermitian. It means that the real part of its Fourier transform is symmetric, whereas the imaginary part is antisymmetric around the k-space center. Thereby, theoretically only one-half of the k-space is required to reconstruct the MR image. However, the reconstructed image is usually complex due to phase shifts, for example related to artifacts mentioned in Section 2.8. Recall that in PC-MRI in particular, information about the velocity is collected thanks to additional phase shifts. Usually between 55 and 75% of the k-space data is collected in partial Fourier acquisitions to be able to reconstruct magnitude images (morphological images). Several algorithms have been proposed to reconstruct partial Fourier data, where the most common are zero-filling, homodyne processing or iterative homodyne processing [89, 128, 129, 130]. However, only the zero-filling ensures that phase information is preserved in the low-spatial frequency range (i.e. near the center of k-space). Zero-filling reconstruction has been shown to introduce fewer artifacts when reconstructing PC-MRI data over methods enforcing Hermitian symmetry [44]. When reconstructing PC-MRI images with zero-filling, it is recommended that at least 75% of the k-space is collected [89].
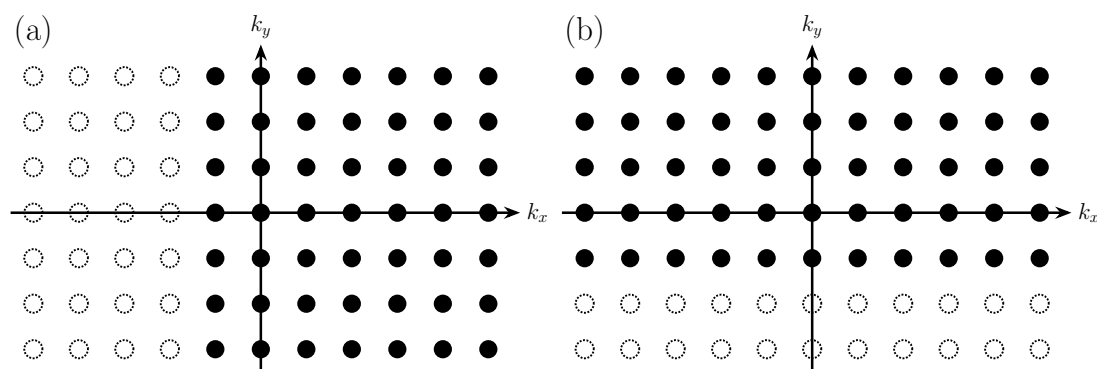
Figure 2.22: (a) Partial Fourier along k_x, or partial echo. (b) Partial Fourier along k_y. Filled circles represent collected data points and dotted circles non-acquired data points.

As illustrated in Fig. 2.22, partial Fourier can be used in the frequency-direction or in the phase-encoding direction, which does not result in the same

effect. When using partial Fourier along the phase-encoding direction, the main goal is to reduce scan time. This can be seen from Eq. (2.97), as N_y (or N_z) decreases. One can see from the same equation that the reduction in the number of frequency-encoded points N_x does not affect the scan time. However, partial Fourier along the frequency-direction allows reducing T_E, and consequently the displacement time T_D mentioned in Sec. 2.8.1. Often called partial echo, it is widely used in angiographic and cardiac applications, in order to reduce flow and motion artifacts. An analysis of the impact of partial echo on 4D flow MRI images is conducted in Chapter 5.

2.9.2 Parallel imaging techniques

Parallel imaging stems from the parallel RF coils presented in Sec. 2.3.3 to collect the signal [131]. The main idea behind parallel imaging is to approximate part of the k-space in the phase-encoding direction thanks to additional RF coil data, namely the spatial sensitivities of each coil of the RF array. Indeed, for each coil, the reconstructed image is weighted by its sensitivity. As some phase-encoding steps are not acquired, scan time is saved. Obviously the direct or indirect measure of the sensitivities is the key of this process to reconstruct images.
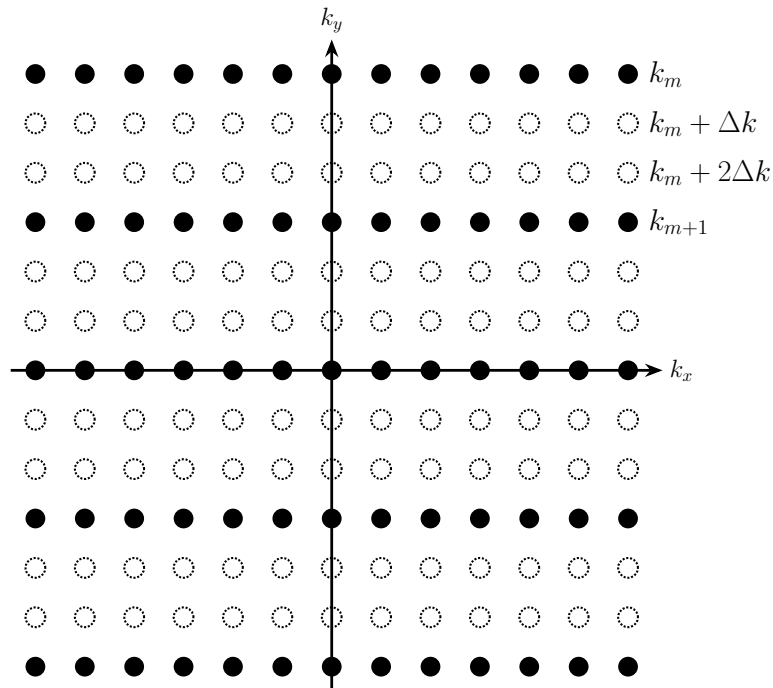
Figure 2.23: Undersampled k-space for parallel imaging with $R = 3$. Only 1 line out of 3 is acquired.

Parallel imaging consists in acquiring undersampled k-spaces, where only one line out of R lines of the fully sampled k-space is acquired. R is called the acceleration factor and is de facto inversely proportional to the acquisition time.

An illustration for $R = 3$ is presented in Fig. 2.23, where k_m denotes the acquired lines and Δk is the phase-encoding step size required for Nyquist sampling, that is $\Delta k = 1/L_y$.

Parallel-imaging techniques can be divided into two main categories. The x-space approach consists in reconstructing the images from the undersampled k-spaces for each coil, which results in aliased images, as they violate the Nyquist sampling theorem. The aliasing artifact is removed afterwards. By contrast, in the k-space approach, the missing k-space lines are synthesized before reconstruction. This section restricts itself to this last approach, as one of these techniques (GRAPPA) is investigated in Chapter 4.

SMASH

SMASH, standing for SiMultaneous Acquisition of Spatial Harmonics [132, 133], relies on the idea that coil sensitivities provide a spatial weighting of the received MR signal, in the same manner as complex exponential Fourier-encoding functions provide a spatial weighting. Thereby, it should be possible to approximate the Fourier functions corresponding to the missing k-space phase-encoding lines as linear combinations of the individual coil sensitivities.

Let us consider the 1D signal along the phase-encoding direction, in the same manner as defined along the readout direction in Section 2.5.1

$$S(k_y) = \int \rho(y)e^{-i2\pi k_y y}dy \tag{2.99}$$

where $\rho(y) = \iint \rho(\boldsymbol{r})dxdz$ represents the effective 1D spin density. Recalling that the effective spin density is proportional to the transverse magnetization M_{xy} and the coil profile $\mathcal{B}_{xy}^*$, $\rho(y)$ can be rewritten as:

$$\rho(y) = M_{xy}(y)\mathcal{B}_{xy}^*(y) \tag{2.100}$$

Combining the two equations and dropping the xy and y subscript for the sake of clarity, the signal s_j collected by the jth RF coil at a measured frequency k_m is given by:

$$s_j(k_m) = \int M(y)\mathcal{B}_j(y)e^{-i2\pi k_m y}dy \tag{2.101}$$

with $j = 1, 2, ..., N_c$ the number of individual coils.

Now the composite signal $\tilde{s}$ that one would like to reconstruct is:

$$\tilde{s}(k_m) = \int T(y)M(y)e^{-i2\pi k_m y}dy \tag{2.102}$$

$$\tilde{s}(k_m + p\Delta k) = \int T(y)M(y)e^{-i2\pi(k_m + p\Delta k)y}dy$$
$$= \int T(y)M(y)e^{-i2\pi k_m y}e^{-i2\pi p\Delta k y}dy \tag{2.103}$$

where $T(y)$ is the target sensitivity function for normalization. The goal of SMASH is to synthesize the complex exponentials $e^{-i2\pi p \Delta k y}$ using linear combinations of coil sensitivities, such that [91]:

$$\sum_{j=0}^{N_c-1} a_j^p \mathcal{B}_j(y) = T(y)e^{-i2\pi p \Delta k y} \tag{2.104}$$

Note in particular that for $p = 0$:

$$\sum_{j=0}^{N_c-1} a_j^0 \mathcal{B}_j(y) = T(y) \tag{2.105}$$

$T(y)$ can be defined by the weights a_j^0 (e.g. uniform unity weights), or in the contrary a_j^0 are fitted to a chosen $T(y)$. A common choice for $T(y)$ is to be a sum-of-squares of coil profiles: $T(y) = \sqrt{\sum_{j=0}^{N_c-1}|\mathcal{B}_j(y)|^2}$.

If the combination in Eq. (2.104) exists, the signal at $k_m + p\Delta k$ becomes:

$$\begin{aligned}
\tilde{s}(k_m + p\Delta k) &= \int M(y)e^{-i2\pi k_m y} \sum_{j=0}^{N_c-1} a_j^p \mathcal{B}_j(y) dy \\
&= \sum_{j=0}^{N_c-1} a_j^p \int M(y)\mathcal{B}_j(y)e^{-i2\pi k_m y} dy \\
&= \sum_{j=0}^{N_c-1} a_j^p s_j(k_m) \tag{2.106}
\end{aligned}$$

In this way, the missing k-space lines can be reconstructed from the acquired lines. Note also that as $k_m + R\Delta k = k_{m+1}$, the signal $\tilde{s}(k_m + p\Delta k) = \tilde{s}(k_{m+1} + (p-R)\Delta k)$ can both be determined as the pth positive harmonic adjacent to line k_m or as the $(p - R)^{\text{th}}$ negative harmonic adjacent to k_{m+1}. This alternative definition can alleviate the fact that approximating harmonic orders comparable to the number of individual coils can be difficult.

That being said, the weights a_j^p still needs to be determined. Rewriting Eq. (2.104) with the following formalism:

$$\sum_{j=0}^{N_c-1} b_{yj} a_{jp} = f_{yp} \tag{2.107}$$

which is a matrix equation of the form:

$$BA = F \implies A = B^{-1}F \tag{2.108}$$

The coil sensitivities are usually measured from the imaged object. It can be done from a separate low-resolution calibration scan, as long as this scan encompasses the region to be reconstructed. In general the coil sensitivities matrix B is not a square matrix, and B^{-1} is obtained via pseudoinverse or singular value decomposition.

AUTO-SMASH

Instead of directly measuring the coil sensitivities, extra Nyquist-sampled lines can be acquired around the k-space center to indirectly measure the sensitivities. This additional lines, called autocalibration signal (ACS) lines, are used to determine the weights a_j^p. In AUTO-SMASH, $R-1$ ACS lines are collected as illustrated in Fig. 2.24.
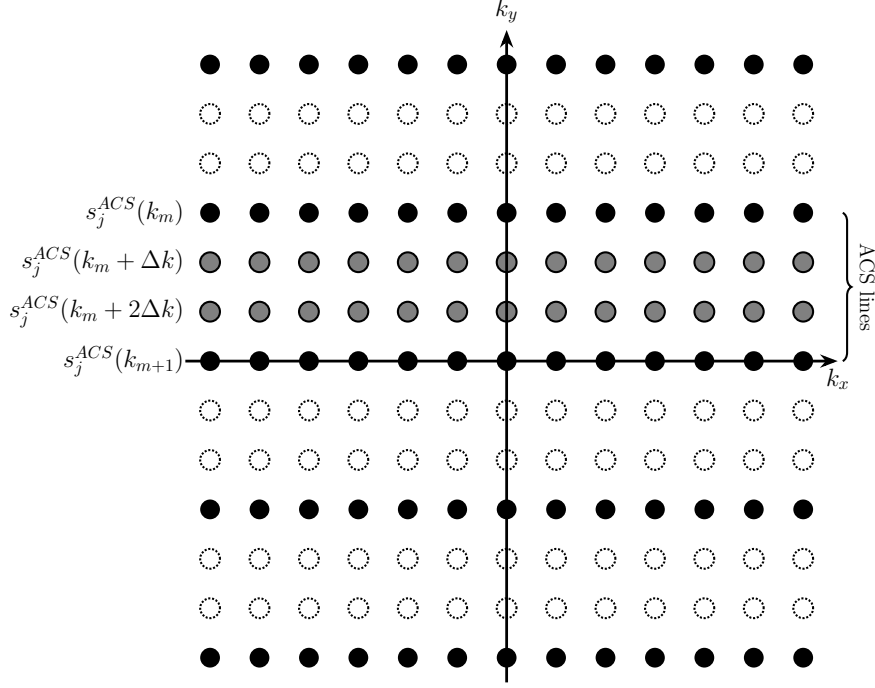
Figure 2.24: k-space for AUTO-SMASH for $R = 3$. In addition to the lines acquired according to Fig. 2.23, autocalibration (ACS) lines are collected (gray circles) in order to determine the weighting factors to reconstruct the missing lines (dotted circles).

According to Eq. (2.106), the composite ACS k-space lines can be expressed as:

$$\tilde{s}^{ACS}(k_m + p\Delta k) = \sum_{j=0}^{N_c-1} a_j^p s_j^{ACS}(k_m) \tag{2.109}$$

Moreover, combining Eq. (2.103) and (2.105), the ACS lines are such that:

$$\tilde{s}^{ACS}(k_m + p\Delta k) = \int \sum_{j=0}^{N_c-1} a_j^0 \mathcal{B}_j(y) M(y) e^{-i2\pi(k_m+p\Delta k)y} dy$$

$$= \sum_{j=0}^{N_c-1} a_j^0 \int \mathcal{B}_j(y) M(y) e^{-i2\pi(k_m+p\Delta k)y} dy$$

$$= \sum_{j=0}^{N_c-1} a_j^0 s_j^{ACS}(k_m + p\Delta k) \tag{2.110}$$

The process is illustrated in Fig. 2.25.
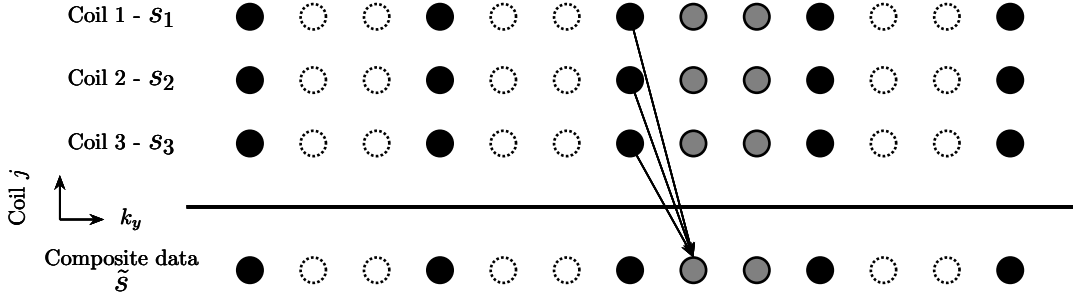
Figure 2.25: Reconstruction for AUTO-SMASH, with 3 coils and $R = 3$. Each circle represents a phase-encoded line, where the black circles are acquired k_m values, the gray ones ACS lines and the dotted ones missing lines. As illustrated with the arrows, a single line k_m acquired in each coil is fit to a single ACS composite point.

By choosing the a_j^0 weights, the a_j^p for $p > 0$ are found in requiring the following equation to hold, where:

$$\sum_{j=0}^{N_c-1} a_j^p s_j^{ACS}(k_m) = \sum_{j=0}^{N_c-1} a_j^0 s_j^{ACS}(k_m + p\Delta k) \qquad (2.111)$$

Note that a certain number of ACS lines are required to determine the a_j^p, and that additional equations can be obtained by fitting the Nyquist-sampled lines present within the ACS region. The same procedures as for SMASH can be used to reconstruct the missing k-space lines.

GRAPPA

GRAPPA, standing for Generalized Autocalibrating Partially Parallel Acquisitions, is an extension of AUTO-SMASH. As for AUTO-SMASH, an ACS region around the center of k-space is collected. In contrary to SMASH and AUTO-SMASH, where a composite k-space is created, individual k-spaces for each coil are created, where data from all coils are used to estimate missing lines for each coil. For a given coil j, the weights in GRAPPA are introduced over the ACS lines as:

$$\tilde{s}_j^{ACS}(k_m + p\Delta k) = \sum_{l=0}^{N_c-1} \sum_{b=0}^{N_b-1} a_{j,l}^{p,b} s_l^{ACS}(k_m + bR\Delta k) \qquad (2.112)$$

where N_b is the number of blocks, or kernels, used for the reconstruction and defined as an acquired Nyquist-sampled k line and $R - 1$ missing lines. Note that for a given number of blocks, more than one reconstruction is possible for each missing line (sliding block reconstruction) as illustrated in Fig. 2.26. The multiple reconstructions for each unacquired line can be combined into a weighted average to create the final reconstructed line.
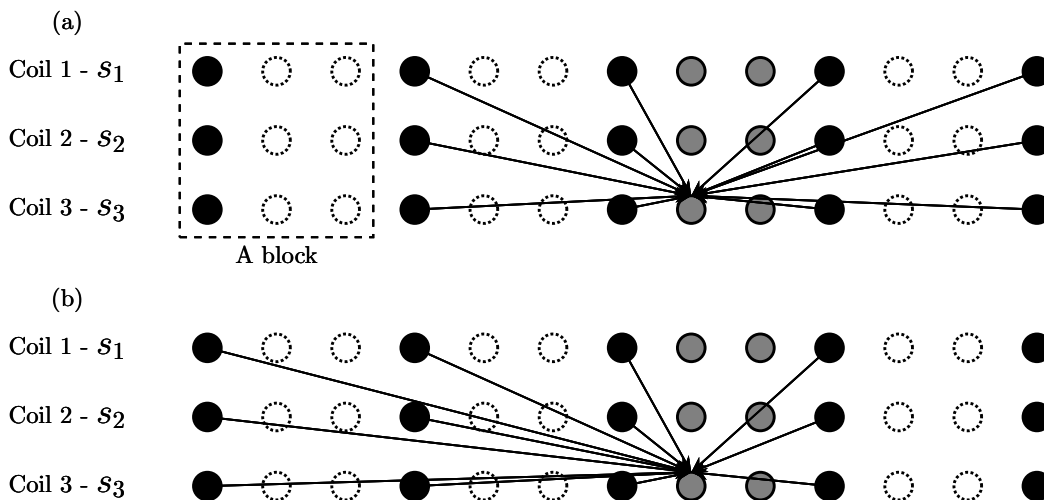
Figure 2.26: (a) Reconstruction for the third coil for GRAPPA, with 3 coils and $R = 3$. Each circle represents a phase-encoded line, where the black circles are acquired k_m values, the gray ones ACS lines and the dotted ones missing lines. More than one line acquired in each coil are fit to an ACS line collected by a single coil (here, the third coil). (b) Another possible reconstruction for the same ACS line acquired by the third coil to perform sliding block reconstruction. Note that no composite signal is created, as opposed to the AUTO-SMASH reconstruction presented in Fig. 2.25.

Once the k-spaces for each individual coil are created, N_c single coil images are reconstructed. They are then combined into the final image, usually using a sum-of-squares reconstruction.

2.9.3 Compressed Sensing

Compressed sensing (CS) is another technique to highly accelerate MRI scans, which has seen increased interest in the past years. The main idea underlying CS MRI is to collect only essential components of the k-space rather than the fully-sampled k-space and to use an iterative optimization process to reconstruct the image. Unlike parallel-imaging, it relies on an incoherent undersampling of the k-space. The two other key elements for CS are sparsifying transformation and nonlinear reconstruction [134].

A typical flowchart of the CS procedure is given in Fig. 2.27 and detailed below [88].

Semi-random undersampled k-space collection (y)

Initialization: Fourier transform reconstruction (x)
Iteration: Updated image (x)

if $||y - Fx||_2^2 \leq \epsilon$

Reconstructed final image

else

Sparsifying transform

Sparsified data denoising

Inverse sparsifying transform + Inverse Fourier transform

Difference k-space $||y - Fx||_2^2$

Difference x-space
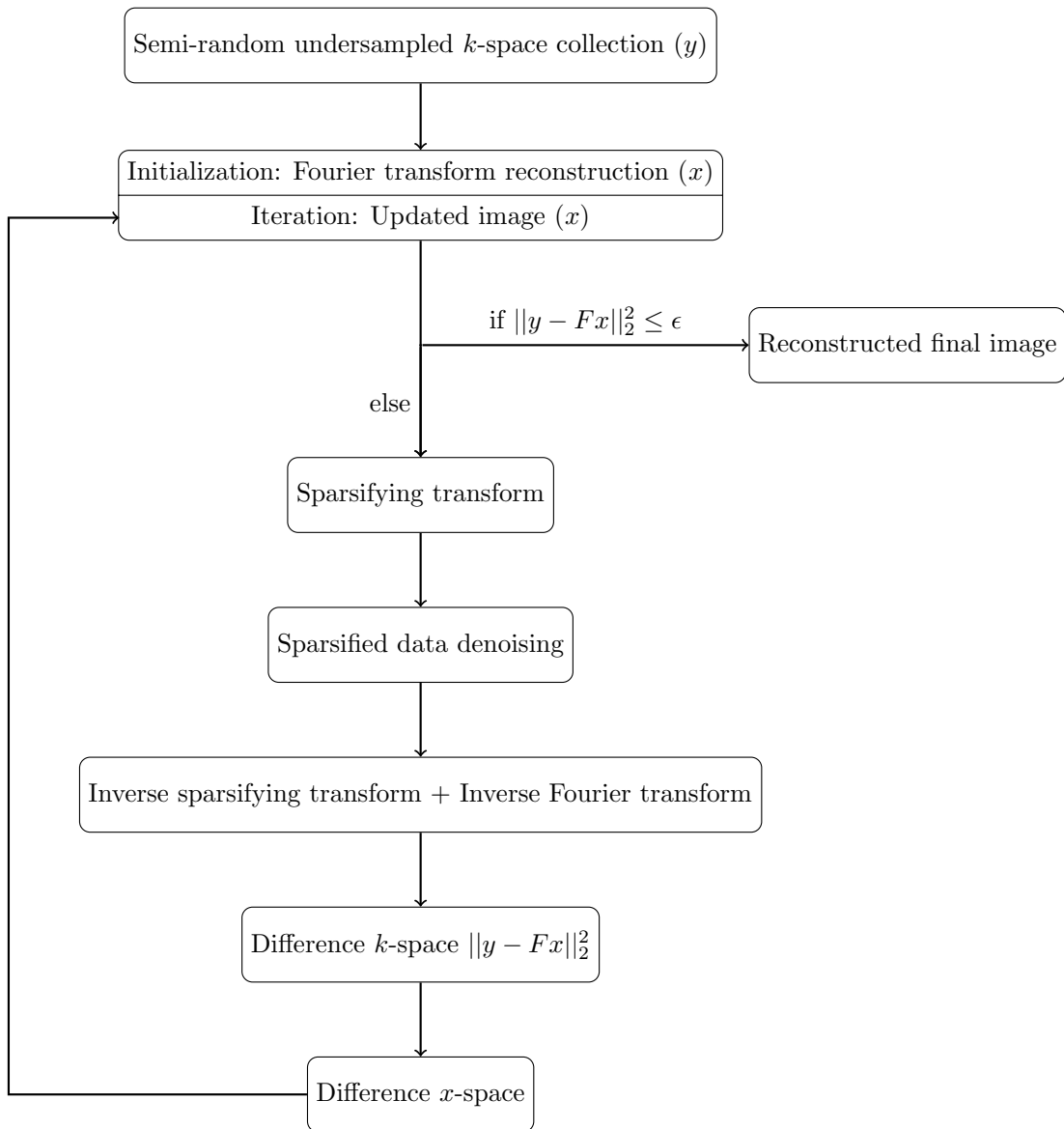
Figure 2.27: Flowchart of a typical compressed-sensing procedure.

First, the undersampled k-space is collected. Coherent undersampling, as for SMASH and GRAPPA, is avoided in order not to have aliasing. Incoherent sampling on the contrary allows to have diffuse noise within the whole image, which is easier to remove. Furthermore, a semi-random pattern is usually followed, as low frequencies contain more information than high frequencies. Preferential sampling near the k-space center can be obtained with a variable density Poisson-disc [135], Gaussian [136] or Golden-angle radial schemes [137].

Once this highly undersampled k-space is acquired, an iterative algorithm is used to reconstruct the image. First, the k-space is Fourier-transformed to create an initial noisy image. A sparsifying transform is applied to this noisy image. This transform possesses the particularity to concentrate meaningful imaging

information in few high-intensity pixels, while the noise is distributed over many pixels of lower intensity. The most common sparsifying transformation is wavelet transformation. The sparsified data is then denoised by nullifying pixels, whose value is below a certain threshold, digital filtering, or subtraction. The denoised data is inverse sparsifying transformed and inverse Fourier transformed, so that a denoised whole k-space is obtained. A difference k-space is created by subtracting this denoised k-space to the measured undersampled k-space and by setting to zero the initially non-acquired points. If the difference k-space is below a predefined threshold ϵ in the least-squares sense, the denoised k-space is deemed consistent enough with the measured k-space. The difference k-space is Fourier transform to create a difference image, which is added to the initial noisy image to build the final image. If the data consistency is not verified, the noisy image is still updated by adding the difference image and the process is reiterated. The algorithm is repeated until the least-square difference of the difference k-space is below ϵ or until a predefined maximal number of iterations is reached. Mathematically, the compressed sensing consists in solving the following optimization problem [88, 134]:

$$min_x \left(||y - Fx||_2^2 + \lambda ||\Phi x||_1 \right) \tag{2.113}$$

where x is the reconstructed image, y the measured k-space data, F the Fourier transform, Φ a sparsifying transform and λ a regularization parameter weighing the relative importance of data consistency (first term) and sparsity (second term).

3

MRI modelling

Chapter contents

In this chapter, several ways to model MRI are presented. First, an in-house code has been developed to illustrate the concepts developed in Chapter 2 in simple configurations. Simplistic GRE and PC-MRI sequences can be build with predefined gradients functions. Corresponding images can be plotted, as well as the evolution of the isochromats phase over time. Second, the YALES2BIO solver is introduced [138, 139]. This in-house numerical software is designed to perform numerical simulations of blood flows in complex geometries. Indeed, computational fluid dynamics coupled with MRI measurements can bring insights into similarities and differences observed with 4D flow MRI. The YALES2BIO solver inherits from the massively parallel YALES2 code developed at CORIA and dedicated to research in turbulent flows. The Navier-Stokes equations (NSE)

are solved on unstructured meshes using a finite-volume method and a high-order non-dissipative numerical scheme. Finally, a framework to simulate MR images is presented in the last part of this chapter, from a manufacturer sequence to reconstruction. The Bloch equations are solved on particles together with the NSE thanks to a dedicated solver within the YALES2BIO platform.

3.1 A toy model to illustrate the Bloch equations

To understand and illustrate some phenomena involved in obtaining the NMR signal and reconstructing the MR image based on this signal, a toy model has been developed in Python. The goal of this demonstrator is to build the MRI pulse sequence brick by brick, where each gradient consists in a parametrizable function. Several functions are proposed to follow how the magnetization of the spins evolves over time and to reconstruct an idealized image of the morphology or the velocity.

This tool is meant for educational purposes only and is not meant to take all the subtleties of MRI into account. Indeed, the following assumptions and idealizations are made. The equations are solved in the rotational frame of reference, where no off-resonance effects are included. The static magnetic field is considered uniform. The gradients are modelled as perfect rectangles, which is physically impossible to achieve. A more accurate depiction of gradients would be trapezoidal. Nevertheless, rectangular waveforms can be sought as trapezoids with infinite slew rates. Concerning the domain to be imaged, only 1D or 2D images can be simulated. Indeed, 3D images consist in adding a second phase-encoding direction in the same manner as for 2D images. Thereby 2D images are deemed sufficient to illustrate basic MRI phenomena. Furthermore, the field-of-view is discretized in order to have a one-to-one correspondence between the input proton densities and the reconstructed images. That means there is one isochromat per pixel, localized by its position on a Cartesian grid. Each isochromat is associated to initial input data: a proton density, a velocity vector and potentially an acceleration vector. Moreover, only one species is considered, so all isochromats are characterized by the same relaxation times. Finally, the RF pulse is modelled as a rectangular pulse, often called hard pulse, equal to B_1 over a short duration τ_{RF}. Even though this kind of RF pulses are non-selective, the assumption made here is that all isochromats along the line or within the slice of interest are excited in the exact same manner, with the same flip angle and spins outside the field-of-view are neglected.

3.1.1 Input file

To design the sequence, some parameters are needed as inputs. The conventional MRI coordinate system presented in Section 2.5 is used in the code: x refers to

the frequency-encoded direction (readout), y to the (first) phase-encoded direction and z to the slice-select direction (not modelled here, where only one perfect slice is excited).

As mentioned above, the RF pulse is modelled as a hard pulse. The sequence is designed such that the RF pulse starts at $t = 0$. The amplitude B_1 (in μT) and the flip angle α (in degrees) are needed as inputs. The duration of the RF pulse is such that:

$$\tau_{RF} = \frac{\alpha}{\gamma B_1} \frac{\pi}{180} \tag{3.1}$$

The RF pulse is oriented along x and the initial magnetization vector is such that $\boldsymbol{M_0} = [0, 0, M_0]$, so that the magnetization vector after the RF pulse is only in the (yz)-plane. Field-of-view data are required, namely the size of the domain to be imaged $L_x \times L_y$ and the pixel resolution $\Delta x \times \Delta y$. They are related to the number of pixels $N_x \times N_y$ as:

$$N_x = \frac{L_x}{\Delta x} \quad ; \quad N_y = \frac{L_y}{\Delta y} \tag{3.2}$$

Two machine parameters are needed: the maximal gradient strength G_{max} (in mT/m) and the bandwidth BW of the receiver coil (in Hz/pixel). BW is equivalent to the digitization rate of the signal, and is thus related to the sampling time T_s by:

$$BW = \frac{N_x}{T_s} \tag{3.3}$$

The densities, velocities and accelerations are declared in a table format. In these tables, each cell localized at the coordinates (i, j) is interpreted as the spin isochromat in the pixel (i, j), with coordinates $x = i\Delta x$ and $y = j\Delta y$. Thereby, at each position, a scalar density, a velocity vector and an acceleration vector are associated (note that they can be potentially equal to zero). Global T_1 and T_2 relaxation times are required as well. Finally, the velocity-encoding parameter V_{ENC} in the 3 directions has to be set as well.

3.1.2   Gradients as building blocks

The gradients can be seen as the building blocks of the MR pulse sequence. In chapter 2, various types of gradients have been mentioned, to spatially encode the signal, to compensate artifacts induced by flow or on the contrary to encode information about the velocity. Four sets of gradients are available in the Python MR demonstrator: the readout and prephasing gradients, the flow-compensation along the readout direction, the velocity-encoding bipolar gradient and the phase-encoding gradients. The gradients are added one after the other in a so-called chronogram, where their changes in amplitude over time are kept. The time instants saved in the chronogram are only the ones when at least one gradient changes amplitude. This defines the pulse sequence.

Readout and prephasing gradients

As mentioned in Section 2.5.1, the readout gradient is the gradient during which the signal is acquired. A prephasing gradient is required before the readout gradient in order to form an echo during the readout lobe. Both gradients are modelled in the same function, as they work together. The echo happens in the middle of the readout lobe when the full k-space is acquired, at the time instant T_E. The gradient strength G_r of the readout and its duration τ_r are defined as:

$$G_r = \frac{2\pi BW}{\gamma L_x} \quad ; \quad \tau_r = T_s = \frac{N_x}{BW} \qquad (3.4)$$

The duration of the readout gradient is by definition equal to the sampling time. The dwell time, which is the delay between two consecutive sampling instants, is given by:

$$t_d = \frac{1}{BW} \qquad (3.5)$$

For an odd number of points, as the k-space is sampled in a symmetrical manner, the first instant collected is at $t_{r,b} + \frac{1}{2BW}$, where $t_{r,b}$ denotes the beginning of the readout gradient. For an even number of points, the k-space is collected in an asymmetrical way, where there is one spatial frequency k_x more in the negative range compared to the positive one. The first instant collected therefore matches the beginning of the readout lobe. With these designs, the frequency $k_x = 0$ is collected at T_E for both odd and even number of points.

Concerning the prephasing gradient, it is only the area under its lobe which determines when the echo peak forms for static isochromats. In this case, the area under the prephasing lobe should be equal to half the area under the readout gradient. In the demonstrator, two options are available to design the pre-phasing gradient. The first option is to use the maximal gradient strength G_{max}. This leads to the shortest possible prephasing gradient and can be used for a static image. The second option is the one that has to be chosen to produce images of the velocity. The gradient strength of the prephasing gradient is set to $-G_r$ and its duration lasts half the one of the readout gradient. Such a gradient is compatible with the flow-compensating gradient along the readout direction.

Flow-compensating gradient along the readout direction

The flow-compensating gradient is an extra bipolar gradient, which is meant to cancel the 0th and 1st-order moments at T_E in Eq. (2.89).

As it is important to minimize the time between the RF pulse and the echo time T_E because of T_2 relaxation and the presence of body-induced background magnetic field gradients [91], the flow-compensating gradient is usually combined with the pre-phasing and readout gradients in a so-called $1\bar{2}1$ waveform [89], where the pre-phasing gradient is defined by the second option mentioned in last paragraph. In this design, the pre-phasing gradient has to be such that its gradient strength is the opposite of the one of the readout gradient and its duration is

half the one of the readout. Concerning the flow-compensating gradient, it is a bipolar gradient, whose 2nd lobe is superimposed on the pre-phasing gradient. The duration of the flow-compensating gradient is the same as the readout gradient and the magnitude of the 1st lobe is equal to G_r and the 2nd one $-G_r$.

Velocity-encoding bipolar gradient

As mentioned earlier in Section 2.7, the shape of the gradient used to encode velocity is bipolar, with two lobes of same duration and opposite gradient strengths. In the present MR demonstrator, the choice has been made to set the duration of the velocity-encoding bipolar gradient equal to τ_r, so that it can be superposed with the flow-compensating and pre-phasing gradients along the (x)-direction. Thereby, the gradient strength of the positive lobe is given by:

$$G_v = \frac{\pi}{\gamma V_{ENC}(\frac{\tau_r}{2})^2} \tag{3.6}$$

with V_{ENC} in m.s^{-1} corresponds to the maximal expected velocity

To reconstruct the velocity, two sequences are needed in order to cancel out the background phase effects (ϕ_0). A first possibility is to play two sequences with the same bipolar gradient, yet with opposite polarity. In this particular case, there is no need for a flow-compensating gradient, only the pre-phasing and readout gradients are required in addition to the bipolar gradient. Another method, which is preferentially used in 4D flow MRI (cf. Section 2.7), is to have a reference sequence (e.g. a pulse sequence velocity-compensated along the readout direction) and the same sequence yet with a bipolar gradient.

Note that the bipolar gradient design presented here can be used to encode any direction x, y or z.

Phase-encoding gradient

To reconstruct 2D images, besides being encoded in frequency, the isochromats have to be encoded in phase by the so-called phase-encoding gradient. While the readout gradient should be sampled at specific time instants corresponding to the needed k_x, the phase-encoding gradient is such that it leads to a different k_y at each repetition time T_R, where there are as many repetition times as the number of lines N_y along the y-direction in the image. This means that in comparison to the previous paragraphs, the aforementioned basis sequence will be repeated N_y times, yet the phase-encoding gradient will be incremented for every repetition time.

The usual design of the phase gradient for a Cartesian sampling is to go from the most positive k_y frequency to the most negative one. Thereby, to encode the most positive frequency, the maximum gradient strength G_{max} is usually chosen. The most positive frequency $k_{y,max}$ is thus given by:

$$k_{y,max} = \frac{\gamma}{2\pi} \int_{t_{y,b}}^{t_{y,b}+\tau_y} G_{max} \, dt = \frac{\gamma G_{max}\tau_y}{2\pi} \tag{3.7}$$

where $t_{y,b}$ is the beginning of the phase-encoding gradient and τ_y its duration. As there are $\frac{n_y-1}{2}$ spatial frequencies sampled from each side of $k_y = 0$, $k_{y,max}$ is also defined as

$$k_{y,max} = \frac{n_y - 1}{2}\Delta k_y = \frac{n_y - 1}{2}\frac{1}{L_y} \tag{3.8}$$

Combining these two expressions of $k_{y,max}$ results in the following condition on τ_y:

$$\tau_y = \frac{\pi(N_y - 1)}{\gamma G_{max}L_y} \tag{3.9}$$

For the next T_R, the duration τ_y is kept, and the gradient strength decreased such that for the ith T_R:

$$G_y(T_{R,i}) = G_{max}\left(1 - \frac{2i}{N_y - 1}\right) \tag{3.10}$$

3.1.3 Analytic 1D example

In this analytic example, the phase behavior associated with the gradients presented in the last section is derived for a simple 1D case. From now on, a slightly different convention is followed to express the signal in order to define the dephasing as a positive quantity. Eq. (2.39) becomes:

$$S(t) = \iiint_V e^{-\frac{t-t_0}{T_2}}\rho(\boldsymbol{r})e^{-i\phi(\boldsymbol{r},t)}d^3r \tag{3.11}$$

The study is restrained to the x direction, with the position and the velocity having components along this direction only (no acceleration term is considered). Furthermore, only the case of an odd number of pixels N_x is presented, which implies a symmetrical sampling during the readout. With the new convention, the general expression given in Eq. (2.89) for the phase in 1D, expanded from the initial time instant $t_{exp} = t_0$, reduces to:

$$\phi(x(t), t) - \phi_0 = \gamma x_0 \int_{t_0}^t G_x(t')dt' + \gamma v_x \int_{t_0}^t G_x(t')(t' - t_0)dt' \tag{3.12}$$
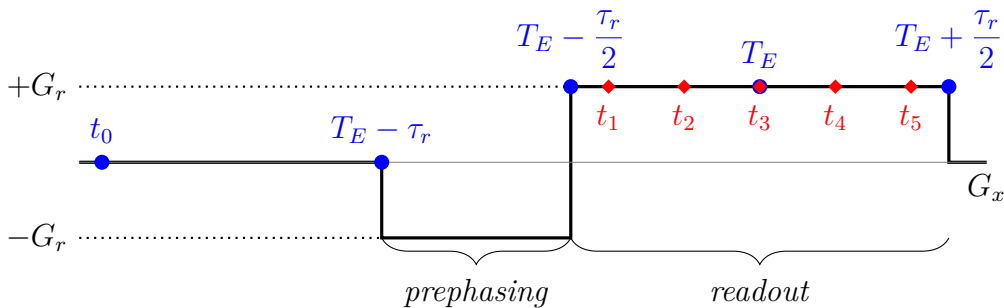
Figure 3.1: Chronogram with a prephasing and a readout gradient. Time instants of collected signal for $N_x = 5$ are displayed in red.

Let us first consider only the prephasing and readout gradients, presented in Fig. 3.1. Note the choice for the prephasing gradient to be compatible with flow-compensation. The chronogram of this sequence contains two fixed time instants: t_0, which corresponds to the end of the RF pulse, and T_E the echo time in the middle of the readout gradient. By construction, the prephasing gradient starts at $T_E - \tau_r$ and ends at $T_E - \frac{\tau_r}{2}$, which matches the beginning of the readout. The readout ends at $T_E + \frac{\tau_r}{2}$. Furthermore, let us call t_p the pth time instant when the signal is collected (with $p = [1, 2, ..., N_x]$), such that

$$t_p = T_E + \frac{\tau_r}{2} \left(\frac{2p-1}{N_x} - 1 \right) \tag{3.13}$$

Note that in order to comply with the definitions of the readout duration τ_r and dwell time $t_d = t_{p+1} - t_p$, given respectively in Eq. (3.4) and (3.5), the first time instant does not occur at $T_E - \frac{\tau_r}{2}$, but at $t_1 = T_E - \frac{\tau_r}{2} \left(1 - \frac{1}{N_x} \right)$. The last time instant occurs at $t_{N_x} = T_E + \frac{\tau_r}{2} \left(1 - \frac{1}{N_x} \right)$ for symmetric reasons. Furthermore, $t_p = T_E$ for $p = \frac{N_x+1}{2}$.

The spatial frequency k_x collected at t_p is given by:

$$k_x(t_p) = \frac{\gamma}{2\pi} \int_{t_0}^{t_p} G_x(t) dt = \frac{1}{2\pi} \frac{\gamma G_r \tau_r}{2} \left(\frac{2p-1}{N_x} - 1 \right) \tag{3.14}$$

The phase can be analytically solved at these specific time instants:

$$\phi(x, T_E - \tau_r) - \phi_0 = 0$$

$$\phi(x, T_E - \frac{\tau_r}{2}) - \phi_0 = \gamma x_0 \int_{T_E - \tau_r}^{T_E - \frac{\tau_r}{2}} (-G_r) dt + \gamma v_x \int_{T_E - \tau_r}^{T_E - \frac{\tau_r}{2}} (-G_r)(t - t_0) dt$$
$$= -\frac{\gamma G_r \tau_r}{2} \left(x_0 + v_x \left((T_E - t_0) - \frac{3}{4} \tau_r \right) \right)$$

$$\phi(x, t_p) - \phi_0 = \phi(x, t_p) - \phi(x, T_E - \frac{\tau_r}{2}) + \phi(x, T_E - \frac{\tau_r}{2}) - \phi_0$$
$$= \gamma x_0 G_r \int_{T_E - \frac{\tau_r}{2}}^{T_E + \frac{\tau_r}{2}\left(\frac{2p-1}{N_x} - 1\right)} dt + \gamma v_x G_r \int_{T_E - \frac{\tau_r}{2}}^{T_E + \frac{\tau_r}{2}\left(\frac{2p-1}{N_x} - 1\right)} (t - t_0) \, dt$$
$$- \frac{\gamma G_r \tau_r}{2} \left(x_0 + v_x \left((T_E - t_0) - \frac{3}{4} \tau_r \right) \right)$$
$$= \frac{\gamma G_r \tau_r}{2} \left(\frac{2p-1}{N_x} - 1 \right) (x_0 + v_x (T_E - t_0))$$
$$+ \frac{\gamma G_r \tau_r^2}{8} v_x \left(\left(\frac{2p-1}{N_x} - 1 \right)^2 + 2 \right)$$
$$= 2\pi k_x(t_p) (x_0 + v_x (T_E - t_0)) + \frac{2\pi^2}{\gamma G_r} k_x^2(t_p) + \frac{\gamma G_r \tau_r^2}{4} v_x \tag{3.15}$$

In particular, for $t_{\frac{N_x+1}{2}} = T_E$, the phase is:

$$\phi(x, T_E) - \phi_0 = \frac{\gamma G_r \tau_r^2}{4} v_x \qquad (3.16)$$

As expected, the phase does not cancel out at T_E when the isochromats are moving. This additional phase shift leads to blurring and signal loss [91]. Note also that the first term in Eq. (3.15) shows a shift in position ; the spin is spatially encoded at the position $x_0 + v_x(T_E - t_0)$, instead of x_0, which matches the position of the spin at the echo.
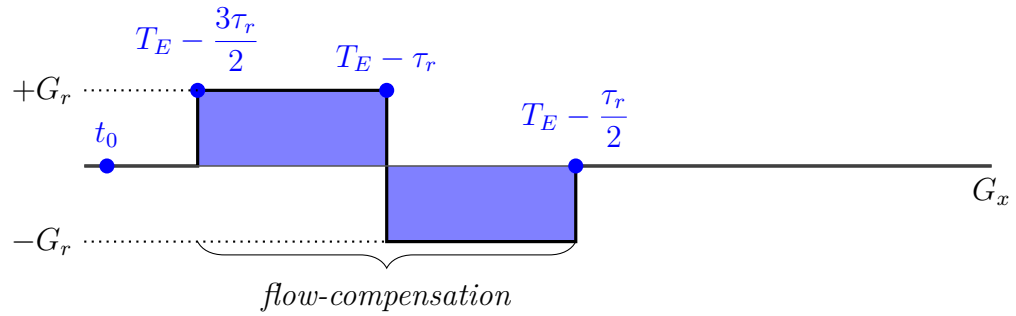
(a) Partial chronogram with flow-compensating gradient
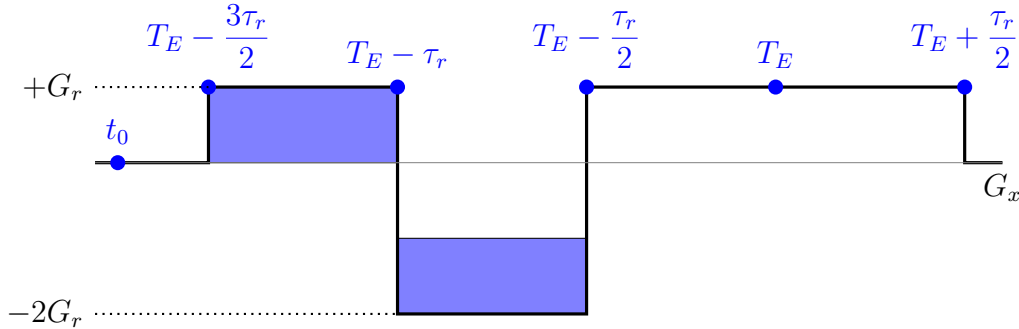
(b) Full chronogram for flow-compensated frequency-encoding.

Figure 3.2: Sequence with flow-compensation in the readout direction. 3.2b corresponds to the superposition of the partial sequences in Fig. 3.1 and Fig. 3.2a.

Let us now investigate how adding a velocity-compensating gradient allows to achieve a phase back to zero at echo time, as it would have been the case with static isochromats. The pulse sequence is presented in Fig. 3.2. By construction, this bipolar gradient starts at $T_E - \frac{3\tau_r}{2}$ and ends when the readout starts at $T_E - \frac{\tau_r}{2}$.

The phase is evaluated at the time instants, when the gradient changes:

$$\phi(x, T_E - \frac{3\tau_r}{2}) - \phi_0 = 0$$

$$\phi(x, T_E - \tau_r) - \phi_0 = \gamma x_0 \int_{T_E - \frac{3\tau_r}{2}}^{T_E - \tau_r} G_r dt + \gamma v_x \int_{T_E - \frac{3\tau_r}{2}}^{T_E - \tau_r} G_r(t - t_0) dt$$

$$= \frac{\gamma G_r \tau_r}{2} \left(x_0 + v_x \left((T_E - t_0) - \frac{5}{4}\tau_r \right) \right)$$

$$\phi(x, T_E - \frac{\tau_r}{2}) - \phi_0 = \gamma x_0 \int_{T_E - \tau_r}^{T_E - \frac{\tau_r}{2}} (-2G_r) dt + \gamma v_x \int_{T_E - \tau_r}^{T_E - \frac{\tau_r}{2}} (-2G_r)(t - t_0) dt$$

$$+ \frac{\gamma G_r \tau_r}{2} \left(x_0 + v_x \left((T_E - t_0) - \frac{5}{4}\tau_r \right) \right)$$

$$= -\frac{\gamma G_r \tau_r}{2} \left(x_0 + v_x \left((T_E - t_0) - \frac{\tau_r}{4} \right) \right)$$

$$\phi(x, t_p) - \phi_0 = \gamma x_0 G_r \int_{T_E - \frac{\tau_r}{2}}^{T_E + \frac{\tau_r}{2}\left(\frac{2p-1}{N_x} - 1 \right)} dt + \gamma v_x G_r \int_{T_E - \frac{\tau_r}{2}}^{T_E + \frac{\tau_r}{2}\left(\frac{2p-1}{N_x} - 1 \right)} (t - t_0) \ dt$$

$$- \frac{\gamma G_r \tau_r}{2} \left(x_0 + v_x \left((T_E - t_0) - \frac{\tau_r}{4} \right) \right)$$

$$= \frac{\gamma G_r \tau_r}{2} \left(\frac{2p-1}{N_x} - 1 \right) (x_0 + v_x(T_E - t_0)) + \frac{\gamma G_r \tau_r^2}{8} \left(\frac{2p-1}{N_x} - 1 \right)^2 v_x$$

$$= 2\pi k_x(t_p) (x_0 + v_x(T_E - t_0)) + 2\pi \frac{\pi}{\gamma G_r} k_x^2(t_p) v_x$$

$$\tag{3.17}$$

At $t_{\frac{N_x+1}{2}} = T_E$, by definition $k_x(T_E) = 0$ and the phase equals zero as well thanks to the flow-compensation. Haacke et al. [91] underline that more than being equal to zero, this means that the phase at the echo is constant and does not depend on the velocity v_x. Furthermore, they state that for most physiological velocities, the effect of the non-linear velocity-dependent last term in Eq. (3.17) can be neglected.

(a) Partial chronogram with velocity-encoding gradient.

(b) Full chronogram for flow-compensated velocity-encoding along (x).
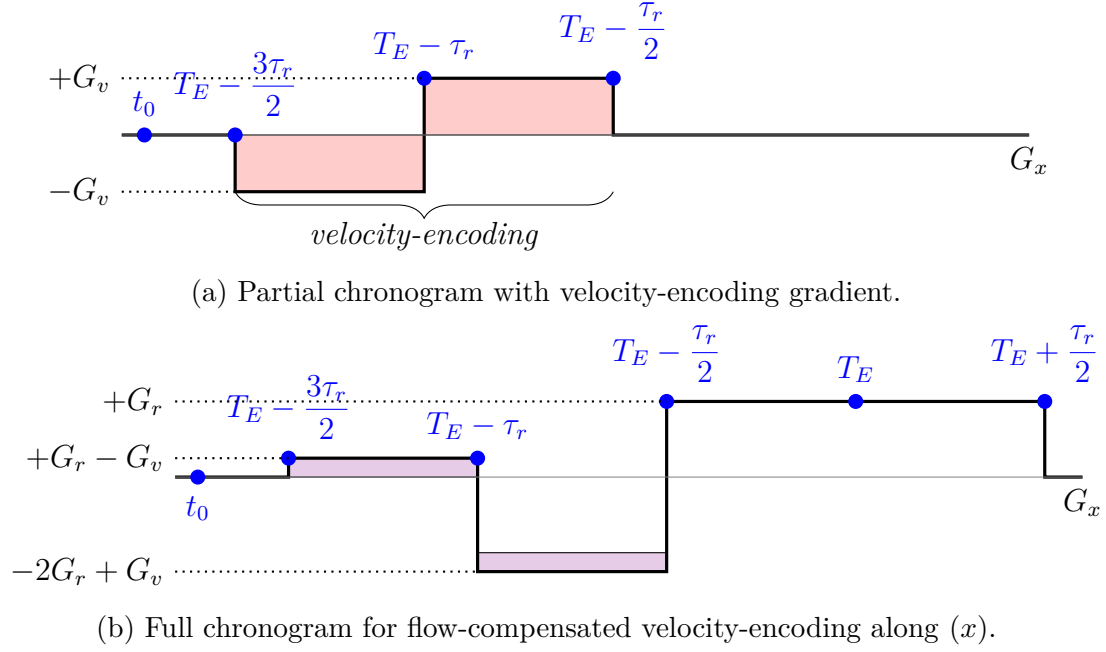
Figure 3.3: Sequence with a velocity-encoding gradient in the readout direction. 3.3b corresponds to the superposition of the gradients in Fig. 3.2b and Fig. 3.3a

.

Let us now add a bipolar gradient in the sequence in order to encode the velocity along x. The sequence is illustrated in Fig. 3.3.

The phase evolves during the sequence as:

$$\phi(x, T_E - \frac{3\tau_r}{2}) - \phi_0 = 0$$

$$\phi(x, T_E - \tau_r) - \phi_0 = \gamma x_0 \int_{T_E - \frac{3\tau_r}{2}}^{T_E - \tau_r} (G_r - G_v)dt + \gamma v_x \int_{T_E - \frac{3\tau_r}{2}}^{T_E - \tau_r} (G_r - G_v)(t - t_0)dt$$

$$= \frac{\gamma(G_r - G_v)\tau_r}{2}\left(x_0 + v_x\left((T_E - t_0) - \frac{5}{4}\tau_r\right)\right)$$

$$\phi(x, T_E - \frac{\tau_r}{2}) - \phi_0 = \gamma x_0 \int_{T_E - \tau_r}^{T_E - \frac{\tau_r}{2}} (-2G_r + G_v)dt$$

$$+ \gamma v_x \int_{T_E - \tau_r}^{T_E - \frac{\tau_r}{2}} (-2G_r + G_v)(t - t_0)dt$$

$$+ \frac{\gamma(G_r - G_v)\tau_r}{2}\left(x_0 + v_x\left((T_E - t_0) - \frac{5}{4}\tau_r\right)\right)$$

$$= -\frac{\gamma G_r \tau_r}{2}\left(x_0 + v_x(T_E - t_0)\right) + \frac{\gamma(G_r + 2G_v)}{2}\left(\frac{\tau_r}{2}\right)^2 v_x t$$

78

$$\phi(x, t_p) - \phi_0 = \gamma x_0 G_r \int_{T_E - \frac{\tau_r}{2}}^{T_E + \frac{\tau_r}{2}\left(\frac{2p-1}{n_x} - 1\right)} d\tau + \gamma v_x G_r \int_{T_E - \frac{\tau_r}{2}}^{T_E + \frac{\tau_r}{2}\left(\frac{2p-1}{n_x} - 1\right)} (t - t_0) \ dt$$

$$- \frac{\gamma G_r \tau_r}{2} \left(x_0 + v_x(T_E - t_0)\right) + \frac{\gamma(G_r + 2G_v)}{2} \left(\frac{\tau_r}{2}\right)^2 v_x$$

$$= 2\pi k_x(t_p) \left(x_0 + v_x(T_E - t_0)\right) + 2\pi \frac{\pi}{\gamma G_r} k_x^2(t_p) v_x + \gamma G_v \left(\frac{\tau_r}{2}\right)^2 v_x$$

$$= 2\pi k_x(t_p) \left(x_0 + v_x(T_E - t_0)\right) + 2\pi \frac{\pi}{\gamma G_r} k_x^2(t_p) v_x + \frac{\pi}{V_{ENC}} v_x$$

$$(3.18)$$

At T_E, $\mathcal{M}_1 \neq 0$, since $\phi(x, T_E) - \phi_0 = \dfrac{\pi}{V_{ENC}} v_x$.

Let us denote ϕ_x the phase obtained in Eq. (3.18) and ϕ_{ref} the phase obtained in Eq. (3.17). At each position x for each readout instant t_p, the phase difference is given by:

$$\phi_x(x, t_p) - \phi_{ref}(x, t_p) = \frac{\pi}{V_{ENC}} v_x \qquad (3.19)$$

The phase difference allows to reconstruct the velocity along the x-direction, providing that $|v_x| \leq V_{ENC}$. It leads otherwise to phase wrapping. One has to keep in mind that this "perfect" velocity reconstruction is made under the assumption that the velocity is constant over time during encoding (i.e. there is no acceleration), and even from one sequence to the other.

To image a two-dimensional image, a phase-encoding gradient is necessary to encode the second dimension. Let us investigate the theoretical example of a sequence only composed of a phase-encoding gradient, presented in Fig. 3.4. Indeed, to encode a 1D image, the usual process is to encode the signal in frequency only. As it will be shown by studying the phase evolution during the sequence, the signal does not depend on T_E and the time instant when the signal has to be collected is completely arbitrary as long as it occurs after the phase-encoding gradient. The spatial frequency k_y collected at T_E (or any time greater than $t_{y,f}$, the end of the phase-encoding gradient) for the ith T_R is given by:

$$k_y(T_E) = \frac{\gamma}{2\pi} \int_{t_0}^{t_E} G_y(t) dt = \frac{\gamma}{2\pi} G_y(T_{R,i}) \tau_y \qquad (3.20)$$
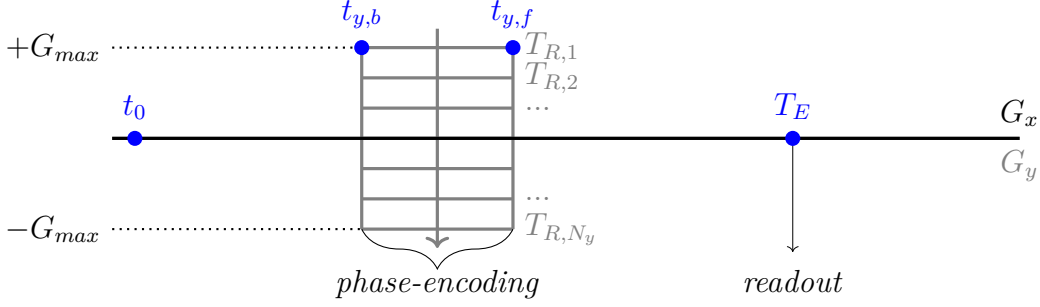
Figure 3.4: Sequence with a phase-encoding gradient. $t_{y,b}$ and $t_{y,f} = t_{y,b} + \tau_y$ are the start and end time of the phase-encoding gradient, respectively. This sequence has to be repeated N_y times, with the gradient strength decreasing from $+G_{max}$ to $-G_{max}$. The readout gradient is reduced to only one time instant, where the only sampled frequency is $k_x = 0$ (and thereby $G_x = 0$).

The phase for each repetition time $T_{R,i}$ is given by:

$$\phi(y, t_{y,b}) - \phi_0 = 0$$

$$
\begin{aligned}
\phi(y, t_{y,f}) - \phi_0 &= \gamma y_0 \int_{t_{y,b}}^{t_{y,f}} G_y(T_{R,i}) dt + \gamma v_y \int_{t_{y,b}}^{t_{y,f}} G_y(T_{R,i})(t - t_0) dt \\
&= \gamma G_y(T_{R,i})(t_{y,f} - t_{y,b}) \left(y_0 + v_y \left(\frac{t_{y,b} + t_{y,f}}{2} - t_0 \right) \right) \quad (3.21) \\
&= 2\pi k_y(T_{R,i}) \left(y_0 + v_y \left(\frac{t_{y,b} + t_{y,f}}{2} - t_0 \right) \right)
\end{aligned}
$$

One can remark some similarities with the frequency-encoded sequence with a flow-compensating gradient. Instead of encoding the phase at the position y_0, it is encoded at the shifted position where the isochromats are located in the middle of the phase-encoding gradient $y_0 + v_y \left(\frac{t_{y,b} + t_{y,f}}{2} - t_0 \right)$. Recall that in the former example, the isochromats were encoded in the middle of the readout gradient, i.e. at the echo time T_E. In contrary to this latter example, there is no additional contribution of v_y which would correspond to noise in the phase-encoding direction. However, one can note that frequency- and phase-encoding lead to a difference in the position where the isochromats are encoded. Since the phase-encoding gradient has to be over before the readout gradient starts, the two spatial direction can never be encoded simultaneously. This delay leads to the well-known flow misregistration artifact, already mentioned in Sec. 2.8.1. Furthermore, while the spatial and velocity encoding can be synchronized along the phase-encoding direction, this is not the case for the readout direction.

3.1.4 Demonstrator examples

Some examples coming from the MR demonstrator are presented in this section to illustrate the concepts introduced in the previous chapter. The demonstrator has been restricted to gradient echo sequences.

Sequence building

An example of how a sequence is built by adding the gradients one after the other is provided in Fig. 3.5. All the available gradients are presented in this sequence. The pre-phasing and readout gradients are first added into the chronogram (a), as they are the basis of a 1D GRE sequence. The pulse sequence is then flow-compensated along the same direction (b). A bipolar velocity-encoding gradient can be added, e.g. along the z (c). In order to extend the FOV to a 2D image, a phase-encoding gradient is needed along the y direction (d). Note that the order to add the gradients does not matter.
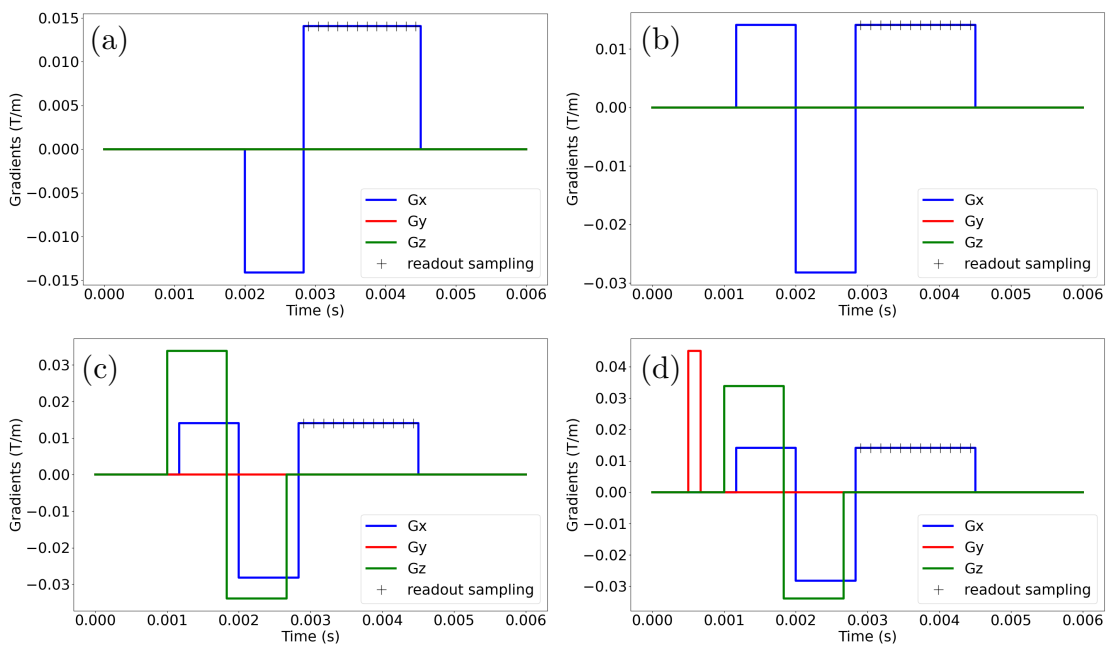
Figure 3.5: Illustration of a sequence building. (a) Pre-phasing and readout gradients. (b) Adding the flow-compensation gradient along the readout direction. (c) Adding a bipolar velocity-encoding gradient along z. (d) Adding a phase-encoding gradient along y (only the first encoding step for $k_{y,max}$ is displayed).

Signal and moments

Following the example in the last paragraph, a flow-compensated 1D gradient sequence including a bipolar gradient along the z direction is built. The resulting chronogram is presented in Fig. 3.6. Since this is a 1D sequence, only the $k_y = 0$ frequency is phase-encoded, and the gradient along y is zero during the whole sequence.
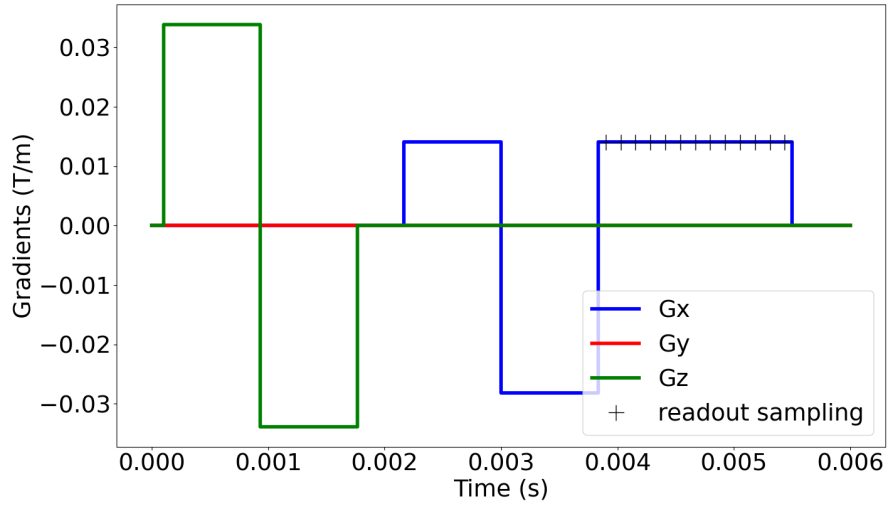
Figure 3.6: Flow-compensated 1D gradient sequence with a bipolar gradient.

The gradient moments of order 0 and 1 (cf. Section 2.7) produced by this sequence are displayed in Fig. 3.7. In this example, there are 3 orders of magnitude of difference between $\mathcal{M}_0$ and $\mathcal{M}_1$. As expected, both moments along x cancel out in the middle of the readout thanks to the flow-compensation. Should there be no flow-compensation, $M_{1,x}$ cancels at a different time instant as illustrated in Fig. 3.8.
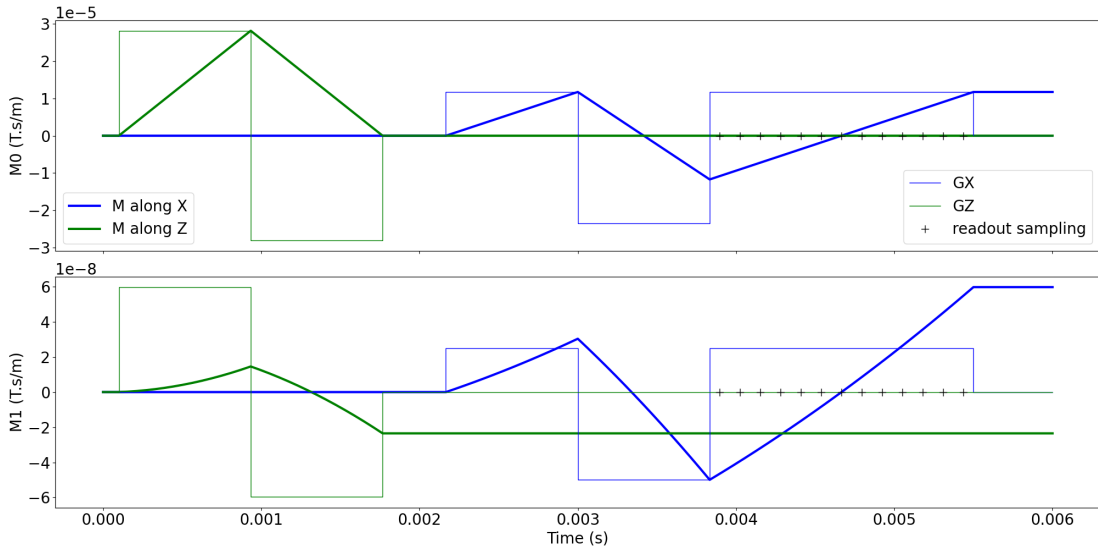
Figure 3.7: Zeroth (upper graph) and first (lower graph) moments associated to the sequence in Fig. 3.6. The sequence is plotted with the same color coding in thin lines for reference (arbitrary units).
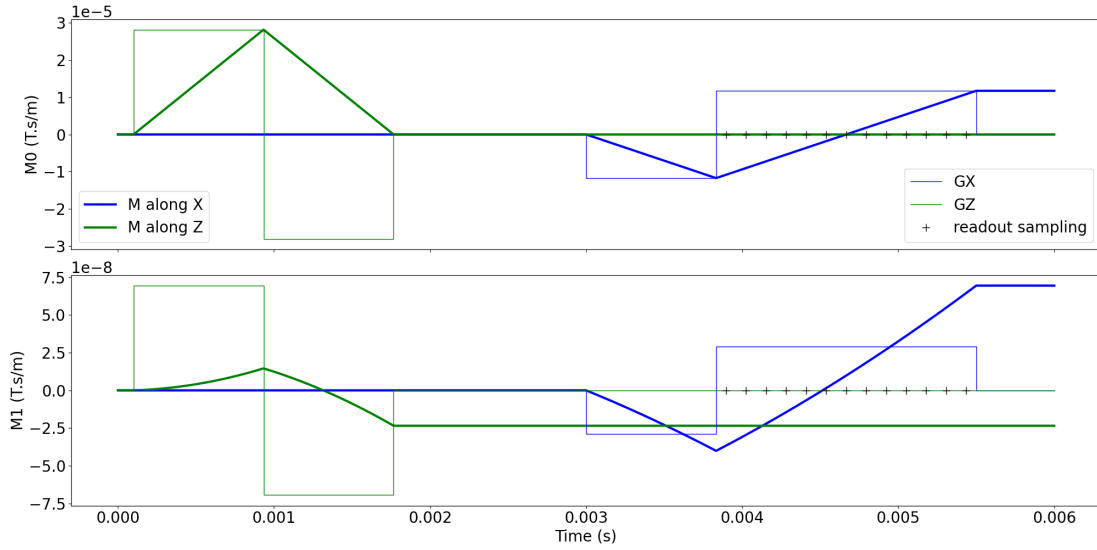
Figure 3.8: Zeroth (upper graph) and first (lower graph) moments without flow-compensation.

Finally, the demonstrator allows to plot the evolution of the signal during the sequence using Eq. (3.11), where the volume integral is replaced by a summation on the isochromats. The signal obtained for 13 isochromats only located by their x-coordinate (unidimensional FOV) is displayed in Fig. 3.9. In (a), the isochromats are static while in (b) they move with a constant velocity along z. Their phase can be expressed in this 1D example as:

$$
\begin{aligned}
\phi(x(t), t) - \phi_0 = & \gamma x_0 \int_{t_0}^{t} G_x(t') dt' \\
& + \gamma \int_{t_0}^{t} \left(v_x G_x(t') + v_y G_y(t') + v_z G_z(t') \right) (t' - t_0) dt'
\end{aligned}
\tag{3.22}
$$

Note that the gradient G_y and G_z do not appear in the first term, as the voxels are only localized along x in this specific case ($y_0 = z_0 = 0$). Yet, each "1D voxel" is associated with an initial velocity vector $\boldsymbol{v}(t_0) = [v_x, v_y, v_z]$. $\boldsymbol{v}(t_0) = [0, 0, 0]$ in (a), while $\boldsymbol{v}(t_0) = [0, 0, v_z]$ in (b). Thereby according to Eq. (3.11) and (3.22), only the T_2-relaxation acts on the signal during the bipolar gradient in (a), as there is no spatial dependency along z. However, the non-zero v_z in (b) induces an additional dephasing during the bipolar gradient, which is also noticeable in the readout.
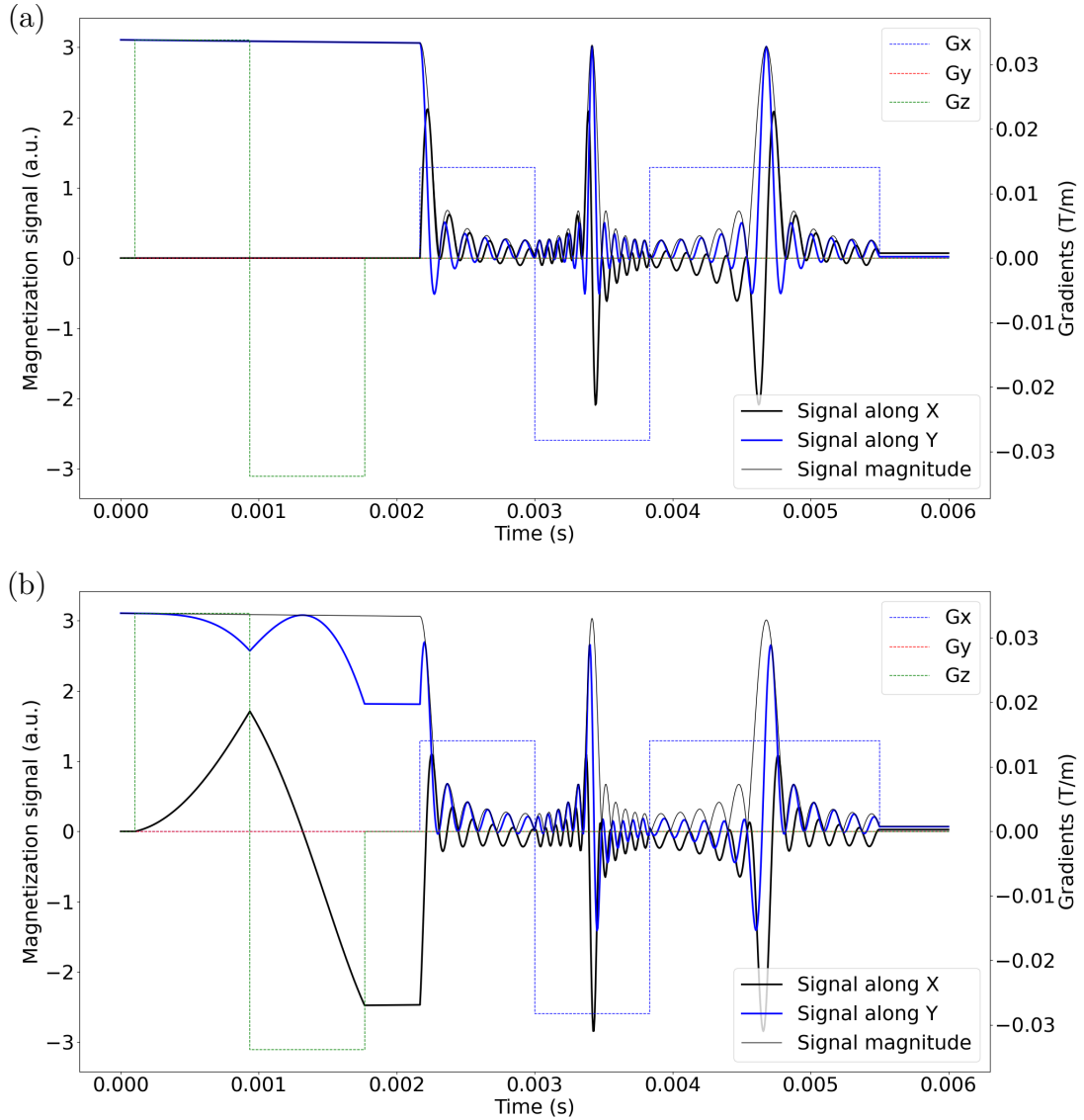
Figure 3.9: Signal evolution for $T_2 = 0.15$ s throughout the sequence (a) for static isochromats and (b) for isochromats moving with a constant velocity along z.

Magnitude reconstruction in 1D

The k-space is computed for a flow-compensated 1D GRE pulse sequence. The magnitude image along x is reconstructed by taking the magnitude of the inverse FFT of the k-space. The resulting images are presented in Fig. 3.10 for $T_2 = 0.15$ s and $T_2 \to \infty$, where the latest corresponds to neglecting the relaxation. When the relaxation is omitted, the proton density is perfectly reconstructed, while a lower density is reconstructed when taking the relaxation into account. Yet, the morphology is well-captured.
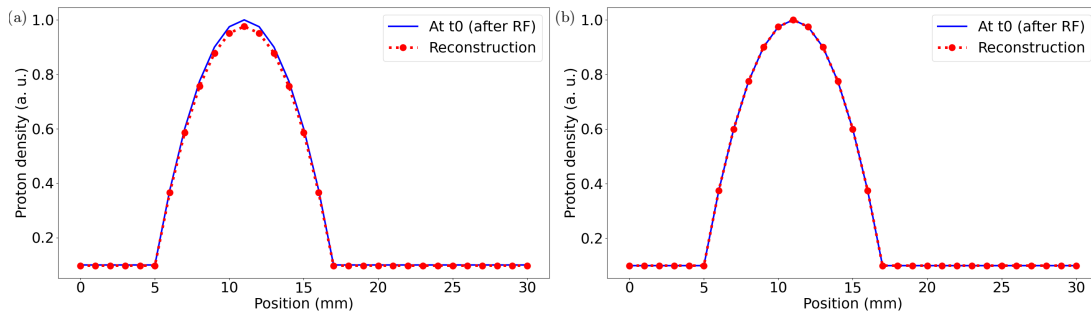
Figure 3.10: Magnitude reconstruction (a) for $T_2 = 0.15$ s and (b) for $T_2 \to \infty$.

Associating a velocity v_x to the isochromats allows to illustrate the misregistration artifact (cf. Section 2.8.1). The aliasing artifact coming from an undersampled k-space, as represented in Section 2.9.2 on parallel imaging (cf. Fig. 2.23), can also be illustrated on this example. If only a frequency out of 3 ($R = 3$) is collected, three repetitions of the object to be imaged are reconstructed, yet with a lower amplitude. Both artifacts are displayed in Fig. 3.11. Note the additional ringing artifact observed in (a).
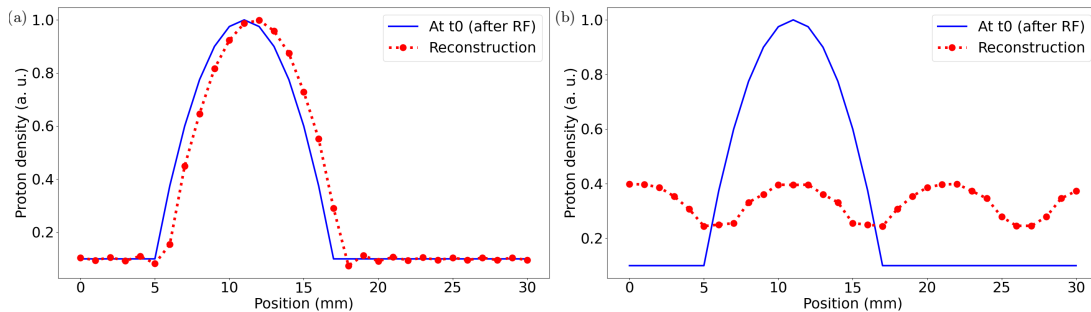
Figure 3.11: Artifacts in magnitude reconstruction. (a) Misregistration artifact (and Gibbs' ringing) (b) Aliasing due to k-space undersampling.

Magnitude and velocity reconstruction in 2D

A second dimension can be added in the demonstrator thanks to the phase-encoding gradient. Two sequences are simulated and displayed in Fig. 3.12: a 2D GRE reference sequence with flow-compensation and the same sequence with an additional bipolar gradient to encode the through-plane velocity v_z.
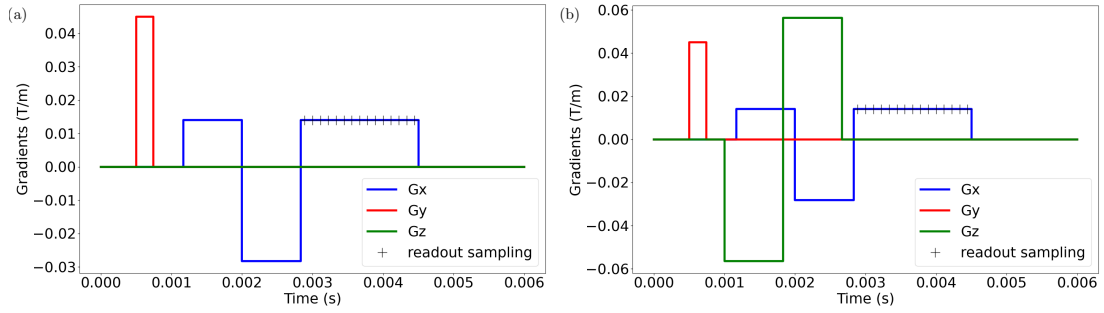
Figure 3.12: (a) Reference sequence. (b) Sequence with velocity-encoding in the z-direction. Note that the y-axis is scaled by the greatest gradient present in the sequence. That is why the scale differs between the two images.

Their simulations lead to two complex k-spaces. As mentioned earlier, the magnitude of the inverse FFT allow to reconstruct a magnitude image for each sequence, as illustrated in Fig. 3.13 for the reference sequence. While for $T_2 \to \infty$ the input proton density is perfectly reconstructed, this figure corresponds to the case $T_2 = 0.15$ s. An attenuation on the reconstructed magnitude image is noticeable due to the T_2-relaxation. To reconstruct the velocity, the phase of the inverse FFT of both k-space is required according to Eq. (2.95). The expected and reconstructed velocity field in the z direction are presented in Fig. 3.14. The velocity field is accurately reconstructed, since both phase images are impacted by the T_2-relaxation in the same manner.
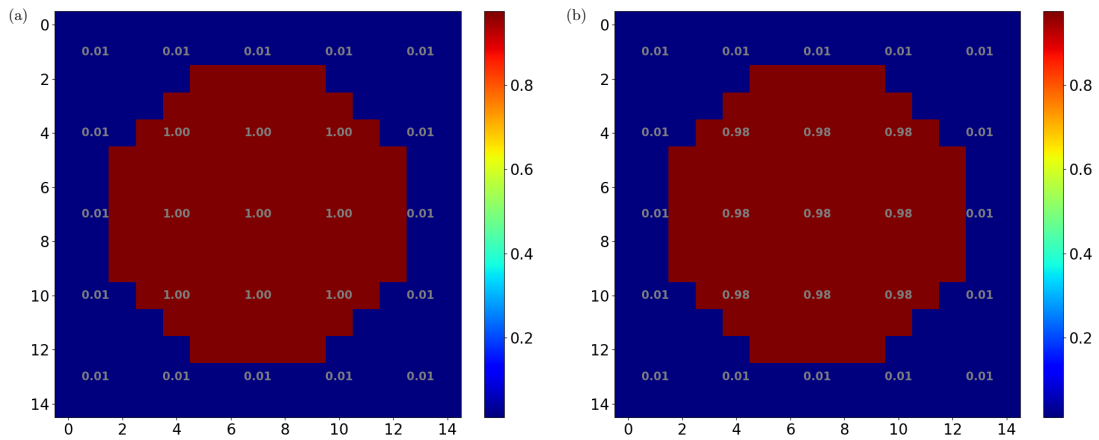
Figure 3.13: (a) Input proton density (a.u.). (b) Reconstructed magnitude image (a.u.). The values in some pixels are specified in gray for reference.
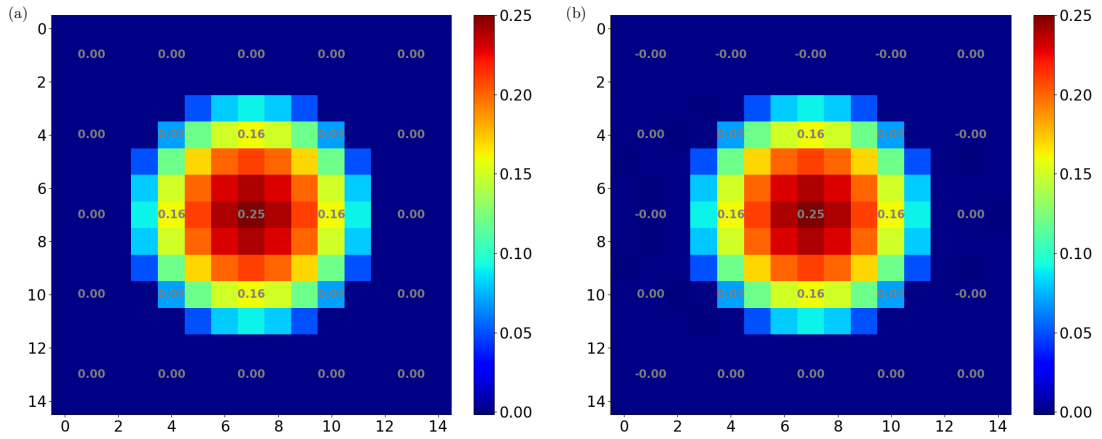
Figure 3.14: (a) Input velocity field v_z (m/s). (b) Reconstructed velocity field v_z (m/s). The values in some pixels are specified in gray for reference.

As in the previous example, adding a velocity field in the x-direction induces misregistration. The phenomenon produced by adding a constant velocity field v_x is illustrated in Fig. 3.15 for both the reconstructed magnitude image and velocity. Note that this test case is really unlikely, as the velocity is prescribed along the object plane. For impermeable walls, this plane velocity is necessarily very low.
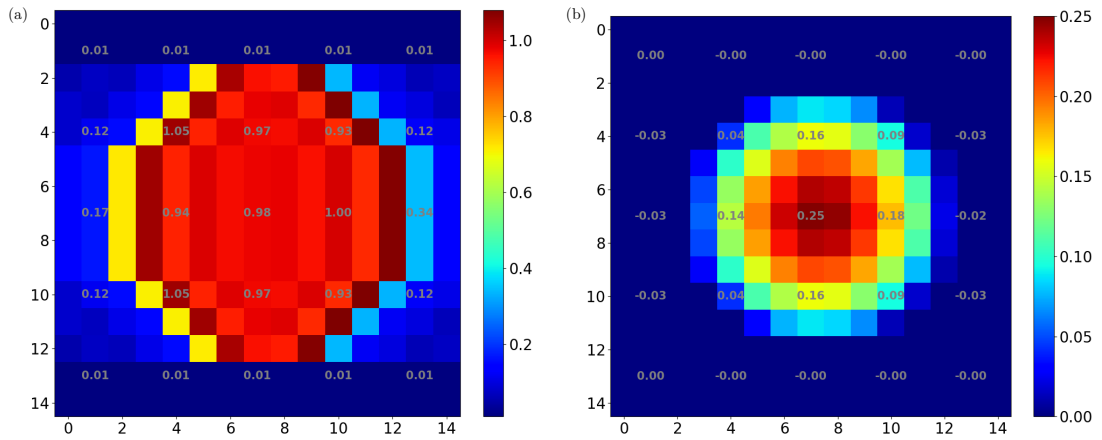
Figure 3.15: (a) Misregistered reconstructed magnitude image (a.u.). (b) Misregistered reconstructed velocity field v_z (m/s). The values in some pixels are specified in gray for reference.

3.2 Complex hemodynamics simulations: the YALES2BIO solver

3.2.1 Incompressible Navier-Stokes equations

Blood is a suspension composed of cells and proteins in a liquid plasma, presents a non-Newtonian behavior with complex rheological properties. However, its

behavior in the context of large vessels experiencing high shear rates can be well modelled as an incompressible Newtonian fluid [140]. The well-known Navier-Stokes equations (NSE) describe the motion of an incompressible Newtonian fluid as:

$$
\begin{cases}
\dfrac{\partial \boldsymbol{u}}{\partial t} + \nabla \cdot (\boldsymbol{u} \otimes \boldsymbol{u}) = -\dfrac{\nabla p}{\rho} + \nu \nabla \cdot (\nabla \boldsymbol{u}) + \dfrac{\boldsymbol{f}}{\rho} \\
\nabla \cdot \boldsymbol{u} = 0
\end{cases}
\tag{3.23}
$$

where $\boldsymbol{u}$ is the velocity vector, p the pressure, ρ the fluid density, ν the kinematic viscosity and $\boldsymbol{f}$ a possible volumetric force. The first equation expresses the conservation of momentum of the system, and the second the mass conservation. No analytical solution of the NSE has been found yet. The YALES2BIO code provides a numerical method to approximate the solution. It uses a finite-volume fourth-order scheme, adapted to unstructured meshes, that will be introduced in the next sections.

3.2.2   Finite-volume spatial discretization

In order to numerically solve the NSE, the fluid domain of interest has to be divided in smaller mesh elements. A finite-volume method is used in YALES2BIO, where the spatial discretization procedure is based on the integration of the equations on small polyhedral control volumes (CVs). This approach is common in the field of computational fluid dynamics, as the integral formulation of the discretized surface forces conserves the momentum. The node-centered CV, of nodal volume V_i, utilized in the code are illustrated in 2D in Fig. 3.16. The set of CVs is referred to as the dual mesh.
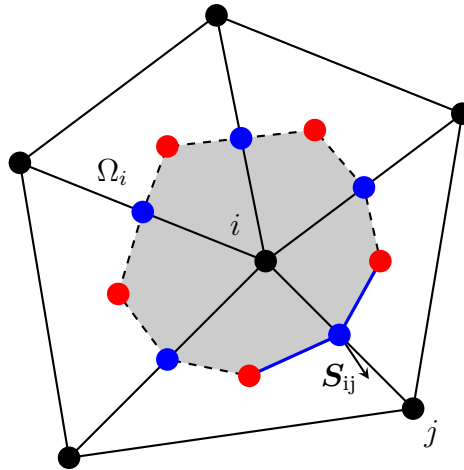
Figure 3.16: Control volume Ω_i around the node i of an unstructured triangular mesh. The CV is built by linking the centroids of adjacent mesh elements (red dots) and the midpoints of the edges containing the node i (blue dot). The surface patch S_{ij} to the node pair (i, j) is highlighted in blue, and $\boldsymbol{S}_{ij} = S_{ij}\boldsymbol{n}_{ij}$ is its associated non-normalized pair face normal.

Integrating the momentum equation given in Eq. (3.23) over the control volume Ω_i presented in Fig. 3.16 leads to:

$$\int_{\Omega_i} \frac{\partial \boldsymbol{u}}{\partial t} dV = \int_{\Omega_i} \nabla \cdot \left(-\boldsymbol{u} \otimes \boldsymbol{u} - \frac{p}{\rho} \mathbb{I} + \nu \nabla \boldsymbol{u} \right) dV + \int_{\Omega_i} \frac{\boldsymbol{f}}{\rho} dV \qquad (3.24)$$

The first volume integral in the right-hand side of the equation can be expressed as a surface integral thanks to Ostrogradsky's theorem:

$$\int_{\Omega_i} \frac{\partial \boldsymbol{u}}{\partial t} dV = \oint_{\partial \Omega_i} \left(-\boldsymbol{u} \otimes \boldsymbol{u} - \frac{p}{\rho} \mathbb{I} + \nu \nabla \boldsymbol{u} \right) \cdot d\boldsymbol{S} + \int_{\Omega_i} \frac{\boldsymbol{f}}{\rho} dV \qquad (3.25)$$

where $\partial \Omega_i$ denotes the boundary of the control volume Ω_i. As illustrated in Fig. 3.16, to each pair of nodes (i, j) is associated a part of the CV surface. The face associated to the node pair (i, j) is denoted S_{ij}, of normal vector $\boldsymbol{S}_{\text{ij}} = S_{ij} \boldsymbol{n}_{\text{ij}}$. Note that here the use of ij does not refer to an implicit summation, but to the node pair (i, j). Thereby, the control volume is bounded by N_{fi} faces of surface S_{ij} and the close surface integral can be rewritten as the sum of the integrals on each face:

$$\int_{\Omega_i} \left(\frac{\partial \boldsymbol{u}}{\partial t} - \frac{\boldsymbol{f}}{\rho} \right) dV = \sum_{j=1}^{N_{fi}} \int_{S_{ij}} \left(-\boldsymbol{u} \otimes \boldsymbol{u} - \frac{p}{\rho} \mathbb{I} + \nu \nabla \boldsymbol{u} \right) \cdot d\boldsymbol{S} \qquad (3.26)$$

From the last equation, it appears that there is a need to express the integral of the unsteady terms and body force over the control volume. This is equivalent to finding the average of these quantities over the control volume, since the average of an arbitrary function ϕ over the CV Ω_i is defined as:

$$\bar{\phi}_{\Omega_i} = \frac{1}{V_i} \int_{\Omega_i} \phi dV \qquad (3.27)$$

Using Einstein notation, the second-order Taylor expansion about the CV node i of coordinates x_i is given by:

$$\phi = \phi|_i + (x^k - x_i^k) \frac{\partial \phi}{\partial x^k}\bigg|_i + \frac{1}{2}(x^k - x_i^k)(x^l - x_i^l) \frac{\partial^2 \phi}{\partial x^k \partial x^l}\bigg|_i + \mathcal{O}\left(\Delta x^3\right) \qquad (3.28)$$

where Δx refers to the length scale representative for the size of the CV. The volume integral of ϕ can be rewritten according to this expansion in Taylor series:

$$\begin{aligned}
\int_{\Omega_i} \phi dV = & \int_{\Omega_i} \phi|_i dV \\
& + \int_{\Omega_i} (x^k - x_i^k) \frac{\partial \phi}{\partial x^k}\bigg|_i dV \\
& + \int_{\Omega_i} \frac{1}{2}(x^k - x_i^k)(x^l - x_i^l) \frac{\partial^2 \phi}{\partial x^k \partial x^l}\bigg|_i dV \\
& + \int_{\Omega_i} \mathcal{O}\left(\Delta x^3\right) dV
\end{aligned} \qquad (3.29)$$

In the same manner, the surface integral in the right-hand side of Eq. (3.26) has to be discretized. The average of the variable ϕ over the pair face S_{ij} is given by:

$$\bar{\phi}_{S_{ij}} = \frac{1}{\boldsymbol{S}_{\text{ij}}} \int_{S_{ij}} \phi d\boldsymbol{S} \tag{3.30}$$

The pair face S_{ij} depends on the contributions of both CV nodes i and j. In the following, $\phi|_{ij}$ represents the value of ϕ at the midpoint of the edge connecting the nodes i and j and of coordinates $\boldsymbol{x}_{ij}$ such that

$$\phi|_{ij} = \frac{\phi|_i + \phi|_j}{2} \tag{3.31}$$

where $\phi|_i$ and $\phi|_j$ represents respectively the contribution of i and j.

The second-order spatial discretization, thoroughly described in the PhD thesis of Vantieghem [141], is first presented. The average of ϕ over the CV is approximated by its nodal value:

$$\int_{\Omega_i} \phi dV \approx \phi|_i V_i \tag{3.32}$$

This first-order accurate expression becomes second-order accurate if the center of mass of the CV, that is $\boldsymbol{x}_{\bar{i}} = \bar{\boldsymbol{x}}_{\Omega_i} = \frac{1}{V_i} \int_{\Omega_i} \bar{\boldsymbol{x}} dV$, is located at the node position i. This is true on locally orthogonal meshes.

The gradient, divergence and Laplacian operator can be discretized using the same method. The gradient of a function ϕ is approximated as:

$$\int_{\Omega_i} \nabla \phi dV \approx \nabla \phi|_i V_i \tag{3.33}$$

Moreover, the Ostrogradsky's theorem allows to rewrite the volume integral as a surface integral:

$$\int_{\Omega_i} \nabla \phi dV = \oint_{\partial \Omega_i} \phi d\boldsymbol{S} = \sum_{j=1}^{N_{fi}} \int_{S_{ij}} \phi d\boldsymbol{S} \approx \sum_{j=1}^{N_{fi}} \phi|_{ij} \boldsymbol{S}_{\text{ij}} \tag{3.34}$$

Expressing the value ϕ at the midpoint of the edge between the nodes i and j using Taylor series gives

$$\int_{\Omega_i} \nabla \phi dV \approx \sum_{j=1}^{N_{fi}} \frac{\phi|_i + \phi|_j}{2} \boldsymbol{S}_{\text{ij}} \tag{3.35}$$

This approximation is second-order accurate by construction of the CV, as demonstrated in [141]. Thereby, the discretization stencil for the gradient operator $\mathcal{G}$ is given by:

$$\mathcal{G}(\phi)|_i = \frac{1}{V_i} \sum_{j=1}^{N_{fi}} \frac{\phi|_i + \phi|_j}{2} \boldsymbol{S}_{\text{ij}} \tag{3.36}$$

The same approach is used to define the stencil for the discrete divergence of a vector $\boldsymbol{u}$:

$$\mathcal{D}(\boldsymbol{u})|_i = \frac{1}{V_i} \sum_{j=1}^{N_{fi}} \frac{\boldsymbol{u}|_i + \boldsymbol{u}|_j}{2} \cdot \boldsymbol{S}_{ij} \tag{3.37}$$

The same process is also used for the Laplacian operator. Indeed, the most direct way to compute the Laplacian would be to apply the gradient operator followed by the divergence operator. However, this would lead to a non-compact stencil, source of non-physical behavior when solving a Poisson equation. Similarly to Eq. (3.34), the volume integral can be rewritten as:

$$\int_{\Omega_i} \nabla \cdot \nabla \phi \, dV = \oint_{\partial \Omega_i} \nabla \phi \cdot d\boldsymbol{S} \approx \sum_{j=1}^{N_{fi}} (\nabla \phi)|_{ij} \cdot \boldsymbol{S}_{ij} \tag{3.38}$$

If $\boldsymbol{S}_{ij}$ is parallel to the edge connecting the nodes i and j, as would be the case for an orthogonal mesh, a second-order accurate estimate of the scalar product is found to be:

$$(\nabla \phi)|_{ij} \cdot \boldsymbol{S}_{ij} = \frac{\phi|_j - \phi|_i}{||\boldsymbol{x}_j - \boldsymbol{x}_i||} ||\boldsymbol{S}_{ij}|| + \mathcal{O}\left(\Delta x^2\right) \tag{3.39}$$

and the Laplacian operator becomes:

$$\mathcal{L}(\phi)|_i = \sum_{j=1}^{N_{fi}} \frac{\phi|_j - \phi|_i}{||\boldsymbol{x}_j - \boldsymbol{x}_i||} ||\boldsymbol{S}_{ij}|| \tag{3.40}$$

On unstructured meshes, the assumption that a CV face normal is parallel to the (i, j) edge is generally not true and all components of the gradient have to be approximated at the CV face. To minimize the errors associated to the Laplacian operator presented in last equation, care should be taken in using meshes with a cell skewness as low as possible. Besides, Vantieghem proposes the addition of a skewness correction term in the computation of the Laplacian [141].

A fourth-order accurate spatial discretization scheme on regular grids is also implemented in YALES2BIO, and detailed in the PhD thesis of Kraushaar [142]. The first step, called deconvolution of the finite-volume integration, consists in expressing the nodal values as a function of the volume averages calculated at the CV barycenter. The second step entails calculating the fluxes between neighboring CVs thanks to the resulting nodal values.

According to the Taylor expansion in (3.29) and with the assumption that the gradients are uniform on the cell, the average of a function ϕ over the CV can be rewritten:

$$\bar{\phi}_{\Omega_i} = \phi|_i + \overline{\delta x_i}^k \frac{\partial \phi|_i}{\partial x^k} + \frac{1}{2} \overline{\delta^2 x_i}^{kl} \frac{\partial^2 \phi|_i}{\partial x^k \partial x^l} + \mathcal{O}\left(\Delta x^3\right) \tag{3.41}$$

where

$$\overline{\delta x_i}^k = \frac{1}{V_i} \int_{\Omega_i} (x^k - x_i^k) dV \tag{3.42}$$

$$\overline{\delta^2 x_i}^{kl} = \frac{1}{V_i} \int_{\Omega_i} (x^k - x_i^k)(x^l - x_i^l) dV \tag{3.43}$$

According to Kraushaar [142], Eq. (3.41) can be inverted since it can be seen as a continuous filtered field. The nodal value $\phi|_i$ is thus given by:

$$\phi|_i = \bar{\phi}_{\Omega_i} - \overline{\delta x_i}^k \frac{\partial \bar{\phi}_{\Omega_i}}{\partial x^k} - \left(\frac{1}{2}\overline{\delta^2 x_i}^{kl} - \overline{\delta x_i}^k \overline{\delta x_i}^j\right) \frac{\partial^2 \bar{\phi}_{\Omega_i}}{\partial x^k \partial x^l} + \mathcal{O}\left(\Delta x^3\right) \qquad (3.44)$$

In particular, at the barycenter of the CV denoted $x_{\bar{i}}$, the equation reduces to:

$$\phi|_{\bar{i}} = \bar{\phi}_{\Omega_i} - \left(\frac{1}{2}\overline{\delta^2 x_{\bar{i}}}^{kl}\right) \frac{\partial^2 \bar{\phi}_{\Omega_i}}{\partial x^k \partial x^l} + \mathcal{O}\left(\Delta x^3\right) \qquad (3.45)$$

The deconvolution is then applied to compute the flux over the CV boundary $\partial\Omega$, shared between i and j nodes. The value of ϕ at the pair midpoint, as defined in Eq. (3.31), can be rewritten using the 2$^{\text{nd}}$-order Taylor expansion in Eq. (3.28). After some algebra (cf. [142] for details), $\phi|_{ij}$ reads:

$$
\begin{aligned}
\phi|_{ij} = {} & \left(\frac{\bar{\phi}_{\Omega_i} + \bar{\phi}_{\Omega_j}}{2}\right) + \frac{1}{2}\left(\overline{\delta x_i}^k + \overline{\delta x_j}^k\right) \frac{\partial}{\partial x^k}\left(\frac{\bar{\phi}_{\Omega_i} + \bar{\phi}_{\Omega_j}}{2}\right) \\
& + \frac{1}{2}\left(\frac{\delta x_{\bar{i},ij}^k \delta x_{\bar{j},ij}^l + \delta x_{\bar{i}}^k \delta x_{\bar{j}}^l}{2} - \frac{\overline{\delta^2 x_{\bar{i}}^{kl}} + \overline{\delta^2 x_{\bar{j}}^{kl}}}{2}\right) \frac{\partial^2}{\partial x^k \partial x^l}\left(\frac{\bar{\phi}_{\Omega_i} + \bar{\phi}_{\Omega_j}}{2}\right) \\
& + \mathcal{O}\left(\Delta x^3\right)
\end{aligned}
\qquad (3.46)
$$

where $\delta x_{\bar{i},ij}^k = x_{ij}^k - x_{\bar{i}}^k$.

For this higher order spatial discretization, the spatial scheme is fourth-order accurate for regular (orthogonal) grids, and reduces to third-order for quasi-homogeneous unstructured meshes [142].

3.2.3 Time advancement scheme

One issue when numerically solving the incompressible Navier-Stokes equations is the absence of state equation that drives the evolution of the pressure. Pressure and velocity are implicitly coupled due to the mass conservation equation, and pressure can be interpreted as a variable to enforce continuity. So-called fractional-step methods are used to separate the pressure gradient from the other terms in the momentum equation. The idea is to project the velocity field $\boldsymbol{u}$ onto a divergence-free field, thanks to an intermediate velocity $\boldsymbol{u}^*$. The fractional-step method implemented in YALES2BIO is based on the original algorithm developed by Chorin [143], later modified by Kim and Moin [144].

Let us first consider an Euler explicit scheme to illustrate the algorithm, where the NSE are semi-discretized in time as:

$$\frac{\boldsymbol{u}^{n+1} - \boldsymbol{u}^n}{\Delta t} = -\boldsymbol{u}^n \cdot \nabla \boldsymbol{u}^n + \nu \nabla \cdot (\nabla \boldsymbol{u}^n) - \nabla \left(\frac{p}{\rho}\right)^{n+\frac{1}{2}} + \frac{\boldsymbol{f}^n}{\rho} \qquad (3.47)$$

Note that in YALES2BIO, the velocity is expressed at time steps n and $n+1$, whereas the pressure is computed at shifted time steps $n-1/2$ and $n+1/2$. The velocity $\boldsymbol{u}^{n+1}$ can not directly be calculated, as $\left(\frac{p}{\rho}\right)^{n+\frac{1}{2}}$ is unknown.

Based on the known velocity $\boldsymbol{u}^n$, a first intermediate velocity field $\hat{\boldsymbol{u}}$ is computed, including the pressure gradient at time $n - \frac{1}{2}$:

$$\frac{\hat{\boldsymbol{u}} - \boldsymbol{u}^n}{\Delta t} = -\boldsymbol{u}^n \cdot \nabla \boldsymbol{u}^n + \nu \nabla \cdot (\nabla \boldsymbol{u}^n) - \nabla \left(\frac{p}{\rho}\right)^{n-\frac{1}{2}} + \frac{\boldsymbol{f}^n}{\rho} \qquad (3.48)$$

with the boundary condition $\hat{\boldsymbol{u}}|_{\partial\Omega} = \boldsymbol{u}^{n+1}|_{\partial\Omega}$. The pressure contribution at $n - \frac{1}{2}$ is removed from the second intermediate velocity field $\boldsymbol{u}^*$:

$$\frac{\boldsymbol{u}^* - \hat{\boldsymbol{u}}}{\Delta t} = \nabla \left(\frac{p}{\rho}\right)^{n-\frac{1}{2}} \qquad (3.49)$$

While $\hat{\boldsymbol{u}}$ is only first-order time-accurate, the following boundary conditions are second-order accurate:

$$\boldsymbol{u}^*|_{\partial\Omega} = \boldsymbol{u}^{n+1}|_{\partial\Omega} + \Delta t \nabla \left(\frac{p}{\rho}\right)^{n-\frac{1}{2}} \qquad (3.50)$$

$$\left.\frac{\partial p^{n+\frac{1}{2}}}{\partial \boldsymbol{n}}\right|_{\partial\Omega} = 0 \qquad (3.51)$$

Now that $\boldsymbol{u}^*$ has been defined, one can write that:

$$\frac{\boldsymbol{u}^{n+1} - \boldsymbol{u}^*}{\Delta t} = -\nabla \left(\frac{p}{\rho}\right)^{n+\frac{1}{2}} \qquad (3.52)$$

Applying the divergence operator on Eq. (3.52) results in :

$$\nabla \cdot \left(\frac{\boldsymbol{u}^{n+1} - \boldsymbol{u}^*}{\Delta t}\right) = -\nabla \cdot \nabla \left(\frac{p}{\rho}\right)^{n+\frac{1}{2}} \qquad (3.53)$$

This equation results in an elliptic Poisson equation on the pressure due to the incompressibility constraint $\nabla \cdot \boldsymbol{u}^{n+1} = 0$:

$$\frac{\nabla \cdot \boldsymbol{u}^*}{\Delta t} = \nabla \cdot \nabla \left(\frac{p}{\rho}\right)^{n+\frac{1}{2}} \qquad (3.54)$$

Using the Laplacian operator discretization presented in Section 3.2.2, this equation can be written as a linear system $\boldsymbol{A}\boldsymbol{p} = \boldsymbol{b}$, where $\boldsymbol{A}$ is the Laplacian operator weights and $\boldsymbol{b}$ the integral of divergence of predicted velocity $\boldsymbol{u}^*$ divided by time step. Iterative methods of the type Conjugate Gradient are well-suited to solve such linear systems. Several iterative solvers are available in YALES2BIO. A Deflated Preconditioned Conjugate Gradient (DPCG) algorithm, developed by Malandain [145], is used in the present work.

The intermediate velocity $\hat{\boldsymbol{u}}$ is advanced in time using a low-storage 4$^{\text{th}}$-order Runge-Kutta scheme (RK4). Other time schemes are implemented in YALES2BIO, such as the TFV4A scheme [142], but are not presented here. Rewriting Eq. (3.48) as a function f:

$$\frac{\hat{\boldsymbol{u}} - \boldsymbol{u}^n}{\Delta t} = f(\boldsymbol{u}^n, p^{n-\frac{1}{2}}) \tag{3.55}$$

the velocity $\hat{\boldsymbol{u}}$ is advanced with the RK4 scheme such that:

$$\begin{cases} \boldsymbol{u}^{(1)} = \boldsymbol{u}^n + \dfrac{1}{4}\Delta t \; f(\boldsymbol{u}^n, p^{n-\frac{1}{2}}) \\[2mm] \boldsymbol{u}^{(2)} = \boldsymbol{u}^n + \dfrac{1}{3}\Delta t \; f(\boldsymbol{u}^{(1)}, p^{n-\frac{1}{2}}) \\[2mm] \boldsymbol{u}^{(3)} = \boldsymbol{u}^n + \dfrac{1}{2}\Delta t \; f(\boldsymbol{u}^{(2)}, p^{n-\frac{1}{2}}) \\[2mm] \hat{\boldsymbol{u}} = \boldsymbol{u}^n + \Delta t \; f(\boldsymbol{u}^{(3)}, p^{n-\frac{1}{2}}) \end{cases} \tag{3.56}$$

3.2.4 Turbulence modelling

In fluid dynamics, the Reynolds number Re is a dimensionless quantity characteristic of the laminar-turbulent transition, which can be expressed as:

$$Re = \frac{\rho u L}{\mu} \tag{3.57}$$

where ρ is the fluid density, μ the dynamic viscosity, u the characteristic velocity and L the characteristic length. It can be interpreted as the ratio of the inertial forces to the viscous forces, thereby quantifying their relative importance for a given flow configuration.

Low Reynolds numbers correspond to laminar flow regimes, where flow streamlines remain almost parallel from one to another. At high Reynolds numbers (i.e. when inertia is much larger than viscous damping), turbulence arises. Turbulent flows experience chaotic three-dimensional changes in pressure and flow velocity and contain a large range of temporal scales and spatial structures. The typical Reynolds numbers found in the large arteries indicate that their associated flow regimes fall into the laminar-turbulent transition, and therefore turbulence has to be taken into account when simulating blood flows.
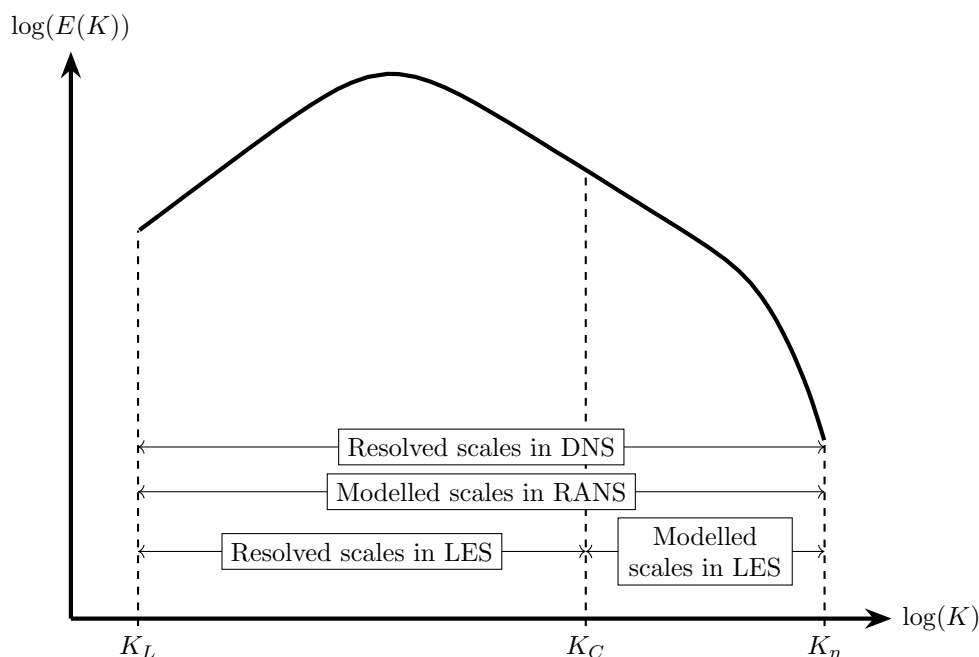
Figure 3.17: Overview of the different CFD approaches on a typical spectrum of turbulent kinetic energy E as function of the wavenumber K (proportional to the inverse of the length scales). K_C denotes the cut-off wavenumber associated to the filtering operator applied to the NSE in LES. K_L and K_η are respectively associated with the largest and with the dissipative scales.

Different numerical methods exist in order to simulate turbulent flows. The most straightforward approach is the Direct Numerical Simulation (DNS). In such simulations, the mesh should be fine enough to explicitly resolve all the spatio-temporal scales generated by turbulence. However, this approach require large computational resources. Another approach is the Reynolds-Averaged Navier-Stokes (RANS), where only the time-averaged flow field is computed and all the scales of the turbulent spectrum are modelled. Although attractive as less computationally demanding, RANS models have been reported to be poorly predictive in the case of transitional flows at moderate Reynolds numbers [70].

In the present work, a third approach is followed called the Large-Eddy Simulations (LES). In LES, the large turbulent structures (eddies) are resolved by solving spatially low-pass filtered Navier-Stokes equations, whereas the smaller scales are modelled using a subgrid-scale (SGS) model. The three CFD approaches are summarized in Fig. 3.17.

The low-pass spatial filtering process in LES corresponds to a spatial convolution product such that for a field of interest $\Phi(\boldsymbol{x}, t)$, the filtered field $\overline{\Phi}(\boldsymbol{x}, t)$ is given by:

$$\overline{\Phi}(\boldsymbol{x}, t) = \int_\Omega \Phi(\boldsymbol{y}, t) G_\Delta(\boldsymbol{y} - \boldsymbol{x}) d\boldsymbol{y} \tag{3.58}$$

where G_Δ is the filtering kernel associated to the filter size Δ, that is the cube root of the mesh cell volume, and Ω the flow domain. G_Δ satisfies a normal

distribution, so that $\int_\Omega G_\Delta(\boldsymbol{x})d\boldsymbol{x} = 1$. Now that the filter operator has been introduced, the variable Φ can be split into a resolved component $\overline{\Phi}$ involving scales larger than Δ and a modelled sub-grid fluctuating component Φ' for the scales smaller than Δ:

$$\Phi(\boldsymbol{x},t) = \overline{\Phi}(\boldsymbol{x},t) + \Phi'(\boldsymbol{x},t) \tag{3.59}$$

Under the hypothesis that filtering and differentiation commute, applying the filter operator $\overline{\cdot}$ to Eq. (3.23) leads to:

$$\begin{cases} \dfrac{\partial \overline{[\boldsymbol{u}]}}{\partial t} + \nabla \cdot \overline{[\boldsymbol{u} \otimes \boldsymbol{u}]} = -\dfrac{\nabla \overline{[p]}}{\rho} + \nu \nabla \cdot (\nabla \overline{[\boldsymbol{u}]}) + \dfrac{\boldsymbol{f}}{\rho} \\ \nabla \cdot \overline{[\boldsymbol{u}]} = 0 \end{cases} \tag{3.60}$$

which can be rewritten using Einstein notation as

$$\begin{cases} \dfrac{\partial \overline{u_i}}{\partial t} + \dfrac{\partial \overline{u_i u_j}}{\partial x_j} = -\dfrac{1}{\rho}\dfrac{\partial \overline{p}}{\partial x_i} + \nu \dfrac{\partial^2 \overline{u_i}}{\partial^2 x_j} + \dfrac{f_i}{\rho} \\ \dfrac{\partial \overline{u_i}}{\partial x_i} = 0 \end{cases} \tag{3.61}$$

One would like to split up the nonlinear filtered advection term $\overline{u_i u_j}$, as it requires the knowledge of the unknown unfiltered velocity field. Let us introduce the residual stress tensor

$$\tau^R(u_i, u_j) = \tau_{ij}^R = \overline{u_i u_j} - \overline{u_i}\,\overline{u_j} \tag{3.62}$$

which allows rewriting Eq. (3.61) as:

$$\begin{cases} \dfrac{\partial \overline{u_i}}{\partial t} + \dfrac{\partial \overline{u_i}\,\overline{u_j}}{\partial x_j} = -\dfrac{1}{\rho}\dfrac{\partial \overline{p}}{\partial x_i} + \nu \dfrac{\partial^2 \overline{u_i}}{\partial^2 x_j} - \dfrac{\partial \tau_{ij}^R}{\partial x_j} + \dfrac{f_i}{\rho} \\ \dfrac{\partial \overline{u_i}}{\partial x_i} = 0 \end{cases} \tag{3.63}$$

Germano proposes the following decomposition of the residual stresses [146]:

$$\tau_{ij}^R = \underbrace{\overline{\overline{u_i}\,\overline{u_j}} - \overline{\overline{u_i}}\,\overline{\overline{u_j}}}_{\mathcal{L}_{ij}} + \underbrace{\overline{\overline{u_i}u_j' + u_i'\overline{u_j}} - \overline{\overline{u_i}}\,\overline{u_j'} - \overline{u_i'}\,\overline{\overline{u_j}}}_{\mathcal{C}_{ij}} + \underbrace{\overline{u_i'u_j'} - \overline{u_i'}\overline{u_j'}}_{\mathcal{R}_{ij}} \tag{3.64}$$

$\mathcal{L}_{ij}$ is the Leonard stress, which represents the interactions among large scales, and can be computed from the filtered values. $\mathcal{C}_{ij}$ is the sub-grid scale cross stress representing the energy transfer between large and small structures and $\mathcal{R}_{ij}$ is the sub-grid scale Reynolds stress representing the energy dissipation of the small scales.

τ_{ij}^R describes the effect of unresolved scales, it is therefore unknown and needs the introduction of a turbulent sub-grid scale (SGS) model to close the momentum

conservation equation. The Boussinesq eddy viscosity assumption states that the dissipative effects can be modeled with an eddy viscosity ν^{SGS} such that:

$$\tau_{ij}^R = -2\nu^{SGS}\overline{S}_{ij} \tag{3.65}$$

where $\overline{S}_{ij} = \frac{1}{2}\left(\frac{\partial \overline{u_i}}{\partial x_j} + \frac{\partial \overline{u_j}}{\partial x_i}\right)$ is the rate of strain tensor of the resolved scales. Under this hypothesis, Eq. (3.63) become:

$$\begin{cases} \dfrac{\partial \overline{u_i}}{\partial t} + \dfrac{\partial \overline{u_i}\,\overline{u_j}}{\partial x_j} = -\dfrac{1}{\rho}\dfrac{\partial \overline{p}}{\partial x_i} + \left(\nu + \nu^{SGS}\right)\dfrac{\partial^2 \overline{u_i}}{\partial^2 x_j} + \dfrac{f_i}{\rho} \\ \dfrac{\partial \overline{u_i}}{\partial x_i} = 0 \end{cases} \tag{3.66}$$

As highlighted in this equation, only the sub-grid scale turbulent viscosity ν^{SGS} needs to be modelled under the Boussinesq hypothesis. Various SGS models have been developed in the literature. Most of them share the following form:

$$\nu^{SGS} = (C\Delta)^2\mathcal{D}(\overline{\boldsymbol{u}}) \tag{3.67}$$

where $\mathcal{D}$ is a differential operator of the model acting on the resolved velocity field and C is the model constant, determined theoretically or numerically to produce the proper amount of dissipation in the simple case of decaying isotropic turbulence. The first model of this kind is the classical Smagorinsky model, which defines the differential operator as:

$$\mathcal{D}(\overline{\boldsymbol{u}}) = 2\sqrt{\overline{S}_{ij}\overline{S}_{ij}} \tag{3.68}$$

However, this model is known to be very dissipative near walls, preventing the transition to turbulence from occurring.

The SGS model preferred in the present thesis is the σ-model developed by Nicoud et al. [147]. The differential operator is computed as:

$$\mathcal{D}(\overline{\boldsymbol{u}}) = \frac{\sigma_3(\sigma_1 - \sigma_2)(\sigma_2 - \sigma_3)}{\sigma_1^2} \tag{3.69}$$

where $\sigma_1 \geq \sigma_2 \geq \sigma_3 \geq 0$ are the three singular values of the resolved velocity gradient tensor and the model constant $C \approx 1.35$ upon initial model development. This model meets several interesting properties to simulate cardiovascular flows. The SGS viscosity vanishes for a variety of canonical flows, where the structure of the velocity gradient tensor indicates laminar flow features, hence where no SGS viscosity is expected. This property is well suited for transitional flows. Furthermore, the σ-model has shown better agreement than the dynamic Smagorinsky model compared to experimental data in the case of a pulsatile jet impinging a flat-plate in the presence of a cross-flow [148]. Such a configuration is relevant to cardiovascular flows [77].

3.3 From a realistic sequence to a synthetic MRI

3.3.1 Bloch solver

A numerical approach to simulate 4D flow MRI has been developed and validated by Puiseux during his PhD [20], where the Navier-Stokes and Bloch equations are simultaneously solved using an Eulerian-Lagrangian formalism. The YALES2BIO solver previously introduced in Section 3.2 is used to resolve the Navier-Stokes equations. The Bloch equations are solved on isochromats, carrying a magnetization vector advanced in time. The isochromats are modelled as Lagrangian particles, whose position is updated at each iteration. The main steps of the CFD-MRI simulation procedure are illustrated in Fig. 3.18 and are briefly presented hereinafter. More details, including validation test cases, can be found in [20, 86].
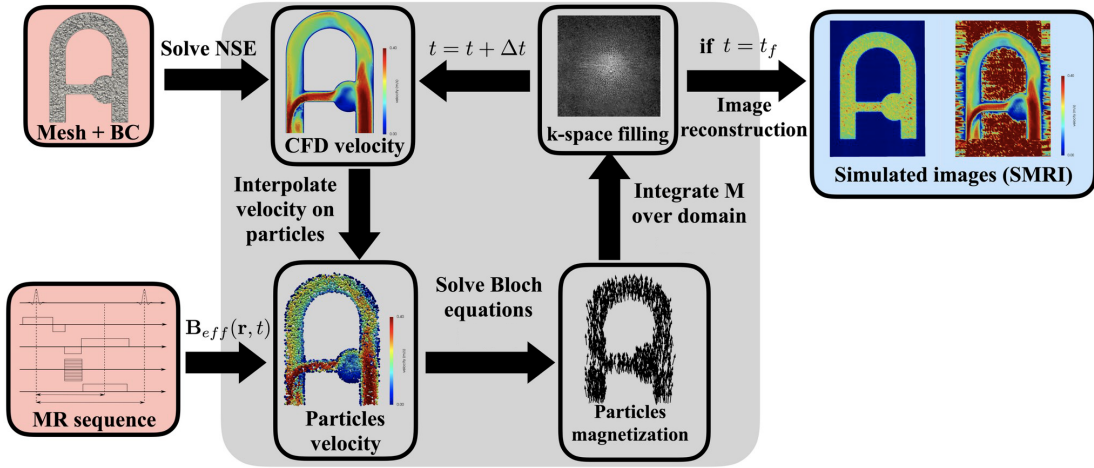
Figure 3.18: Main steps of the CFD-MRI procedure as implemented in YALES2BIO. NSE: Navier-Stokes Equations, BC: Boundary Conditions, t_f: final time of the simulation. The gray block corresponds to the simulation framework kernel, while the red and blue blocks are respectively the inputs and outputs of the simulation. Figure taken from [86].

Particles seeding and RF-spoiling

The isochromats are modelled as N_p Lagrangian particles within the fluid domain. At the initial RF pulse, $N_{p,el}$ particles are injected inside each element of the discretized fluid Eulerian grid following a uniformly random distribution. According to [19], at least 3 particles/direction/voxel are required to achieve en error on the MR signal below 1.5%. Puiseux et al. reported the use of a spin density of 48 particles/voxel to mitigate the error on the MR signal while keeping a reasonable simulation time [86]. For a given isotropic voxel size, this corresponds to the injection of 8 particles per tetrahedral element of the same characteristic length. Each particle p has an associated set of magnetic properties (T_1, T_2, M_0) and an

98

isochromat volume defined as $w^p = \frac{V_{el}}{N_{p,el}}$, where V_{el} corresponds to the volume of the element where the particle p is located. Furthermore, each injected particle is prescribed with an initial magnetization $\boldsymbol{M}_{inj} = (0, 0, M_z^{SS})$, where M_z^{SS} is the steady-state magnetization defined in Section 2.6.1. As mentioned in Section 2.7.1, 4D flow MRI sequences are usually RF-spoiled in order to eliminate the transverse magnetization at the end of a repetition before the next RF pulse. The particles seeding strategy takes advantage of this spoiling. Instead of simulating the RF-spoiling, it is modelled by suppressing the particles of the fluid domain and by re-seeding the N_p particles at the state of the initial RF pulse, with their magnetization vector reset to their initial value $\boldsymbol{M}_{inj}$. This allows to have a perfect spoiling, as the transverse magnetization is back to zero, while keeping a homogeneous distribution of the particles and avoiding areas of spurious signal due to either accumulation or lack of particles.

Fluid-particle velocity interpolation and temporal discretization

To advance the position of the particles, the Navier-Stokes equations are first solved on the fixed numerical mesh of the fluid domain, as presented in Section 3.2.3. The Eulerian velocity field is advanced of a time step Δt_{CFD}, which is fixed by a Courant–Friedrichs–Lewy (CFL) condition. The CFL number is computed at each edge n as

$$CFL_n = \frac{U_n \Delta t}{\Delta x_n} \tag{3.70}$$

where U_n is the velocity at the pair n and Δx_n the pair element length. The stability condition for the convection term in the Navier-Stokes equations states that $\max(CFL_n) \leq CFL_{stab}$. In the present work, $CFL_{stab} = 0.9$, such that during an iteration, a fluid particle can not travel more than 90% of the smallest mesh element size. Once advanced, the CFD velocity field is interpolated on the particles with an inverse distance weighting interpolation. The particle position $\boldsymbol{x}^p$ can then be advanced as:

$$\boldsymbol{x}^p(t + \Delta t_{MRI}) = \boldsymbol{x}^p(t) + \int_t^{t+\Delta t_{MRI}} \boldsymbol{u}(\boldsymbol{x}^p, t)dt \tag{3.71}$$

where Δt_{MRI} is the time step associated to the particle advancement and $\boldsymbol{u}$ the interpolated velocity. The integration is performed with a third-order Runge-Kutta method (RK3).

The numerical time-step Δt_{MRI} depends on the discretization of the Bloch equations. To ensure numerical stability and sufficient temporal resolution, a multi-criterion time-stepping approach is adopted, such that

$$\Delta t_{MRI} = \min(\Delta t_{CFD}, \Delta t_{stab}, \Delta t_{mag}, \Delta t_{grad}, \Delta t_{seq}) \tag{3.72}$$

Δt_{stab} is a stability criterion derived for the explicit Runge-Kutta scheme used to numerically advance the Bloch equations and is defined as:

$$\Delta t_{stab} = \frac{2}{T_2 \left(\frac{1}{T_2^2} + \left(\frac{\gamma}{2\pi} B_{z,max} \right)^2 \right)} \tag{3.73}$$

where $B_{z,max}$ corresponds to the maximum z-component of the magnetic field prescribed to a particle.

Δt_{mag} is another time step constraint to capture the stiff variations of the magnetization induced by abrupt changes in the effective magnetic field. Recall that in the rotating frame of reference, the effective magnetic field is expressed as (cf. Eq. (2.12) and (2.45)):

$$\boldsymbol{B}_{\text{eff}} = \begin{bmatrix} B_1(t)\cos\left(\Delta\omega_1 t\right) \\ -B_1(t)\sin\left(\Delta\omega_1 t\right) \\ \boldsymbol{G}(t)\cdot\boldsymbol{r} + \Delta B_z(\boldsymbol{r},t) \end{bmatrix} \underbrace{=}_{\substack{\text{on-resonance} \\ \text{condition}}} \begin{bmatrix} B_1(t) \\ 0 \\ \boldsymbol{G}(t)\cdot\boldsymbol{r} \end{bmatrix} \tag{3.74}$$

This additional constraint is defined as:

$$\Delta t_{mag} = \frac{2\pi b_n}{\gamma B_{\text{eff,max}}} \tag{3.75}$$

where $B_{\text{eff,max}}$ is the maximum effective magnetic field imposed to a particle and the user-defined dimensionless Bloch number b_n corresponds to the fraction of revolution described by the spin with maximum precessing frequency during one iteration. In the present work, b_n is set equal to 1 accordingly to the time convergence study in Puiseux's PhD work [20].

Δt_{grad} is an additional time step to ensure that each gradient ramp is sampled with at least ten time points:

$$\Delta t_{grad} = \min_{i=\{x,y,z\}}\left(0.1\frac{G_{i,max}}{|\frac{\partial G_i}{\partial t}|}\right) \tag{3.76}$$

where $G_{i,max}$ is the maximum gradient strength specified in the sequence along the axis $i = \{x,y,z\}$.

Finally, Δt_{seq} is a time constraint based on the sequence chronogram to ensure adequate sampling of the RF waveform and of the gradients, as well as to collect the signal at the correct time instants during the readout.

Note that to avoid redundant CFD computations, the fluid velocity is kept constant during a fluid iteration, that is until the sum of all Δt_{MRI} equals to Δt_{CFD}.

Semi-analytic solution to the Bloch equations

A semi-analytical solution to the Bloch equations is implemented in the Bloch solver. During RF excitations, a full numerical integration (RK4) is used, whereas a less computationally-demanding analytical resolution is performed when gradient-only magnetic events or relaxation occur. This approach is valid as long as the gradient waveforms can be described analytically.

In the analytical resolution, the gradients waveforms are described as piecewise linear functions over a set of time intervals $[t^m, t^{m+1}]$. Thereby, the phase can be

decomposed as a sum of piecewise analytical expressions over these time intervals and reads:

$$\phi(\boldsymbol{x}^p, t^n) = \sum_{m=0}^{n-1} \gamma \left(a^m \Delta t^m + b^m \left(\Delta t^m \right)^2 + c^m \left(\Delta t^m \right)^3 \right) \tag{3.77}$$

where

$$\begin{aligned} \Delta t^m &= t^{m+1} - t^m \\ a^m &= \boldsymbol{x}^p(t^m) \cdot \boldsymbol{G}(t^m) \\ b^m &= \frac{1}{2} \boldsymbol{x}^p(t^m) \cdot \frac{d\boldsymbol{G}}{dt}\bigg|_m + \boldsymbol{u}^p(t^m) \cdot \boldsymbol{G}(t^m) \\ c^m &= \frac{1}{3} \boldsymbol{u}^p(t^m) \cdot \frac{d\boldsymbol{G}}{dt}\bigg|_m \end{aligned} \tag{3.78}$$

The transverse magnetization is computed by introducing the description of the phase derived in Eq. (3.77) in the following equation:

$$M_{xy}(\boldsymbol{x}^p, t^n) = |M_{xy}(\boldsymbol{x}^p, t_0)| e^{i\phi(t_0)} e^{-\frac{(t^n - t_0)}{T_2}} e^{-i\gamma\phi(\boldsymbol{x}^p, t^n)} \tag{3.79}$$

where t_0 denotes the end of the last RF pulse. The particle position is updated from the velocity vector at the end of each sub-iteration on the particles.

Signal reception

M_{xy} is integrated over the entire flow domain Ω at each readout events. The collected complex signal is obtained as the following sum over the N_p particles present in Ω:

$$s(t^n) = \sum_{p=1}^{N_p} w^p M_{xy}(\boldsymbol{x}^p, t^n) \mathcal{B}_{xy}(\boldsymbol{x}^p) \tag{3.80}$$

where $\mathcal{B}_{xy}$ is the receive coil sensitivity profile and w^p the isochromat volume (cf. Section 3.3.1). In the present work, only one coil perfectly uniform over the entire domain is considered $\mathcal{B}_{xy} = 1$.

3.3.2 MR sequence as input to the Bloch solver

In Puiseux's PhD work, the MR sequences used as inputs were generated using the JEMRIS sequence development interface [15]. The format used as input to the Bloch solver has been extended in the present work to be able to read more realistic MR sequences, namely issued from IDEA (Siemens Healthineers, Erlangen, Germany), the Siemens Healthineers' software to design MR sequences. The primary feature of this software consists in programs for writing pulse sequences. It also provides a user interface, where imaging parameters can be adjusted as if one were to launch a protocol on an actual MR scanner. This interface allows for example to use the same set of parameters of an experimental protocol, as long

as the sequence to be used is available in the IDEA environment. Simulating a sequence in IDEA through this user interface generates several files, containing the resulting discretized chronogram, global sequence parameters (e.g. dimension of the FOV, pixels number...) or information on the individual T_R. The design of new pulse sequences is out of scope of the present thesis. Yet, commercialized 3D FLASH (SSFP sequence, see Section 2.6.2) and prototype 4D flow MRI sequences have been provided by Siemens and studied in the present work, with different sets of parameters. Note that both sequences are RF-spoiled.

In-house scripts have been developed in Python to convert these files into YALES2BIO inputs under the HDF5 format. The gradients are expressed as trapezoidal waveforms, so that the points of interest are the start and end points of each ramp and plateau. Only these time points and their associated gradient strength are gathered in the HDF5 files, and a file for each gradient direction (readout, phase-encoding and slice-selection) are created. As mentioned earlier, an idealized RF-spoiling is performed and particles are suppressed and reinjected at each RF pulse. Thereby, data about gradients occurring after the ADC and participating in the spoiling such as rewinders are discarded from the input files, as well as all gradients happening during repetitions, where no ADC is present. Indeed, the effect of these gradients on the transverse magnetization would be lost as soon as the RF-spoiling occurs.

Concerning the excitation pulse, IDEA files provide the duration and flip angle of the RF pulse, as well as a very refined temporal discretization. This discretization would result in a large number of time steps to simulate the RF pulse. Knowing that the pulses in the sequences that are used in this work are of the Hanning-filtered sinc type, this function is fitted to the discrete points provided by the files to adjust amplitude and timing. Based on the fit, a description of the RF with fewer points is found. The number of points to describe the RF is deemed large enough, if the relative difference between the prescribed flip angle and the flip angle induced by the RF pulse description with fewer points is lower than 1.5%. The same RF pulse is used throughout the sequences investigated in this work, so that the input file relative to the RF only contains data about the first RF. Only the starting time instants of each RF are needed to simulate all RF pulses in the sequence. This information, along with the start points of the ADC throughout the sequence and the dwell time between two consecutive sampling instants during the readout, is stored in an additional input file with sequence parameters.

3.3.3 Reconstruction

Magnitude and velocity images are reconstructed with an in-house Python script. When simulating a 3D FLASH sequence, the signal collected at the time instant t^n corresponds to a unique point (k_x, k_y, k_z). Yet, when simulating a 4D flow sequence, this signal at t_n corresponds to a unique point $(k_x, k_y, k_z, \text{phase number}, \text{direction})$, where direction stands either for the reference or for the velocity-encoded direction

of the repetition time. Note that the reference or the velocity-encoded direction can also be a combination of different directions (e.g. $v_x - v_y + v_z$ [112]). While the input files are created, an extra file is concurrently written as a "k-space map" that documents the order how the signal will be collected. This map allows to reorganize the signal collected during the simulation, in which each data is saved one after the other. The signal can then be reconstructed for each phase number and each direction. In order to reorder each k-space according to the input order expected by the inverse FFT function of the Pythonic NumPy library (https://numpy.org), each k-space is first multiply by a mask to compensate for the half field-of-view and the one-half pixel shifts [89]. Finally, for a given phase and a given direction, the complex image I is reconstructed from the reordered complex k-space S as:

$$I = \text{FFT}^{-1}(S) \tag{3.81}$$

and the magnitude image is given by:

$$I_{mag} = |I| \tag{3.82}$$

The velocity map u_i along each encoding direction i is obtained as:

$$u_i = \arg\left(\frac{I_i}{I_{ref}}\right) \frac{V_{ENC,i}}{\pi} \tag{3.83}$$

3.3.4   Test cases

Two test cases have been developed to ensure that the new format adopted to read Siemens-based input sequences allowed to reconstruct the expected images. The first one consists in simulating a 3D FLASH sequence on a simple geometry to control that the reconstruction process does not generate false geometric distortions. The second test case presents a 4D flow simulation on an analytical Poiseuille flow in a pipe.

3D FLASH on a pipe

A 3D FLASH (Fast Low Angle SHot) sequence has been generated in IDEA with the following properties: fully-sampled k-space with $64 \times 32 \times 8$ voxels and a field-of-view of $320 \times 150 \times 40$ mm^3. The object to be imaged in a pipe, whose mesh has a characteristic length of 5 mm. The mesh and the FOV are presented together in Fig. 3.19. Note that the object to be imaged is fully included within the FOV, so that no aliasing is expected. In particular, the FOV dimension along the readout direction is very large due to limitations in IDEA, probably as it is not meant to model such reduced FOV. This also means that the oversampling is superfluous in this test case. Yet, the oversampling along the readout direction (here, X direction) is set by default to 2 in Siemens sequences. Hence, 128 points are collected along this direction.
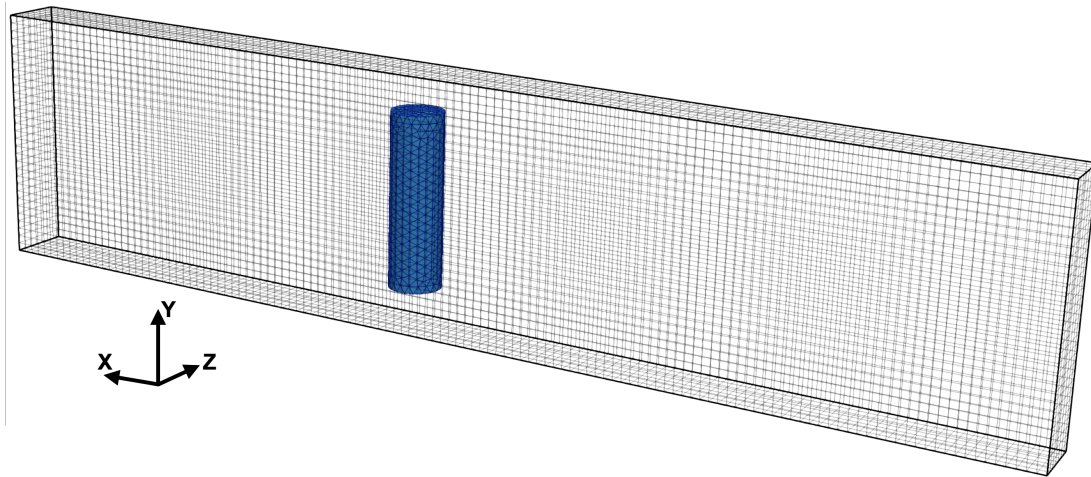
Figure 3.19: Field-of-view and object to be imaged in the test case using a 3D FLASH sequence.

The simulation lasted slightly over a minute and a half on 4 processors. The reconstruction is presented in Fig. 3.20 along the three midplanes. The reconstruction is in good agreement with the boundaries of the pipe geometry.
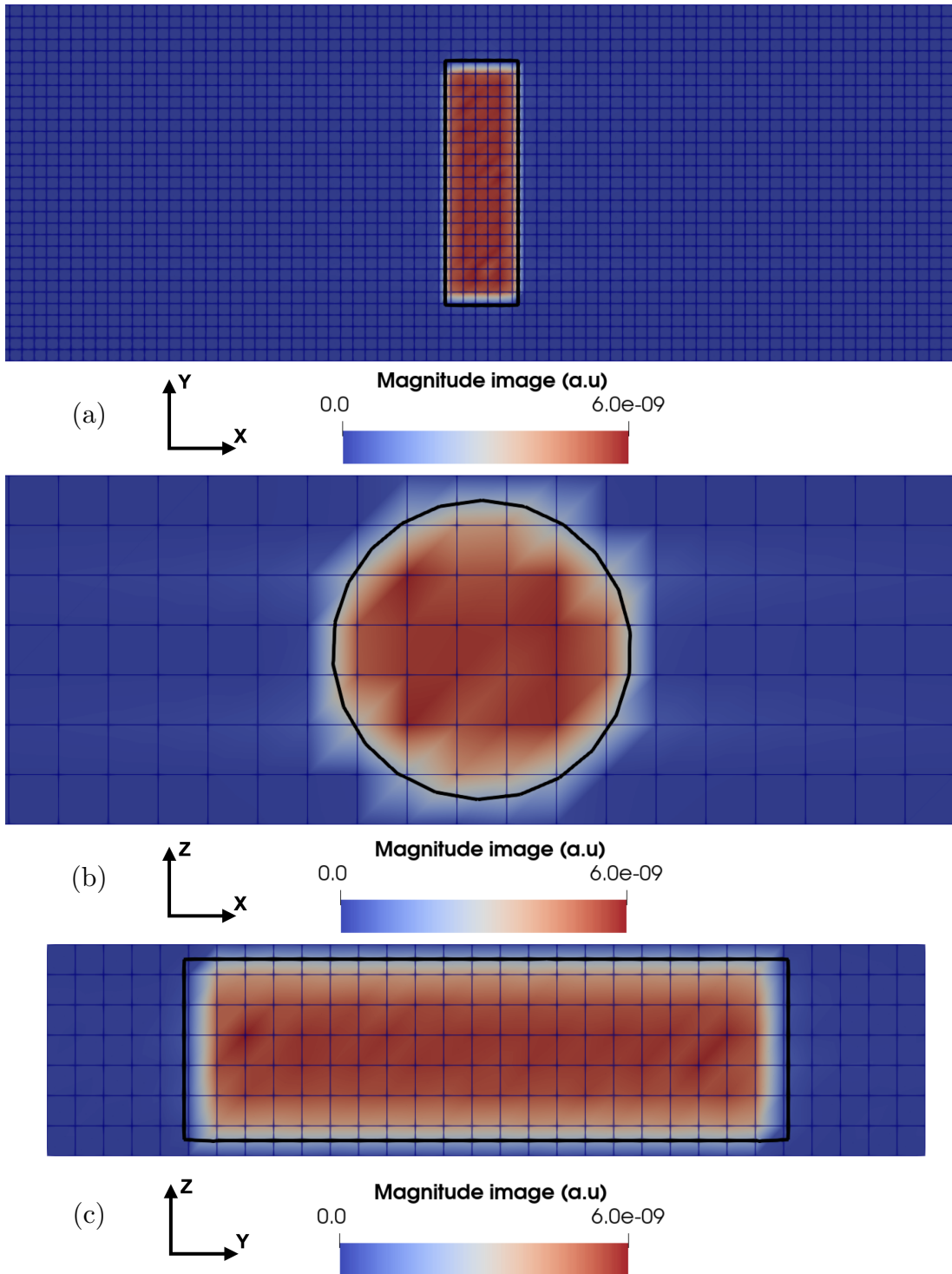
Figure 3.20: Reconstructed magnitude image. The black lines represent the outline of the pipe in the slice depicted. (a) Coronal midplane. (b) Transverse midplane. (c) Sagittal midplane.

4D flow on an analytical pulsatile Poiseuille flow

A 4D Flow MRI sequence has been generated in IDEA with the following properties: fully-sampled k-space with $64 \times 35 \times 8$ voxels and a field-of-view of $320 \times 150 \times 40$ mm^3. The V_{ENC} is set to 1 m/s in each direction. There is an oversampling in the readout direction (X) set to 2, as well as partial Fourier, so that 112 points are collected along this direction. An analytical pulsatile Poiseuille flow is prescribed in a pipe of radius $R = 40$ mm, oriented along the slice-selection direction Z. The pulsatile through-plane velocity w is prescribed as

$$w(r, t) = w_{max} \left(1 - \frac{r^2}{R^2} \right) \frac{(1 + \cos(\frac{2\pi}{T}t))}{2} \tag{3.84}$$

where r is the radial coordinate with respect to the center of the pipe, $w_{max} = 0.6$ m/s is the peak velocity, and $T = 1.0296$ s is the time period of the velocity, which can be assimilated to the RR-interval in vivo. The velocity along the two other directions is zero. The FOV and the geometry are presented in Fig. 3.21.
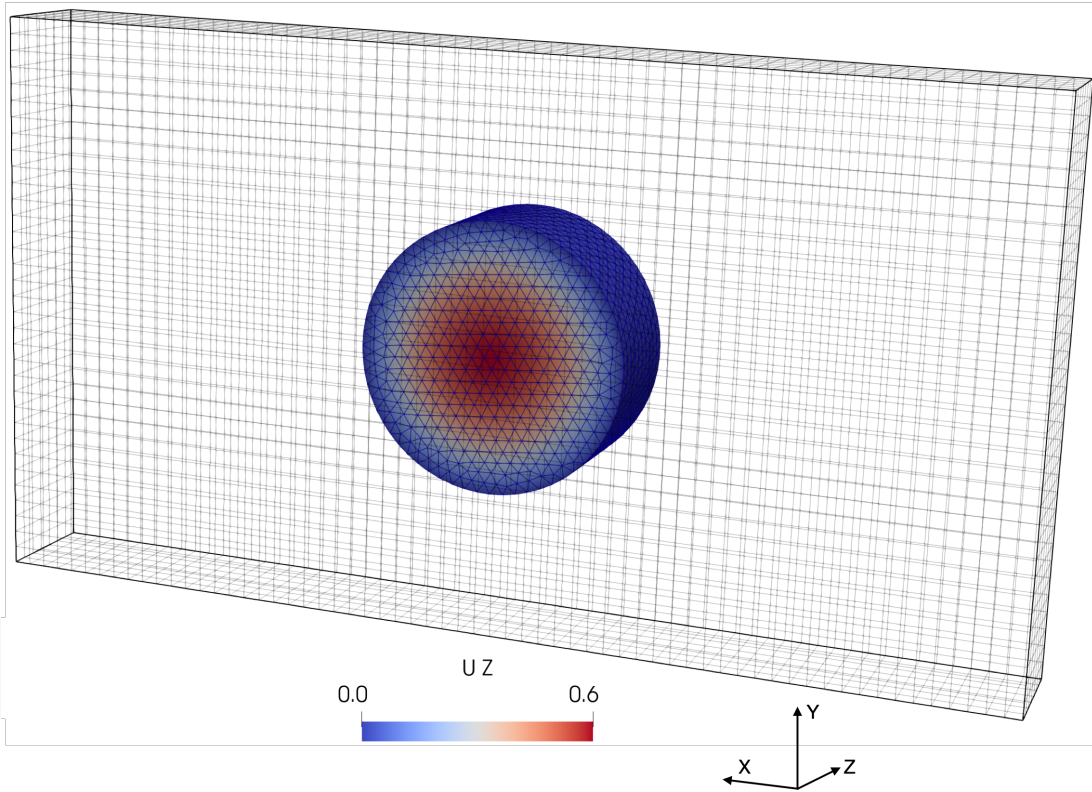
Figure 3.21: Geometry and through-plane velocity field within the FOV to be imaged using a 4D flow MRI sequence.

To reconstruct the magnitude and velocity images, the k-spaces are zero-filled for the non-acquired points due to the use of partial Fourier [44, 89]. The magnitude image is presented in the coronal and sagittal midplanes in Fig. 3.22.
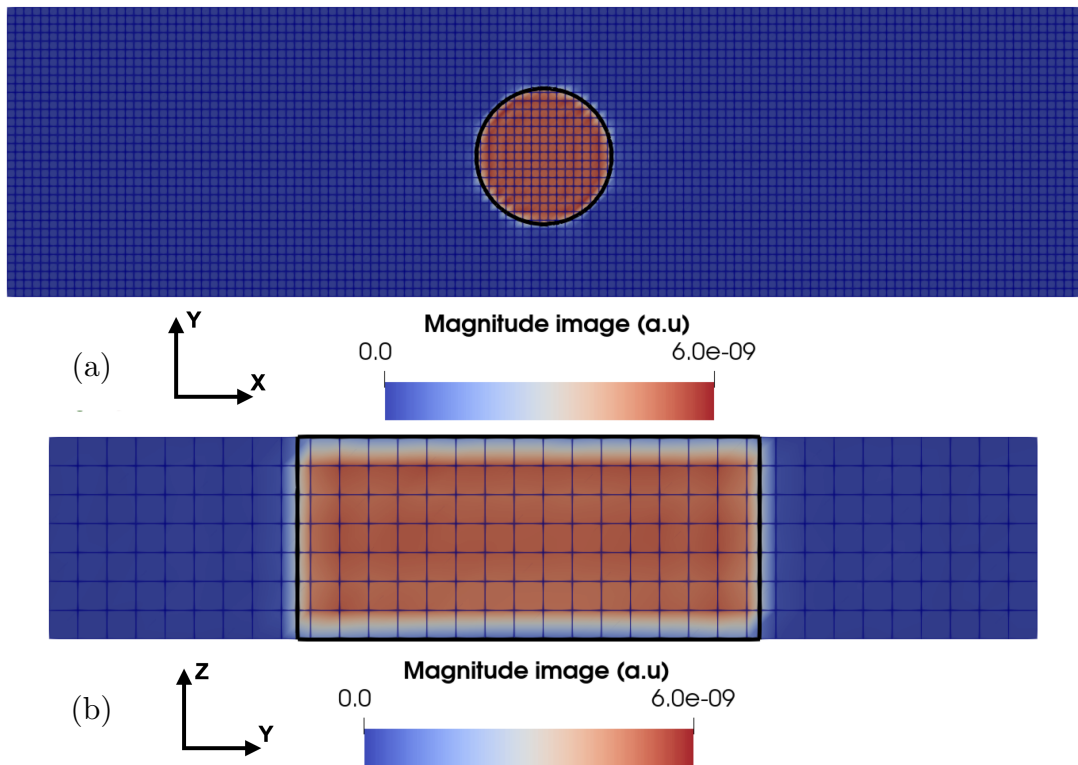
Figure 3.22: Reconstructed magnitude image. The black lines represent the outline of the pipe in the slice depicted. (a) Coronal midplane. (b) Sagittal midplane.
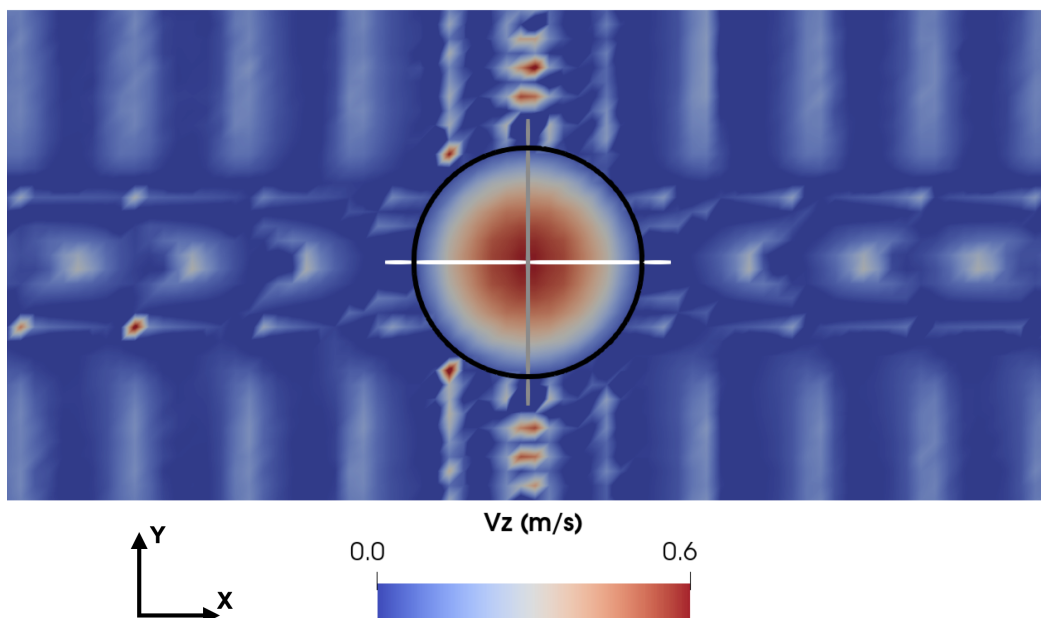
Figure 3.23: Reconstructed velocity field along Z. The black line represents the outline of the pipe. The white and gray lines are the midlines along which the velocity profiles are plotted in Fig. 3.24.

The reconstructed velocity for one phase is presented in Fig. 3.23 and the associated velocity profiles along X and Y are plotted against the analytic velocity field in Fig. 3.24. Good agreement is found between the reconstructed and analytic velocity field for each phase within the pipe. Note that only the fluid mesh is seeded with particles, such that no signal is collected outside the pipe, leading to random phases in the exterior voxels. This can explain the reconstructed velocity outside the Poiseuille flow, which is not zero, contrary to what was expected.
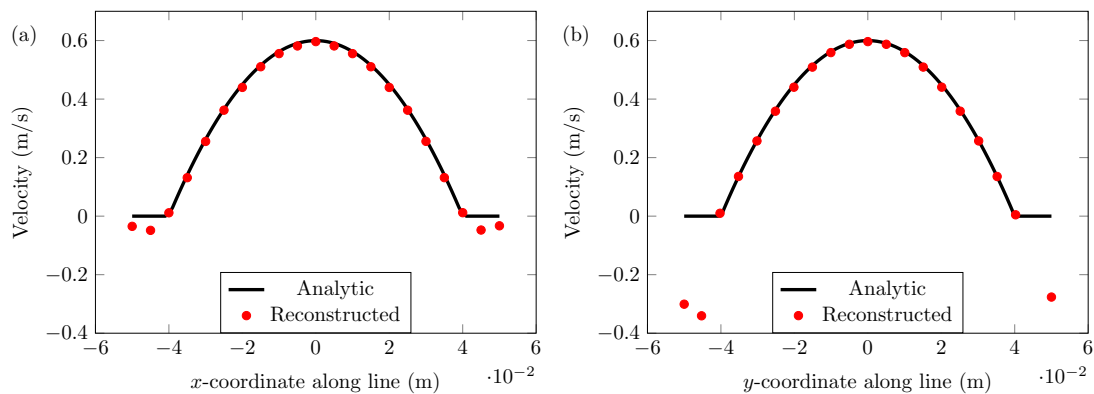
Figure 3.24: Velocity profiles along (a) the x-midline (white line in Fig. 3.23) and (b) the y-midline (gray line in Fig. 3.23).

4

Assessment of accelerated sequences of 4D flow MRI

Chapter contents

In this chapter, hemodynamic biomarkers obtained by accelerated sequences of 4D flow MRI are evaluated under complex flow conditions. The investigated sequences are GRAPPA with acceleration factor R = 2, 3 and 4, and compressed sensing with R = 7.6. The assessment of the accelerated sequences are performed on an in-house pulsatile flow phantom, together with a nonaccelerated fully-sampled acquisition. CFD simulations based on the experimentally measured flow fields are conducted for additional comparison. The velocity fields are compared on non-derived quantities: velocity profiles, flow rates and peak velocities. While all modalities (experimental and simulated) depicted qualitatively similar hemodynamic patterns, a trend for all MR scans to overestimate velocity profiles and peak velocities as compared to CFD is noticed in regions associated with

high velocity or acceleration. Voxel-wise comparisons between the MRI scans highlight larger discrepancies at the voxels located near the phantom's boundary walls. Correcting the MR images for eddy currents appears essential to report flow rates measurements complying with the principle of mass conservation and achieve a good agreement between all modalities.

This chapter is part of: Morgane Garreau, Thomas Puiseux, Solenn Toupin, Daniel Giese, Simon Mendez, Franck Nicoud, and Ramiro Moreno. Accelerated sequences of 4D flow MRI using GRAPPA and compressed sensing: A comparison against conventional MRI and computational fluid dynamics. Published in Magnetic Resonance in Medicine, 88(6):2432-2446, December 2022. [21]

4.1 Introduction

2D phase-contrast (PC) MRI is a well-established blood flow measurement technique to evaluate cardiovascular disorders such as valvular diseases, aortopathies, or congenital heart diseases [149, 150]. More recently, time-resolved 3D PC imaging, referred to as *4D flow MRI*, has gained significant interest for its ability to provide in-vivo quantification of blood flow dynamics inside a 3D volume over the cardiac cycle [151, 152]. Whereas 2D PC imaging is operator-dependent for plane positioning, 4D flow imaging provides a retrospective flow quantification at any location within the acquired volume. In addition to providing comprehensive velocity and vascular motion in a single scan, 4D flow MRI also opens access to advanced hemodynamic biomarkers such as wall shear stress (WSS) [42], pulse wave velocity [45] or relative pressure [41]. To this respect, 4D flow MRI has the potential to become a gold-standard practice in clinical routine. However, the clinical applicability of this technology remains hampered by its inherently long scan duration, which is further worsened by respiratory gating techniques for motion compensation. Despite the use of parallel imaging techniques (e.g., GRAPPA and SENSE) with typical acceleration factors of 2-3, 4D flow scan times still range between 5 and 15min. Therefore, alternative acceleration techniques have been developed over the years to further shorten 4D flow scan duration, by exploiting spatiotemporal correlations: k-t GRAPPA [153, 154], broad-use linear acquisition speed-up technique (k-t BLAST) [155], and non-Cartesian acquisition sampling [106], to cite a few. However, these strategies are limited by long reconstruction times, mostly offline, making them hardly compatible with clinical workflows.

In the last years, a compressed sensing (CS) 4D flow framework has shown great potential for decreasing the scan time with a reconstruction performed inline in less than 5 min [156, 157]. This performance was achieved using a k-t accelerated Cartesian pulse sequence with a variable-density phyllotaxis undersampling and L_1-regularized wavelet-based reconstruction. Ma et al. [156] first demonstrated the feasibility of this framework in vitro using a realistic aorta flow phantom with various CS acceleration factors, and for 20 healthy volunteers with a CS acceleration factor of R=7.7. Pathrose et al. [157] assessed the same framework

on patients with aortic diseases with three different CS factors (R=5.7, 7.7 and 10.2) compared to a GRAPPA-accelerated sequence (R=2). Both studies have consistently shown a significant underestimation of measured maximum velocity and flow within 10%-15%, as for derived parameters like wall shear stress (WSS). The higher the CS acceleration factor, the higher the underestimation. However, the factors leading to this underestimation are still not fully understood, even though both studies suggest that spatiotemporal undersampling and regularization could be responsible for this trend. Moreover, whereas GRAPPA-accelerated sequences are considered as clinical gold standard, they are expected to induce additional flow quantification errors as compared to fully sampled (FS) k-space sequences [158]. To characterize the nature of the errors, it is relevant to compare a CS-accelerated sequence with a FS sequence, where no undersampling is involved. Also, standalone parameters such as the mass conservation can also be relevant to estimate the degree of discrepancies [22], with no need of reference measurement. Additionally, significant underestimations of WSS are generally observed, partly because of partial volume effects and low spatiotemporal resolution [159]. Given the growing interests for evaluating the WSS clinically, substantial efforts are being undertaken to propose sophisticated reconstruction methods [42, 83, 160]. However, whereas little attention is generally paid to assess the quality of the input velocity measurements, it is a prerequisite step to properly reconstruct the WSS.

Alternatively, the flow field can be predicted by coupling MRI measurements with Computational Fluid Dynamics (CFD) [6, 8, 161, 162]. This approach bypasses the experimental limitations inherent to MRI acquisitions, such as spatiotemporal resolution or noise, while satisfying the fluid mechanics laws. CFD coupled to MRI has already proven capable of providing the flow fields with high fidelity under well-controlled in vitro conditions [10, 163], whereas moderate correlations have been reported for patient-specific MRI-based simulations [53, 164], or superresolution of 4D flow MRI using CFD [67] for velocity and flow rates. Indeed, the choice of the CFD strategy is crucial to accurately predict the hemodynamics, particularly in such flow regimes where boundary conditions [165] and turbulence models [69, 166], as well as numerical schemes [11], have shown to greatly influence the resulting flow field. In this context, CFD may be used as a third-party modality, yet without being considered a ground-truth, to confirm and quantify the discrepancies observed with 4D flow MRI.

The main objective of this study was to investigate the flow errors induced by GRAPPA- and CS-accelerated 4D flow MRI sequences under complex flow conditions. The experiments were conducted on a previously designed pulsatile flow phantom for which the geometry yields flow patterns similar to the complex flow structures observed in vivo: recirculation, flow split, large-scale transitioning turbulence features etc. High correlation between nonaccelerated 4D flow MRI sequence and CFD was already demonstrated in this well-controlled environment following appropriate postprocessing methods [10]. In the present study, several 4D flow MRI scans with GRAPPA (R=2, 3, 4, abbreviated respectively G2, G3 and

G4 in the following) and CS (R=7.6) accelerations were acquired and compared with a conventional full k-space sampling sequence. Moreover, a high-fidelity CFD solution fed by boundary conditions compatible with the measured flow field was generated and used as a supplementary means to characterize the flow measurement errors

4.2   Methods

The phantom experiment, along with the CFD simulation process, have been described previously in Puiseux et al. [10], where more details are available. A summary is given hereafter.

4.2.1   Phantom experimental setup
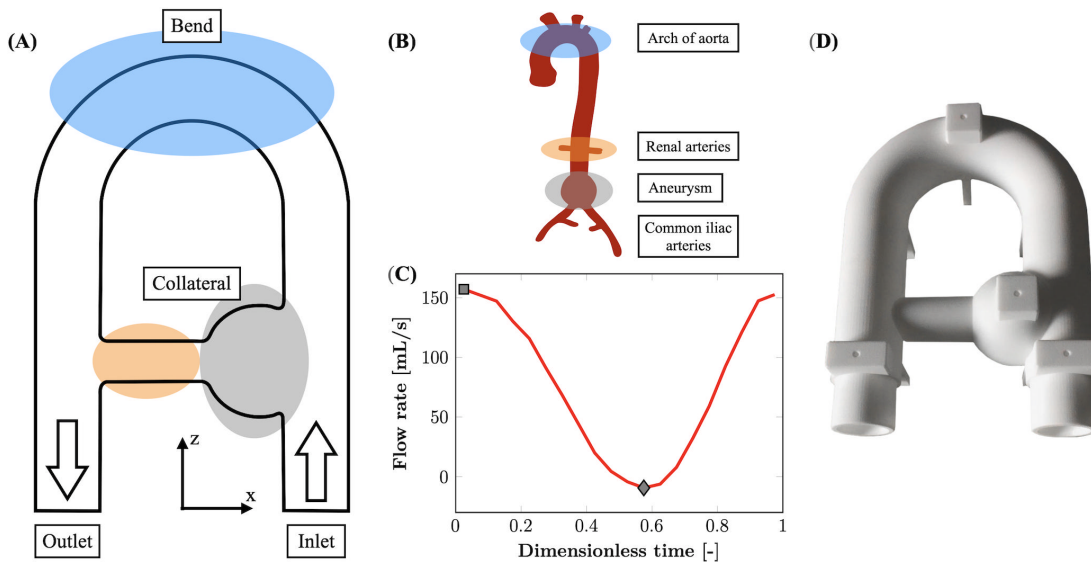
Figure 4.1: Phantom geometry and flow regime. (A) Sketch of the flow phantom. (B) Analogy with cardiovascular system. (C) Flow rate at the inlet for the fully sampled 4D flow acquisition corrected according to the postprocessing procedure detailed in the corresponding section. The square and the diamond correspond to peak systole and end diastole, respectively. (D) Photograph of the 3D-printed flow phantom.

A rigid flow phantom made up with nylon was designed to reproduce complex flow patterns as reported in the cardiovascular system 4.1(A-B). The phantom was embedded into a silicone bath to increase the signal-to-noise (SNR) and connected to a programmable pump (CardioFlow 5000 MR, Shelley Medical Imaging Technologies, London, Ontario, Canada) installed outside the 5 Gauss line via pipes. The pulsatile flow rate delivered by the pump 4.1(C) was measured by means of an ultrasonic flowmeter (UF25B100 Cynergy3 components Ltd,

Wimborne, Dorset, UK) placed upstream of the entrance of the phantom. A schematic representation of this experimental setup can be found in [10]. By analogy with the cardiac cycle, the times of maximum and minimum flow rates are referred to as peak systole and end diastole, respectively. A blood-mimicking fluid was supplied to the phantom circuit with kinematic viscosity $\nu = 4.02 \times 10^{-6}$ m^2/s, density $\rho = 1020$ kg/m^3, and relaxation times $T_1 = 0.85$ s and $T_2 = 0.17$ s at 1.5 Tesla.

4.2.2 MRI data acquisitions

MRI data were obtained thanks to a 1.5T Siemens MAGNETOM Sola (Siemens Healthcare, Erlangen, Germany) using a prototype 4D flow MRI sequence. The sequence was retrospectively gated using a simple 4-point velocity-encoding scheme [112]. The electrocardiogram trigger needed for gating was simulated by means of an MRI-compatible fake finger (MR Finger, Shelley Medical Imaging Technologies, London, Ontario, Canada). It delivered an infrared signal synchronized with the pump waveform cycle and interpreted as an electrocardiogram signal via the peripheral pulse unit of the MRI scanner. Thereby, what is referred to as cardiac cycle in the following is the pump cycle, whose averaged duration is close to 1 s. A FS sequence and several GRAPPA (R=2,3,4) and CS (R=7.6) accelerated sequences were acquired. The acquisition and reconstruction frameworks used for the latter pulse sequence can be found in [156]. The main scan parameters, among which are echo time T_E, repetition time T_R, and 3D velocity encoding (V_{ENC}), are listed in 4.1.

Imaging technique	FS	G			CS
Acceleration rate, R	-	2	3	4	7.6
Scan time (min:s)	42:40	21:20	14:40	10:40	5:35
FOV (mm^3)	$256 \times 256 \times 72$				
Acquired voxel size (mm^3)	$2 \times 2 \times 2$				
Receiver bandwidth (Hz/pixel)	383				
Flip angle (°)	7				
V_{ENC} (x, y, z) (cm/s)	70-20-70				
T_E (ms)	4.15				3.70
T_R (ms)	6.48				6.04
Temporal resolution (ms)	51.8				48.3
Number of reconstructed cardiac phases	20				25

Table 4.1: Imaging parameters. CS, compressed sensing; FS, fully sampled; G, GRAPPA; VENC, velocity encoding.

4.2.3 CFD simulations

The simulations were carried out using the in-house YALES2BIO solver presented in Section 3.2. Due to the complex geometry used in this study to induce large scale fluctuations, as well as the flow regime being in the laminar–turbulent transition, the large eddy simulation (LES) strategy was preferred to the Reynolds-averaged Navier-Stokes (RANS) modeling, where all the scales are averaged and the entire turbulence spectrum is modeled.

The fluid was modeled as incompressible Newtonian with the already mentioned mechanical properties. A tetrahedral-based mesh of the phantom with a characteristic cell size of 0.7 mm was generated with GAMBIT 2.4.6 (ANSYS, Inc., Canonsburg, PA) and used to solve the incompressible Navier-Stokes equations. A zero-pressure condition was prescribed at the outlet, whereas a no-slip condition was imposed at the solid boundaries. Regarding the inlet boundary condition, a pixel-based inflow was derived from the MRI acquisition velocity field, which was corrected according to the postprocessing procedure detailed in the following section. Hence, one CFD simulation by MR acquisition was generated.

The mesh cell size was defined using a mesh sensitivity analysis. Four different tetrahedral-based meshes were investigated based on the inlet provided by the FS acquisition: a coarse one with 622 thousand cells (cell size = 1.3 mm), a medium one with 1284 thousand cells (cell size = 1.0 mm), a fine one with 3812 thousand cells (cell size = 0.7 mm), and a finer one with 27 million cells (cell size = 0.35 mm). The relative error on the phase-averaged velocity magnitude (cf. definition in the postprocessing section) between the two latter meshes came to 0.9% of the maximum velocity magnitude found for the finer mesh. Thereby, the velocity field was considered to be spatially converged and independent of the spatial resolution for the fine mesh. More details on the numerical accuracy (sensitivity analysis on mesh, phase-averaging, and turbulence resolution) can be found in [167].

(A)   **(B)**
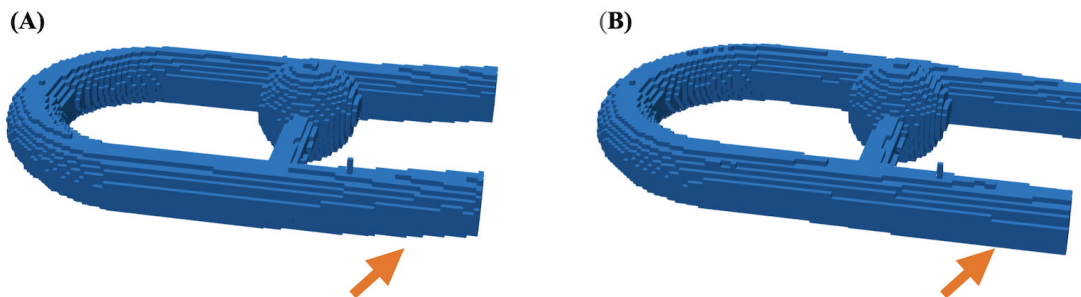
Figure 4.2: Distortion correction presented as a threshold on the image magnitude. (A) Before distortion correction. (B) After correction. The correction is applied on the whole phantom, but its effect is more noticeable at the inlet and outlet, as highlighted by the orange arrows.

4.2.4   Postprocessing

The 4D flow data went through an in-house postprocessing procedure programmed in Python (http://www.python.org, version 3.8.2). Maxwell terms [123], as well as in-plane distortions induced by the nonlinearities of the magnetic gradient field, were corrected within the reconstruction process of the MRI system. An additional correction in the through-plane direction based on the knowledge of the phantom geometry was performed. To do so, the distorted volume was segmented thanks to a threshold on the magnitude images and a second-order polynomial fit was performed on the coordinates of the centerline throughout the parallel branches of the main pipe. The fit found was used to relocate the voxels position along the through-plane direction such that the centerline lies in the coronal plane. Note that every voxel underwent this correction, but the further away from the isocenter (localized above the collateral), the greater the position shift (see Fig. 4.2). Further corrections consisted in noise masking and phase unwrapping. A presegmentation of the flow volume was obtained by thresholding the image magnitude averaged over time for registration purposes only. The resulting presegmented volume was registered onto the computational model thanks to an iterative closest point algorithm. Finally, an eddy current correction was implemented according to Lorenz et al. method [168], based on the assumption that the velocity field measured in static regions should be exactly zero. The silicone bath surrounding the flow phantom was used for this purpose. After segmentation, the voxels belonging to this static region were fitted with a linear function of the space coordinates using a least squares method. This was done for each time frame and velocity direction. The corrected velocity field was obtained by subtraction of the fitted plane. The velocity field resulting from the application of all the corrections described above is referred to as the corrected MR in what follows. All MR acquisitions underwent these same postprocessing steps.

To compare MRI acquisitions with CFD simulations, the latter went through phase-averaging and downsampling following the procedure described in Puiseux et al [10]. The reason for phase-averaging the CFD velocity field is that there are cycle-to-cycle fluctuations when simulating such an unsteady flow lying in the laminar-turbulent transition [77]. Furthermore, the MR signal is also acquired over numerous cardiac cycles. Thereby, 40 cardiac cycles were simulated. The first 10 cycles were taken out of the comparison to cancel the effect of the initial condition (zero velocity condition). The resulting CFD velocity field, phase-averaged over the last 30 simulated cardiac cycles, was then downsampled on an image grid with the same spatial resolution as the MRI acquisitions. This "low-resolution" field is referred to as *CFD_LR* thereafter, whereas *CFD_HR* refers to the "true" CFD.

Because both the CFD_LR and corrected MR velocity fields were finally expressed on the same grid, and the phantom geometry is a priori known, the segmentation of the flow volume was obtained by thresholding the CFD_LR velocity magnitude averaged over time.

4.2.5 Comparison methods

The different MRI modalities were quantitatively compared by conducting Bland-Altman analysis to evaluate the agreement (bias $\pm$ standard deviation, SD) between the pointwise velocity fields obtained from FS and accelerated MR sequences, as well as with the CFD_LR fields. Furthermore, the L_2-norm (also called Euclidean distance) was used as a metric to measure the pointwise similarity between the velocity fields obtained from the different methods. The normalized L_2-norm calculated at each node position $\boldsymbol{x}$ and at each time instant t for two fields A and B is expressed as:

$$L_2(\boldsymbol{x}, t) = \frac{\sqrt{(u_A - u_B)^2 + (v_A - v_B)^2 + (w_A - w_B)^2}}{||\overline{\boldsymbol{u}_{bulk}}||} \tag{4.1}$$

where $\boldsymbol{u} = (u, v, w)$ is the velocity vector associated to the node at the position $\boldsymbol{x}$, and $||\overline{\boldsymbol{u}_{bulk}}|| = 0.144$ m/s is the time-averaged bulk velocity magnitude measured at the inlet surface for the FS acquisition.
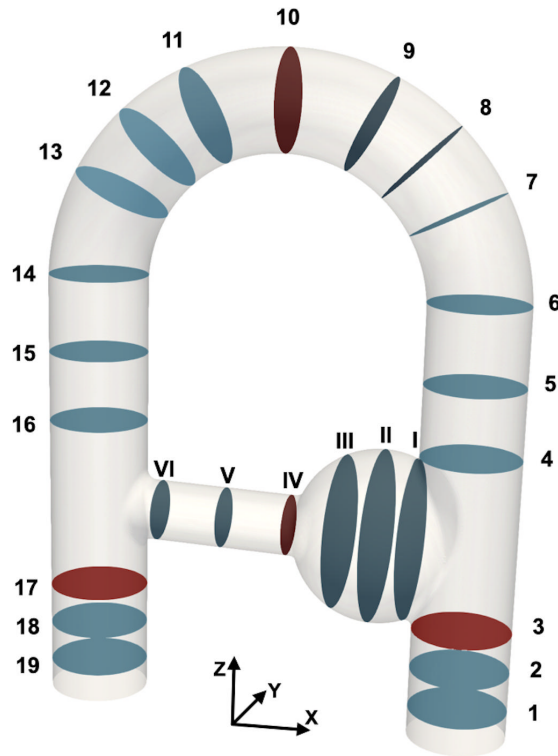
Figure 4.3: Labeling of the planes used to analyze the differences between the velocity fields measured with the different modalities. The planes in the main duct are numbered 1–19 from inlet to outlet, and the planes in the collateral duct are numbered I to VI. The planes in red are highlighted for better readability of 4.10.

Velocity profiles, flow rates, and peak velocities were studied in 19 planes along the main duct and 6 along the collateral duct, numbered respectively 1 to 19 and I to VI from the inlet side to the outlet side (see Fig. 4.3). Some comparisons are said to be performed on all voxels, whereas others are done on inner voxels only. *All voxels* designates all the voxels segmented from the flow volume (cf. Section 4.2.4) with edge voxels straddling the phantom walls included, whereas inner voxels corresponds to the voxels strictly included in the phantom without the edge voxels. For each MRI modality, the segmentation includes about 53,500 voxels, against around 26,800 inner voxels.
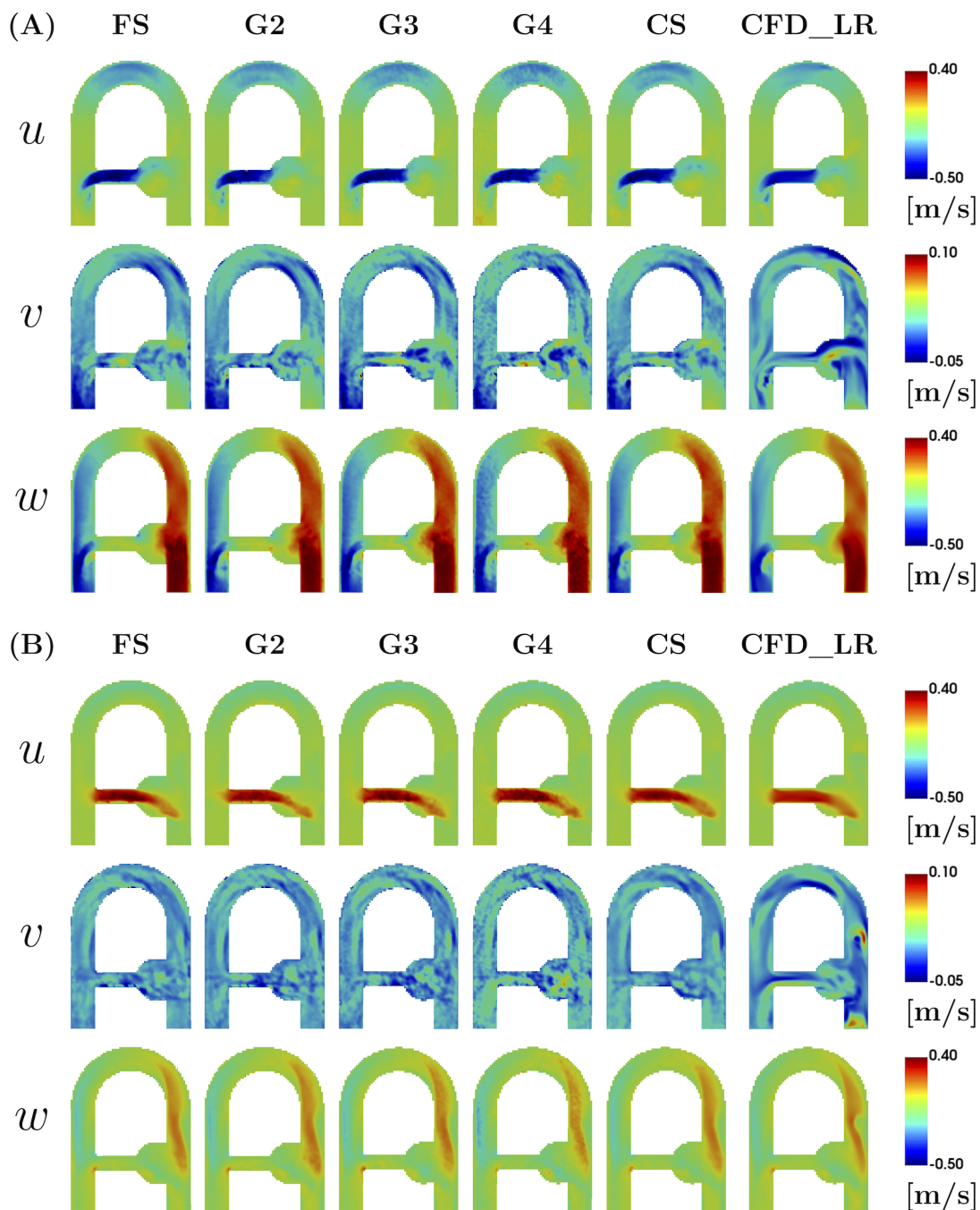
Figure 4.4: Velocity fields in the coronal plane at (A) peak systole and (B) end diastole (cf. 4.1(C)). The rows represent the velocity components $\boldsymbol{u} = (u, v, w)$. The columns show the low-resolution downsampled CFD (CFD_LR) and MRI acquisitions. CFD, computational fluid dynamics; CFD_LR, computational fluid dynamics–low-resolution; CS, compressed sensing; FS, fully sampled; G, GRAPPA.

4.3 Results

Scan times achieved for the FS; G2; G3; G4; and CS 4D flow MRI are 42:40, 21:20, 14:40, 10:40, and 5:35 min, respectively. Investigating whether this strong acceleration comes with a measurable degradation of the quality of the results is the objective of the following subsections.

4.3.1 Flow structures and velocity profiles

As presented in Fig. 4.4, the main flow structures are similarly captured by all sequences and by CFD_LR for the velocity components u and w both at peak systole and end diastole, whereas more disturbed results are found for the low velocity field v. From now on, the results presented in this study will focus on the FS, G3 and CS acquisitions for the sake of clarity. Indeed, because it can already be visually noticed in Fig. 4.4, the G4 velocity field appears noisier in comparison to the other sequences, and the quantitative comparisons lead to poor outcomes for this acquisition. Good results are found for G2, but due to its long acquisition time the preference has been to present the comparisons with G3. To further motivate this choice, the global L_2-norm over all voxels is presented in Fig. 4.5.
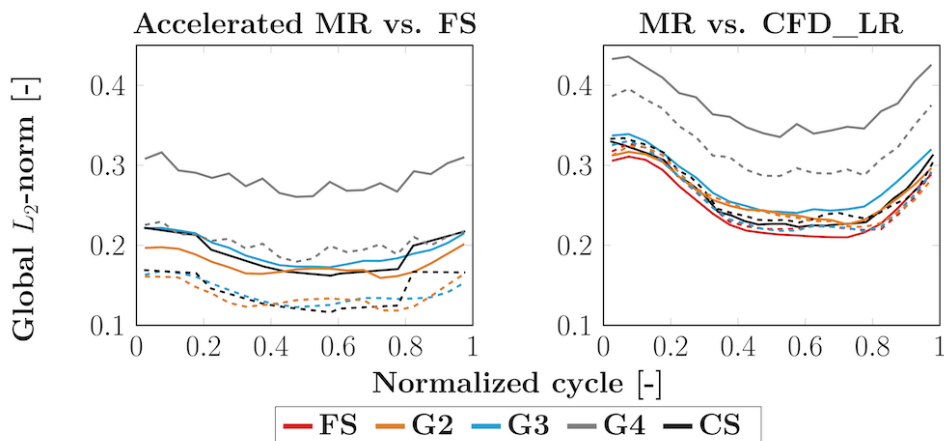
Figure 4.5: Global L_2-norm of the velocity vector differences along the cardiac cycle for all MR acquisitions. On the left, the accelerated MR sequences are compared to the fully sampled MR acquisition. On the right, the MR sequences are compared to CFD_LR. The solid lines refer to the average over all voxels of the segmented volume, whereas the dashed ones correspond to the average over the voxels strictly included inside the phantom segmentation.

The flow structures are further apprehended thanks to vector-based visualization of the MRI and corresponding CFD_HR and CFD_LR. Fig. 4.6 displays the velocity vector field in the whole phantom, as well at the middle plane of the aneurysm-like region for the FS acquisition along with the corresponding CFD_HR and CFD_LR fields. Although the CFD_LR partially mimics the MRI acquisition process, the flow structures localizations are well reproduced. At peak systole, counterrotating vortices are observed for both the FS acquisition and the CFD simulations, although localized higher in the slice for the MRI as compared to CFD simulations.
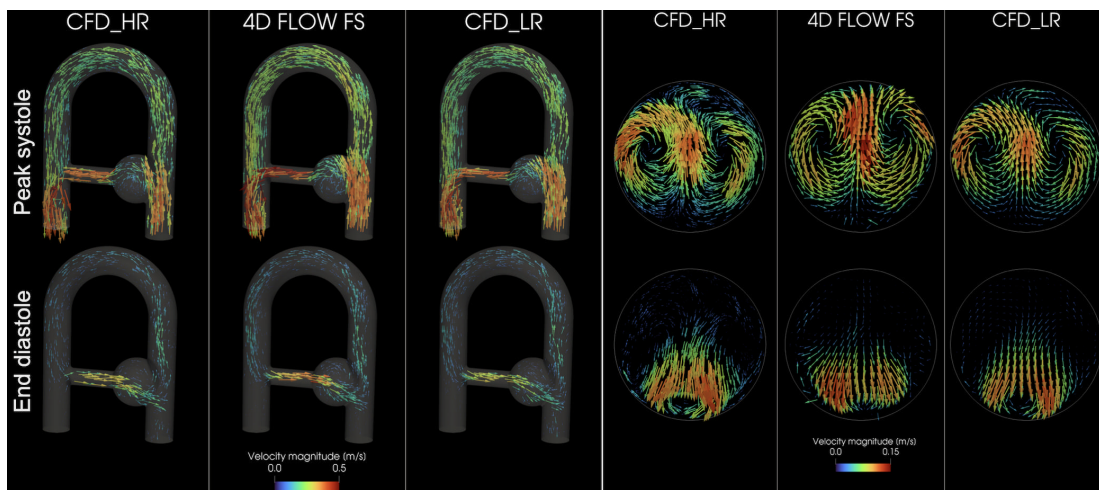
Figure 4.6: 3D vector-based visualization of the FS acquisition and the CFD simulations at peak systole (on the top row) and end diastole (on the bottom row). The whole phantom is displayed on the left-hand side, whereas a slice in the middle of the aneurysm-like region (corresponding to the slice II in Fig. 4.3) is presented on the right-hand side. The vectors are scaled by velocity magnitude.

The velocity profiles for the three MRI methods are presented in Fig. 4.7, along with those obtained from the CFD simulations. Whereas velocity profiles are globally in good agreement for all MRI modalities, the MRI velocity tends to overestimate the CFD one, especially in regions and at time instants of high velocity or acceleration (e.g., sections V and 17 at peak systole in Fig. 4.7). Moreover, a lateral shift of the MR profiles with respect to the CFD profiles is noticeable in the collateral duct. Finally, a small overestimation of the FS as compared to CS and G3 (14.7% and 12.3% for peak velocity, respectively) can be observed at peak systole in section V.
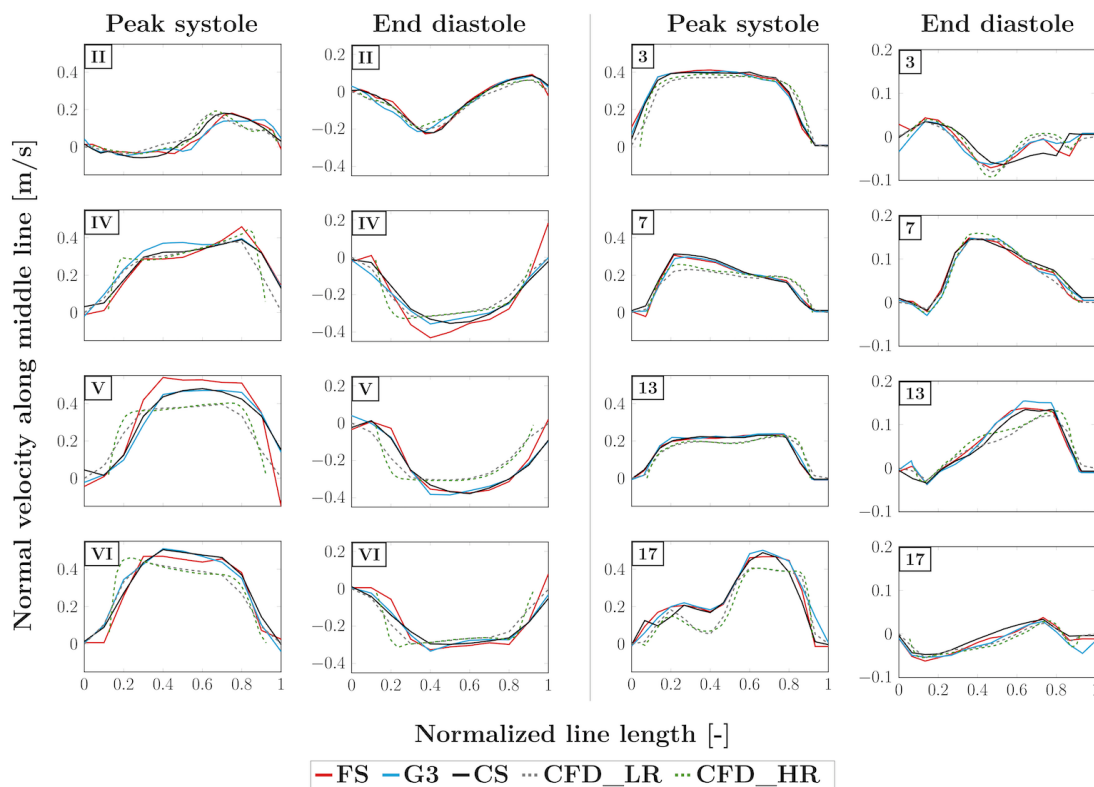
Figure 4.7: Velocity profiles along lines located in the coronal plane passing through the middle of the phantom. The velocity displayed corresponds to the projection onto the normal of the planes perpendicular to the ducts, referenced as in Fig. 4.3 (the corresponding slice number is indicated in the corner of each graph).

4.3.2 Statistical comparison

A Bland-Altman analysis is performed to assess the velocity magnitude agreement between FS acquisition and the other modalities. Results are displayed in Fig. 4.8. It is observed that the voxels straddling the phantom wall are responsible for the most part of the velocity dispersion for all sequences and time points. Indeed, when comparing 4D flow acquisitions two by two with all voxels, the maximal errors on velocities form linear patterns seen on both sides of the bias in the plots. The voxels forming these lines correspond to the limit case, where one of the velocity magnitudes is almost zero (as expected close to the wall), whereas the other is not, producing the slope of ± 2. One can observe that this line is only seen in the upper part of the plot for the comparison against CFD_LR. This is because of the noise-free high-resolution CFD, given that the downsampling process consists in interpolating the high-resolution CFD velocity field onto a subdivision of the MRI grid and to average the velocities of the subvoxels present within each voxel of the MRI grid. Thereby, a voxel straddling the phantom wall will have a CFD_LR velocity, which is an average of velocities for subvoxels

121

within the phantom and zeros for subvoxels outside. In contrast, an MR edge voxel is capturing isochromats velocities and noise.
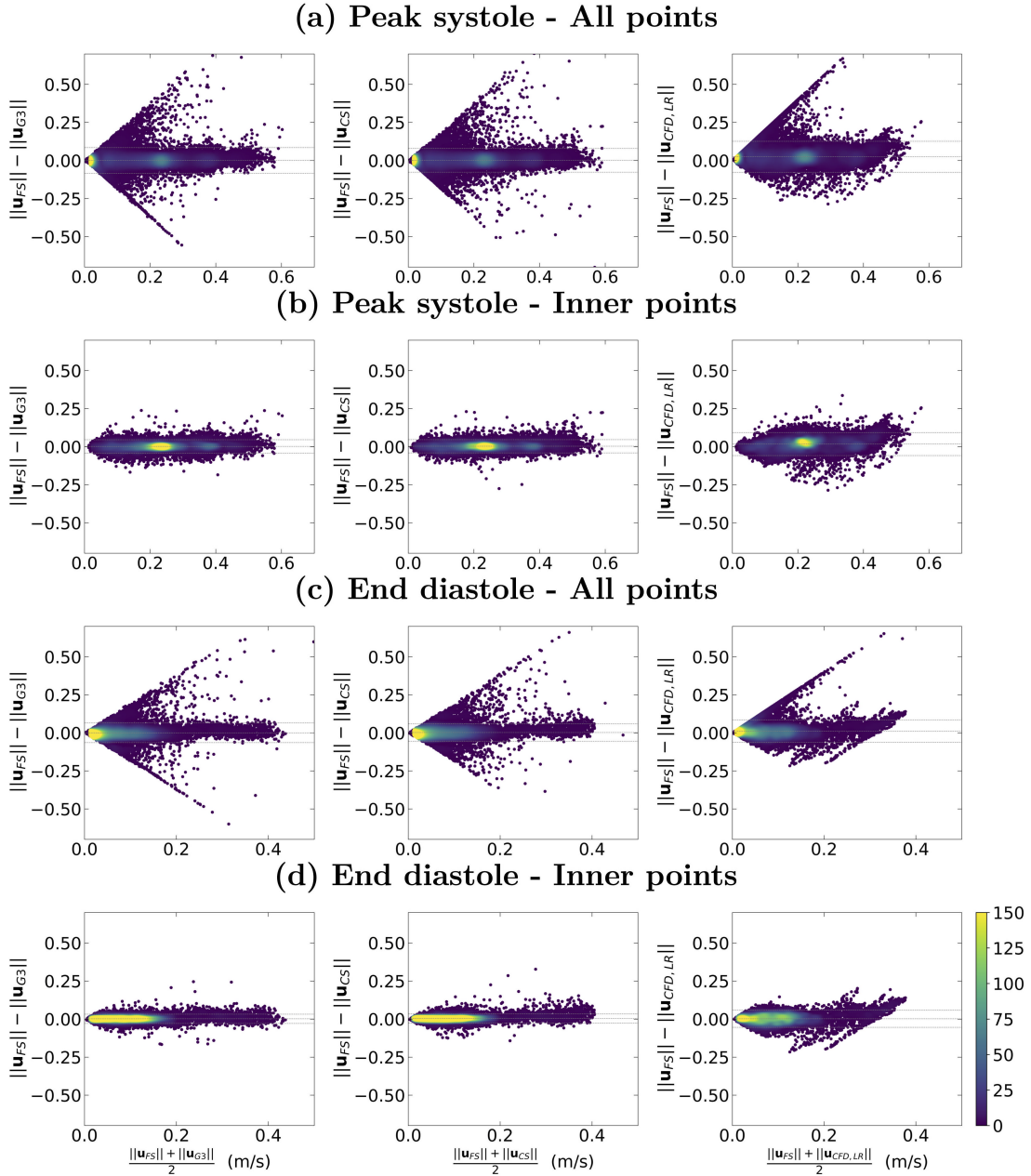
Figure 4.8: Bland–Altman plots for analyses of FS MR acquisition against G3, CS, and CFD_LR. "All points" refers to comparisons where all voxels of the phantom are included, whereas the voxels straddling the wall are removed in the "inner points" comparisons.

Once these edge voxels are taken out of the comparison, good agreement is found with low bias and narrow 95% confidence interval. In this latter comparison, the velocity magnitude difference (reported as bias $\pm$ 1.96 SD, in [m/s]) between FS and, respectively G3, CS and CFD_LR are found to be 0.00 ± 0.04, 0.00 ± 0.04, and 0.02 ± 0.08 at peak systole and 0.00 ± 0.03, 0.00 ± 0.03, and 0.00 ± 0.06 at end diastole. It has yet been noticed that whereas the velocity scattering is rather symmetrical for the comparison with the accelerated MR sequences, there is some shift towards higher velocity magnitudes for FS as compared to CFD_LR.

To have an overview of the global error distribution over time, the L_2-norm over all voxels is computed and presented in Fig. 4.9. Good agreements are found with respect to the FS acquisition, with an average L_2-norm [unitless] decreasing from 0.193 to 0.141 for G3 and from 0.188 to 0.143 for CS when removing the edge voxels. When comparing the MR data with CFD_LR, the error increases from 0.248 to 0.254 for FS and from 0.262 to 0.266 for CS, whereas there is a decrease from 0.277 to 0.255 for G3 when taking the edge voxels out of the norm computation. For reference, the average L_2-norm when comparing CFD_LR with CFD_HR is respectively 0.022 and 0.018 [-], respectively, with and without the edge voxels.
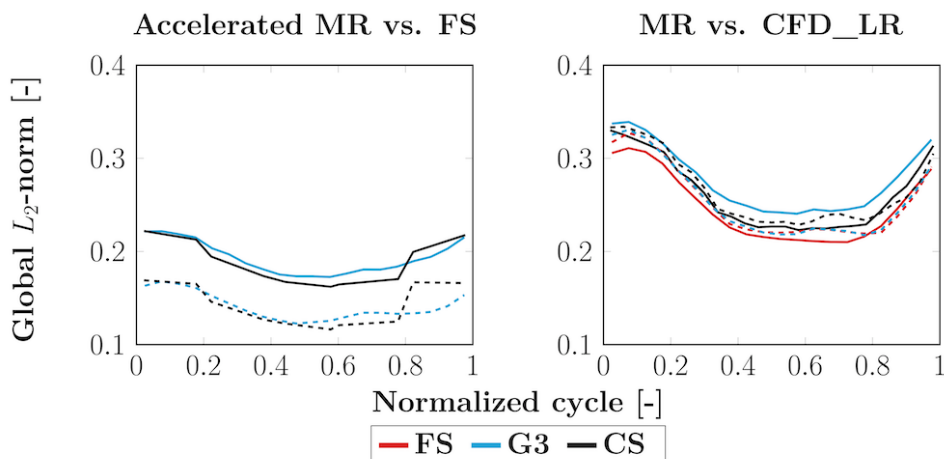
Figure 4.9: Global L_2-norm of the velocity vector differences along the cardiac cycle. On the left, the accelerated MR sequences are compared to the FS MR acquisition. On the right, the MR sequences are compared to CFD_LR. The solid lines refer to the average over all voxels of the segmented volume, whereas the dashed ones correspond to the average over the voxels strictly included inside the phantom segmentation.

123

4.3.3 Flow rates and peak velocities
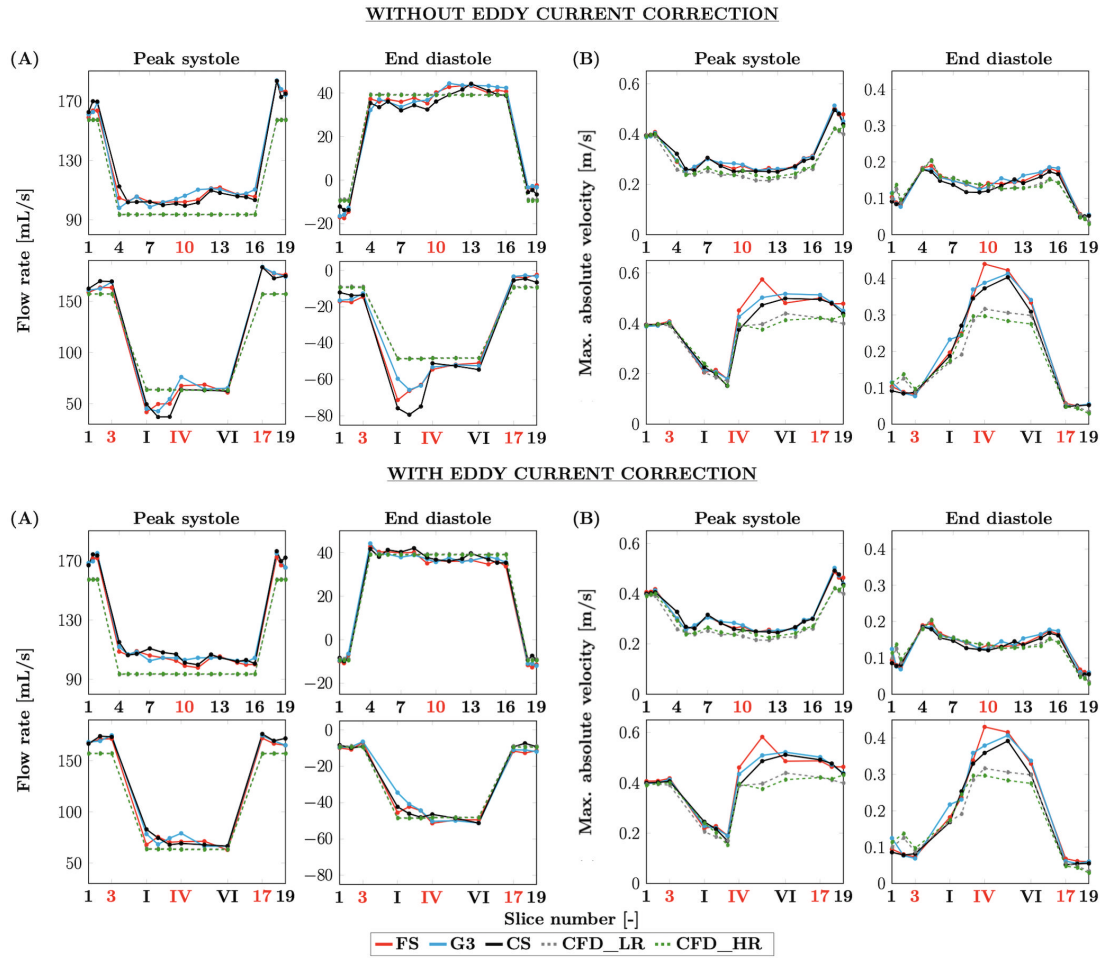
Figure 4.10: Flow rates (computed on all voxels) and peak velocities (computed on inner voxels only) for the velocity fields before (on the top) and after eddy current correction (at the bottom). Both are divided in (A) flow rates and (B) peak velocities at peak systole and end diastole. Above: along the main duct, from planes 1 to 19. Below: along the collateral duct, from planes 1–3, I–VI, and 17–19, as referenced in Fig. 4.3. The slice numbers in red indicate the planes, which were highlighted in Fig. 4.3 and are only meant to make the plots more readable.

Volumetric flow rates and peak velocities are presented in Fig. 4.10(A) and (B), respectively. These quantities are presented for the MR velocity fields before and after eddy currents correction to highlight how this correction acts on the data. The patterns observed for the three MR modalities are globally quite similar. The eddy currents correction helps in regularizing the measured flow rates throughout the phantom, thereby better complying with the principle of mass conservation (note that the CFD method used here is designed to meet this principle). Indeed, the flow rates observed at the inlet and at the outlet are more consistent with

124

each other when the effect of the eddy currents is removed. Also note the drop in the aneurysm-like region (between planes III and IV), which disappears when the correction is applied, leading to better agreement between the measurements along the collateral. At peak systole, the flow rates observed in the main duct tend to be overestimated by the MR acquisitions with respect to the CFD simulation. Concerning the peak velocities, although those from the CFD are globally smaller than those from the MRI, similar patterns are observed. Note that to avoid any noise due to partial volume effects at the phantom wall, the peak velocities are computed only on inner voxels, as for the Bland-Altman plots in Fig. 4.8. Yet, it has been reported that keeping the edge voxels improves the flow rates measurements [169]. Thus, these voxels are included to compute the flow rates displayed in Fig. 4.10.

4.4   Discussion

The aim of this study is to evaluate several acceleration techniques of 4D flow MRI, namely GRAPPA R=2, 3, 4 and prototypal CS R=7.6 sequences, against gold-standard FS k-space as well as CFD simulations. In order to compare all acquisitions under the same well-controlled conditions, a rigid flow phantom is used in vitro and simulated in silico. Such a setup presents many advantages as compared to in vivo situations because it removes some sources of uncertainties associated with wall motion, segmentation errors, and blood rheology. The usual postprocessing (Maxwell terms, distortions, noise masking, phase unwrapping and eddy currents correction) is applied to MR images and the CFD data is phase-averaged and downsampled towards the MRI resolution to enable comparison on the same grid.

Qualitatively, all modalities show good visual velocity agreement along in-plane directions x and z. However, the through-plane (y) velocity v appears to be less replicable from a modality to another. Low velocity-to-noise ratio (VNR) related to generally low v velocities [111] as well as high flow fluctuations could be responsible for these discrepancies.

Quantitatively, the good agreement between both CS and G3 accelerated MRI techniques and the FS acquisition is further confirmed in the Bland-Altman and global L_2-norm plots. For both indicators, a better agreement is found when the voxels located at the phantom walls are removed. The velocities recorded at these points suffer from a poor VNR due to both low velocities and low SNR at the interface. Indeed, the complex signals recorded at voxels straddling the edge include random velocity variations between $\pm V_{ENC}$ due to the plastic phantom walls.

Even though the FS, G3 and CS acquisitions globally agree with each other, some local discrepancies have been noticed. One explanation could be the SNR, which varies depending on the chosen modality. Jung et al. [158] reported higher SNR for Parallel MRI with extended and averaged GRAPPA kernels (PEAK-GRAPPA) as compared to conventional GRAPPA, due to the intrinsic

temporal averaging properties of the first method, which is based on the k-t GRAPPA technique. Since the CS sequence used in this study is also based on a k-t accelerated method, higher SNR is expected for this acquisition, hence higher quality of the PC images. Another ground for the differences between the MR images could arise from the reconstruction framework. Both FS and G3 are reconstructed using the scanner's adaptive combination method [170], which according to Ros et al. [171] leads to signal loss in magnitude images and errors in phase determination. Furthermore, shortening TE has been shown to compensate for higher-order motion encoding [172], and a shorter TE is used for the CS acquisition. Signal loss is also visually noticed for all MR modalities at the outlet region downstream of the collateral branch, especially at peak systole (see Fig. 4.11). O'Brien et al. [173] reported signal attenuation associated with flow errors in high-velocity turbulent jets as studied on a stenotic phantom under steady flow. They suggested that turbulence could be one of the reasons of intravoxel dephasing, leading to signal loss. The dephasing could be further amplified under pulsatile flow, due to temporal accelerations.
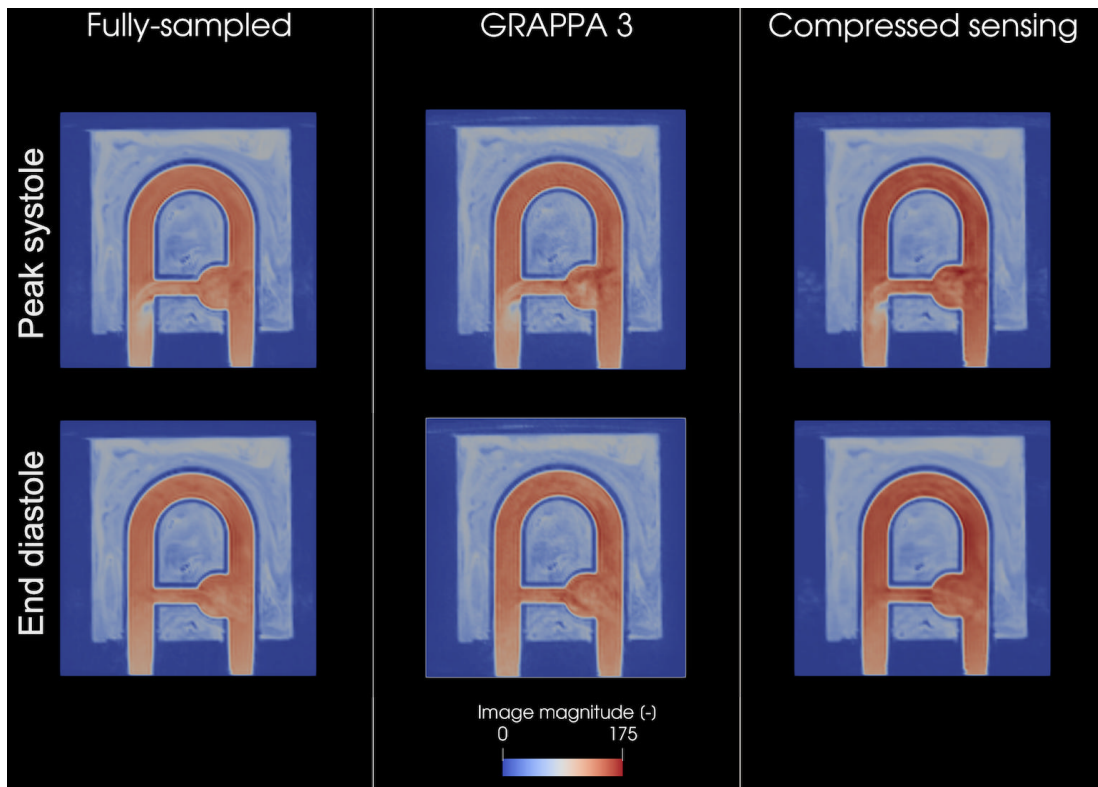
Figure 4.11: Image magnitude before any correction at peak systole (above) and end diastole (below) for the FS, G3 and CS 4D flow MRI acquisitions.

Regarding the comparison with low-resolution CFD, once edge voxels are taken out of the L_2-norm, all MRI modalities present similar outcomes. However, whereas removing the edge voxels reduces the global L_2-norm for each time frame for G3, the error increases for FS and CS for the time instants between peak

systole and end diastole. One explanation of this phenomenon could again come from the averaging of edge voxels. The contribution of the random phase noise in MRI edge voxels can virtually lead to a maximal voxel-wise L_2-error comprised between $[-2V_{ENC}, 2V_{ENC}]$ when comparing two MRI modalities with each other and between $[-V_{ENC}, V_{ENC}]$ when comparing MRI with CFD. Thereby, lower error levels are expected in these voxels in the comparison with respect to CFD. It appears that for FS and CS, the contribution of the edge voxels to the global L_2-norm is lower than the errors arising from the higher velocities found in the inner voxels.

Some discrepancies are also observed between MRI and CFD_LR velocity profiles, notably in the collateral duct and around the junction with the descending main pipe. Concerning peak velocities, they tend to be overestimated by all MRI techniques in regions and time instants associated with high velocity, such as in the main duct at peak systole; or with high acceleration, such as in the narrowing collateral duct (cross-sections IV to VI). These deviations could be related to velocity- and acceleration-induced displacement artifacts [174]. In 4D flow MRI, a spatial misregistration arises when the spins move during the spatial encoding along the different directions. Similarly, velocity-displacement artifacts are induced by acceleration of the spins during the three velocity encodings. Regarding the eddy current correction, it does not appear to affect the trend observed for the peak velocity measurements. Nevertheless, this correction improves the flow rates for all modalities. As the eddy current correction acts everywhere, it benefits the aneurysm-like region in which cross-sections are wider and velocity levels lower; in that region, the improvement of the flow rate assessment is spectacular. Yet, the overall good agreement between MRI and low-resolution CFD for flow rates could also result from compensations of the errors arising from various artifacts (e.g., spatial misregistration, partial volume effects), which do not affect the velocity in the same manner depending on voxel locations. CFD limitations are other sources of differences in the comparisons. A first limitation comes from the boundary condition at the inlet, which is prescribed from experimental data. To study the sensitivity of the inflow waveform onto the predicted flow field, additional CFD simulations have been conducted with the inlet velocity imposed by a 2D cine PC-MRI scan with both a finer voxel size (0.8x0.8x6 mm vs. 2x2x2 mm) and higher temporal resolution (30 reconstructed cardiac phases vs. 20 for the FS acquisition). The 2D cine PC-MRI was acquired during the same protocol as the 4D flow MRI acquisitions, during which the pulsatile flow rate over time was controlled using an ultrasonic flowmeter. Although the 2D cine PC-MRI could not be corrected for eddy currents due to lack of static tissues in the thick acquired slice, no significant differences have been observed between the CFD simulations computed using this experimental acquisition or the 4D flow ones, as illustrated in Fig. 4.12 and 4.13.
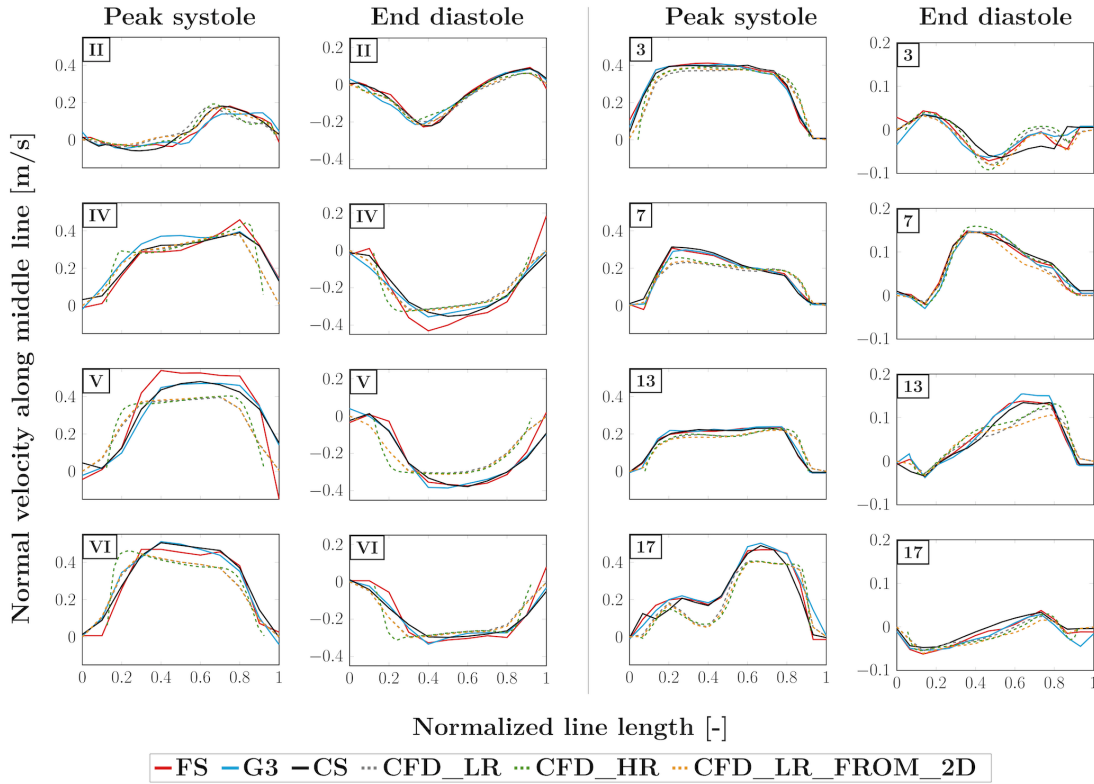
Figure 4.12: Velocity profiles along lines located in the coronal plane passing through the middle of the phantom. The velocity displayed corresponds to the projection onto the normal of the planes perpendicular to the ducts, referenced as in Fig. 4.3. It is the analogous plot of Fig. 4.7, where the curves from the additional downsampled CFD simulations based on a 2D PC-MRI have been added (CFD_LR_FROM_2D). The former curves are kept for reference.

Nevertheless, both the 4D flow acquisitions and the 2D cine PC-MRI scans were acquired with the magnet isocenter centered above the collateral duct. Thus, the inlet boundary of the phantom is more prone to geometric distortion and errors in velocity encoding [127]. Another limitation of our CFD simulations consists of the time instants when the comparisons are made, which could result in a temporal shift between the MRI acquisitions and the simulations. For each cardiac phase, the three velocity directions are sequentially encoded in the PC-MRI acquisition, whereas the simulation displays the velocity vector at the middle of this encoding time window. In particular, the k-space encoding pattern in our acquisitions was the following: flow-compensated reference, y-direction, x-direction, and z-direction. This could potentially explain the flow structures observed in Fig. 4.6, where the MRI patterns seem to be in advance as compared to the CFD, as well as the higher flow rates recorded along the main pipe at peak systole (Fig. 4.10).

WITH EDDY CURRENT CORRECTION
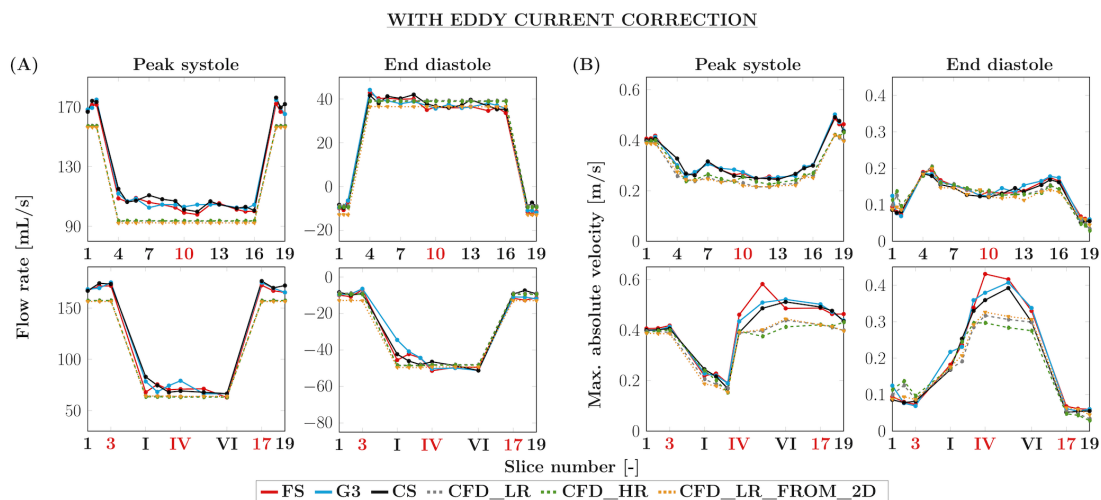
Figure 4.13: Flow rates (computed on all voxels) and peak velocities (computed on inner voxels only) for the velocity fields after eddy current correction, divided in (A) Flow rates and (B) Peak velocities at peak systole and end diastole. Above: along the main duct, from planes 1–19. Below: along the collateral duct, from planes 1–3, I–VI and 17–19, as referenced in Fig. 4.3. It is the analogous plot of Fig. 4.10, where the curves from the additional downsampled CFD simulations based on a 2D PC-MRI have been added (CFD_LR_FROM_2D). The former curves are kept for reference.

As reported by Ma et al. [156] in their flow phantom, good visual agreement and voxel-wise comparison are observed between the CS and conventional 4D flow. Even if some underestimations of the peak velocities by CS with respect to G3 can be noticed in the collateral duct, CS is not clearly found to underestimate the flow rates. An explanation for this discrepancy between the two studies could be the flow phantom and its circuit. The present study is a simplified setup in comparison to the more complex in vivo cardiovascular conditions. By contrast, the phantom developed by Ma et al. was based on the aorta of a healthy subject. Furthermore, the flow was controlled by a pneumatically driven ventricular assist device and pump control unit, whereas a programmable pump is used in the present work. Finally, a realistic aorta pulsatile flow was generated by Ma et al., whereas a sinusoidal flow is investigated in this study. Prescribing an aorta-like inflow waveform, as well as accounting for the blood vessel compliance, could be first steps toward introducing more realistic flow patterns in our phantom circuit. However, the latter would require either knowledge of the wall location during the cardiac cycle or of the mechanical properties of the vessel wall to perform fluid-structure interaction CFD simulations. Also, blood behaves as a non-Newtonian fluid, which makes its rheology more complex than the assumed Newtonian blood-mimicking fluid used in this setup.

In this study, artifacts inherent to all MR modalities have been highlighted. Future work could include implementing postprocessing methods to compensate for artifacts on velocity fields due to acceleration-induced displacement [117] and

to gradient field distortions [127]. Another perspective is to simulate 4D flow MRI to further characterize the observed divergences [86], for instance by considering the Rician distribution of the noise in the magnitude images in MRI [175] or computing acceleration-induced displacement artifacts [118].

4.5   Conclusion

This study demonstrated under in vitro conditions that the highly accelerated CS 4D flow MRI at R = 7.6 shows good agreement with the nonaccelerated FS acquisition, as well as with conventional GRAPPA. However, all modalities suffered from artifacts inherent to the PC acquisition procedure. Further investigations could be carried on in more physiological conditions. Moreover, CFD simulations are a tool of interest to investigate the observed discrepancies, even though it also presents some limitations and care should be taken in modeling the investigated problem.

Impact of the partial echo on simulated 4D flow MRI sequences

Chapter contents

5.1   Introduction

Partial Fourier corresponds to an asymmetric sampling of k-space, as introduced earlier in Section 2.9.1. When this type of sampling is chosen along the phase-encoding and/or slice-encoding direction, it reduces the scan time as less gradient steps along these directions are needed. According to the 2015 consensus statement on 4D Flow MRI [22], a full coverage of the k-space is preferred to ensure high resolution and signal-to-noise ratio (SNR). Should partial Fourier along these two directions be used, the recommendation is to collect at least 75 % of the data. If available on the scanner, it is recommended to prefer the use of an elliptical

k-space, which corresponds to a sampling pattern where the corners of the k-space are omitted, in order to reduce the scanning time. Few recommendations are found about the use of partial Fourier along the readout direction, often referred to as partial echo, asymmetric echo or fractional echo [176]. While it does not reduce the scan time, it is frequently used in 3D MR angiography (MRA) as it mitigates flow artifacts. Indeed, the purpose of this technique is to create an echo occurring before the middle of the readout gradient. As such, it consists in a reduction of the strength and/or duration of the prephasing gradient, and of the potential flow-compensation gradient. This contributes to a reduction of all gradient moments (see Section 2.7), and in particular of the high-order flow artifacts (acceleration, jerk...) when flow-compensation is used [177]. This also mitigates the signal loss in disturbed flows [177, 178]. It reduces the displacement time T_D as well; T_D represents the time delay between the position and velocity encoding times and the echo time T_E, which is by definition the spatial frequency-encoding time [110, 117, 118]. All in all, partial echoes participate in the diminution of the misregistration artifacts. Yet, they lead to an undersampled k-space, and possible errors in the reconstructed velocity fields [179].

Simulation of MRI sequences has emerged as a useful tool to develop and optimize pulse sequences. Several methods specific to phase-contrast MRI simulations have been proposed in the literature. To name a few, Steinman et al. have numerically simulated spatial and velocity displacement artifacts for the encoding times occurring in a 2D and a 3D PC-MRI sequence on an anastomosis geometry [118]. Marshall has simulated a 3D PC-MRI sequence for a normal and a stenosed carotid bifurcation [180]. Petersson et al. proposed a simulation of 3D PC-MRI sequences in the context of non-pulsatile turbulent flow in a stenotic flow phantom [17]. Fortin et al. have performed 2D and 3D PC-MRI simulations on a model of cerebral venous network. These different frameworks and their validation against experimental acquisitions show the feasibility and potential of simulating synthetic PC-MRI images. Going beyond the validation step, numerical simulations have also been used to investigate differences between various sequences. In particular, Klepaczko et al. have developed a numerical framework to simulate MR angiography protocols. They have investigated vessel segmentation algorithms on synthetic 3D time-of-flight (TOF) and PC-MRI images of a normal and a stenosed carotid bifurcation model [181]. They have later expanded their method to evaluate an accelerated 2D PC-MRI with an echo-planar imaging (EPI) readout against conventional 2D and 3D PC-MRI sequences in the context of several models of renal vasculatures [18].

In this work, the impact of partial echo on 4D flow MRI sequences is investigated in the light of MR simulations coupled with CFD. The numerical framework initiated by Puiseux [86] is expanded as presented in Section 3.3. The simulations are conducted in the in-house pulsatile flow phantom geometry presented in Chapter 4. Two flow regimes are imposed at the inlet. The first comes from an almost sinusoidal flow rate, while the second follows a function that models the aortic flow rate. Two realistic 4D flow MRI sequences are investigated: one with

132

full echo, and the other with a partial echo fraction of 0.75.

5.2 Methods

5.2.1 Sequence design

The 4D flow MRI sequences used in this work have been directly provided by Siemens Healthineers. No access to the source code used to generate the sequences has been provided, as the goal of the present study is not to develop a new sequence, but to evaluate realistic clinical sequences. Thanks to the POET sequence simulation tool (Siemens Healthineers, Erlangen, Germany), the parameters of the sequences can be chosen as if one were to use a scanner operator console. The parameters of the two sequences used in this work are summarized in Table 5.1. An explanation about the choices made is provided below.

Partial echo (PE)	No	Yes
Echo symmetry fraction (ESF)	1.0 (full echo)	0.75
Field-Of-View, FOV (mm^3)	$136 \times 56 \times 192$	
Acquired voxel size (mm^3)	$2 \times 2 \times 2$	
Flip angle (°)	7	
Velocity encoding, V_{ENC} (x, y, z) (cm/s)	70-20-70	
Echo time, T_E (ms)	4.20	4.16
Repetition time, T_R (ms)	6.52	6.49
Temporal resolution (ms)	52.16	52.20
Number of acquired cardiac phases	17	
Cardiac period (s)	1.01712	1.01860
Displacement time, T_D (ms)	1.99	1.52

Table 5.1: Sequence parameters. Note that the cardiac period and the displacement time can not be directly specified in IDEA. The displacement time has been computed once the sequence had been generated.

The choice of the parameters aims at matching the experimental parameters presented in chapter 4 [21]. This means that the parameters are adjusted so that the cardiac period matches the cycle duration of 1 s. As in the experimental setup, the acquisition is made in the coronal orientation: the readout, phase-encoding and slice-selecting directions corresponds to the Z, X and Y axes in the scanner reference frame, respectively. Note that there is an oversampling of 2 along the readout direction (Z) by default. The voxels are isotropic (2 mm^3). The V_{ENC} is set to 70 cm/s for the in-plane velocities (along X and Y) and 20 cm/s for the through-plane velocity.

Yet, some modifications have been made. The first modification concerns the size of the FOV. Contrarily to the experimental phantom, there is no static tissue around the flow domain in the digital phantom. Hence, the dimensions of the

FOV have been reduced up to the limit where aliasing would occur. This allows to reduce the simulation time. The size of the FOV with respect to the phantom mesh is presented in Fig. 5.1. Note that the size along (Z) is much larger than the size of the object due to the oversampling.
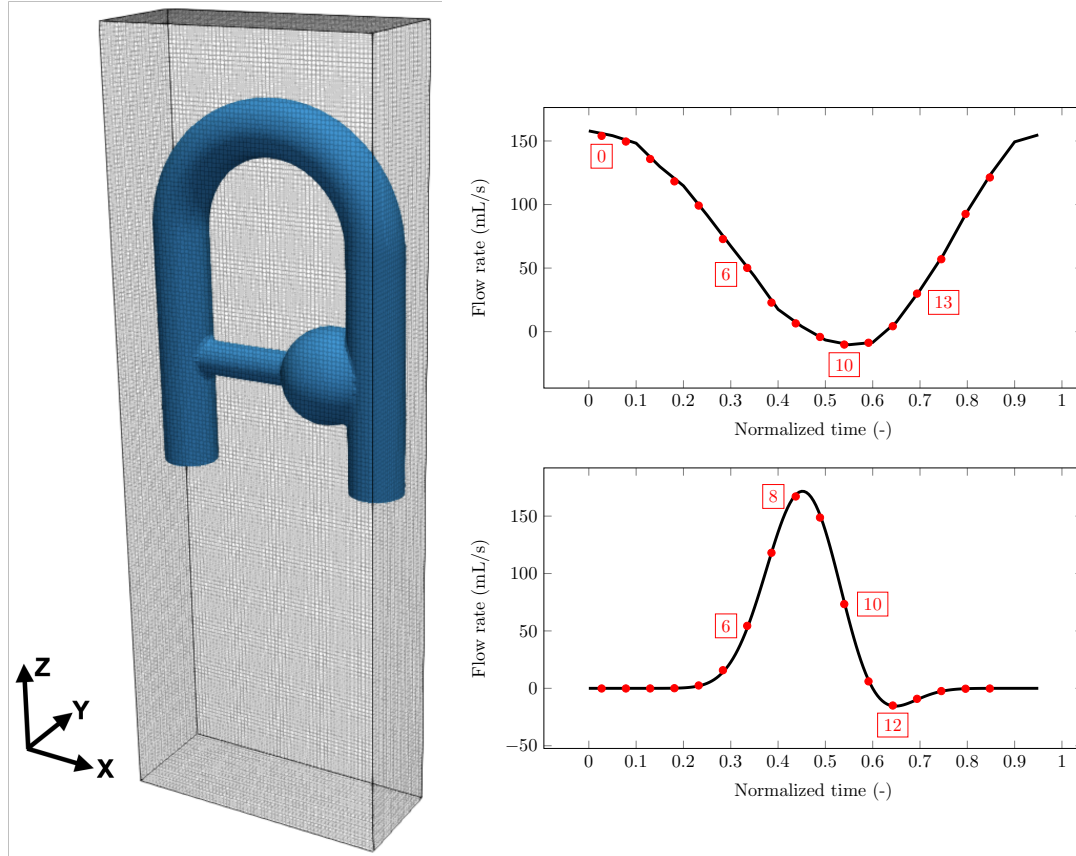
Figure 5.1: Field-of-view, phantom and flow rates. On the left-hand side, the field-of-view and the phantom mesh are depicted. On the right, the two studied flow regimes used as input to the CFD simulations are drawn in black: above the sinusoidal flow rate from experimental data (cf Chapter 4) and below the analytical physiological flow rate (cf Eq. (5.2)). The red dots correspond to the averaged time of each cardiac phase. The number associated to the phases studied hereafter are indicated.

The second modification is due to a limitation of the POET tool used in this work. Indeed, the cardiac cycle duration could not be set, nor could a physiologic signal (e.g., an ECG) be used as input to the simulation. Hence, the temporal parameters have been adjusted in order to achieve a cardiac cycle duration the closest to 1 s. While a retrospective gating has been experimentally used, the prospective gating is found to be more flexible to adjust the parameters, in particular to control the number of acquired (and not reconstructed by view sharing [115]) cardiac phases. Even with this versatility, an uncontrollable and irreducible

time delay exists between two successive cardiac cycles, as experimentally the acquisition stops after collecting the required number of cardiac phases and waits to be triggered by the next desired physiologic event (e.g., next R-wave).

Nevertheless, the fully-sampled sequence with no partial echo is first designed with all the considerations made so far and with the minimal echo time T_E and repetition time T_R. An interleaved symmetric 4-point velocity-encoding scheme is selected [5, 112], which corresponds to the successive acquisition of the same phase-encoding line, yet with four different combinations of velocity-encoding gradients. 2 segments per velocity-encoding direction are collected in each cardiac phase (i.e. $2 \times 4 = 8$ segments).

The cardiac duration closest to 1 s is achieved when 17 cardiac phases per cycle are acquired. The second sequence is set to present a "strong" partial echo according to Siemens' denomination. This corresponds to sampling only half of the negative k frequencies and all of the positive ones. Hence, 75% of the expected full k-space is sampled. In order to compare the two sequences, the same T_R is chosen, but the T_E is reduced to the minimal value available. Note that the small difference of T_R values between the two sequences is due to the rounding up to one digit after decimal in the POET console. Concerning the temporal resolution, the small deviation is likely due to the time delay for retrospective triggering.

In the context of flow MRI, an additional relevant time parameter is the displacement time, which can be defined as the total duration over which the spatial and velocity encoding occur [118]. In the sequences used in this work and as presented by Thunberg et al. [117], all velocity encoding and the spatial encoding along the phase and slice encoding directions can be synchronized. However, by definition, the spatial encoding along the frequency encoding direction occurs during the readout gradient after all other gradients have been played, for a Cartesian sampling. According to Steinman et al. [118], the effective encoding time t_{exp} can be estimated as the time instant when the sensitivity S_2 cancels out, where the sensitivities S_n are defined as:

$$S_n = \frac{\gamma}{n!} \int_{t_0}^{T_E} \Delta G(t)(t - t_{exp})^n dt \qquad (5.1)$$

t_0 denotes the center of the RF pulse and $\Delta G(t)$ is the difference in gradients between the positive and negative velocity encoding lobes associated with the velocity component w encoded along the readout direction. The displacement time T_D is then computed as the delay between t_{exp} and T_E. T_D equals 1.99 ms for full echo and reduces to 1.52 ms for partial echo. While the partial echo resulted in a reduction of the T_E value of about 1%, the reduction in T_D is found to be close to 25%.

5.2.2   MRI-CFD simulations

The simulation were carried out using the MRI-CFD framework implemented in YALES2BIO and presented in Section 3.3. As in the previous chapter, the fluid is

modeled as incompressible and Newtonian with the following characteristics of the blood-mimicking fluid: $\nu = 4.02 \times 10^{-6}$ m^2/s, $\rho = 1020$ kg/m^3, $T_1 = 0.85$ s and $T_2 = 0.17$ s at 1.5 T. The tetrahedral-based mesh of the phantom, generated in Gambit 2.4.6 (ANSYS, Inc., Canonsburg, PA), has a characteristic cell size of 2 mm. The mesh is presented on the left side of Fig. 5.1. 8 particles are seeded by mesh cell, resulting in an initial spin density of 48 particles/voxels to keep a reasonable computing time.

Two pulsatile flow regimes are studied. The first follows the experimental flow rate already presented in Chapter 4, yet dilated to match the cardiac periods, which are slightly above 1 second. From now on, this flow rate is referred to as sinusoidal, since its shape is close to a sinusoid. The second investigated flow is derived from a mathematical model function proposed by Stevens et al., which presents characteristics of the flow into the ascending aorta [182]. The flow rate Q is governed by the following equation:

$$Q(t) = Q_0 \sin^n(\omega t) \cos(\omega t - \phi) \tag{5.2}$$

where $\omega = \frac{\pi}{T_c}$, T_c the period of the cardiac cycle, $n = 13$ and $\phi = \frac{\pi}{10}$ as determined by Stevens et al. Q_0 is a multiplying factor, here tuned to achieve a maximal flow rate comparable to the sinusoidal flow rate, hence minimizing the probabilities to produce velocities higher than the V_{enc}. Both flow rates are presented on the right-hand side of Fig. 5.1.

The use of idealized velocity profiles as inlet boundary conditions have been reported to negatively impact the CFD solution [13]. Hence, one would like to prescribe experimental data instead. Here, only one of the two flow rates comes from experimental data, where pixel-based velocity fields are available. In order to use the same pre-processing method for both flow rates, an averaged normalized velocity field at the inlet is computed. This averaged field is based on the 20 experimentally acquired phases from the non-accelerated sequence presented in chapter 4. The inlet velocity field is then multiplied by the sinusoidal-like and the physiological flow rates, respectively. Note that this means that the CFD simulation conducted in this chapter for the sinusoidal flow is not the same as in chapter 4. Although the flow rate is identical, the velocity profile differs since it is built from the averaged experimental velocity field. In total, four simulations are conducted, that is for both flow rates with and without partial echo (PE). For each simulation, 40 cycles without the coupling with the MRI sequence are first run to evacuate the effect of the initial conditions and for phase-averaging as mentioned in the previous chapter. The last cycle of this CFD simulation is used as input to the four MRI-CFD coupled simulation.

5.2.3 Post-processing

The signal output by the CFD-MRI simulation is reconstructed according to the procedure described in Section 3.3.3. The signal is reorganized in 17×4 k-spaces, i.e. one by cardiac phase and velocity-encoded direction. For the signal

including partial echo, the non-acquired frequencies are zero-filled. While more sophisticated reconstructions of missing k-space frequencies exist, they generally rely on the assumption of Hermitian symmetry of the k-space and of smooth spatial variation of the phase to estimate the phase images. Hence, these methods do not preserve phase information and are not suitable for phase-contrast imaging [89, 183]. Lower noise levels have been reported when reconstructing 4D flow MRI data with zero-filling in contrast to the more complex homodyne reconstruction and projection onto convex sets (POCS) algorithm [184]. No gradient field distortions are modelled in the simulations, hence no correction of the Maxwell terms and eddy currents is required.

The CFD simulations used to compare with the synthetic MRI images (SMRI) are the ones simulated before the coupled CFD-SMRI simulation. From now on, all CFD velocity maps presented refer to the downsampled velocity fields, which have been phase-averaged at the averaged time of the corresponding cardiac phase. The phase-averaging and downsampling processes are performed as detailed in Section 4.2.4.

5.2.4   Comparison methods

The SMRI images without and with the use of partial echo are compared with each other, and also with their corresponding CFD simulation. As highlighted in Fig. 5.1, the FOV is much longer along the (Z) direction. To qualitatively compare all modalities, the SMRI images are thresholded by a binary mask made from the phase-averaged and downsampled CFD velocity fields averaged over the cardiac phases. As already mentioned in the comparison methods in the previous chapter, the normalized L_2-norm, hereafter called root-mean-square error (RMSE), is computed. In order to compare the four SMRI, the normalization is made with respect to the highest expected velocity, that is $V_{ENC} = 0.7$ m/s. For two fields A and B, it reads:

$$RMSE(\boldsymbol{x}, t) = \frac{\sqrt{(u_A - u_B)^2 + (v_A - v_B)^2 + (w_A - w_B)^2}}{\max\left(V_{ENC}\right)} \qquad (5.3)$$

where $\boldsymbol{u} = (u, v, w)$ is the velocity vector associated to the node at the position $\boldsymbol{x}$. The normalized absolute velocity difference along each direction is computed using the same normalization.

5.2.5   Metrics to investigate the sources of errors

The discrepancies observed between CFD and SMRI can occur from various sources or phenomena, such as the acceleration, the turbulence, or the multiple encoding times inherent to the image acquisition process. Acceleration-induced artifacts due to the time delay between velocity and spatial encoding have been reported in the literature [118, 174]. As for turbulence, signal loss and consequent flow errors have been observed in stenotic jets [17, 173].

During the CFD simulation, the acceleration $\frac{D\boldsymbol{u}}{Dt}$ is computed as the sum of the local $\frac{\partial \boldsymbol{u}}{\partial t}$ and convective $(\boldsymbol{u} \cdot \nabla)\boldsymbol{u}$ accelerations. The local acceleration is computed using a first-order upwind finite difference scheme. The acceleration field is phase-averaged in the same manner as the velocity field.

The instantaneous velocity field computed during the simulation can be seen as the sum of the phase-averaged velocity $\overline{\boldsymbol{u}}$ and of an additional fluctuating part u'. The resolved turbulent kinetic energy (TKE) can then be computed as

$$TKE(\boldsymbol{x},t) = \frac{1}{2}\left(\overline{u'^2}(\boldsymbol{x},t) + \overline{v'^2}(\boldsymbol{x},t) + \overline{w'^2}(\boldsymbol{x},t)\right) \tag{5.4}$$

where $\overline{\cdot}$ stands for the phase-averaging.

Finally, another source of discrepancy comes from the multiple encoding times. For instance, the images I_i and I_{ref} in Eq. (3.83) are not acquired at the same time with respect to one cardiac phase duration. To assess this difference, CFD solutions are output for the averaged time of each segment. That corresponds to 8 solutions for each of the 17 phases. The sequences have been created following a symmetric 4-point velocity-encoding scheme, which is similar, yet not exactly equivalent to the balanced 4-point velocity-encoding scheme in [112]. Similarly to this scheme, each acquisition does not encode a specific direction, but a linear combination of velocities. Thereby, for each acquisition, bipolar gradients are played along the 3 directions, with different polarities. Here, the combinations are chosen so that for 4 successive acquisitions, v_x is reconstructed using the first and the second acquisitions, v_z using the first and the third and v_y using the first and the fourth. The first acquisition somehow plays the role of reference, even though it includes bipolar gradients along the 3 encoding-directions as well. On top of that, 2 segments are acquired by cardiac phase. That means that the acquisition pattern is repeated twice. One can then consider that to reconstruct a given velocity at a given cardiac phase, data acquired at 4 distinct time instants (or more exactly 4 distinct time periods) are needed. In an attempt to quantify the impact of these differences in time on the velocity fields, the 8 solutions per cardiac phase are grouped to construct 4 mean velocity fields corresponding to the 4 successive acquisition (the mean is performed on the 2 segments of the same acquisition gradients pattern for a given cardiac phase). Then error maps are constructed for each velocity-encoding direction. For instance for v_x, the mean velocity field corresponding to the first acquisition is subtracted to the mean velocity field corresponding to the second acquisition. For v_z, the mean velocity field corresponding to the "reference" acquisition is subtracted to the third acquisition. This leads to three "time difference" maps for each cardiac phase. In this work, $\Delta \boldsymbol{u}$ denotes the mean of these three "difference" mappings of the velocity fields, and should not be confused with the Laplacian operator.

Figure 5.2: Velocity maps for the sinusoidal flow rate in the coronal middle plane. The phases presented are the ones highlighted in Figure 5.1. $||\boldsymbol{u}||$ is the magnitude of the velocity vector $[u, v, w]$.
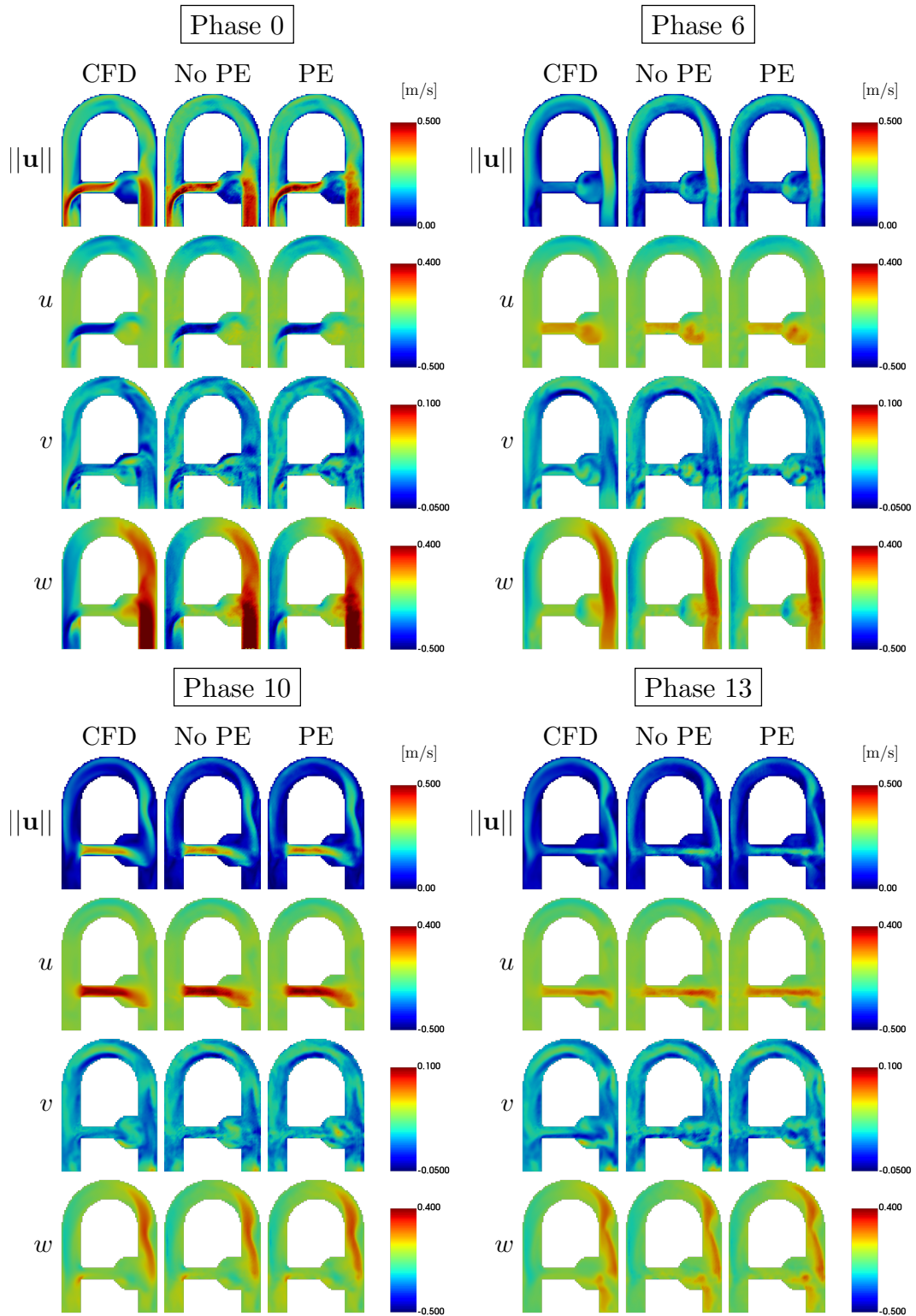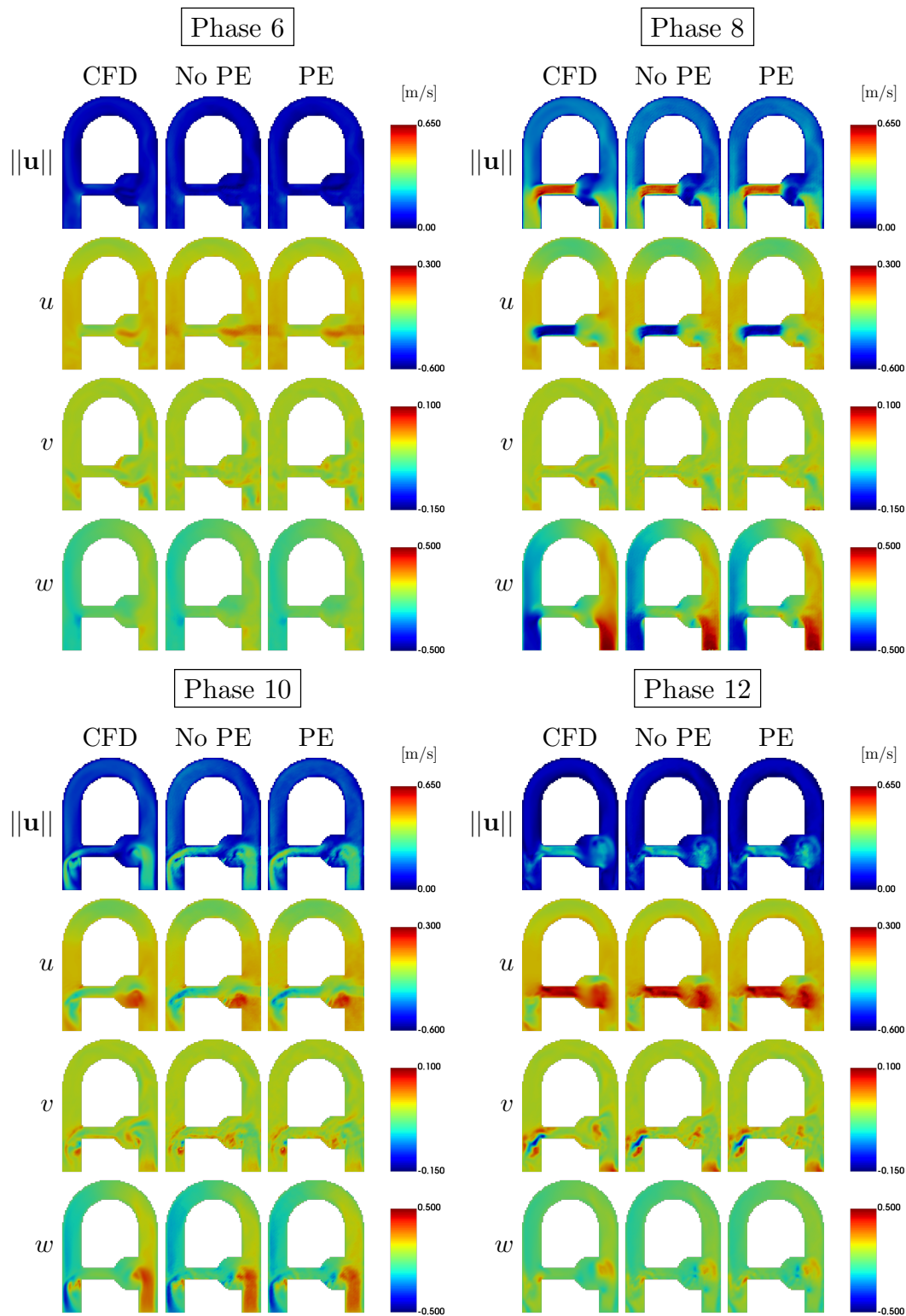
Figure 5.3: Velocity maps for the physiological flow rate in the coronal middle plane. The phases presented are the ones highlighted in Figure 5.1. $||\boldsymbol{u}||$ is the magnitude of the velocity vector $[u, v, w]$.

5.3   Results

5.3.1   Flow structures

The velocity maps for the sinusoidal and physiological flow rates are shown in Fig. 5.2 and 5.3, respectively. Recall that two CFD simulations for each flow are performed to meet the slightly different parameters of the sequences with and without PE. As both simulations are very similar, only the CFD corresponding to the acquisition with PE is presented. Overall, the main flow structures are well represented by SMRI, without and with the use of partial echo. Despite the downsampling, the SMRI velocity fields appear more blurry. Some discrepancies can already be noticed, such as in the collateral for the phase 0 in Fig. 5.2 or in the aneurysm-like region for the phase 10 in Fig. 5.3.

5.3.2   Impact of the use of partial echo

To quantify the differences when using partial echo or not, the normalized absolute differences and the RMSE are computed. The evolution of the errors over time are displayed in Fig. 5.4 and 5.5, respectively for the sinusoidal and for the physiological flow rates. Error maps matching the velocity maps already presented above are shown in Fig. 5.6 and 5.7. From the graphs over time, it appears that the lowest errors are found for the sequence with partial echo for both the sinusoidal and the physiological flow, with the exception of phase 13 of the sinusoidal flow. As expected, the lowest contribution to the average error comes from the low velocities of the velocity component v. The highest contribution comes from the velocity component w, which corresponds to the readout direction z. It is also this contribution that is significantly reduced when partial echo is used. Along x and y, the errors are almost not impacted by the use of partial echo. For the physiological flow, the highest RMSE is found at the phase 10, when the inlet flow is decelerating after peak systole. Concerning the sinusoidal inlet flow rate, while the highest errors are found at peak systole for the full echo readout, they are happening at phase 13 for the partial echo. This phase is characterized by both an increase in the flow rate at the inlet, and backward flow in the collateral and aneurysm according to the velocity maps in Fig. 5.2, and thereby potential sign changes of the velocity components. Contrary to the other cardiac phases for the sinusoidal flow where most of the errors occur around the collateral duct in the partial echo sequence, the errors are spread all over the phantom both for u and w. More generally, the use of partial echo for both types of inlet flow rate reduces the errors in the U-bend, which are mostly found for the w-component. Furthermore, the errors in the collateral and around (aneurysm and jet) seen for the RMSE between SMRI and CFD are not observed for the RMSE between the SMRI. This is especially noticeable for the physiological flow rate. While it shows a relatively good agreement between the two sequences in these regions, it also indicates that there is a discrepancy with the CFD velocity on which SMRI is based.
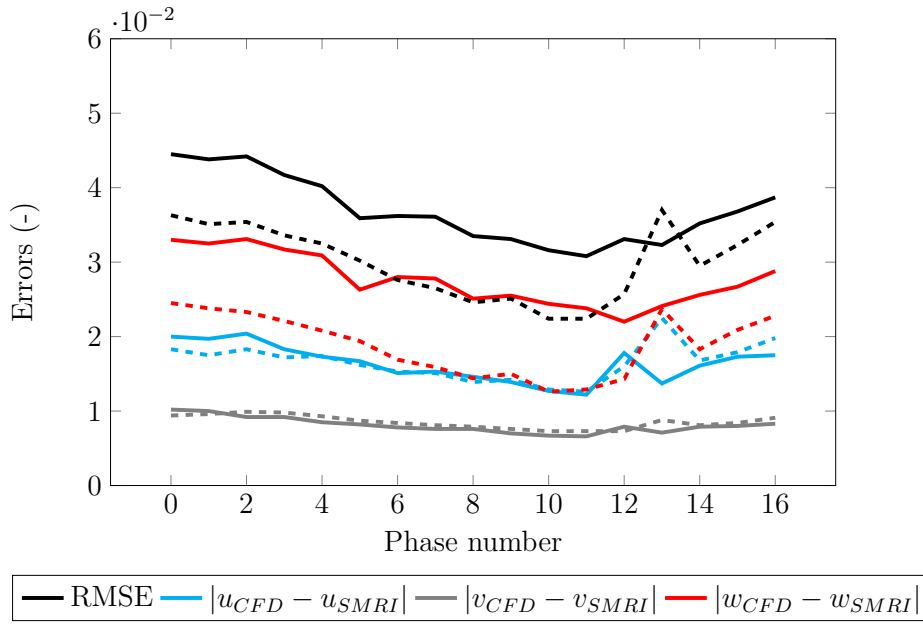
Figure 5.4: Evolution of the errors throughout the cardiac cycle for the sinusoidal flow rate. The plain lines represent the acquisition without PE, while the dashed lines represent the acquisition with PE. All errors are normalized by the maximal $V_{ENC} = 0.7$m/s.
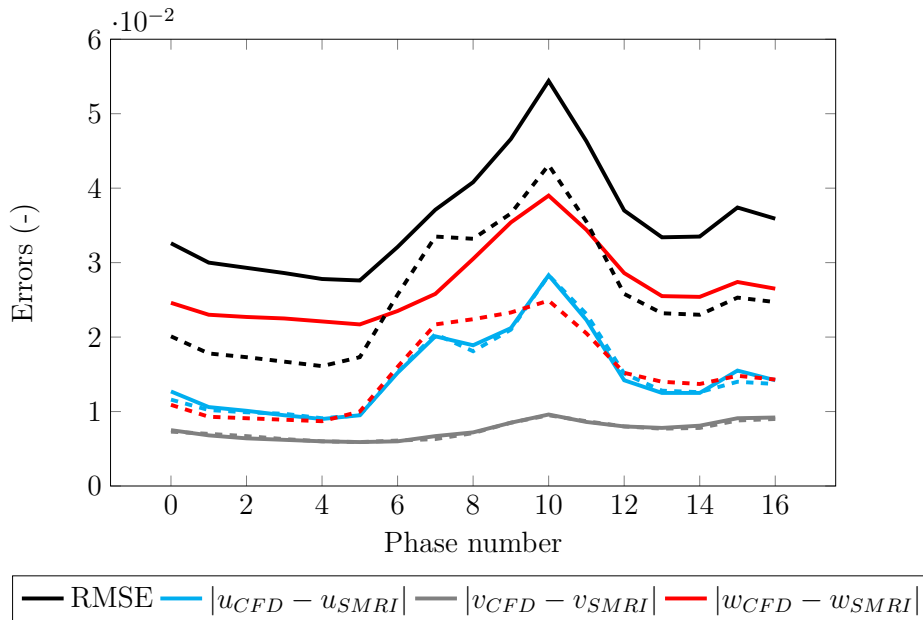
Figure 5.5: Evolution of the errors throughout the cardiac cycle for the sinusoidal flow rate. The plain lines represent the acquisition without PE, while the dashed lines represent the acquisition with PE. All errors are normalized by the maximal $V_{ENC} = 0.7$m/s.
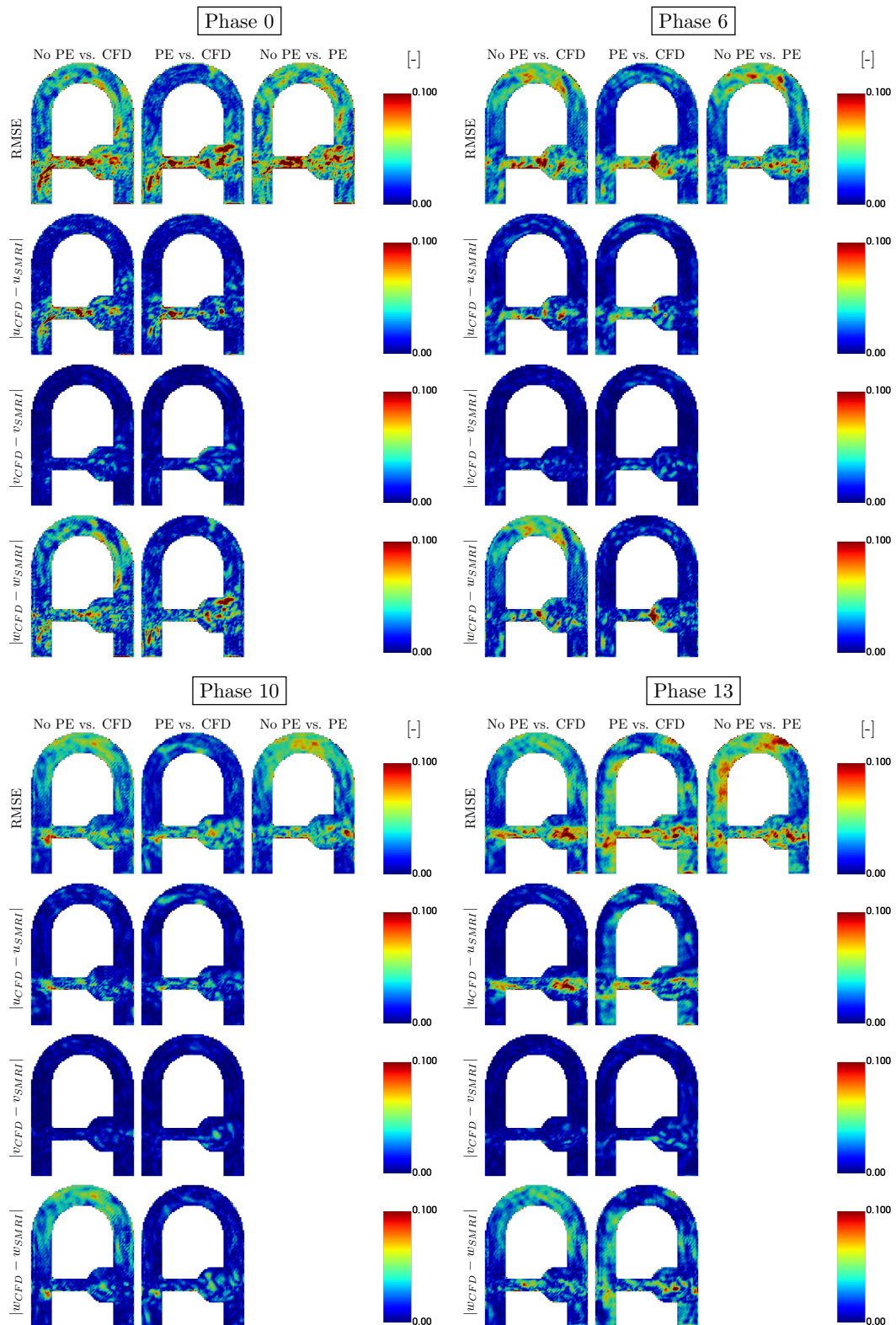
Figure 5.6: Error maps for the sinusoidal flow rate. For each phase, the 1$^{\text{st}}$ and 2$^{\text{nd}}$ columns compare the SMRI, respectively without and with PE, against the corresponding CFD. The last column compares both SMRI fields. All errors are normalized by the maximal $V_{ENC} = 0.7$m/s.
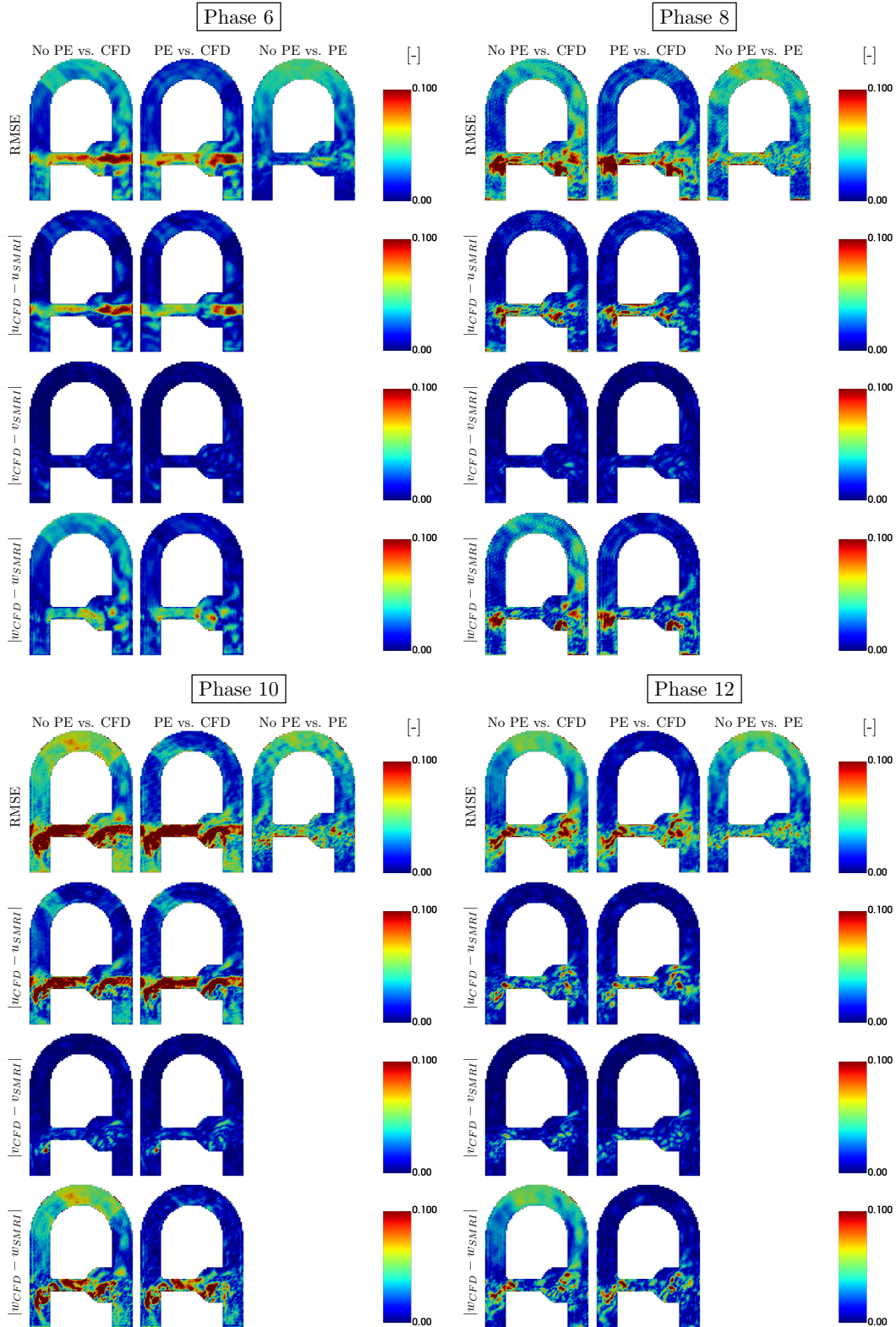
Figure 5.7: Error maps for the sinusoidal flow rate. For each phase, the 1st and 2nd columns compare the SMRI, respectively without and with PE, against the corresponding CFD. The last column compares both SMRI fields. All errors are normalized by the maximal $V_{ENC} = 0.7$m/s.

5.3.3 Origins of errors inherent to the SMRI procedure

As underlined in the last paragraph, while partial echo seems to reduce the RMSE and the errors on w between SMRI and CFD overall (cf. Fig. 5.4 and 5.5), discrepancies are still present between both modalities. In an attempt to understand the origins of these errors inherent to the SMRI procedure, three metrics detailed in section 5.2.5 are investigated: the norm of the acceleration $\left\|\frac{D\mathbf{u}}{Dt}\right\|$, the norm of the velocity difference due to the timings of the different segments within a cardiac phase $\|\Delta\mathbf{u}\|$, and the turbulent kinetic energy (TKE). Thresholds on the RMSE and these three metrics are displayed in Fig. 5.8 and 5.9, respectively for the sinusoidal and the physiological inflow. The threshold on the RMSE corresponds to regions, where the error is higher than 7.5% of the V_{ENC}. Concerning $\left\|\frac{D\mathbf{u}}{Dt}\right\|$ and $\|\Delta\mathbf{u}\|$, the areas correspond respectively to accelerations and velocities, which would induce a displacement greater than a voxel over the duration of one cardiac phase. Finally, the highlighted regions for TKE are the ones above 10% of the mean kinetic energy injected at the inlet.
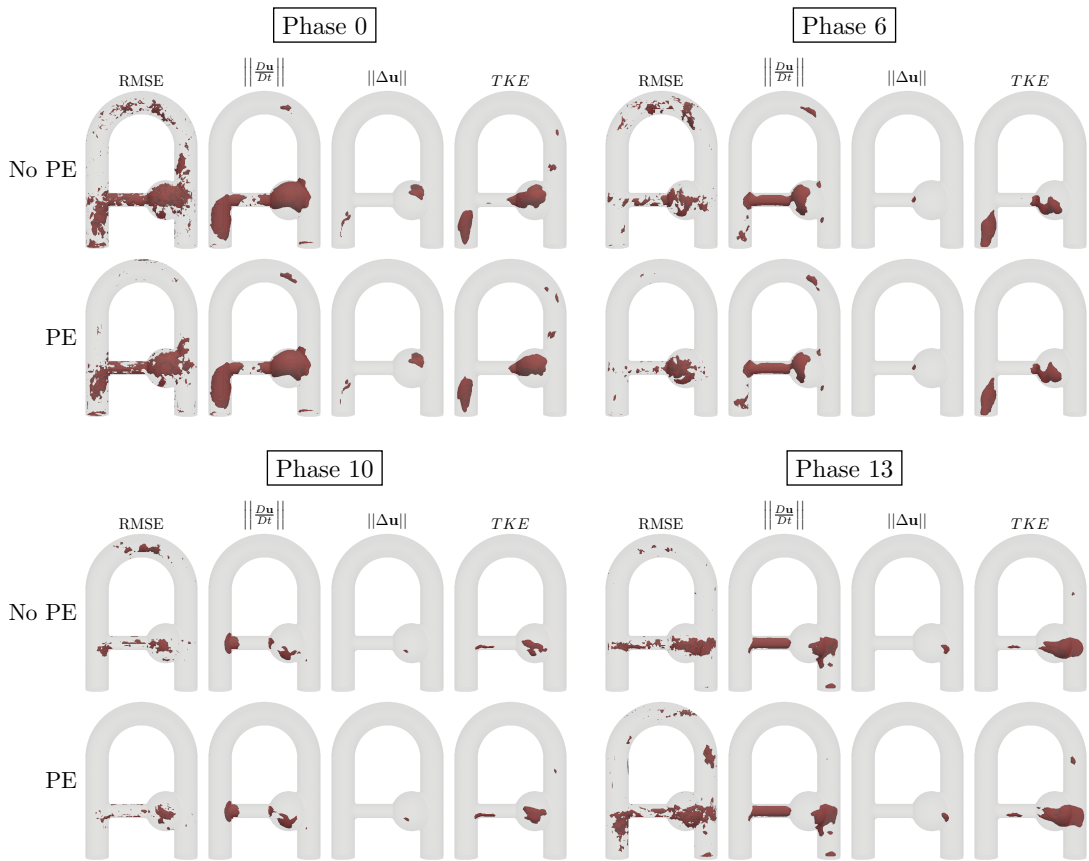
Figure 5.8: Thresholds on the RMSE ($\geq$7.5%), acceleration ($\geq$1.48 m/s^2), velocity difference ($\geq$0.038 m/s) and TKE ($\geq$0.002 m^2/s^2) for the sinusoidal inflow.

The acceleration catches numerous patterns similar to the regions of high RMSE, in particular in the collateral, and in the jet and recirculation when presents.

For the sinusoidal inflow, it seems to be related to the errors in the collateral for the decelerating phase 6 and accelerating phase 13. For the physiological inflow, both $\left\|\frac{D\mathbf{u}}{Dt}\right\|$ and $\|\Delta\mathbf{u}\|$ are correlated with the errors in the collateral for the accelerating and decelerating phases (6 and 10). The TKE mainly explains the errors occurring in the aneurysm-like region, such as in phases 6 and 13 for the sinusoidal flow, and to a lesser extent in phase 8 for the physiological inflow.

Of course, the 3 metrics are not independent, and their simultaneous effects impact the discrepancies between the SMRI and CFD fields. One can note that regions of high acceleration, for instance at the inlet of the physiological flow (phases 6 and 10), do not necessarily result in a high level of error. Furthermore, some regions of high RMSE appear to be uncorrelated with the metrics presented in this study.
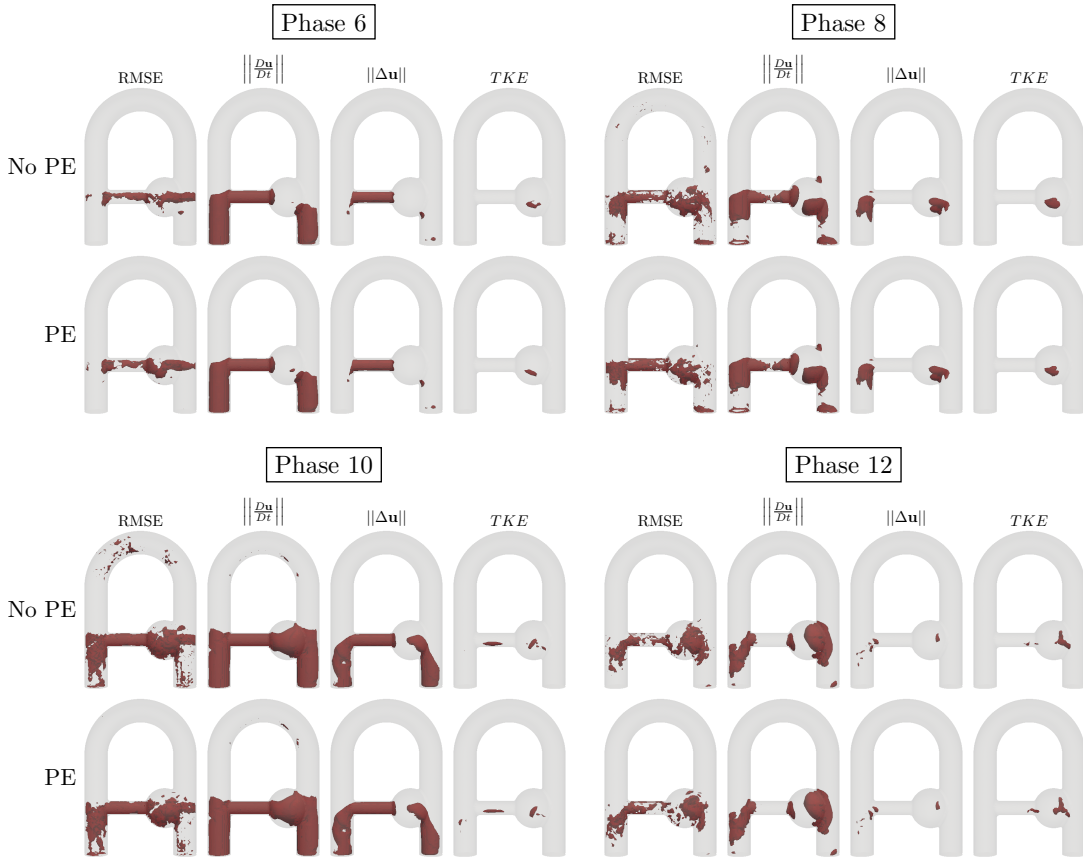
Figure 5.9: Thresholds on the RMSE ($\geq 7.5\%$), acceleration (≥ 1.48 m/s^2), velocity difference (≥ 0.038 m/s) and TKE (≥ 0.0008 m^2/s^2) for the physiological inflow.

5.4   Discussion

The aim of this work is to investigate the use of partial echo in the context of 4D flow MRI. In silico CFD-MRI simulations are conducted on a rigid flow phantom

for two kinds of pulsatile inflow (sinusoidal and close to the ascending aorta flow rate). A full echo and a partial echo covering only 75% of the expected readout are simulated, with all other parameters kept identical up to the restrictions of the sequence design software. This numerical setup allows to investigate the impact of this sequence parameter on the MRI process without experimental artifacts. Indeed, no motion of the phantom itself is simulated, nor are Maxwell terms, eddy currents or gradient nonlinearities. The reconstructed synthetic SMRI velocity fields are compared to the phase-averaged and downsampled velocity fields derived from the CFD fields used to simulate the MRI process.

Qualitatively, the SMRI images are in good agreement with the CFD velocity fields for all components and for both inflows, without and with partial echo. Quantitatively, higher levels of absolute errors are found for the component w of the velocity for the full echo than for the partial echo. Concerning the other two components u and v, the errors levels are pretty similar between both acquisitions. Furthermore, the errors on w are the highest with respect to the other components, although they seem to be reduced to levels comparable to the component u when using partial echo. While u and v are encoded along phase-encoding directions, w is encoded along the frequency-encoded direction. Hence, whereas the spatial and velocity encodings are synchronized for the two first components, there is an incompressible delay between the velocity and the spatial encodings, which occurs around T_E, along the z direction. In the two investigated sequences, the gradients along x (phase-encoding direction) and y (slice-selecting direction) have the same gradient amplitudes and durations. Along the z-axis, not only is the readout gradient shorter, yet with same strength, but the gradients occurring before (prephasing, flow-compensation and velocity-encoding) present a visible reduced amplitude. These differences between the two sequences induce a decrease of the displacement time T_D of about 25% for the partial echo, which can be accountable for the lower errors reported on w [117].

The acceleration shares a lot of common patterns with the RMSE. Indeed, the main assumption of PC-MRI relies on slow changes of the velocities with respect to the temporal resolution, which allows considering velocities as constant and to neglect the higher-order terms [185]. Yet, even in the context of steady flow, convective acceleration can occur in complex geometries, for instance in stenoses or curved vessels [186, 187]. Furthermore, when handling pulsatile flows as in the aorta, the time dependence of acceleration cannot be neglected. While for GRE sequences the temporal resolution matches the repetition time T_R, the common four-point encoding scheme used in the present work result in a four-fold increase, which has to be multiplied by the number of segments per point. Due to the phantom design with its complex geometry and the pulsatile inflows studied in this work, it is not reasonable to assume that velocities are constant over a cardiac phase.

In this work, the metric $||\Delta \mathbf{u}||$ is presented in an attempt to assess the errors due to the velocity variation from segment to segment. While this quantity is close to zero for all phases of the sinusoidal inflow, its level increases around the systolic

peak for the physiological inflow. While it seems to be related to the RMSE, its impact on the error is probably already accounted for in the acceleration.

According to the TKE values, turbulence occurs mainly in the aneurysm-like region, as well as in the jet exiting the collateral. TKE appears as complementary to the acceleration to understand the RMSE. Note that this quantity could not be assessed based on the intravoxel spin velocity standard deviation (IVSD) method proposed by Dyverfeldt et al. [71, 73, 188] due to the symmetric 4-point encoding scheme used in this study. This scheme leads to the same first gradient moments for each segment, which is the only restriction in the use of this method. An asymmetric 4-point encoding scheme could be investigated in a future work to evaluate TKE with this method as well.

Some RMSE regions remain not explained by the three metrics proposed in this work, for instance in the aneurysm and its prolongation above the inlet in phases 6 and 10 of the physiological inflow. The errors in this area could be related to the ghosting artifact. Indeed, the periodic motion of the pulsatile inflow can create coherent phase-shifting in the acquired k-space [189, 190]. The magnitude images corresponding to the reference k-space for the two phases mentioned above, as well as the velocity magnitude fields, are displayed in Fig. 5.10. While at first sight only the expected phantom geometry is observed, saturating the signal intensity reveals one replicate. The inlet and outlet are especially highlighted in the magnitude images. The fact that the replicate propagates along the phase-encoding axis indicates that it is due to an inter-view motion, that is on a timescale longer than T_R [189]. Since two copies of the phantom are noticed, it is likely that the ghosting is related to the fact that 2 segments are encoded per cardiac phase.

There are some limitations to this work. Although more realistic than the sequences used in the preliminary study conducted by Puiseux et al. [86], the sequences are still idealized concerning the spoiling. Indeed, a numerical perfect spoiling is performed instead of being simulated. Furthermore, the frequency of the pulsatile inflow is perfectly matched to the prospective sequence, which does not allow for the consideration of irregular heartbeats. While their absence makes it possible to distinguish sources of errors which only arise from the sequence and the MR process in itself, gradient field distortions (see Section 2.8.4) could be modelled to investigate their impact on the reconstructed velocity fields. In order to achieve a reasonable computing time, a coarse mesh has been used in this study with a characteristic cell size of 2 mm. It would be of interest to conduct additional simulations with finer spatial resolutions. Yet, the CFD resolution used is still below the SMRI resolution, which should mitigate the errors. Furthermore, the spin density exceeds the recommendation of 3 particles/direction/voxel made in [19] to keep an error on the MR signal below 1.5%. Another limitation of the phantom used in this study is its rigid walls. Studying a geometry with moving walls and thereby with properties closer to the elastic walls of the aorta or the heart muscle would be of interest to assess the impact of motion artifacts on the reconstructed velocity fields.

Despite these limitations, the CFD-MRI framework used in this work appears
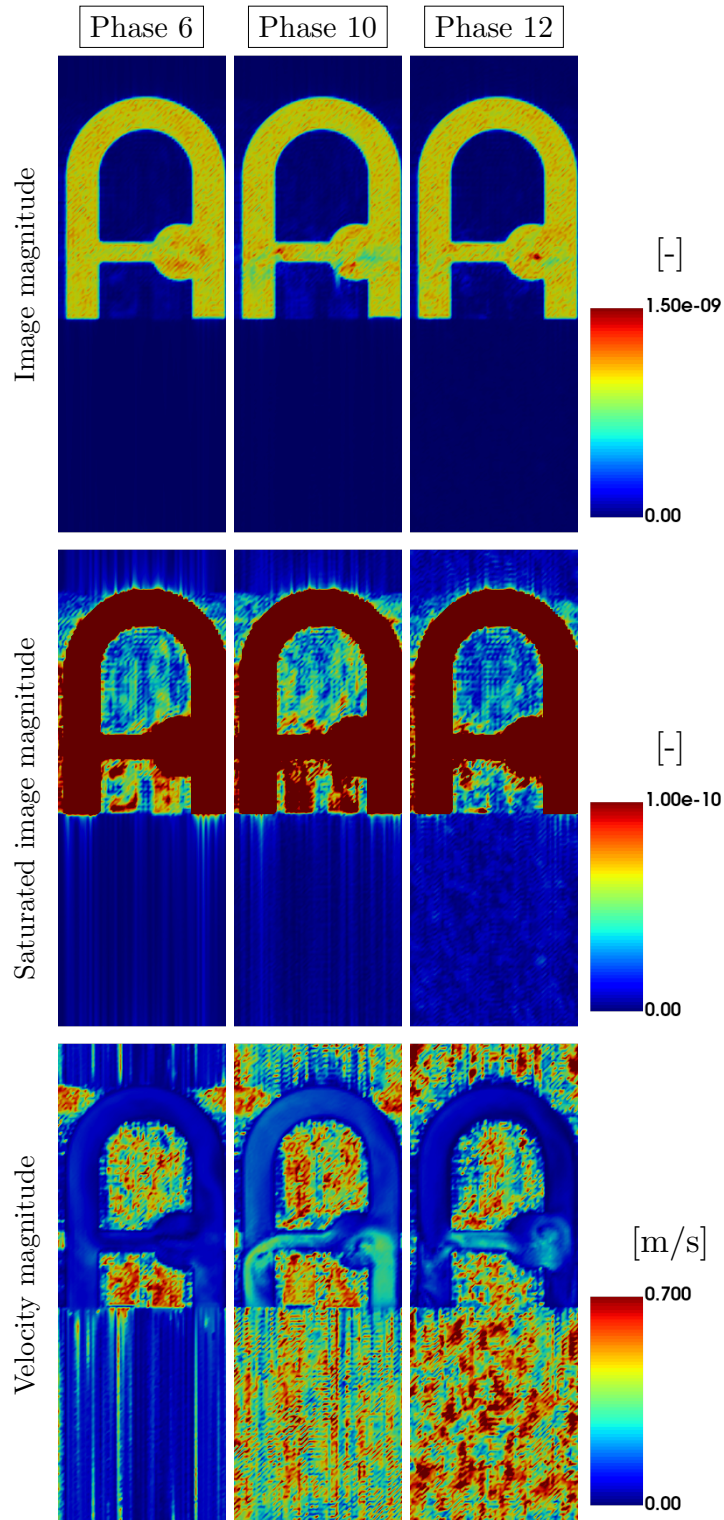
Figure 5.10: Ghosting artifact as seen on magnitude images and velocity magnitude for the physiological inflow. The artifact is visible for phases 6 and 10. Phase 12 is presented as a reference image free of ghosting.

as a useful tool to investigate the design of 4D flow MRI sequences. The present study could be expanded by investigating other strategies to fill the k-spaces. If filled in a Cartesian manner, different interleaved patterns could be investigated, as well as asymmetric encoding scheme for the velocity-encoding. Additionally, the CFD-MRI framework used in this work has the potential to simulate radial or spiral samplings as well. Concerning the phantom presented in this study, other geometries could be investigated such as stenoses. For both flows investigated in this study, partial echo provides better outcomes than full echo as it reduces the displacement artifacts along the readout direction. Yet, reconstructed SMRI velocity fields are not free from errors as compared to the CFD fields, and artifacts inherent to the 4D flow MRI process could be reproduced. These synthetic 4D flow data could be used as input datasets to train machine learning models and physics-informed neural networks [24, 191, 192].

Chapter

6

Conclusion

Chapter contents

The present thesis focuses on 4D flow MRI. The performances of this sequence are assessed with an in vitro experimental set-up, CFD simulations fed with experimental data, as well as SMRI-CFD simulations. Acceleration techniques and their impact on the reconstructed velocity fields are questioned. The effect of the use of the partial echo is evaluated thanks to numerical simulations.

6.1 Main results

6.1.1 Acceleration of 4D flow MRI sequences

In chapter 4, hemodynamic biomarkers are evaluated in accelerated 4D flow MRI sequences, namely GRAPPA with an acceleration factor R = 2, 3, 4 and compressed sensing with R = 7.6. The same biomarkers are also quantified for a nonaccelerated fully sampled k-space acquisition, and for matching CFD simulations based on these five experimentally measured flow fields. All in vitro and in silico experiments are conducted on an in-house pulsatile flow phantom, whose geometry allows investigating complex flow patterns similar to the ones found in the cardiovascular system. Similar hemodynamic patterns are observed for all modalities. Concerning voxel-wise comparisons, the highest discrepancies between the MRI scans are found in the voxels located near the boundary walls of the flow phantom. When compared to the CFD velocity fields, all MRI scans tend to overestimate velocity profiles as well as peak velocities in the regions associated

with high velocity or/and high acceleration. Finally, this study highlights the importance of correcting the eddy currents in the MR images to report flow rates that comply with the principle of mass conservation. Once this correction is performed, good agreement is found between the experimental in vitro flow rates and the ones reported by the CFD simulations [21]. This study suggests that the highly accelerated compressed sensing acquired in 5 min 35 s provides reconstructed velocity fields in good agreement with the almost 43-minute-long fully sampled acquisition. Such a short scan time could help to generalize the use of the 4D flow MRI technology into the clinical routine. Yet, the findings of this study are limited by the use of a rigid phantom with a sinusoidal inflow. Further investigations seem necessary to assess accelerated 4D flow MRI sequences in conditions representative of the in vivo.

6.1.2   Impact of the partial echo on simulated 4D flow MRI sequences

In chapter 5, the CFD-MRI simulation framework initially developed by Puiseux [86] is expanded to simulate more realistic 4D flow MRI sequences issued by manufacturers. The framework is used to investigate the partial echo, a well-known parameter commonly used in angiography, but whose impact on 4D flow MRI reconstructed velocity fields remains unclear. The simulations are conducted in the in-house flow phantom for two types of inflow: an experimental almost sinusoidal one and another one which models the flow rate in the ascending aorta. For both inflows, two 4D flow MRI sequences are investigated: a full echo and a partial echo, which samples only 75% of the full echo. For each inflow, similar hemodynamic patterns are visually observed for the full echo and the partial echo, as well as for their matching CFD simulations. Higher levels of errors with respect to the CFD simulations are reported for the full echo than for the partial echo over the whole cardiac cycle. The use of partial echo mitigates the errors made on the velocity component encoded along the readout direction. Yet, both MRI sequences are not free from errors as compared to the CFD simulations. The turbulent kinetic energy (TKE) and the acceleration appear as complementary good indicators of the regions associated with high levels of errors. Due to the pulsatility of the inflow, ghosting artifact occurs and is potentially responsible for the errors, which could not be explained by the TKE or the acceleration. In a nutshell, the MRI simulation framework has proven its potential in decision-making for parameters optimization, while allowing to reproduce artifacts inherent to the MR process.

6.2   Perspectives

This thesis takes place in the continuity of Puiseux's PhD thesis [20], where proofs of concept for quality control and simulation of 4D flow MRI have been initiated.

In the present work, accelerated sequences of 4D flow MRI have been investigated. Assessing the quality of these sequences is crucial, as the translation of 4D flow MRI into the daily clinical practice is hampered by its long scan time and accelerated sequences have the potential to overcome this issue. Besides, being able to quantify the errors made in such sequences would allow building trustful biomarkers, or at least with known accuracy range, which could be used for decision-making by clinicians. In chapter 4, the comparison of experimental MRI with CFD also allows to highlight the presence of field distortions and errors on flow rates when no appropriate corrections are applied. Hence, this comparative environment appears as a tool of interest to investigate correction algorithms.

The second axis of this work is the development of an MRI simulation framework to simulate realistic constructor sequences. Thought to help with sequence design and optimization of sequence parameters, this framework is used to investigate the partial echo parameter, a parameter which lacks consensus about its usage [22, 176]. Other parameters could be investigated using the same framework: voxel size, number of segments etc. It could also be used to investigate k-space sampling patterns: Cartesian strategies, but also radial or spiral sampling. The MRI simulation framework could be further expanded to simulate other types of MR sequences, such as other magnetic resonance angiography (MRA) sequences, echo-planar imaging (EPI) or diffusion MRI.

While more realistic sequences are simulated in the present thesis, the MRI simulator still does not model some common physical phenomena, such as concomitant gradients, eddy currents or gradient nonlinearities. Adding these sources of gradient field distortions would allow investigating how they affect the reconstructed images and velocity fields, but also to test correction algorithms. Coil sensitivity profiles could also be added into the simulations to investigate parallel imaging reconstruction methods.

With the emergence of machine learning and physics-informed neural networks, the MRI simulation framework appears now as a valuable tool to generate synthetic training datasets, or to build signal dictionaries [16, 23, 24].

Appendix

7.1   Reformulation of the electromotive force

In this appendix, the reformulation of the emf from Eq. (2.22) to Eq. (2.23) is derived, as presented in [91].

Let us start again from Eq (2.22):

$$emf = -\frac{d\Phi}{dt} = -\frac{d}{dt} \iint_S \boldsymbol{B}(t) \cdot \boldsymbol{n} dS$$

According to Maxwell's equations,

$$\boldsymbol{\nabla} \cdot \boldsymbol{B} = 0 \tag{7.1}$$

Using the vector identity $\boldsymbol{\nabla} \cdot (\boldsymbol{\nabla} \times \boldsymbol{V}) = 0$ that for any vector $\boldsymbol{V}$, one can write that $\boldsymbol{B}$ derives from a magnetic vector potential $\boldsymbol{A}$ such that:

$$\boldsymbol{B} = \boldsymbol{\nabla} \times \boldsymbol{A} \tag{7.2}$$

Thereby, using Stokes' theorem, the Eq. (2.21) expressing the flux $\boldsymbol{\Phi}$ can be rewritten in terms of $\boldsymbol{A}$:

$$\Phi = \iint_S \boldsymbol{B}(t) \cdot d\boldsymbol{S} = \oint \boldsymbol{A} \cdot d\boldsymbol{l} \tag{7.3}$$

Furthermore, according to Ampère's circuital law (with Maxwell's addition),

$$\boldsymbol{\nabla} \times \boldsymbol{H} = \boldsymbol{J} + \frac{\partial \boldsymbol{D}}{\partial t} \tag{7.4}$$

where $\boldsymbol{B} = \mu\boldsymbol{H}$, $\boldsymbol{D} = \epsilon\boldsymbol{E}$, ϵ the dielectric constant, μ the permeability and $\boldsymbol{J}$ the electric current density (current per unit area). In MRI, the time dependence is generally ignored. Indeed, the static field independent of time and the gradient fields have mild time dependence. Concerning the RF pulse, it is rather a low frequency signal [91]. In this manner static methods can be used and Eq. (7.4) reduces to:

$$\boldsymbol{\nabla} \times \boldsymbol{B} = \mu_0 \boldsymbol{J} \tag{7.5}$$

where μ_0 is the permeability of free space. According to Eq. (7.2), the curl of $\boldsymbol{B}$ can be expressed as:

$$\boldsymbol{\nabla} \times \boldsymbol{B} = \boldsymbol{\nabla} \times (\boldsymbol{\nabla} \times \boldsymbol{A}) \tag{7.6}$$

$$= \boldsymbol{\nabla} (\boldsymbol{\nabla} \cdot \boldsymbol{A}) - \nabla^2 \boldsymbol{A} \tag{7.7}$$

$\boldsymbol{A}$ can be freely chosen. With the assumption that $\boldsymbol{\nabla} \cdot \boldsymbol{A} = 0$, one can write that:

$$\boldsymbol{\nabla} \times \boldsymbol{B} = -\nabla^2 \boldsymbol{A} \tag{7.8}$$

$$\implies \nabla^2 \boldsymbol{A} = -\mu_0 \boldsymbol{J} \tag{7.9}$$

It can be shown that the solution to this equation is:

$$\boldsymbol{A}(\boldsymbol{r}) = \frac{\mu_0}{4\pi} \int_V \frac{\boldsymbol{J}(\boldsymbol{r}')}{|\boldsymbol{r} - \boldsymbol{r}'|} d^3 r' \tag{7.10}$$

$$= \frac{\mu_0}{4\pi} \sum_{\text{loops } i} I_i \int \frac{d\boldsymbol{l}_i}{|\boldsymbol{r} - \boldsymbol{r}'|} \tag{7.11}$$

where the second line corresponds to a current distribution $\boldsymbol{J}$, which is a sum over a set of i discrete loops carrying a current I_i.

Several phenomena contribute to the current density $\boldsymbol{J}$. In particular, the magnetization current $\boldsymbol{J}_M$ corresponds to the contribution of the magnetization $\boldsymbol{M}$ and expresses as:

$$\boldsymbol{J}_M(\boldsymbol{r}, t) = \boldsymbol{\nabla} \times \boldsymbol{M}(\boldsymbol{r}, t) \tag{7.12}$$

Combining Eq. (7.3), (7.10) and (7.12) with the help of an integration by parts and of the vector identity $\boldsymbol{U} \cdot (\boldsymbol{V} \times \boldsymbol{W}) = -(\boldsymbol{U} \times \boldsymbol{W}) \cdot \boldsymbol{V}$, the flux Φ_M through a coil due to a magnetization source can be expressed as:

$$\Phi_M = \oint \frac{\mu_0}{4\pi} \iiint_V \frac{\boldsymbol{\nabla}' \times \boldsymbol{M}(\boldsymbol{r}')}{|\boldsymbol{r} - \boldsymbol{r}'|} d^3 r' \cdot d\boldsymbol{l}$$

$$= \frac{\mu_0}{4\pi} \iiint_V \oint \left(\left(-\boldsymbol{\nabla}' \frac{1}{|\boldsymbol{r} - \boldsymbol{r}'|} \right) \times \boldsymbol{M}(\boldsymbol{r}') \right) \cdot d\boldsymbol{l} d^3 r'$$

$$= \frac{\mu_0}{4\pi} \iiint_V \boldsymbol{M}(\boldsymbol{r}') \cdot \left(\boldsymbol{\nabla}' \times \oint \frac{d\boldsymbol{l}}{|\boldsymbol{r} - \boldsymbol{r}'|} \right) d^3 r'$$

$$= \iiint_V \boldsymbol{M}(\boldsymbol{r}') \cdot \left(\boldsymbol{\nabla}' \times \frac{\mu_0}{4\pi} \oint \frac{d\boldsymbol{l}}{|\boldsymbol{r} - \boldsymbol{r}'|} \right) d^3 r' \tag{7.13}$$

Taking the curl of Eq. (Eq:solution_vector_potential_2), the term in parentheses in Eq. (7.13) can be identified as the magnetic field per unit current that would be produced by one coil carrying a current I at the point $\boldsymbol{r}'$:

$$\frac{\boldsymbol{B}(\boldsymbol{r}')}{I} = \frac{\boldsymbol{\nabla}' \times \boldsymbol{A}(\boldsymbol{r}')}{I}$$

$$= \frac{1}{I} \left(\boldsymbol{\nabla}' \times \frac{\mu_0}{4\pi} I \oint \frac{d\boldsymbol{l}_i}{|\boldsymbol{r} - \boldsymbol{r}'|} \right)$$

$$= \boldsymbol{\nabla}' \times \frac{\mu_0}{4\pi} \oint \frac{d\boldsymbol{l}_i}{|\boldsymbol{r} - \boldsymbol{r}'|} \tag{7.14}$$

The magnetic field per unit current is denoted $\boldsymbol{\mathcal{B}}^r$ and corresponds to the coil sensitivity. With this notation, Eq. (7.13) reduces to

$$\Phi_M = \iiint_V \boldsymbol{M}(\boldsymbol{r}) \cdot \boldsymbol{\mathcal{B}}^r(\boldsymbol{r})d^3r \tag{7.15}$$

Finally, the derivation of Eq. (7.15) with respect to time allows to find Eq. (2.23):

$$emf = -\frac{d\Phi_M}{dt} = -\frac{d}{dt}\iiint_V \boldsymbol{M}(\boldsymbol{r},t) \cdot \boldsymbol{\mathcal{B}}^r(\boldsymbol{r})d^3r \tag{7.16}$$

where the time dependence of $\boldsymbol{M}$ is made explicit.

Bibliography

[1] Gregory A Roth and GBD 2017 Causes of Death Collaborators. Global, regional, and national age-sex-specific mortality for 282 causes of death in 195 countries and territories, 1980–2017: a systematic analysis for the Global Burden of Disease Study 2017. *The Lancet*, 392(10159):1736–1788, November 2018.

[2] Emanuele Cecchi, Cristina Giglioli, Serafina Valente, Chiara Lazzeri, Gian Franco Gensini, Rosanna Abbate, and Lucia Mannini. Role of hemodynamic shear stress in cardiovascular disease. *Atherosclerosis*, 214(2):249–256, February 2011.

[3] Michael A. Gimbrone and Guillermo García-Cardeña. Vascular endothelium, hemodynamics, and the pathobiology of atherosclerosis. *Cardiovascular Pathology*, 22(1):9–15, January 2013.

[4] David M. Wootton and David N. Ku. Fluid Mechanics of Vascular Systems, Diseases, and Thrombosis. *Annu. Rev. Biomed. Eng.*, 1(1):299–329, August 1999.

[5] Michael Markl, Alex Frydrychowicz, Sebastian Kozerke, Mike Hope, and Oliver Wieben. 4D flow MRI. *J. Magn. Reson. Imaging*, 36(5):1015–1036, November 2012.

[6] Shohei Miyazaki, Keiichi Itatani, Toyoki Furusawa, Teruyasu Nishino, Masataka Sugiyama, Yasuo Takehara, and Satoshi Yasukochi. Validation of numerical simulation methods in aortic arch using 4D Flow MRI. *Heart Vessels*, 32(8):1032–1044, August 2017.

[7] Giovanni Biglino, Daria Cosentino, Jennifer A. Steeden, Lorenzo De Nova, Matteo Castelli, Hopewell Ntsinjana, Giancarlo Pennati, Andrew M. Taylor, and Silvia Schievano. Using 4D Cardiovascular Magnetic Resonance Imaging to Validate Computational Fluid Dynamics: A Case Study. *Front. Pediatr.*, 3, December 2015.

[8] Jonas Lantz, Sophia Bäck, Carl-Johan Carlhäll, Ann Bolger, Anders Persson, Matts Karlsson, and Tino Ebbers. Impact of prosthetic mitral valve orientation on the ventricular flow field: Comparison using patient-specific computational fluid dynamics. *Journal of Biomechanics*, 116:110209, February 2021.

[9] Soroush Heidari Pahlavian, Alexander C. Bunck, Suraj Thyagaraj, Daniel Giese, Francis Loth, Dennis M. Hedderich, Jan Robert Kröger, and Bryn A.

Martin. Accuracy of 4D Flow Measurement of Cerebrospinal Fluid Dynamics in the Cervical Spine: An In Vitro Verification Against Numerical Simulation. *Ann Biomed Eng*, 44(11):3202–3214, November 2016.

[10] Thomas Puiseux, Anou Sewonu, Olivier Meyrignac, Hervé Rousseau, Franck Nicoud, Simon Mendez, and Ramiro Moreno. Reconciling PC-MRI and CFD: An in-vitro study. *NMR in Biomedicine*, 32(5):e4063, May 2019.

[11] K. Valen-Sendstad and D.A. Steinman. Mind the Gap: Impact of Computational Fluid Dynamics Solution Strategy on Prediction of Intracranial Aneurysm Hemodynamics and Rupture Status Indicators. *AJNR Am J Neuroradiol*, 35(3):536–543, March 2014.

[12] F. Nicoud, C. Chnafa, J. Siguenza, V. Zmijanovic, and S. Mendez. Large-Eddy Simulation of Turbulence in Cardiovascular Flows. In Peter Wriggers and Thomas Lenarz, editors, *Biomedical Technology*, volume 84, pages 147–167. Springer International Publishing, Cham, 2018. Series Title: Lecture Notes in Applied and Computational Mechanics.

[13] Keri R. Moyle, Luca Antiga, and David A. Steinman. Inlet Conditions for Image-Based CFD Models of the Carotid Bifurcation: Is it Reasonable to Assume Fully Developed Flow? *Journal of Biomechanical Engineering*, 128(3):371–379, June 2006.

[14] J. Bittoun, J. Taquin, and M. Sauzade. A computer algorithm for the simulation of any Nuclear Magnetic Resonance (NMR) imaging method. *Magnetic Resonance Imaging*, 2(2):113–120, January 1984.

[15] Tony Stöcker, Kaveh Vahedipour, Daniel Pflugfelder, and N. Jon Shah. High-performance computing MRI simulations. *Magn. Reson. Med.*, 64(1):186–193, July 2010.

[16] Carlos Castillo-Passi, Ronal Coronado, Gabriel Varela-Mattatall, Carlos Alberola-López, René Botnar, and Pablo Irarrazaval. KomaMRI.jl: An open-source framework for general MRI simulations with GPU acceleration. *Magnetic Resonance in Med*, 90(1):329–342, July 2023.

[17] Sven Petersson, Petter Dyverfeldt, Roland Gårdhagen, Matts Karlsson, and Tino Ebbers. Simulation of phase contrast MRI of turbulent flow. *Magn. Reson. Med.*, 64(4):1039–1046, June 2010.

[18] Artur Klepaczko, Piotr Szczypiński, Michał Strzelecki, and Ludomir Stefańczyk. Simulation of phase contrast angiography for renal arterial models. *BioMed Eng OnLine*, 17(1):41, December 2018.

[19] Alexandre Fortin, Stéphanie Salmon, Joseph Baruthio, Maya Delbany, and Emmanuel Durand. Flow MRI simulation in complex 3D geometries: Application to the cerebral venous network. *Magn. Reson. Med.*, 80(4):1655–1665, October 2018.

[20] Thomas Puiseux. *Numerical simulations for phase-contrast magnetic resonance imaging.* PhD thesis, Montpellier, November 2019.

[21] Morgane Garreau, Thomas Puiseux, Solenn Toupin, Daniel Giese, Simon Mendez, Franck Nicoud, and Ramiro Moreno. Accelerated sequences of 4D flow MRI using GRAPPA and compressed sensing: A comparison against conventional MRI and computational fluid dynamics. *Magnetic Resonance in Med*, 88(6):2432–2446, December 2022.

[22] Petter Dyverfeldt, Malenka Bissell, Alex J. Barker, Ann F. Bolger, Carl-Johan Carlhäll, Tino Ebbers, Christopher J. Francios, Alex Frydrychowicz, Julia Geiger, Daniel Giese, Michael D. Hope, Philip J. Kilner, Sebastian Kozerke, Saul Myerson, Stefan Neubauer, Oliver Wieben, and Michael Markl. 4D flow cardiovascular magnetic resonance consensus statement. *J Cardiovasc Magn Reson*, 17(1):72, December 2015.

[23] Valery Vishnevskiy, Jonas Walheim, and Sebastian Kozerke. Deep variational network for rapid 4D flow MRI reconstruction. *Nat Mach Intell*, 2(4):228–235, April 2020.

[24] Mojtaba F. Fathi, Isaac Perez-Raya, Ahmadreza Baghaie, Philipp Berg, Gabor Janiga, Amirhossein Arzani, and Roshan M. D'Souza. Super-resolution and denoising of 4D-Flow MRI using physics-Informed deep neural nets. *Computer Methods and Programs in Biomedicine*, 197:105729, December 2020.

[25] Casey M. Fleeter, Gianluca Geraci, Daniele E. Schiavazzi, Andrew M. Kahn, and Alison L. Marsden. Multilevel and multifidelity uncertainty quantification for cardiovascular hemodynamics. *Computer Methods in Applied Mechanics and Engineering*, 365:113030, June 2020.

[26] Jun-Mei Zhang, Liang Zhong, Boyang Su, Min Wan, Jinq Shya Yap, Jasmine P. L. Tham, Leok Poh Chua, Dhanjoo N. Ghista, and Ru San Tan. Perspective on CFD studies of coronary artery disease lesions and hemodynamics: A review. *Int. J. Numer. Meth. Biomed. Engng.*, 30(6):659–680, June 2014.

[27] Kelly A. Young, James A. Wise, Peter DeSaix, Dean H. Kruse, Brandon Poe, Eddie Johnson, Jody E. Johnson, Oksana Korol, J. Gordon Betts, and Mark Womble. *Anatomy and Physiology.* OpenStax, Houston, Texas, first edition edition, April 2013.

[28] Michael F. O'Rourke and Junichiro Hashimoto. Mechanical Factors in Arterial Aging. *Journal of the American College of Cardiology*, 50(1):1–13, July 2007.

[29] S. Laurent, J. Cockcroft, L. Van Bortel, P. Boutouyrie, C. Giannattasio, D. Hayoz, B. Pannier, C. Vlachopoulos, I. Wilkinson, H. Struijker-Boudier, and on behalf of the European Network for Non-invasive Investigation of

Large Arteries. Expert consensus document on arterial stiffness: methodological issues and clinical applications. *European Heart Journal*, 27(21):2588–2605, September 2006.

[30] Rashid Afkhami and Sarah Johnson. Wave reflection: More than a round trip. *Medical Engineering & Physics*, 92:40–44, June 2021.

[31] Rodrigo Méndez Rojano, Simon Mendez, and Franck Nicoud. Introducing the pro-coagulant contact system in the numerical assessment of device-related thrombosis. *Biomech Model Mechanobiol*, 17(3):815–826, June 2018.

[32] Thomas W.L. Scheeren and Michael A.E. Ramsay. New Developments in Hemodynamic Monitoring. *Journal of Cardiothoracic and Vascular Anesthesia*, 33:S67–S72, August 2019.

[33] M M Sette. A novel flow and pressure catheter for complete interventional cardiology physiology management. *European Heart Journal*, 42(Supplement_1):ehab724.1198, October 2021.

[34] Hack-Lyoung Kim and Thomas Weber. Pulsatile Hemodynamics and Coronary Artery Disease. *Korean Circ J*, 51(11):881, 2021.

[35] Harminder Gill, Joao Fernandes, Omar Chehab, Bernard Prendergast, Simon Redwood, Amedeo Chiribiri, David Nordsletten, Ronak Rajani, and Pablo Lamata. Evaluation of aortic stenosis: From Bernoulli and Doppler to Navier-Stokes. *Trends in Cardiovascular Medicine*, 33(1):32–43, January 2023.

[36] Kristoffer Lindskov Hansen, Michael Bachmann Nielsen, and Jørgen Arendt Jensen. Vector velocity estimation of blood flow – A new application in medical ultrasound. *Ultrasound*, 25(4):189–199, November 2017.

[37] Morten Smedsrud Wigen, Solveig Fadnes, Alfonso Rodriguez-Molares, Tore Bjastad, Marius Eriksen, Knut Haakon Stensath, Asbjorn Stoylen, and Lasse Lovstakken. 4-D Intracardiac Ultrasound Vector Flow Imaging–Feasibility and Comparison to Phase-Contrast MRI. *IEEE Trans. Med. Imaging*, 37(12):2619–2629, December 2018.

[38] Florian Vixège, Alain Berod, Pierre-Yves Courand, Simon Mendez, Franck Nicoud, Philippe Blanc-Benon, Didier Vray, and Damien Garcia. Full-volume three-component intraventricular vector flow mapping by triplane color Doppler. *Phys. Med. Biol.*, 67(9):095004, May 2022.

[39] E. L. Hahn. Detection of sea-water motion by nuclear precession. *Journal of Geophysical Research (1896-1977)*, 65(2):776–777, 1960. _eprint: https://onlinelibrary.wiley.com/doi/pdf/10.1029/JZ065i002p00776.

162

[40] Lars Wigström, Lars Sjöqvist, and Bengt Wranne. Temporally resolved 3D phase-contrast imaging. *Magn. Reson. Med.*, 36(5):800–803, November 1996.

[41] Tino Ebbers, Lars Wigström, Ann F. Bolger, Jan Engvall, and Matts Karlsson. Estimation of relative cardiovascular pressures using time-resolved three-dimensional phase contrast MRI: 3D Relative Cardiovascular Pressures. *Magn. Reson. Med.*, 45(5):872–879, May 2001.

[42] Wouter V. Potters, Pim Van Ooij, Henk Marquering, Ed vanBavel, and Aart J. Nederveen. Volumetric arterial wall shear stress calculation based on cine phase contrast MRI: Volumetric Wall Shear Stress Calculation. *J. Magn. Reson. Imaging*, 41(2):505–516, February 2015.

[43] Petter Dyverfeldt, Andreas Sigfridsson, John-Peder Escobar Kvitting, and Tino Ebbers. Quantification of intravoxel velocity standard deviation and turbulence intensity by generalizing phase-contrast MRI. *Magn. Reson. Med.*, 56(4):850–858, October 2006.

[44] Jonas Walheim, Alexander Gotschy, and Sebastian Kozerke. On the limitations of partial Fourier acquisition in phase-contrast MRI of turbulent kinetic energy. *Magn. Reson. Med*, 81(1):514–523, January 2019.

[45] Michael Markl, Wolf Wallis, Stefanie Brendecke, Jan Simon, Alex Frydrychowicz, and Andreas Harloff. Estimation of global aortic pulse wave velocity by flow-sensitive 4D MRI: Global Aortic Pulse Wave Velocity. *Magn. Reson. Med.*, 63(6):1575–1582, June 2010.

[46] Paul D Morris, Andrew Narracott, Hendrik Von Tengg-Kobligk, Daniel Alejandro Silva Soto, Sarah Hsiao, Angela Lungu, Paul Evans, Neil W Bressloff, Patricia V Lawford, D Rodney Hose, and Julian P Gunn. Computational fluid dynamics modelling in cardiovascular medicine. *Heart*, 102(1):18–28, January 2016.

[47] Evangelos Boutsianis, Michele Guala, Ufuk Olgac, Simon Wildermuth, Klaus Hoyer, Yiannis Ventikos, and Dimos Poulikakos. CFD and PTV Steady Flow Investigation in an Anatomically Accurate Abdominal Aortic Aneurysm. *Journal of Biomechanical Engineering*, 131(1):011008, January 2009.

[48] Eduardo Soudah, E. Y. K. Ng, T. H. Loong, Maurizio Bordone, Uei Pua, and Sriram Narayanan. CFD Modelling of Abdominal Aortic Aneurysm on Hemodynamic Loads Using a Realistic Geometry with CT. *Computational and Mathematical Methods in Medicine*, 2013:1–9, 2013.

[49] Mariana Simão, Jorge Ferreira, António C. Tomás, José Fragata, and Helena Ramos. Aorta Ascending Aneurysm Analysis Using CFD Models towards Possible Anomalies. *Fluids*, 2(2):31, June 2017.

[50] Yiemeng Hoi, Scott H. Woodward, Minsuok Kim, Dale B. Taulbee, and Hui Meng. Validation of CFD Simulations of Cerebral Aneurysms With Implication of Geometric Variations. *Journal of Biomechanical Engineering*, 128(6):844–851, December 2006.

[51] Matthew D. Ford, Hristo N. Nikolov, Jaques S. Milner, Stephen P. Lownie, Edwin M. DeMont, Wojciech Kalata, Francis Loth, David W. Holdsworth, and David A. Steinman. PIV-Measured Versus CFD-Predicted Flow Dynamics in Anatomically Realistic Cerebral Aneurysm Models. *Journal of Biomechanical Engineering*, 130(2):021015, April 2008.

[52] Mona Alimohammadi, Joseph M Sherwood, Morad Karimpour, Obiekezie Agu, Stavroula Balabani, and Vanessa Díaz-Zuccarini. Aortic dissection simulation models for clinical support: fluid-structure interaction vs. rigid wall models. *BioMed Eng OnLine*, 14(1):34, December 2015.

[53] Chlöe H. Armour, Baolei Guo, Simone Saitta, Selene Pirola, Yifan Liu, Zhihui Dong, and Xiao Yun Xu. Evaluation and verification of patient-specific modelling of type B aortic dissection. *Computers in Biology and Medicine*, 140:105053, January 2022.

[54] Zhonghua Sun and Lei Xu. Computational fluid dynamics in coronary artery disease. *Computerized Medical Imaging and Graphics*, 38(8):651–663, December 2014.

[55] Alessandro Candreva, Giuseppe De Nisco, Maurizio Lodi Rizzini, Fabrizio D'Ascenzo, Gaetano Maria De Ferrari, Diego Gallo, Umberto Morbiducci, and Claudio Chiastra. Current and Future Applications of Computational Fluid Dynamics in Coronary Artery Disease. *Rev. Cardiovasc. Med.*, 23(11):377, November 2022.

[56] Alain Berod, Christophe Chnafa, Simon Mendez, and Franck Nicoud. A heterogeneous model of endovascular devices for the treatment of intracranial aneurysms. *Numer Methods Biomed Eng*, 38(2), February 2022.

[57] Xinwei Song, Houston G. Wood, and Don Olsen. Computational Fluid Dynamics (CFD) Study of the 4th Generation Prototype of a Continuous Flow Ventricular Assist Device (VAD). *Journal of Biomechanical Engineering*, 126(2):180–187, April 2004.

[58] Vladeta Zmijanovic, Simon Mendez, Vincent Moureau, and Franck Nicoud. About the numerical robustness of biomedical benchmark cases: Interlaboratory FDA's idealized medical device. *Int J Numer Method Biomed Eng*, 33(1), January 2017.

[59] Christoph Roloff, Daniel Stucht, Oliver Beuing, and Philipp Berg. Comparison of intracranial aneurysm flow quantification techniques: standard PIV

vs stereoscopic PIV vs tomographic PIV vs phase-contrast MRI vs CFD. *J NeuroIntervent Surg*, 11(3):275–282, March 2019.

[60] P. Van Ooij, A. Guédon, C. Poelma, J. Schneiders, M. C. M. Rutten, H. A. Marquering, C. B. Majoie, E. vanBavel, and A. J. Nederveen. Complex flow patterns in a real-size intracranial aneurysm phantom: phase contrast MRI compared with particle image velocimetry and computational fluid dynamics. *NMR Biomed.*, 25(1):14–26, January 2012.

[61] Dorothea I. Hollnagel, Paul E. Summers, Dimos Poulikakos, and Spyros S. Kollias. Comparative velocity investigations in cerebral arteries and aneurysms: 3D phase-contrast MR angiography, laser Doppler velocimetry and computational fluid dynamics. *NMR Biomed.*, 22(8):795–808, October 2009.

[62] Edward Ferdian, Avan Suinesiaputra, David J. Dubowitz, Debbie Zhao, Alan Wang, Brett Cowan, and Alistair A. Young. 4DFlowNet: Super-Resolution 4D Flow MRI Using Deep Learning and Computational Fluid Dynamics. *Front. Phys.*, 8:138, May 2020.

[63] Pietro Dirix, Stefano Buoso, Eva S. Peper, and Sebastian Kozerke. Synthesis of patient-specific multipoint 4D flow MRI data of turbulent aortic flow downstream of stenotic valves. *Sci Rep*, 12(1):16004, September 2022.

[64] Ali Bakhshinejad, Ahmadreza Baghaie, Alireza Vali, David Saloner, Vitaliy L. Rayz, and Roshan M. D'Souza. Merging computational fluid dynamics and 4D Flow MRI using proper orthogonal decomposition and ridge regression. *Journal of Biomechanics*, 58:162–173, June 2017.

[65] Giacomo Annio, Ryo Torii, Ben Ariff, Declan P. O'Regan, Vivek Muthurangu, Andrea Ducci, Victor Tsang, and Gaetano Burriesci. Enhancing Magnetic Resonance Imaging With Computational Fluid Dynamics. *Journal of Engineering and Science in Medical Diagnostics and Therapy*, 2(4):041010, November 2019.

[66] Vinicius C. Rispoli, Jon F. Nielsen, Krishna S. Nayak, and Joao L. A. Carvalho. Computational fluid dynamics simulations of blood flow regularized by 3D phase contrast MRI. *BioMed Eng OnLine*, 14(1):110, December 2015.

[67] Isaac Perez-Raya, Mojtaba F. Fathi, Ahmadreza Baghaie, Raphael H. Sacho, Kevin M. Koch, and Roshan M. D'Souza. Towards multi-modal data fusion for super-resolution and denoising of 4D-Flow MRI. *Int J Numer Meth Biomed Engng*, 36(9), September 2020.

[68] Yuan-Cheng Fung. *Biomechanics*. Springer, New York, NY, 1993.

[69] Emily Louise Manchester, Selene Pirola, Mohammad Yousuf Salmasi, Declan P. O'Regan, Thanos Athanasiou, and Xiao Yun Xu. Evaluation of

Computational Methodologies for Accurate Prediction of Wall Shear Stress and Turbulence Parameters in a Patient-Specific Aorta. *Front. Bioeng. Biotechnol.*, 10:836611, March 2022.

[70] Sonu S. Varghese, Steven H. Frankel, and Paul F. Fischer. Modeling Transition to Turbulence in Eccentric Stenotic Flows. *Journal of Biomechanical Engineering*, 130(1):014503, February 2008.

[71] Magnus Ziegler, Jonas Lantz, Tino Ebbers, and Petter Dyverfeldt. Assessment of turbulent flow effects on the vessel wall using four-dimensional flow MRI: Turbulent Flow Effects on Vessel Wall. *Magn. Reson. Med.*, 77(6):2310–2319, June 2017.

[72] Johannes Töger, Matthew J. Zahr, Nicolas Aristokleous, Karin Markenroth Bloch, Marcus Carlsson, and Per-Olof Persson. Blood flow imaging by optimal matching of computational fluid dynamics to 4D-flow data. *Magn Reson Med*, 84(4):2231–2245, October 2020.

[73] Belen Casas, Jonas Lantz, Petter Dyverfeldt, and Tino Ebbers. 4D Flow MRI-based pressure loss estimation in stenotic flows: Evaluation using numerical simulations: Pressure Loss Estimation in Stenotic Flows Using 4D Flow MRI. *Magn. Reson. Med.*, 75(4):1808–1821, April 2016.

[74] Umberto Morbiducci, Raffaele Ponzini, Diego Gallo, Cristina Bignardi, and Giovanna Rizzo. Inflow boundary conditions for image-based computational hemodynamics: Impact of idealized versus measured velocity profiles in the human aorta. *Journal of Biomechanics*, 46(1):102–109, January 2013.

[75] Irene E. Vignon-Clementel, C. Alberto Figueroa, Kenneth E. Jansen, and Charles A. Taylor. Outflow boundary conditions for three-dimensional finite element modeling of blood flow and pressure in arteries. *Computer Methods in Applied Mechanics and Engineering*, 195(29-32):3776–3796, June 2006.

[76] S. Pirola, Z. Cheng, O.A. Jarral, D.P. O'Regan, J.R. Pepper, T. Athanasiou, and X.Y. Xu. On the choice of outlet boundary conditions for patient-specific analysis of aortic flow using computational fluid dynamics. *Journal of Biomechanics*, 60:15–21, July 2017.

[77] C. Chnafa, S. Mendez, and F. Nicoud. Image-Based Simulations Show Important Flow Fluctuations in a Normal Left Ventricle: What Could be the Implications? *Ann Biomed Eng*, 44(11):3346–3358, November 2016.

[78] Ryoichi Kose and Katsumi Kose. BlochSolver: A GPU-optimized fast 3D MRI simulator for experimentally compatible pulse sequences. *Journal of Magnetic Resonance*, 281:51–65, August 2017.

[79] Christos G. Xanthis and Anthony H. Aletras. coreMRI: A high-performance, publicly available MR simulation platform on the cloud. *PLoS ONE*, 14(5):e0216594, May 2019.

[80] Ryoichi Kose and Katsumi Kose. An Accurate Dictionary Creation Method for MR Fingerprinting Using a Fast Bloch Simulator. *MRMS*, 19(3):247–253, 2020.

[81] Christian Guenthner, Thomas Amthor, Mariya Doneva, and Sebastian Kozerke. A unifying view on extended phase graphs and Bloch simulations for quantitative MRI. *Sci Rep*, 11(1):21289, October 2021. Number: 1 Publisher: Nature Publishing Group.

[82] Christos G. Xanthis, Ioannis E. Venetis, A. V. Chalkias, and Anthony H. Aletras. MRISIMUL: A GPU-Based Parallel Approach to MRI Simulations. *IEEE Trans. Med. Imaging*, 33(3):607–617, March 2014.

[83] Sven Petersson, Petter Dyverfeldt, and Tino Ebbers. Assessment of the accuracy of MRI wall shear stress estimation using numerical simulations. *J. Magn. Reson. Imaging*, 36(1):128–138, July 2012.

[84] Hojin Ha, Jonas Lantz, Henrik Haraldsson, Belen Casas, Magnus Ziegler, Matts Karlsson, David Saloner, Petter Dyverfeldt, and Tino Ebbers. Assessment of turbulent viscous stress using ICOSA 4D Flow MRI for prediction of hemodynamic blood damage. *Sci Rep*, 6(1):39773, December 2016.

[85] Matthias Weigel. Extended phase graphs: Dephasing, RF pulses, and echoes - pure and simple: Extended Phase Graphs. *J. Magn. Reson. Imaging*, 41(2):266–295, February 2015.

[86] Thomas Puiseux, Anou Sewonu, Ramiro Moreno, Simon Mendez, and Franck Nicoud. Numerical simulation of time-resolved 3D phase-contrast magnetic resonance imaging. *PLoS ONE*, 16(3):e0248816, March 2021.

[87] Mark A. Griswold, Peter M. Jakob, Robin M. Heidemann, Mathias Nittka, Vladimir Jellus, Jianmin Wang, Berthold Kiefer, and Axel Haase. Generalized autocalibrating partially parallel acquisitions (GRAPPA). *Magn. Reson. Med.*, 47(6):1202–1210, June 2002.

[88] Mathias Blasche and Christoph Forman. Compressed Sensing – the Flowchart. *MAGNETOM Flash*, 66(3/2016), March 2016.

[89] Matt A. Bernstein, Kevin F. King, and Xiaohong Joe Zhou. *Handbook of MRI Pulse Sequences*. Elsevier, September 2004.

[90] I. I. Rabi, J. R. Zacharias, S. Millman, and P. Kusch. A New Method of Measuring Nuclear Magnetic Moment. *Phys. Rev.*, 53(4):318–318, February 1938.

[91] Robert W. Brown, Y.-C. Norman Cheng, E. Mark Haacke, Michael R. Thompson, and Ramesh Venkatesan. *Magnetic Resonance Imaging: Physical Principles and Sequence Design*. John Wiley & Sons, June 2014.

[92] F. Bloch. Nuclear Induction. *Phys. Rev.*, 70(7-8):460–474, October 1946.

[93] H. C. Torrey. Bloch Equations with Diffusion Terms. *Phys. Rev.*, 104(3):563–565, November 1956.

[94] Bernd André Jung and Matthias Weigel. Spin echo magnetic resonance imaging. *J. Magn. Reson. Imaging*, 37(4):805–817, April 2013.

[95] Cecil E Hayes, William A Edelstein, John F Schenck, Otward M Mueller, and Matthew Eash. An efficient, highly homogeneous radiofrequency coil for whole body NMR imaging at 1.5T. *Journal of Magnetic Resonance (1969)*, 63(3):622–628, 1985.

[96] Sheikh Faisal Ahmad, Young Cheol Kim, Ick Chang Choi, and Hyun Deok Kim. Recent Progress in Birdcage RF Coil Technology for MRI System. *Diagnostics*, 10(12):1017, November 2020.

[97] K. Lezhennikova, C. Simovski, R. Abdeddaim, R. Balafendiev, and S. Glybovski. Extending a birdcage coil for magnetic resonance imaging of a human head with an artificial magnetic shield. *Photonics and Nanostructures - Fundamentals and Applications*, 43:100890, February 2021.

[98] Sergio Solis-Najera, Gianella Cuellar, Ruiliang Wang, Dardo Tomasi, and A. Rodríguez. Transceiver 4-leg birdcage for high field MRI: Knee imaging. *Revista Mexicana de Física*, 54(3):215–221, June 2008.

[99] Cecil E. Hayes and Leon Axel. Noise performance of surface coils for magnetic resonance imaging at 1.5 T: Surface-coil noise for MRI at 1.5 T. *Med. Phys.*, 12(5):604–607, September 1985.

[100] Bernhard Gruber, Martijn Froeling, Tim Leiner, and Dennis W.J. Klomp. RF coils: A practical guide for nonphysicists: RF Coils. *J. Magn. Reson. Imaging*, 48(3):590–604, September 2018.

[101] David J Larkman and Rita G Nunes. Parallel magnetic resonance imaging. *Phys. Med. Biol.*, 52(7):R15–R55, April 2007.

[102] Boris Keil and Lawrence L. Wald. Massively parallel MRI detector arrays. *Journal of Magnetic Resonance*, 229:75–89, April 2013.

[103] Li Feng. Golden-Angle Radial MRI: Basics, Advances, and Applications. *Magnetic Resonance Imaging*, 56(1):45–62, July 2022.

[104] Markus Untenberger, Zhengguo Tan, Dirk Voit, Arun A. Joseph, Volkert Roeloffs, K. Dietmar Merboldt, Sebastian Schätz, and Jens Frahm. Advances in real-time phase-contrast flow MRI using asymmetric radial gradient echoes: Real-Time Phase-Contrast Flow MRI. *Magn. Reson. Med.*, 75(5):1901–1908, May 2016.

[105] Bénédicte M.A. Delattre, Robin M. Heidemann, Lindsey A. Crowe, Jean-Paul Vallée, and Jean-Noël Hyacinthe. Spiral demystified. *Magnetic Resonance Imaging*, 28(6):862–881, July 2010.

[106] Hadrien Dyvorne, Ashley Knight-Greenfield, Guido Jajamovich, Cecilia Besa, Yong Cui, Aurélien Stalder, Michael Markl, and Bachir Taouli. Abdominal 4D Flow MR Imaging in a Breath Hold: Combination of Spiral Sampling and Dynamic Compressed Sensing for Highly Accelerated Acquisition. *Radiology*, 275(1):245–254, April 2015.

[107] Daniel D. Traficante. Relaxation. Can T2, be longer than T1? *Concepts Magn. Reson.*, 3(3):171–177, July 1991.

[108] Michael Markl and Jochen Leupold. Gradient echo imaging. *J. Magn. Reson. Imaging*, 35(6):1274–1289, June 2012.

[109] Y. Zur, M. L. Wood, and L. J. Neuringer. Spoiling of transverse magnetization in steady-state sequences. *Magnetic Resonance in Medicine*, 21(2):251–263, 1991.

[110] Dwight G. Nishimura, John I. Jackson, and John M. Pauly. On the nature and reduction of the displacement artifact in flow images. *Magn. Reson. Med.*, 22(2):481–492, December 1991.

[111] Anders Nilsson, Karin Markenroth Bloch, Marcus Carlsson, Einar Heiberg, and Freddy Ståhlberg. Variable velocity encoding in a three-dimensional, three-directional phase contrast sequence: Evaluation in phantom and volunteers. *J. Magn. Reson. Imaging*, 36(6):1450–1459, December 2012.

[112] Norbert J. Pelc, Matt A. Bernstein, Ann Shimakawa, and Gary H. Glover. Encoding strategies for three-direction phase-contrast MR imaging of flow. *J. Magn. Reson. Imaging*, 1(4):405–413, July 1991.

[113] D.N. Firmin, P.D. Gatehouse, J.P. Konrad, G.Z. Yang, P.J. Kilner, and D.B. Longmore. Rapid 7-dimensional imaging of pulsatile flow. In *Proceedings of Computers in Cardiology Conference*, pages 353–356, London, UK, 1993. IEEE Comput. Soc. Press.

[114] Michael Markl, Frandics P. Chan, Marcus T. Alley, Kris L. Wedding, Mary T. Draney, Chris J. Elkins, David W. Parker, Ryan Wicker, Charles A. Taylor, Robert J. Herfkens, and Norbert J. Pelc. Time-resolved three-dimensional phase-contrast MRI. *J. Magn. Reson. Imaging*, 17(4):499–506, April 2003.

[115] T K Foo, M A Bernstein, A M Aisen, R J Hernandez, B D Collick, and T Bernstein. Improved ejection fraction and flow velocity estimates with use of view sharing and uniform repetition time excitation with fast cardiac techniques. *Radiology*, 195(2):471–478, May 1995. Publisher: Radiological Society of North America.

[116] Mariana B. L. Falcão, Lorenzo Di Sopra, Liliana Ma, Mario Bacher, Jérôme Yerly, Peter Speier, Tobias Rutz, Milan Prša, Michael Markl, Matthias Stuber, and Christopher W. Roy. Pilot tone navigation for respiratory and cardiac motion-resolved free-running 5D flow MRI. *Magnetic Resonance in Med*, 87(2):718–732, February 2022.

[117] Per Thunberg, Lars Wigström, Tino Ebbers, and Matts Karlsson. Correction for displacement artifacts in 3D phase contrast imaging: Displacement Artifacts in 3D PC Imaging. *J. Magn. Reson. Imaging*, 16(5):591–597, November 2002.

[118] David A. Steinman, C. Ross Ethier, and Brian K. Rutt. Combined analysis of spatial and velocity displacement artifacts in phase contrast measurements of complex flows. *J. Magn. Reson. Imaging*, 7(2):339–346, March 1997.

[119] Marc Kouwenhoven, Mark B. M. Hofman, and Michiel Sprenger. Motion Induced Phase Shifts in MR: Acceleration Effects in Quantitative Flow Measurements—A Reconsideration. *Magn. Reson. Med.*, 33(6):766–777, June 1995.

[120] M.F Salfity, J.M Huntley, M.J Graves, O Marklund, R Cusack, and D.A Beauregard. Extending the dynamic range of phase contrast magnetic resonance velocity imaging using advanced higher-dimensional phase unwrapping algorithms. *J. R. Soc. Interface.*, 3(8):415–427, June 2006.

[121] Michael Loecher, Eric Schrauben, Kevin M. Johnson, and Oliver Wieben. Phase unwrapping in 4D MR flow with a 4D single-step laplacian algorithm: 4D Laplacian Unwrapping for 4D Flow MRI. *J. Magn. Reson. Imaging*, 43(4):833–842, April 2016.

[122] Haben Berhane, Michael B. Scott, Alex J. Barker, Patrick McCarthy, Ryan Avery, Brad Allen, Chris Malaisrie, Joshua D. Robinson, Cynthia K. Rigsby, and Michael Markl. Deep learning-based velocity antialiasing of 4D flow MRI. *Magnetic Resonance in Med*, 88(1):449–463, July 2022.

[123] Matt A. Bernstein, Xiaohong Joe Zhou, Jason A. Polzin, Kevin F. King, Alexander Ganin, Norbert J. Pelc, and Gary H. Glover. Concomitant gradient terms in phase contrast MR: Analysis and correction. *Magn. Reson. Med.*, 39(2):300–308, February 1998.

[124] Whittier R. Myers, Michael Mößle, and John Clarke. Correction of concomitant gradient artifacts in experimental microtesla MRI. *Journal of Magnetic Resonance*, 177(2):274–284, December 2005.

[125] Jost M. Kollmeier, Oleksandr Kalentev, Jakob Klosowski, Dirk Voit, and Jens Frahm. Velocity vector reconstruction for real-time phase-contrast MRI with radial Maxwell correction. *Magnetic Resonance in Med*, 87(4):1863–1875, April 2022.

170

[126] Allen D. Elster. What is pre-emphasis and how does it reduce eddy currents? http://mriquestions.com/what-is-pre-emphasis.html.

[127] M. Markl, R. Bammer, M.T. Alley, C.J. Elkins, M.T. Draney, A. Barnett, M.E. Moseley, G.H. Glover, and N.J. Pelc. Generalized reconstruction of phase contrast MRI: Analysis and correction of the effect of gradient field distortions. *Magn. Reson. Med.*, 50(4):791–801, October 2003.

[128] D.C. Noll, D.G. Nishimura, and A. Macovski. Homodyne detection in magnetic resonance imaging. *IEEE Trans. Med. Imaging*, 10(2):154–163, June 1991.

[129] Zhi-Pei Liang, Fernando E. Boada, R. Todd Constable, E. Mark Haacke, Paul C. Lauterbur, and Michael R. Smith. Constrained Reconstruction Methods in MR Imaging. *Reviews of Magnetic Resonance in Medicine*, 4:67–185, 1992.

[130] G. McGibney, M. R. Smith, S. T. Nichols, and A. Crawley. Quantitative evaluation of several partial fourier reconstruction algorithms used in mri. *Magn. Reson. Med.*, 30(1):51–59, July 1993.

[131] Robin M. Heidemann, Özkan Özsarlak, Paul M. Parizel, Johan Michiels, Berthold Kiefer, Vladimir Jellus, Mathias Müller, Felix Breuer, Martin Blaimer, Mark A. Griswold, and Peter M. Jakob. A brief review of parallel magnetic resonance imaging. *European Radiology*, 13(10):2323–2337, October 2003.

[132] Daniel K. Sodickson and Warren J. Manning. Simultaneous acquisition of spatial harmonics (SMASH): Fast imaging with radiofrequency coil arrays. *Magn. Reson. Med.*, 38(4):591–603, October 1997.

[133] Daniel K. Sodickson, Charles A. McKenzie, Michael A. Ohliger, Ernest N. Yeh, and Mark D. Price. Recent advances in image reconstruction, coil sensitivity calibration, and coil array design for SMASH and generalized parallel MRI. *MAGMA*, 13(3):158–163, January 2002.

[134] M. Lustig, D.L. Donoho, J.M. Santos, and J.M. Pauly. Compressed Sensing MRI. *IEEE Signal Process. Mag.*, 25(2):72–82, March 2008.

[135] Mehdi H. Moghari, Martin Uecker, Sébastien Roujol, Majid Sabbagh, Tal Geva, and Andrew J. Powell. Accelerated whole-heart MR angiography using a variable-density poisson-disc undersampling pattern and compressed sensing reconstruction: Accelerated Whole-Heart MRA. *Magn. Reson. Med.*, 79(2):761–769, February 2018.

[136] Yoann Le Montagner, Elsa Angelini, and Jean-Christophe Olivo-Marin. Comparison of reconstruction algorithms in compressed sensing applied to biological imaging. In *2011 IEEE International Symposium on Biomedical*

Imaging: From Nano to Macro, pages 105–108, Chicago, IL, USA, March 2011. IEEE.

[137] Li Feng, Robert Grimm, Kai Tobias Block, Hersh Chandarana, Sungheon Kim, Jian Xu, Leon Axel, Daniel K. Sodickson, and Ricardo Otazo. Golden-angle radial sparse parallel MRI: Combination of compressed sensing, parallel imaging, and golden-angle radial sampling for fast and flexible dynamic volumetric MRI: iGRASP: Iterative Golden-Angle RAdial Sparse Parallel MRI. *Magn. Reson. Med.*, 72(3):707–717, September 2014.

[138] Simon Mendez and Franck Nicoud. YALES2BIO. https://imag.umontpellier.fr/~yales2bio/.

[139] Simon Mendez, Alain Bérod, Christophe Chnafa, Morgane Garreau, Etienne Gibaud, Anthony Larroque, Stephanie Lindsey, Marco Martins Afonso, Pascal Mattéoli, Rodrigo Mendez Rojano, Dorian Midou, Thomas Puiseux, Julien Sigüenza, Pierre Taraconat, Vladeta Zmijanovic, and Franck Nicoud. YALES2BIO: A General Purpose Solver Dedicated to Blood Flows. In *Biological Flow in Large Vessels*, pages 183–206. John Wiley & Sons, Ltd, 2022. Section: 7 _eprint: https://onlinelibrary.wiley.com/doi/pdf/10.1002/9781119986607.ch7.

[140] E W Merrill and G A Pelletier. Viscosity of human blood: transition from Newtonian to non-Newtonian. *Journal of Applied Physiology*, 23(2):178–182, August 1967.

[141] Stijn Vantieghem. *Numerical simulations of quasi-static magnetohydrodynamics using an unstructured finite volume solver: development and applications.* PhD thesis, Université Libre de Bruxelles, Bruxelles, January 2011.

[142] Matthias Kraushaar. *Application of the compressible and low-Mach number approaches to Large-Eddy Simulation of turbulent flows in aero-engines.* PhD thesis, Institut National Polytechnique Toulouse, Toulouse, December 2011.

[143] Alexandre Joel Chorin. Numerical solution of the Navier-Stokes equations. *Math. Comp.*, 22(104):745–762, 1968.

[144] J Kim and P Moin. Application of a fractional-step method to incompressible Navier-Stokes equations. *Journal of Computational Physics*, 59(2):308–323, June 1985.

[145] Mathias Malandain. *Simulation massivement parallèle des écoulements turbulents à faible nombre de Mach.* PhD thesis, Institut National des Sciences Appliquées de Rouen, Rouen, 2013.

[146] M. Germano. A proposal for a redefinition of the turbulent stresses in the filtered Navier–Stokes equations. *Phys. Fluids*, 29(7):2323, 1986.

[147] Franck Nicoud, Hubert Baya Toda, Olivier Cabrit, Sanjeeb Bose, and Jungil Lee. Using singular values to build a subgrid-scale model for large eddy simulations. *Physics of Fluids*, 23(8):085106, August 2011.

[148] Hubert Baya Toda, Olivier Cabrit, Karine Truffin, Gilles Bruneaux, and Franck Nicoud. Assessment of subgrid-scale models with a large-eddy simulation-dedicated experimental database: The pulsatile impinging jet in turbulent cross-flow. *Physics of Fluids*, 26(7):075108, July 2014.

[149] Kate Hanneman, Milani Sivagnanam, Elsie T. Nguyen, Rachel Wald, Andreas Greiser, Andrew M. Crean, Sebastian Ley, and Bernd J. Wintersperger. Magnetic Resonance Assessment of Pulmonary (QP) to Systemic (QS) Flows Using 4D Phase-contrast Imaging. *Academic Radiology*, 21(8):1002–1008, August 2014.

[150] Ana Alvarez, Vicente Martinez, Gonzalo Pizarro, Manuel Recio, and Jose Ángel Cabrera. Clinical use of 4D flow MRI for quantification of aortic regurgitation. *Open Heart*, 7(1):e001158, February 2020.

[151] Julio Garcia, Alex J. Barker, and Michael Markl. The Role of Imaging of Flow Patterns by 4D Flow MRI in Aortic Stenosis. *JACC: Cardiovascular Imaging*, 12(2):252–266, February 2019.

[152] Natasha Barker, Benjamin Fidock, Christopher S. Johns, Harjinder Kaur, Gareth Archer, Smitha Rajaram, Catherine Hill, Steven Thomas, Kavitasagary Karunasaagarar, David Capener, Abdullah Al-Mohammad, Alexander Rothman, David G. Kiely, Andrew J. Swift, James M. Wild, and Pankaj Garg. A Systematic Review of Right Ventricular Diastolic Assessment by 4D Flow CMR. *BioMed Research International*, 2019:1–8, March 2019.

[153] Bernd Jung, Aurélien F. Stalder, Simon Bauer, and Michael Markl. On the undersampling strategies to accelerate time-resolved 3D imaging using k-t-GRAPPA: Time-Resolved 3D-GRAPPA. *Magn. Reson. Med.*, 66(4):966–975, October 2011.

[154] Susanne Schnell, Michael Markl, Pegah Entezari, Riti J. Mahadewia, Edouard Semaan, Zoran Stankovic, Jeremy Collins, James Carr, and Bernd Jung. *k-t* GRAPPA accelerated four-dimensional flow MRI in the aorta: Effect on scan time, image quality, and quantification of flow and wall shear stress. *Magn. Reson. Med.*, 72(2):522–533, August 2014.

[155] Arshad Zaman, Manish Motwani, James J. Oliver, Gerard Crelier, Laura E. Dobson, David M. Higgins, Sven Plein, and John P. Greenwood. 3.0T, time-resolved, 3D flow-sensitive MR in the thoracic aorta: Impact of *k-t*

BLAST acceleration using 8- versus 32-channel coil arrays: 4D Flow MR in the Thoracic Aorta. *J. Magn. Reson. Imaging*, 42(2):495–504, August 2015.

[156] Liliana E. Ma, Michael Markl, Kelvin Chow, Hyungkyu Huh, Christoph Forman, Alireza Vali, Andreas Greiser, James Carr, Susanne Schnell, Alex J. Barker, and Ning Jin. Aortic 4D flow MRI in 2 minutes using compressed sensing, respiratory controlled adaptive k-space reordering, and inline reconstruction. *Magn Reson Med*, 81(6):3675–3690, June 2019.

[157] Ashitha Pathrose, Liliana Ma, Haben Berhane, Michael B. Scott, Kelvin Chow, Christoph Forman, Ning Jin, Ali Serhal, Ryan Avery, James Carr, and Michael Markl. Highly accelerated aortic 4D flow MRI using compressed sensing: Performance at different acceleration factors in patients with aortic disease. *Magn. Reson. Med.*, 85(4):2174–2187, April 2021.

[158] Bernd Jung, Matthias Honal, Peter Ullmann, Jürgen Hennig, and Michael Markl. Highly *k-t* -space-accelerated phase-contrast MRI. *Magn. Reson. Med.*, 60(5):1169–1177, November 2008.

[159] Jeremy Szajer and Kevin Ho-Shon. A comparison of 4D flow MRI-derived wall shear stress with computational fluid dynamics methods for intracranial aneurysms and carotid bifurcations — A review. *Magnetic Resonance Imaging*, 48:62–69, May 2018.

[160] Sébastien Levilly, Marco Castagna, Jérôme Idier, Félicien Bonnefoy, David Le Touzé, Saïd Moussaoui, Perrine Paul-Gilloteaux, and Jean-Michel Serfaty. Towards quantitative evaluation of wall shear stress from 4D flow imaging. *Magnetic Resonance Imaging*, 74:232–243, December 2020.

[161] C. Chnafa, K. Valen-Sendstad, O. Brina, V.M. Pereira, and D.A. Steinman. Improved reduced-order modelling of cerebrovascular flow distribution by accounting for arterial bifurcation pressure drops. *Journal of Biomechanics*, 51:83–88, January 2017.

[162] Carolin Wüstenhagen, Kristine John, Sönke Langner, Martin Brede, Sven Grundmann, and Martin Bruschewski. CFD validation using in-vitro MRI velocity data – Methods for data matching and CFD error quantification. *Computers in Biology and Medicine*, 131:104230, April 2021.

[163] Jelena Bock, Johannes Töger, Sebastian Bidhult, Karin Markenroth Bloch, Per Arvidsson, Mikael Kanski, Håkan Arheden, Frederik Testud, Andreas Greiser, Einar Heiberg, and Marcus Carlsson. Validation and reproducibility of cardiovascular 4D-flow MRI from two vendors using 2 × 2 parallel imaging acceleration in pulsatile flow phantom and in vivo with and without respiratory gating. *Acta Radiol*, 60(3):327–337, March 2019.

[164] Catriona Stokes, Mirko Bonfanti, Zeyan Li, Jiang Xiong, Duanduan Chen, Stavroula Balabani, and Vanessa Díaz-Zuccarini. A novel MRI-based data

fusion methodology for efficient, personalised, compliant simulations of aortic haemodynamics. *Journal of Biomechanics*, 129:110793, December 2021.

[165] D. Gallo, G. De Santis, F. Negri, D. Tresoldi, R. Ponzini, D. Massai, M. A. Deriu, P. Segers, B. Verhegghe, G. Rizzo, and U. Morbiducci. On the Use of In Vivo Measured Flow Rates as Boundary Conditions for Image-Based Hemodynamic Models of the Human Aorta: Implications for Indicators of Abnormal Flow. *Ann Biomed Eng*, 40(3):729–741, March 2012.

[166] Romana Perinajová, Joe F. Juffermans, Jonhatan Lorenzo Mercado, Jean-Paul Aben, Leon Ledoux, Jos J. M. Westenberg, Hildo J. Lamb, and Saša Kenjereš. Assessment of turbulent blood flow and wall shear stress in aortic coarctation using image-based simulations. *BioMed Eng OnLine*, 20(1):84, December 2021.

[167] Morgane Garreau, Thomas Puiseux, Ramiro Moreno, Simon Mendez, and Franck Nicoud. A pulsatile 3D flow relevant to thoracic hemodynamics: CFD - 4D Flow MRI comparison, 2021. https://kbwiki.ercoftac.org/w/index.php/CFD_Simulations_AC7-04.

[168] Ramona Lorenz, Jelena Bock, Jeff Snyder, Jan G. Korvink, Bernd A. Jung, and Michael Markl. Influence of eddy current, Maxwell and gradient field corrections on 3D flow visualization of 3D CINE PC-MRI data: Impact Phase Offset Errors on Particle Traces. *Magn. Reson. Med.*, 72(1):33–40, July 2014.

[169] Jing Jiang, Paul Kokeny, Wang Ying, Chris Magnano, Robert Zivadinov, and E. Mark Haacke. Quantifying errors in flow measurement using phase contrast magnetic resonance imaging: comparison of several boundary detection methods. *Magnetic Resonance Imaging*, 33(2):185–193, February 2015.

[170] David O. Walsh, Arthur F. Gmitro, and Michael W. Marcellin. Adaptive reconstruction of phased array MR imagery. *Magn. Reson. Med.*, 43(5):682–690, May 2000.

[171] Christian Ros, S. Witoszynskyj, K. H. Herrmann, and J. R. Reichenbach. Reconstruction of phase images for GRAPPA accelerated Magnetic Resonance Imaging. In R. Magjarevic, J. H. Nagel, Jos Vander Sloten, Pascal Verdonck, Marc Nyssen, and Jens Haueisen, editors, *4th European Conference of the International Federation for Medical and Biological Engineering*, volume 22, pages 803–806. Springer Berlin Heidelberg, Berlin, Heidelberg, 2009. Series Title: IFMBE Proceedings.

[172] F. Ståhlberg, L. Søndergaard, C. Thomsen, and O. Henriksen. Quantification of complex flow using MR phase imaging—A study of parameters influencing the phase/velocity relation. *Magnetic Resonance Imaging*, 10(1):13–23, January 1992.

[173] Kieran R. O'Brien, Brett R. Cowan, Manali Jain, Ralph A.H. Stewart, Andrew J. Kerr, and Alistair A. Young. MRI phase contrast velocity and flow errors in turbulent stenotic jets. *J. Magn. Reson. Imaging*, 28(1):210–218, July 2008.

[174] Richard Frayne and Brian K. Rutt. Understanding acceleration-induced displacement artifacts in phase-contrast MR velocity measurements. *J. Magn. Reson. Imaging*, 5(2):207–215, March 1995.

[175] Hákon Gudbjartsson and Samuel Patz. The rician distribution of noisy mri data. *Magn. Reson. Med.*, 34(6):910–914, December 1995.

[176] Malenka M. Bissell, Francesca Raimondi, Lamia Ait Ali, Bradley D. Allen, Alex J. Barker, Ann Bolger, Nicholas Burris, Carl-Johan Carhäll, Jeremy D. Collins, Tino Ebbers, Christopher J. Francois, Alex Frydrychowicz, Pankaj Garg, Julia Geiger, Hojin Ha, Anja Hennemuth, Michael D. Hope, Albert Hsiao, Kevin Johnson, Sebastian Kozerke, Liliana E. Ma, Michael Markl, Duarte Martins, Marci Messina, Thekla H. Oechtering, Pim Van Ooij, Cynthia Rigsby, Jose Rodriguez-Palomares, Arno A. W. Roest, Alejandro Roldán-Alzate, Susanne Schnell, Julio Sotelo, Matthias Stuber, Ali B. Syed, Johannes Töger, Rob Van Der Geest, Jos Westenberg, Liang Zhong, Yumin Zhong, Oliver Wieben, and Petter Dyverfeldt. 4D Flow cardiovascular magnetic resonance consensus statement: 2023 update. *J Cardiovasc Magn Reson*, 25(1):40, July 2023.

[177] A J Evans, D B Richardson, R Tien, J R MacFall, L W Hedlund, R Heinz, O Boyko, and H D Sostman. Poststenotic signal loss in MR angiography: effects of echo time, flow compensation, and fractional echo. *AJNR*, 14(3):721–729, June 1993.

[178] Steven N. Urchuk and Donald B. Plewes. Mechanisms of flow-induced signal loss in MR angiography. *J. Magn. Reson. Imaging*, 2(4):453–462, July 1992.

[179] Liang Zhong, Eric M. Schrauben, Julio Garcia, Sergio Uribe, Stuart M. Grieve, Mohammed S.M. Elbaz, Alex J. Barker, Julia Geiger, Sarah Nordmeyer, Alison Marsden, Marcus Carlsson, Ru-San Tan, Pankaj Garg, Jos J.M. Westenberg, Michael Markl, and Tino Ebbers. Intracardiac 4D Flow MRI in Congenital Heart Disease: Recommendations on Behalf of the ISMRM Flow & Motion Study Group: Intracardiac 4D Flow MRI in CHD. *J Magn Reson Imaging*, 50(3):spcone–spcone, September 2019.

[180] Ian Marshall. Computational simulations and experimental studies of 3D phase-contrast imaging of fluid flow in carotid bifurcation geometries. *J. Magn. Reson. Imaging*, 31(4):928–934, April 2010.

[181] Artur Klepaczko, Andrzej Materka, Piotr Szczypinski, and Michal Strzelecki. Numerical Modeling of MR Angiography for Quantitative Validation of

Image-Driven Assessment of Carotid Stenosis. *IEEE Trans. Nucl. Sci.*, 62(3):619–627, June 2015.

[182] Scott A. Stevens, William D. Lakin, and Wolfgang Goetz. A differentiable, periodic function for pulsatile cardiac output based on heart rate and stroke volume. *Mathematical Biosciences*, 182(2):201–211, April 2003.

[183] Gilberto Szarf, Yoav Dori, Dan Rettmann, Aylin Tekes, Khurram Nasir, Luciano Amado, Thomas K.F. Foo, and David A. Bluemke. Zero filled partial fourier phase contrast MR imaging: In vitro and in vivo assessment. *J. Magn. Reson. Imaging*, 23(1):42–49, January 2006.

[184] Jonas Walheim and Sebastian Kozerke. On Partial Fourier Acquisition in 4D Flow MRI of Mean Velocities and Turbulent Kinetic Energy. *Proc. Intl. Soc. Mag. Reson. Med*, 25, 2017.

[185] Michael Markl. Velocity Encoding and Flow Imaging, 2005. https://ece-classes.usc.edu/ee591/library/Markl-FlowImaging.pdf.

[186] John N. Oshinski, David N. Ku, Daryl E. Bohning, and Roderic I. Pettigrew. Effects of acceleration on the accuracy of MR phase velocity measurements. *J. Magn. Reson. Imaging*, 2(6):665–670, November 1992.

[187] Hannes Dillinger, Jonas Walheim, and Sebastian Kozerke. On the limitations of echo planar 4D flow MRI. *Magn Reson Med*, 84(4):1806–1816, October 2020.

[188] Petter Dyverfeldt, Roland Gårdhagen, Andreas Sigfridsson, Matts Karlsson, and Tino Ebbers. On MRI turbulence quantification. *Magnetic Resonance Imaging*, 27(7):913–922, September 2009.

[189] Michael Hoff, Jalal Andre, and Brent Stewart. Artifacts in Magnetic Resonance Imaging. In *Image Principles, Neck, and the Brain*, pages 165–190. CRC Press, May 2016.

[190] L D Jou and D Saloner. A numerical study of magnetic resonance images of pulsatile flow in a two dimensional carotid bifurcation A numerical study of MR images. *Medical Engineering*, 1998.

[191] George Em Karniadakis, Ioannis G. Kevrekidis, Lu Lu, Paris Perdikaris, Sifan Wang, and Liu Yang. Physics-informed machine learning. *Nat Rev Phys*, 3(6):422–440, May 2021.

[192] Edward Ferdian, David J. Dubowitz, Charlene A. Mauger, Alan Wang, and Alistair A. Young. WSSNet: Aortic Wall Shear Stress Estimation Using Deep Learning on 4D Flow MRI. *Front. Cardiovasc. Med.*, 8:769927, January 2022.

Abstract

The study of hemodynamics, i.e. the dynamics of blood flow, is considered by the medical community as an essential biomarker to characterize the onset and the development of cardiovascular pathologies. Historically, magnetic resonance imaging (MRI), a non-invasive and non-ionizing technique, allows reconstructing morphological images of the biological tissues. Recent progresses have made it possible to access the temporal evolution of the blood velocity field in the three spatial directions. This technique, known as 4D flow MRI, is still little used in the clinical practice due to its low spatiotemporal resolution and its long scan time.

This thesis aims at studying how the 4D flow MRI sequence performs. To begin with, the impact of accelerated sequences (GRAPPA, compressed sensing) on reconstructed velocity fields is studied in a framework combining experimental measurements in a flow phantom and computational fluid dynamics (CFD) simulations. It is shown that the highly accelerated sequence with compressed sensing is in good agreement with numerical simulation as long as appropriate corrections are applied, namely with respect to the eddy currents. Then, the impact of a sequence parameter, namely partial echo, is investigated. The study is conducted thanks to a methodology coupling the simulation of the MR acquisition process with CFD and allowing to reconstruct synthetic MR images (SMRI). This configuration is freed from experimental errors and allows to only focus on the errors intrinsic to the MRI process. Two realistic constructor sequences, without and with partial echo, are simulated for two types of flow in a numerical flow phantom. For both flows, the sequence with partial echo results in overall better results. It suggests that the mitigation of the displacement artifacts made possible by the partial echo has a greater impact than the reduced MR signal acquired that it induces. Furthermore, the coupled MRI-CFD simulation appears as a tool of interest in the context of sequence design and optimization. It could be expanded to other types of MR sequences.

Keywords : Hemodynamics, Computational fluid dynamics (CFD), 4D flow MRI, MRI simulation.

Résumé

L'étude de l'hémodynamique, c'est-à-dire de la dynamique du sang, est considérée par la communauté médicale comme un biomarqueur essentiel pour caractériser l'apparition et le développement de pathologies cardiovasculaires. Historiquement, l'imagerie par résonance magnétique (IRM), technique non-invasive et non-ionisante, permet de reconstruire des images morphologiques des tissus biologiques. De récents progrès lui donnent aussi accès à l'évolution temporelle du champ de vitesse du sang dans les trois directions de l'espace. Cette technique, connue sous le nom d'IRM de flux 4D, est encore peu utilisée dans la pratique clinique étant donné sa faible résolution spatio-temporelle et sa longue durée d'acquisition.

Cette thèse a pour but d'étudier les performances de la séquence de flux 4D. Dans un premier temps, l'impact de séquences accélérées (GRAPPA, compressed sensing) sur la reconstruction des champs de vitesse est étudié dans un cadre combinant mesures expérimentales sur un fantôme imageur de flux et simulations de mécanique des fluides numérique (MFN). On montre que l'acquisition hautement accélérée avec compressed sensing est en bon accord avec la simulation numérique si les corrections appropriées sont appliquées, notamment par rapport aux courants de Foucault. Dans un second temps, l'impact d'un paramètre de séquence, l'écho partiel, est examiné. L'étude est conduite avec une méthodologie couplant la simulation du processus d'acquisition IRM avec la MFN et permettant de reconstruire des images synthétiques d'IRM. Cette configuration permet de s'affranchir des erreurs expérimentales pour s'intéresser uniquement aux erreurs intrinsèques au processus IRM. Deux séquences constructeur réalistes, sans et avec écho partiel, sont simulées sur deux types d'écoulement dans un fantôme de flux numérique. Pour les deux écoulements, la séquence avec écho partiel donne globalement de meilleurs résultats. Il est ainsi suggéré que l'effet d'atténuation des artéfacts de déplacement permis par l'écho partiel est plus important que celui de réduction du signal IRM acquis. De plus, la simulation couplée IRM-MFN apparaît comme un outil d'intérêt dans le contexte de la conception et de l'optimisation de séquences IRM et pourrait être étendu à d'autres types de séquences.

Mots-clefs : Hémodynamique, Mécanique des fluides numérique (MFN), IRM de flux 4D, simulation d'IRM.